Cold Energy Storage: Fundamentals and Applications

Yanping Du

Submitted in accordance with the requirements for the degree of
Doctor of Philosophy in Engineering

The University of Leeds
Institute of Particle Science and Engineering
School of Chemical and Process Engineering

October 2014

The candidate confirms that the work submitted is his own and that appropriate credit has been given where reference has been made to the work of others.

Acknowledgements

I would like to extend the deepest gratitude to my academic supervisor, Prof. Yulong Ding, for his invaluable supervision and useful suggestions throughout my research work. His knowledge, insight on research, skills on communication, cooperation and time management will provide me with lifelong wealth. I would like to express my extraordinary appreciations for his moral encouragement during my PhD study. His selfless support enables me to complete my research successfully.

I am indebted to my previous supervisor, Prof. Changying Zhao (now in Shanghai Jiaotong University) for his patient guidance on my research. His ways of thinking and strong academic competence will have remarkable influence in my career.

I gratefully acknowledge UK Engineering and Physical Sciences Research Council (EPSRC Reference EP/F060955/1) for the three-year financial support and Institute of Particle Science and Engineering (University of Leeds) for providing me fantastic research sources and environment.

I want to express my sincere thanks to my colleagues in Prof. Ding's research group, for their valuable comments on my research and enthusiastic support to my personal life. Specifically, I am obliged to Dr. Yongliang Li, Dr. Yunhong Jiang, Mr David Lawlor, Ms Jan Bell, Dr. Xinjing Zhang and Dr. Sanjeeva Witharana.

I would like to give my appreciations to my parents and brothers. My father Xiaocai Du and mother Zaoqing Peng give me all of their love and understanding, while my two elder brothers Jianxin Du and Xinyan Du offer me continuous support during my PhD.

Last not least, my gratitude also extends to my wife, Ying Li. She encouraged and assisted me whenever I need regardless of her own stress without any complaints. Without her encouragement and support, I could not imagine how the life would be and how difficult it is for completing my PhD study.

Abstract

This thesis concerns cold energy storage (CES) technology. Such a technology produces cold energy by consuming electricity in a refrigerator and stores cold energy in an eutectic phase change material (PCM) in a temperature range of $\frac{1}{2} \cdot T_a < T_{PCM} < T_a$ (T_{PCM} is the PCM storage temperature and T_a is the environmental temperature), resulting in a cold exergy efficiency less than 100%. The stored cold energy can be either directly extracted by a cold discharge process or utilized through a Rankine cycle at peak hours for electricity generation.

The aim of the research is to study fundamental aspects and address the scientific and technological challenges associated with the CES technology. Methods for storing high grade, high energy density and temperature-adaptive cold energy are to be developed. Another objective is to develop innovative solutions for enhancing charge/ discharge processes. Particular attention is paid to the use of a prototype CO_2 based CES system to investigate the feasibility of CES technology for small scale systems.

In this work, a criteria for PCM selection for high grade and high energy density cold storage is established. For enhancing charging/ discharging rate of a PCM device, metal foams are embedded in PCM to form a PCM composite. Parametric study on the CES system is done based on a CO_2 Rankine cycle for achieving an optimal cold storage efficiency. Investigations have been carried out on the performance of a small scale CES system. These include CES with an open and a close Rankine cycle and a piston based engine for cold to power conversion in the cycle.

A method for improving grade of stored cold energy is using eutectic salt-water solutions for forming a binary/ ternary cold storage system, by which the eutectic temperature is lowered. PCMs with lower freezing temperature and smaller molecular weight are selected as components in the binary/ ternary system. However, due to the potential issue of compatibility of PCM molecular structures, it is critical to select PCMs which have comparable melting temperatures and compatible molecular structures.

PCM composite is formed by embedding metal foams in PCM solutions. Cold discharging rate, defined as the power transfer of cold energy per unit time during the discharge process, is greatly affected by thermal diffusivity and thermal conductivity of the PCM composite. Combined effect of cold

radiation and convection is to be considered for assessing the value of cold discharging rate, which becomes more significant for large PCM capsules under low PCM temperatures and low Reynolds number (Re).

Cold utilisation in a CES system using Rankine cycles is theoretically studied. Storage efficiency of the CES system is a round trip efficiency of electricity, which is defined as ratio of output electricity to the input electricity. A storage efficiency as high as 43.9% has been shown to be possible for the CES system. However, the storage efficiency is generally between 30%~40% in consideration of the actual efficiencies of cryogen pump, regenerator, engine and refrigerator.

Piston based engines with a new valve scheme is experimentally investigated. Compared with small engine, large engine system has apparently larger capacity for power generation, but the engine efficiency is reduced due to the block of the exhaust gas in the chamber. In the presented case study, the efficiency of the large engine is 38.5% while the storage efficiency of the CES system is approximately 22.0%. In the point view of net electricity output for peak-shifting, CES is a feasible technology that need to be further developed.

In brief, the work of the CES research are summarized as follows:

- Improvement of cold charging/ discharging rate by embedding open-cell metal foams in PCM;
- Assessment of cold discharging rate by considering the combined effect of cold radiation and convection;
- Optimization of cold storage efficiency by developing computer program based on sub-critical CO_2 properties;
- Cold to power conversion by using a piston based engine coupled with a new valve scheme.

Table of Contents

List of Tables

List of Figures

Abbreviations

BDC	Bottom Dead Centre
BES	Battery energy storage
CAES	Compressed air energy storage
CCC	Converging Combustion Chamber
CEU	Cold Extraction Unit
CES	Cold Energy Storage
COP	Coefficient Of Performance
CSU	Cold Storage Unit
DSC	Differential Scanning Calorimetry
DSM	Demand Side Management
EC	Electricity consumption for driving the motor
EG	Ethylene Glycol
EHR	Exhaust Heat Recovery
EM	Net electricity consumption on motor
EP	Electricity contributed by engine
FDM	Finite Difference Method
FEM	Finite Element Method
FES	Flywheel energy storage
GTD	Gliding Temperature Difference
HCED	Heat Conducting Enhancement Device
HES	Hydrogen energy storage
HEX	Heat Exchanger
HTF	Heat Transfer Fluid
HTU	Heat Transfer Unit

LA	Lauric Acid
LNG	Liquefied Natural Gas
NTU	Number of Transfer Unit
ORC	Organic Rankine Cycle
PCM	Phase Change Materials
PHES	Pumped-hydroelectric energy storage
RAC	Refrigeration and Air Conditioning
SA	Stearic Acid
SCC	Specific Cooling Capacity
SCES	Super capacitor energy storage
SMES	Super conducting magnetic energy storage
TDC	Top Dead Centre
TES	Thermal Energy Storage

Nomenclature

A	cross-section area of chamber (m^2)
Bi_v	Biot number of a volume
$Bi_{v,e}$	effective Biot number of a volume
Bi_x, Bi_r	Biot number in the x, r direction
C_p	heat capacity of PCM capsules ($kJ/(kg \cdot K)$)
Cp_1, Cp_2	specific heat capacity of component 1 and 2 ($kJ/(kg \cdot K)$)
Cp_e	effective heat capacity ($kJ/(kg \cdot K)$)
Cp_{es}	effective heat capacity of solid PCM ($kJ/(kg \cdot K)$)
Cp'_{1l}, Cp'_{2l}	equivalent heat capacity for pure liquid 1 and 2 ($kJ/(kg \cdot K)$)
Cp_l, Cp_s	specific heat capacity of liquid and solid PCM ($kJ/(kg \cdot K)$)
Cp_p, Cp_f	heat capacity of particle and PCM solution ($kJ/(kg \cdot K)$)
EP_{theo}	theoretical power generation by engine (W)
E_{cool}	electricity consumed by refrigerator for producing coolant (J)
$E'_{cool}(t)$	electricity consumption rate (W)
E_d	energy storage density (kJ/kg)
E_{heat}	electricity consumption in super heater (J)
E_g	energy storage grade
E_{x,Q_0}	cold exergy in PCM (J)
Fo_x, Fo_r	Fourier number in the x, r direction
h	heat transfer coefficient ($W/(m^2 \cdot K)$)
h_e	equivalent heat transfer coefficient ($W/(m^2 \cdot K)$)
h_i	enthalpy of state point in Rankine cycle (kJ/kg)
k_{po}	Poisson factor
k_{eff}, k_e, k_m	effective thermal conductivity ($W/(m \cdot K)$)
k_f	thermal conductivity of fluid (PCM) ($W/(m \cdot K)$)
k_l	thermal conductivity of liquid ($W/(m \cdot K)$)

k_p	thermal conductivity of particles ($W/(m \cdot K)$)
L	length of chamber (m)
$\dot{m}_{CO_2}$	mass flow rate of CO_2 (kg/s)
$\dot{m}_{H_2O}$	mass flow rate of water (kg/s)
$\dot{m}_{in}$	mass flow rate at the engine inlet (kg/s)
$\overline{\dot{m}_{in}}$	average mass flow rate at the engine inlet (kg/s)
M	molecular weight (g/mol)
Nu	Nusselt number
Pr	Prandtl number
P_B, P_C	pressure at point B and C (bar)
P_h	compressed pressure (bar)
Por_1	electricity consumption for driving the motor (W)
Por_2	engine power (W)
$Por_{\max}$	the rated power of the ABB motor drive system (W)
Q_0	heat absorption from environment (J)
Q_2	heat released by exhausted CO_2 in Rankine cycle (J)
Q_c'	cold charging rate (W)
q_{equ}	equivalent heat flux (W/m^2)
q_{con}, q_{rad}	heat flux by convection and radiation (W/m^2)
r_{nano}	radius of the nanolayer (m)
Re	Reynolds number
R_{equ}	equivalent thermal resistance (K/W)
R_{con}, R_{rad}	thermal resistance of convection and radiation (K/W)
R_g	gas constant (for air it is 287.05 $J/(kg \cdot K)$)
R_{ideal}	ideal gas factor (8.314 $J/(mol \cdot K)$)
R_{PCM}	radius of the PCM capsule (m)
t_1	opening time for the injection process (s)
t_{rs}, t_{re}	staring time and final time of melting (s)
TR_{ca}	thermal resistance of capsulation materials (K/W)

Tor_1	torque contribued by electricity consumption ($N \cdot m$)
Tor_2	torque contributed by engine ($N \cdot m$)
$Tor_{\max}$	the maximum torque on the motor ($N \cdot m$)
T_0	initial temperature of PCM (^oC)
T_1	freezing point of water (^oC)
T_2	freezing point of EG (^oC)
T_3	freezing point of EG and water solution (^oC)
T_4	PCM temperature after cooling (^oC)
T_a	ambient temperature (^oC)
T_{air}	air temperature (^oC)
T_{cold}	reference temperature for defining cold grade (^oC)
T_{engine}	engine inlet temperature (^oC)
T_{envi}	environmental temperature (^oC)
T_f	fluid temperature (^oC)
$T_{f,i}$	freezing temperature of the compound i (^oC)
T_{H_2O}	water temperature (^oC)
T_{in}	gas temperature at the inlet of engine (^oC)
T_{inside}	temperature at the centre of the PCM capsule (^oC)
T_{opt}	optimum temperature (^oC)
T_{PCM}	PCM temperature (^oC)
T_r	freezing point of PCM (^oC)
$T_s(t)$	temperature of PCM capsules at time t (^oC)
T_{si}	initial temperature of PCM capsules (^oC)
T_w	surface temperature of the PCM capsule (^oC)
$\overline{T}$	average temperature of the PCM capsule (^oC)
T_β	temperature of β phase fluid in porous media (^oC)
$< T_\beta >$	volume averaged temperature of β phase fluid (^oC)
v	specific volume of gas (m^3/kg)
V	volume of engine chamber (m^3)

$\overline{\dot{V}_{in}}$	average volume flow rate at the engine inlet (m^3/s)
V_β	volume of β phase fluid (m^3)
w	specific power by engine (kJ/kg)
W	total power by engine (W)
$\overline{W}$	average power by engine (W)
W_e	electricity generation by engine (W)
W_p	electricity consumption by pump (W)
W_s	net dynamic power of the Rankine cycle (W)
x	location of piston from the TDC (m)
x_i	molar fraction of the compound i
$x_{pe,1}$, $x_{pe,2}$, $x_{e,3}$	partial-eutectic composition for 1, 2 and 3

Greek Symbols

ϕ_1, ϕ_2	volume fraction of component 1 and 2
ρ	density of PCM capsules (kg/m^3)
ρ_1, ρ_2	density of component 1 and 2 (kg/m^3)
$\overline{\rho}$	averaged density (kg/m^3)
β	state of the PCM solution
$\Theta(x, y, \tau)$	dimensionless excess temperature
ε_s	radiant emissivity
σ	Boltzmann constant (5.67×10^{-8})
δ_{ca}	thickness of capsulation materials (m)
δ_{nano}	thickness of the nanolayer (m)
ΔH_{ls}	latent heat of PCM (kJ/kg)
$\varepsilon_r(t)$	liquid fraction of the PCM during phase change
λ_{ca}	thermal conductivity of capsulation materials ($W/(m\cdot K)$)
ω	motor speed (rpm)
η_{CES}	storage efficiency of CES system

η_{engine}	efficiency of engine
η_{pump}	efficiency of pump
η_h	heat efficiency of Rankine cycle
η_{regen}	efficiency of regenerator
η_{refrig}	efficiency of refrigerator
η'_{engine}	Actual engine efficiency
ε	performance of the heat exchanger
φ	volume fraction of particles
α	ratio of p-crank angle to 180 degree
γ	ratio of nanolayer thickness to particle radius
$\varepsilon_r(t)$	liquid fraction of the PCM

Chapter 1
Introduction

This chapter gives a brief introduction to the background of the cold energy storage (CES) technology, describes the motivation for carrying out the research, and highlights the main scientific and technological challenges of the CES technology, leading to the main aim and specific objectives of this PhD work. Finally, the layout of the thesis is outlined.

1.1 Background

1.1.1 The need for energy storage

Three of main energy challenges are sustaining supply of electrical energy, demand side management (DSM) and effective utilisation of renewable energy [1]. Energy storage can play significant role in all these aspects and has therefore attracted more and more attention in recent years. The importance of energy storage lies in its ability to deal with fluctuation of electricity demand (demand side) and intermittency of renewable resources (supply side) on top of many other advantages.

1.1.1.1 Fluctuation of electricity energy demand

Electrical energy demand fluctuates significantly with time and location. Figure 1.1 shows the fluctuation of daily electricity load in different countries. It is seen that the electrical energy demand in peak hours is approximately 1.5 times the off-peak hours on average. Considerably high difference is seen in some countries such as Japan, where the ratio exceeds 2 times [2]. Peak time occupies about 60% of an average day [3], and the cost difference is also significant.

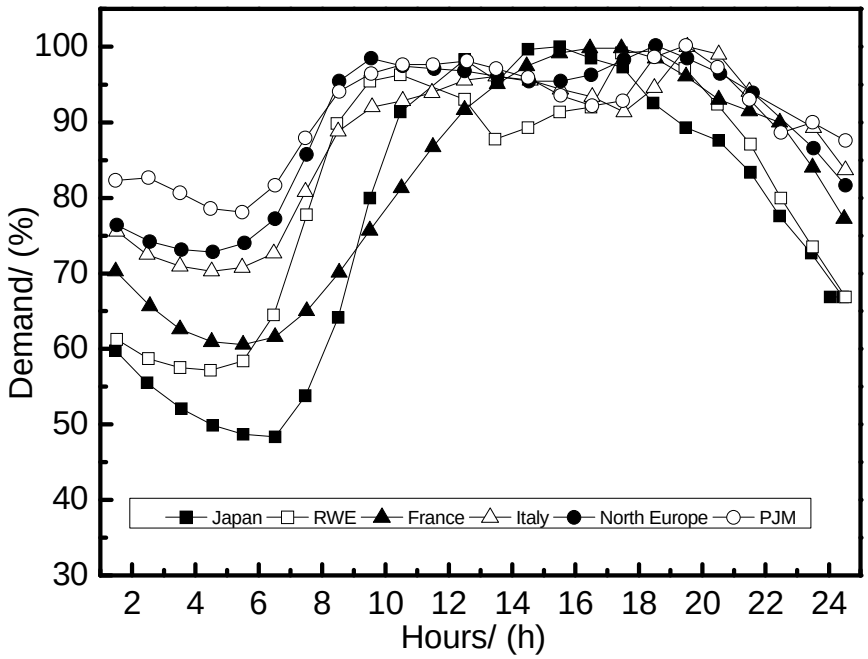

Figure 1.1 Fluctuation of daily electricity load (data from [2])

The effect of demand fluctuation on the economic aspects is further demonstrated in the following:

- Power suppliers. Due to higher electricity consumption in peak time, both cost-effective base-load power plants (e.g. coal-fired and nuclear) and flexible load but less-effective power plants (e.g. oil and gas-fired) are operated to meet the demand. During off-peak time, expensive power plant should be switched off. However, the overall generation costs cannot be effectively reduced, due to compensation for adjusting power generation facilities for peak shifting.
- Consumers. There are different ways to address the issue of expensive electricity, including energy storage, demand side response, interconnection, and flexible generation. These methods are competing with each other and no one is definitely winning. As one of the effective approaches for reducing the cost of electricity, energy storage is highly attractive to customers due to its ability to deal with the unpredictability of the energy demand.

1.1.1.2 Intermittency of renewable resources

Both solar and wind energy resources are intermittent and have a lack of long term predictability.

The intermittency of wind energy can be illustrated in Figure 1.2(a) [4]. Figure 1.2(a) shows on-shore capacity factors of wind energy in high, medium, and low wind cases, where the capacity factor is the ratio of the actual power production to the maximum power capacity of the plant, and is

generally in the range of 20%~40%. One can see from Figure 1.2(a) that, in most time of a year, wind force is far below the installed power capacity due to low estimated capacity factor of around 20%, leading to unreliable electricity supply to the grid.

The intermittency of solar energy can be illustrated in Figure 1.2(b) [5]. Figure 1.2(b) represents the monthly solar energy supply in 1999 in UK. It is seen that the lowest solar energy supply is less than 200 MW in January, which occupies 12.2% of the highest supply in June. As a result, backup costs for solar power plans are increased. Furthermore, the electricity generation by solar energy is not improved in terms of high electricity demand, leading to a shortage of electricity supply in high-demand months.

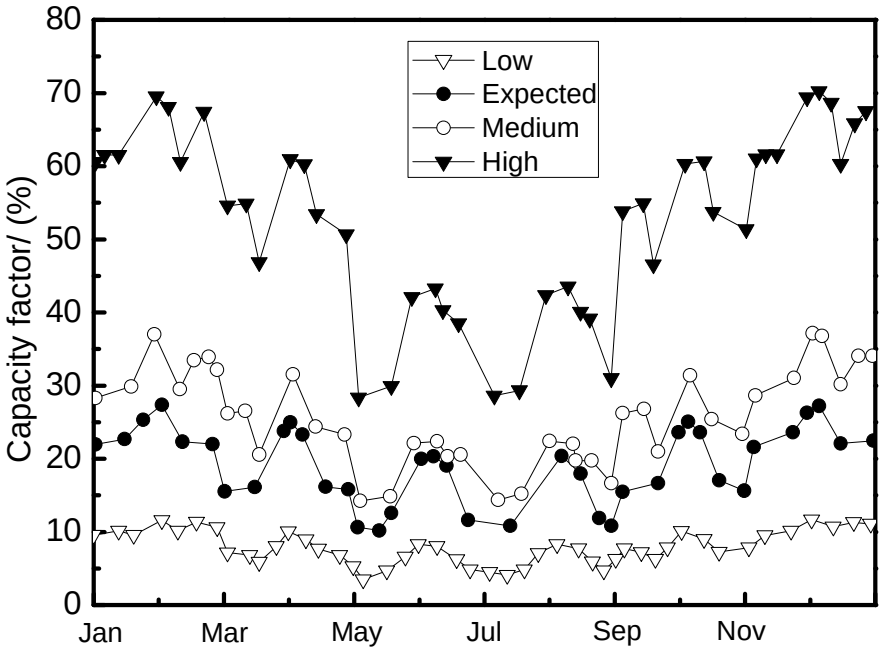

(a)

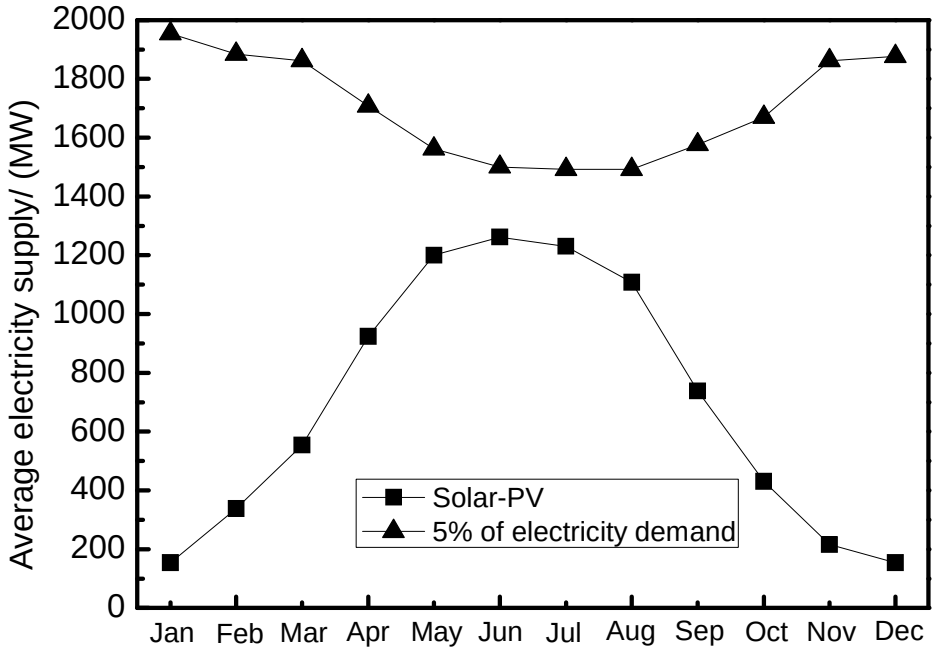

(b)

Figure 1.2 Intermittency of renewable resources: (a) on-shore capacity factor of wind energy (data from [4]); (b) intermittent solar energy supply by month in UK (data from [5])

1.1.2 Cold energy storage technology

As one of the potentially feasible solutions for reducing the effects of demand fluctuation and supply intermittency, energy storage is gaining increasing attention. Except for CES technology, there are many established energy storage technologies. Examples include pumped-hydroelectric energy storage (PHES), compressed air energy storage (CAES), thermal energy storage (TES), battery energy storage (BES), flywheel energy storage (FES), super capacitor energy storage (SCES), super conducting magnetic energy storage (SMES) and hydrogen energy storage (HES).

- Technical maturity. PHES is a mature energy storage technology that accounts for more than 99% of bulk storage capacity worldwide. Developed technologies includes CAES, TES, BES, FES, SCES, SMES, HES. Commercialized systems for these technologies are available; but the competitiveness of large scale system for actual applications still need to be proved. Compared with mature or developed energy storage technologies, CES technology is a developing technology that has being investigated by various research organizations. CES technology is compared with established energy storage technologies as follow:
- Storage efficiency. Technologies such as BES (Li-ion battery), FES,

SCES and SMES have a very high storage efficiency of more than 90%, while technologies such as PHES, CAES and BES (excluding Li-ion battery) have medium efficiency in the range of 60%~90%. Currently, CES is a low-efficient technology that can utilize less of 50% of the stored cold energy that is converted by electricity.

- Energy storage density. The energy storage density is defined as the stored energy divided by the volume or mass of the system. PHES, FES, SCES and SMES have energy storage density below 30 Wh/kg. As a comparison, CES, CAES, TES and BES (conventional batteries) has relatively higher density.
- Life time. The life time of BES is relatively short due to the chemical deterioration during the operating time. However, mechanical energy storage (i.e. PHES and CAES) and thermal energy storage (i.e. TES and CES) have long life time.
- Environmental concern. CES technology has positive environmental effect while technologies including PHES, CAES, BES, SMES have negative influences.
- Capital cost. As other technologies such as PHES, CAES, TES and BES, CES technology has a low capital cost.

Due to the benefits of high energy storage density, long life time, little environmental concern and low capital cost, CES is highly potential to be commercially used in the future.

As one of TES technologies, CES technology can utilize low cost electricity in off-peak time and waste heat recovery from renewable energies and industrial processes. This allows electricity to be stored in the forms of sensible and latent heat cold energy with improved efficiency. Although sensible heat energy storage has higher possible heat capacity, latent heat energy storage has been a subject of many investigations due to large energy storage density and small temperature fluctuation during the phase change process [5-10]. This work concerns the use of cold energy storage, particularly latent heat based storage method.

Physically, cold energy storage covers a wide temperature range below the environmental temperature. For applications close to the ambient conditions, cold storage can be divided into three categories [10-11]: (i) Chilled water storage; (ii) PCM cold storage; (iii) Ice or ice slurry storage. The cold storage density in chilled water storage systems is approximately 12 kW/m^3, resulting in a large space requirement for storing cold. Although ice or ice slurry storage has a cold storage density of as high as 73 kW/m^3, the

application is restricted due to contradiction of ice melting point and the temperature of applied environment, particularly for deep cold storage applications [11].

Due to the advantages of the PCMs, cold storage based on such materials has been a hot topic over the past few decades. The PCMs used for energy storage can be further divided into single-component PCMs, and binary and multi-component PCMs, which is categorized as eutectic and non-eutectic PCMs. Eutectic PCMs have high thermal conductivity, large latent heat and narrow phase change temperature range under eutectic composition [12]. Consequently, in this study, the characteristics of cold energy storage based on eutectic PCM solutions are investigated .

1.2 Main scientific and technological challenges in the CES technology

1.2.1 Small cold storage density

Cold storage density is the specific cold energy stored in PCM solution, which can be defined as in Eq. (1.1):

$$E_d = \begin{cases} Cp_l \cdot (T_a - T_{PCM}) & (T_{PCM} > T_r) \\ Cp_l \cdot (T_a - T_r) + \Delta H_{ls} + Cp_s \cdot (T_r - T_{PCM}) & (T_{PCM} \le T_r) \end{cases} \quad (1.1)$$

In which Cp_l and Cp_s are specific heat capacity of liquid and solid PCM; T_{PCM} , T_a and T_r are the PCM storage temperature, ambient temperature and melting point of PCM, respectively; ΔH_{ls} is the latent heat of PCM. One can see that cold storage density is mainly determined by latent heat, heat capacity of the PCM and the temperature difference between the PCM and the environment. Since all of the above parameters can be improved by using eutectic PCM solutions, the cold storage density can be largely increased.

However, in a binary or ternary PCM solution, the improvement of cold storage density is challenged by the phase separation and low super cooling [13]. Phase separation causes loss of solidification enthalpy, resulting in a decreased cold storage density [14]. While super cooling causes super cooling degree in a PCM solution, leading to a reduced cold energy storage under the phase change temperature.

Methods for addressing the phase separation issue are suggested as the addition to water of a gelling agent (e.g. polymer) [15] and a thickening agent (e.g. cellulose derivatives) [16]. By adding nucleating agents or exerting

physical fields, super cooling degree can be effectively restrained [17]. Common nucleating agents include carbon nanofibers, copper and titanium oxide, potassium sulphate and borax [12].

1.2.2 Low cold charging/discharging rate

Cold charging/ discharging rate represents the heat releasing/ absorption per unit time (W) during the cold charge/ discharge processes. For PCM based cold storage, low thermal conductivity of PCMs is a challenge that limits the charge/ discharge kinetics [18-20]. This challenge can be addressed by using heat transfer intensification methods.

There are many ways to enhance heat transfer, which can be divided into three categories: (i) thermal conductivity improvement through the addition of materials with a high thermal conductivity in PCM; (ii) contact area increase through the use of embedded fins in PCM, capsules of PCM, or multi-tube configuration; (iii) convective heat transfer enhancement of PCM by direct contact of insoluble PCM and heat transfer fluid.

1.2.3 Low exergy efficiency in power generation

Cold exergy in PCM ($T_{PCM} < T_a$) is defined as the maximum useful power that is obtained in the process of heat absorption Q_0 from environment, which can be calculated as:

$$E_{x,Q_0} = (\frac{T_a}{T_{PCM}} - 1) \cdot Q_0 \tag{1.2}$$

In which T_a , T_{PCM} are the ambient temperature and PCM storage temperature, respectively. From the above equation, the exergy efficiency is obtained:

$$\eta_{Ex} = \frac{E_{x,Q_0}}{Q_0} = (\frac{T_a}{T_{PCM}} - 1) \tag{1.3}$$

which is improved with the decrease of PCM storage temperature. Cold energy storage (CES) is defined when PCM storage temperature is in the range of $\frac{1}{2} \cdot T_a < T_{PCM} < T_a$, leading to an exergy efficiency of less than 100%. While the storage is called as cryogenic energy storage in the condition of $T_{PCM} < \frac{1}{2} \cdot T_a$. Theoretically, the exergy efficiency of cryogenic energy storage can be larger than 100%. Comparisons of the above categories of cold storage are illustrated in Table 1.1.

Table 1.1 Features of two categories of cold storage

Categories / Features	Cold energy storage (CES)	Cryogenic energy storage
Storage temperature	$\frac{1}{2}\cdot T_a < T_{PCM} < T_a$	$T_{PCM} < \frac{1}{2}\cdot T_a$
Storage media	Eutectic/ non eutectic PCMs	Liquid coolant (liquid N2, CH4, air, ect)
Cold forms	Sensible heat + solid-liquid latent heat	Sensible heat + gas-liquid latent heat
Dynamic properties	Weak (due to large viscosity)	Strong
Exergy efficiency	<100%	>100% (theoretically)

The above definition of exergy efficiency is based on reversible Carnot cycle, leading to the maximum cold exergy efficiency. Open Rankine cycle and close Brayton cycle have been largely investigated for utilizing cold exergy stored in PCMs on automotive purposes [21-22]. It was reported that cryogenic energy storage system based on liquid nitrogen has a low exergy efficiency of 40%~50% according to current energy consumption of typical air liquefaction processes[23].

In consideration of actual engine efficiency in a power generation system, the exergy efficiency is even lower due to loss of exergy in the process, such as gas leakage and insufficient gas expanding. For instance, with an engine efficiency of 70%, the total exergy efficiency of the cold energy storage is reduced to 28%~35%.

Although thermal dynamic cycles and engine technology have been largely investigated [21-22, 24-25], low exergy efficiency of cold energy storage system is still a big issue that need to be addressed.

In this work, the above scientific and technological challenges are discussed for achieving a feasible cold energy storage system that can be used in small scale district.

1.3 Aim and objectives of this research

The aim of this work is to address the scientific and technological challenges outlined above. The specific objectives are:

- to develop high grade, high energy density and temperature-adaptive storage technologies for cold energy storage;
- to develop methods for enhancing charge/ discharge kinetics; and
- to use a prototype CO_2 based CES system to investigate the feasibility of CES technology.

To meet the above specific objectives, the focuses of the work are on the following:

(A) Establishment of a method for PCM selection for high grade and high energy density cold storage;

(B) Investigation of charge/ discharge enhancement using metal foams as a matrix in PCM;

(C) Optimization of energy storage efficiency through a subcritical CO_2 Rankine cycle;

(D) Development of a piston based engine system for power generation in the CES system.

1.4 Layout of the thesis

The thesis consists of 7 chapters of introduction, literature review, cold energy storage, cold extraction (by direct discharge), cold utilisation (through thermodynamic cycles), cold to power conversion, and conclusions. They are briefly outlined in the following:

Chapter 2 provides a comprehensive literature review on improving cold energy storage, cold extraction, cold utilisation, and cold to power conversion in CES systems.

Chapter 3 reports the study of properties of eutectic water-salt solutions (as cold storage media) with an aim to establish a method for PCM selection to achieve a high cold storage density.

Chapter 4 discusses the method for enhancing the cold discharging rate of a CES system, including a heat transfer analysis of PCM embedded in metal foams and an overall assessment of cold discharging rate considering the combined effect of heat convection and cold radiation.

Chapter 5 describes the work on a cold energy storage based on a sub critical CO_2 Rankine cycle. This includes simulation and optimization of a closed Rankine cycle and experimental work on an open Rankine cycle.

Chapter 6 presents the work on a piston based engine for the CES technology with the closed Rankine cycle. This includes experimental study and theoretical analysis of engine performance.

Chapter 7 summarizes the main conclusions of the work and provides recommendations for the future work.

Chapter 2
Literature Review

This chapter provides a comprehensive review of published work for CES study. The focus is on methods and technologies for improving performance of a CES system, including cold energy storage, cold extraction, cold utilisation and cold to power conversion.

2.1 Improvements on cold storage

Cold storage discussed here is defined as producing cold energy by consuming electricity in a refrigerator and storing cold in PCMs in a temperature range of $\frac{1}{2} \cdot T_a < T_{PCM} < T_a$, resulting in a cold exergy efficiency less than 100%. In this section, solutions for improving cold energy storage in a refrigerator are reviewed. These include PCM based refrigerators, design of evaporators and PCM cold storage in the refrigerator.

2.1.1 PCM based refrigerators

Expect for small cold storage density, slow discharge kinetics and low exergy efficiency for power generation, an additional but main disadvantage of the CES technology is temperature fluctuations during the charge and discharge processes. This leads to a decrease in the coefficient of performance (COP) of refrigerators and hence losses of electricity and reduction in the cold storage efficiency [26-28]. Due to the ability to maintain temperatures during phase change, PCM based refrigerators have been proposed for use in CES systems [29].

A PCM based refrigerator in a CES system uses PCM located inside the refrigerator to reduce temperature fluctuations due to natural heat loss, door opening, defrost operations and electrical energy failures during the charge and discharge processes [30].

The effects of the use of PCM on energy consumptions and temperature fluctuations under the above situations have been investigated by various groups [31-36]. Effect of door opening were carried out in [31-32]. Gin et al [31] used NH_4Cl-water solution (mass fraction of NH_4Cl:19.5%, freezing point: -15.4 ^{O}C) in a domestic freezer with an aim to reduce temperature fluctuation due to door opening. They showed 7% reduction of energy consumption due to the use of PCM. Oro et al [32] used a commercial PCM

of Climsel-18 (sodium nitrate dissolved in water with some additives, freezing point: -18^{O}C) in a commercial freezer in a frequent door opening situation. It was found that the temperature of the freezer was approximately 4~6^{O}C lower by using PCM at different locations in the freezer.

Defrost operations have been investigated in [33-34]. Frost is formed on the coil surface of the refrigerator in the condition of temperature lower than dew point of atmosphere and freezing point of water. Due to the COP of the freezer is affected by the frosting effect, periodic defrost operations are significant for reducing energy consumption during charge/ discharge processes [33]. Defrost cycles in a PCM based refrigerator using aqueous ammonium chloride solution as a cold carrier were studied [34]. The use of PCM reduced the temperature fluctuations and a decrease in the electricity consumption by 8% could be achieved during the defrost cycles.

No electricity supply situations were largely investigated [32, 35-36]. Oro et al [32] claimed that the interior temperature of the PCM based refrigerator can maintain -12~-14^{O}C within 3 hours' electrical energy failure, due to the latent cold energy extraction from PCM. Critoph [35] and Telto et al [36] investigated the COP and temperature fluctuations of refrigerator in the case of electrical energy failure using eutectic salt-water solutions as PCMs in the refrigerator. The freezer with the PCM could supply cold continuously without an electrical energy supply for 5~9 hours. This was twice longer than that without the use of PCM. The COP of the system was found to be improved by 10%~30%.

PCM based refrigerators under the above situations have significant effects on the increase of COP of refrigerator and hence energy saving during cold energy storage. The focus of this research is on PCM locations and orientation and PCM integration with refrigerator with an aim of improving cold storage efficiency.

2.1.1.1 PCM locations and orientation

For maintaining a stable temperature of a refrigerator, PCM is often located inside internal walls of the freezer or close to the evaporator [37-40]. Onyejekwe [37] studied the effect of location of a PCM (NaCl-water solution) container inside a domestic freezer. A vertical orientation could reduce the variation of temperature in the freezer, compared with the horizontal case. The results also showed that the PCM placed very close to the base of the freezer led to a larger COP of the freezer. Gin and Farid [38-39] placed PCM (NH_4Cl-water solution) panels on the internal walls of a domestic freezer.

Energy consumptions with the PCM panels were measured during defrost cycles and compared with that without PCM. The effects of frequent door opening and no electrical energy supply situations were examined. Figure 2.1 shows temperature fluctuations in the case of no energy supply. It is seen that the use of PCM gives much lower temperature fluctuations, indicating a reduced energy consumption in the PCM loaded refrigerator.

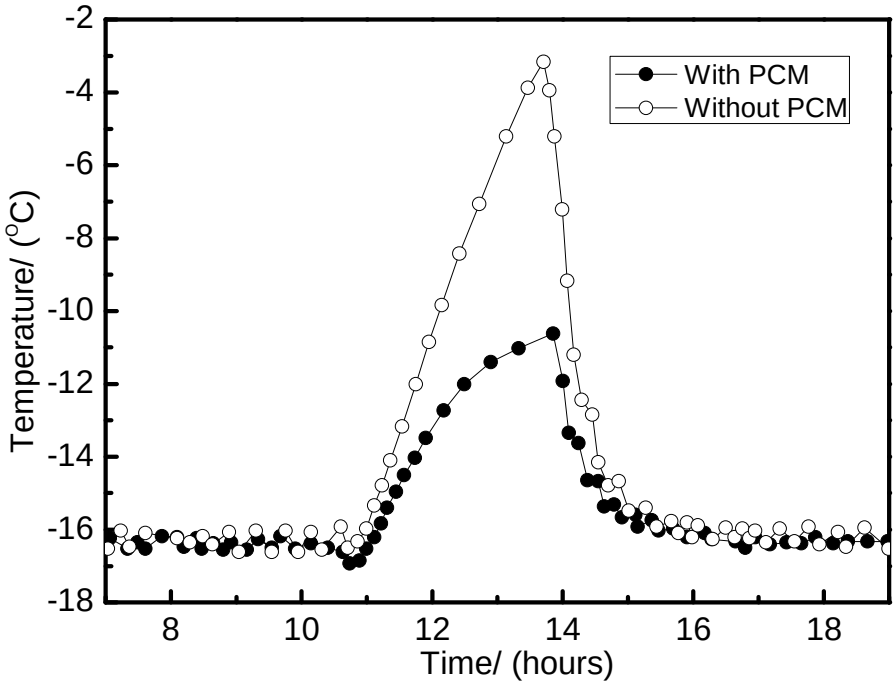

Figure 2.1 Temperature fluctuations in refrigerator with electrical energy loss (data from [39])

Azzouz et al [40-41] investigated the use of PCM in a position close to the evaporator of a refrigerator. They showed that the frequency of starts and stops of the compressor due to temperature fluctuation was significantly reduced. The COP of the freezer was found to be increased by 5%~15%. When the electrical energy source was shut, the refrigeration could maintain several hours.

The results so far indicate that the use of PCM at positions close to evaporators is much better than that placed in internal walls in the refrigerator. Due to cold energy compensation by PCM at positions close to the evaporator, evaporating temperature in the refrigerating cycle maintains a low value, leading to smaller temperature fluctuation and lower energy consumption in the freezer. The influence of evaporating temperature on COP of a refrigerator has been demonstrated with details by Liu [42].

2.1.1.2 Integration of PCM with refrigerator

Apart from minimising temperature fluctuations in refrigerators for cold storage, PCM can also be used in refrigeration and air conditioning (RAC) systems to provide capacity for reducing the cold load fluctuations. This has been used as a method for the demand side management (DSM) [43]. Integration of PCM with refrigerator occurs through heat exchangers (HEX) in the refrigerating cycle. Energy consumption in such cases can be reduced, leading to an increased cold storage efficiency in CES system.

Incorporating heat exchangers containing PCM into different locations of refrigeration cycles has been investigated [44-46]. These positions include after condenser as a cold load, before condenser as a pre-condenser and after an evaporator. A diagram of a PCM containing heat exchanger connected to a refrigerating cycle is shown in Figure 2.2.

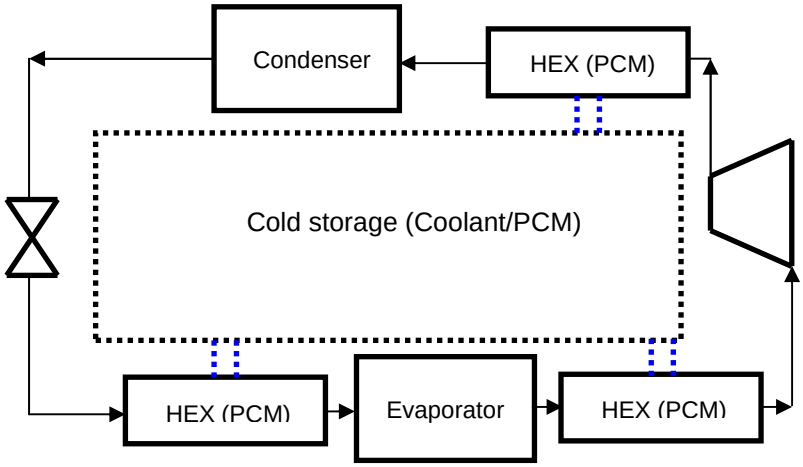

Figure 2.2 PCM containing heat exchangers integrated into a refrigerator

PCM integration with refrigerators can be classified into two categories in terms of purposes of the PCM module:

(a) to supply an artificial cold load during night time. Since electrical consumption for cold storage is smaller at night due to lower ambient temperature, the excessive off-peak electricity could be stored as cold in PCM panels integrated in refrigerators for use in day time. Ure [44] reported that peak plant efficiency was improved by 10% in the condition of increasing sub-cooling level by 15 K. PCM heat exchangers integrated into a real plant under the UK climate conditions has been experimentally investigated by Wang et al [45]. They showed that energy consumption could be reduced by up to 8% and COP of refrigerators could be improved by 6% when lowering refrigerant temperature by locating PCM heat

exchangers before the condenser as a pre-condenser in the refrigerator system.

(b) to limit super heat of refrigerant by providing thermal capacitance. The refrigerant temperature can be super heated after evaporation, which would affect the COP of refrigerators, leading to a decreased cold storage efficiency. Ure [44] claimed a peak efficiency increase by 15% in the case of reducing super heating of refrigerant by 5 K. As reported by Wang et al [45], the benefits of limiting super heating was significantly affected by extra pressure drop in the pipeline due to the addition of PCM heat exchangers in the refrigerator cycle. However, the increase of pressure drop could be effectively restrained through controller operation in the real plant [45-46].

From the above review, one can see that, with the integration of PCM panels or heat exchangers into refrigerators, both the COP of the refrigerator and the cold storage efficiency of the PCM based refrigerator are improved. However, heat transfer behaviours in the integrated systems need to be further studied.

2.1.2 Design of evaporators

Evaporator is one of the most important components in the refrigerating cycle. For improving cold storage efficiency, the following three aspects need to be considered: (i) heat transfer area; (ii) size effect on heat transfer performance; (iii) irreversibility due to evaporation. In this section, internally finned evaporators, micro-finned or channelled evaporators and dual evaporators are reviewed.

2.1.2.1 Internally finned evaporators

The use of fins on evaporators is an effective method for increasing heat transfer area. Since the main thermal resistance is on the inner refrigerant side of evaporators, internally finned evaporators have been designed and studied [47-49].

Tan et al. [47] experimentally investigated heat transfer enhancement of a round-type fin inside an evaporator installed in refrigerating vehicles. Water was used as the PCM located outside the evaporator, while cryogenic nitrogen was used as the refrigerant flowing inside the evaporator. The thermal resistance on the nitrogen side in the internally finned evaporator was reduced from 0.56 K/W to 0.02 K/W. Consequently, the cold storage efficiency was largely improved.

Wu et al [48] proposed a flat-type louvered fin evaporator for refrigerators. R404A was used inside the evaporator as the refrigerant while air flowed across as the heat source. Compared with round-type heat exchangers, the heat transfer coefficient of flat-type fin evaporator was found to be increased by 13%. Kim et al [49] further investigated the air-side heat transfer performance of flat-type tube and multi-louvered fin heat exchangers. The effects of flow depths, louvered fin angles and fin pitches were investigated. The influence of fin pitch was relatively small. However, both flow depth and fin angle had significant effects on heat transfer coefficients. With flow depth decreasing, heat transfer was enhanced. With fin angle increasing from 15^o to 30^o, the heat transfer coefficient was improved by at least 15%. It was noted that the effect of fin angle was dependent on flow depth, fin pitch and also other parameters.

However, for both the round-type and flat-type fins, when evaporating temperature of refrigerant is lower than the freezing point of PCM stored in the refrigerator, remarkable solidification layer is formed along both radial and axial directions of the evaporator. This increases the thermal resistance in the evaporator. The thermal resistance ratio of solidification layer is defined as the thermal resistance of the solid layer on the surface of evaporator to the total thermal resistance of the heat exchanger, as shown in Figure 2.3. It is also noticed that with time increasing, thermal resistance of solidification layer outside the evaporator plays a more dominant role in the heat transfer performance beyond about 60 minutes. With increasing of temperature difference between the refrigerant and the PCM, the negative influence of the solidification layer becomes more and more significant, which needs to be addressed in the design of an evaporator in a refrigerating cycle.

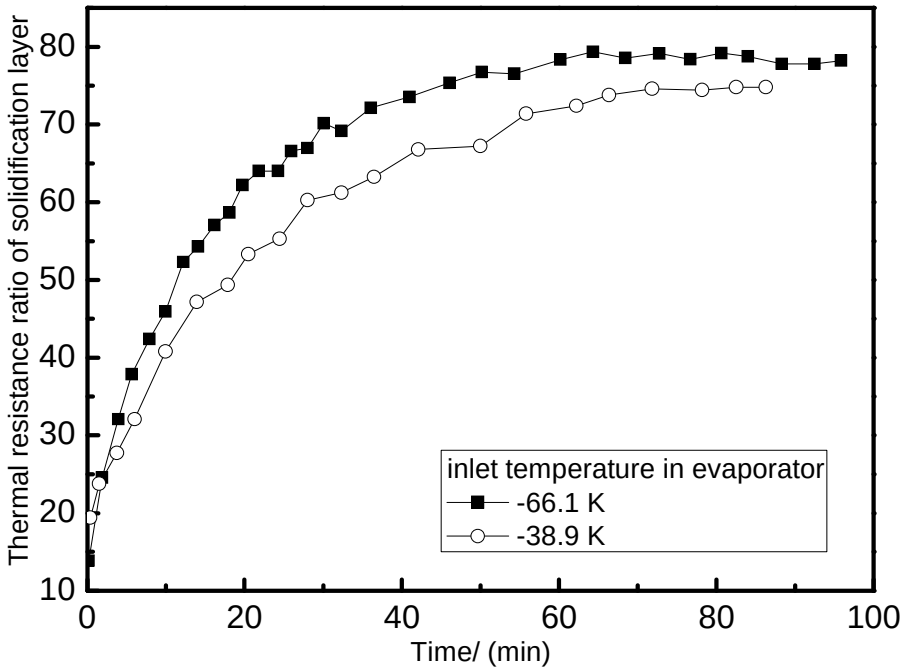

Figure 2.3 Distribution of thermal resistance ratio (%) of the solidification layer (data from [47])

2.1.2.2 Micro finned or channelled evaporators

A potential solution to enhance heat transfer performance is the use of micro-finned or micro-channelled heat exchangers for evaporators and condensers [50-54].

Typical examples of micro-fin surface are summarized in Table 2.1. When used in an evaporator, heat transfer can be enhanced by up to 100% [50]. Schlager et al [51] studied the effect of the use of configurations with an angle of 15^o,18^o and 25^o with R-22 as a working fluid. They found that the heat transfer coefficients with the use of micro-fins were considerably larger than that using conventional fins.

Table 2.1 The characteristics of micro-fin

Characters	Tube diameter	No. fins	Fin height	Fin pitch	Helix angle	Country of manufacturer	Heat transfer enhancement
triangular section helix angle	6.35~15.9 *mm*	60~80	0.30~0.35 *mm*	0.58~0.76 *mm*	8~30 degree	Japan Europe USA	up to 100%

Micro-channel heat exchangers have been studied by numerous researchers. Ravigururajan et al [52] conducted an experimental study on

micro-channel heat exchangers for two-phase flows using a large range of heat flux and mass flux. Heat transfer coefficient was related to the heat flux, the mass flux, the quality and the surface super heat. Jiang et al [53] investigated forced convection heat transfer in micro-channel heat exchangers. They found that the maximum heat transfer coefficient in the micro-channel heat-exchangers was 13.3 $kW/(m^2 \cdot K)$ at a mass flow rate of 0.34 kg/s, which was 7 times higher than that in tube-shell heat exchangers for water-water heat exchange. Some of the overall heat transfer data for water-water micro-channel heat exchangers are summarized in Table 2.2.

Table 2.2 Heat transfer coefficients for water-water micro-channel heat exchangers

Researchers	Channel width (mm)	Channel depth (mm)	Overall heat transfer coefficient ($kW/(m^2 \cdot K)$)
Cross et al[50]	0.4	0.3	4.0
Bier et al[51]	0.1	0.078	22.8
Kang et al[52]	0.26	0.08	6.44
Jiang et al[53]	0.2	0.6	13.3

Han et al [54] reviewed the heat transfer characteristics in micro-channel heat exchangers. They regarded different heat transfer characteristics of conventional heat exchangers from micro-channelled ones was due to the small scale effect which enhanced the fluid compressibility, the drag coefficient, the surface force effect and the impact of axial heat conduction of micro-channel walls.

2.1.2.3 Dual evaporators

For a traditional refrigerator, the refrigerant temperature in its evaporator is much lower than that of the storage medium (e.g. PCM solution). A large temperature difference has a negative effect on the coefficient of performance (COP) of the refrigerator due to irreversibility of heat transfer processes. This can be alleviated by the use of a dual evaporator in the refrigerator system.

An example is the Lorenz-Meutzner (LM) cycle based refrigerating system. In such a system, two evaporators are connected in series, termed F-

evaporator in the freezer compartment and R-evaporator in the cold storage compartment, as demonstrated in Figure 2.4. A Zeotropic refrigerant mixture is used as the working fluid. This results in an appropriate gliding temperature difference (GTD) between the two evaporators. For cold energy storage charged by the R-evaporator, the average temperature difference between the refrigerant and cold carrier is consequently reduced, leading to the improved COP and cold storage efficiency due to reduced irreversibility of the cold charge process.

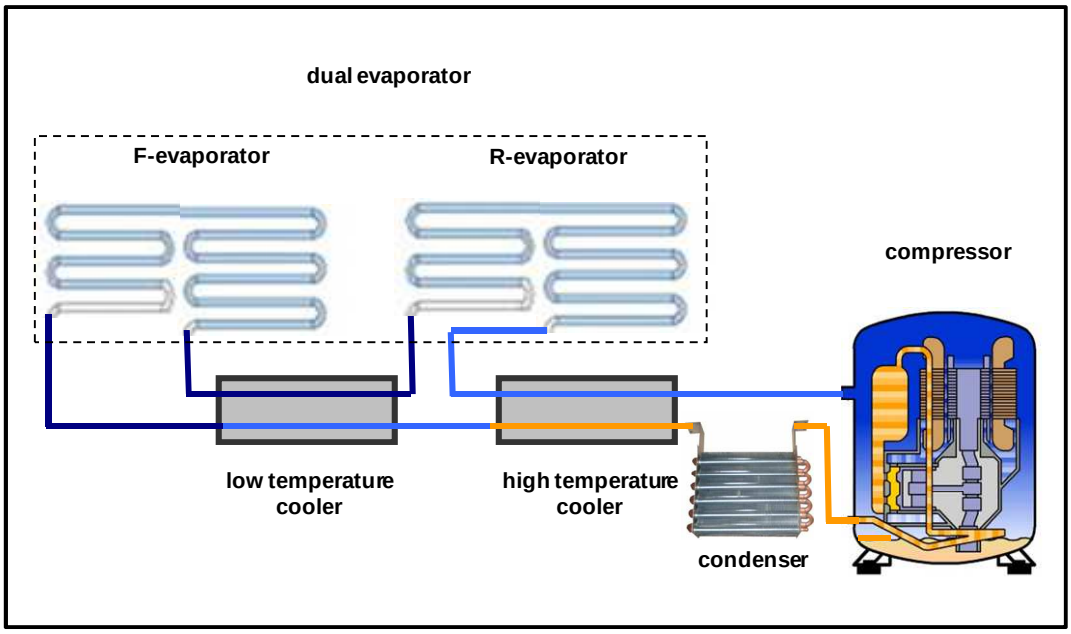

Figure 2.4 Lorenz-Meutzner cycle based refrigerating system

Radermacher et al [55] reported that the use of a dual evaporator refrigerator based on the Lorenz-Meutzner cycle could save up to 20% electricity when using R22/R11 mixture as the refrigerant.

Various methods have been proposed to improve the performance of dual evaporators [56-58]. Tulapurkar et al [56] designed a dual evaporator based domestic refrigerator with appropriate PCM. Off-time of the compressor in the refrigeration cycle was prolonged due to the use of the sub-cooling PCM in dual evaporators. Compared with the conventional single-evaporator refrigeration cycle, the COP of the above system was improved by approximately 20%. Gerlach et al [57] studied the size of the R-evaporator in a dual-evaporator based refrigerator. They found that enlarging the size of the cold storage evaporator (R-evaporator) had no significant effects on improving COP of the refrigerator. However, the enlargement did contribute to the increase of the storage capacity. Miyazaki et al [58] proposed a design

of dual-evaporator refrigerator driven by waste heat through a three-bed adsorption cycle. It was found that the COP and the specific cooling capacity (SCC) in the chiller system were improved by 70% and 50%, respectively.

2.1.3 PCM cold storage

In a cold storage unit (CSU), cold storage density and cold grade are two important factors that affect the performance. These two factors could be improved by using PCM cold storage with high latent heat and low storage temperature.

Based on the above and discussion before, one can draw an ideal list of requirements for PCMs: large latent heat, proper freezing temperature, high thermal conductivity, low super cooling and excellent cyclic and chemical stability [59]. Obviously, it is less likely that one can find ideal PCMs. In the following, various PCMs are briefly summarized.

2.1.3.1 Non-eutectic water-salt solutions storage

Non-eutectic water-salt solutions usually have medium latent heat and thermal conductivity. The advantages of such materials are that they are less corrosive and little super cooling. As a result, this type of PCMs can be used in cases regarding high cyclic operations and chemical stability. The mostly common used non-eutectic water-salt solution PCMs are listed and discussed as follows.

(1) Alcohol based water solutions for industrial refrigeration

This has been studied extensively due to favourable latent heat, thermal conductivity and flow resistance as a cold carrier in cold storage systems. The freezing point of the solution tuned by changing alcohol concentration.

Hägg et al [60] investigated the relationship between the freezing point and concentration of alcohol solutions including propylene glycol, ethanol, ethylene glycol, glycerol and methyl alcohol. Figure 2.5 shows the results. One can see that glycerol water solutions are better for suppressing the freezing point, which can be applied to a precise control of the cold temperature in medical treatment. In contrary, methyl alcohol is better for lowering the freezing point.

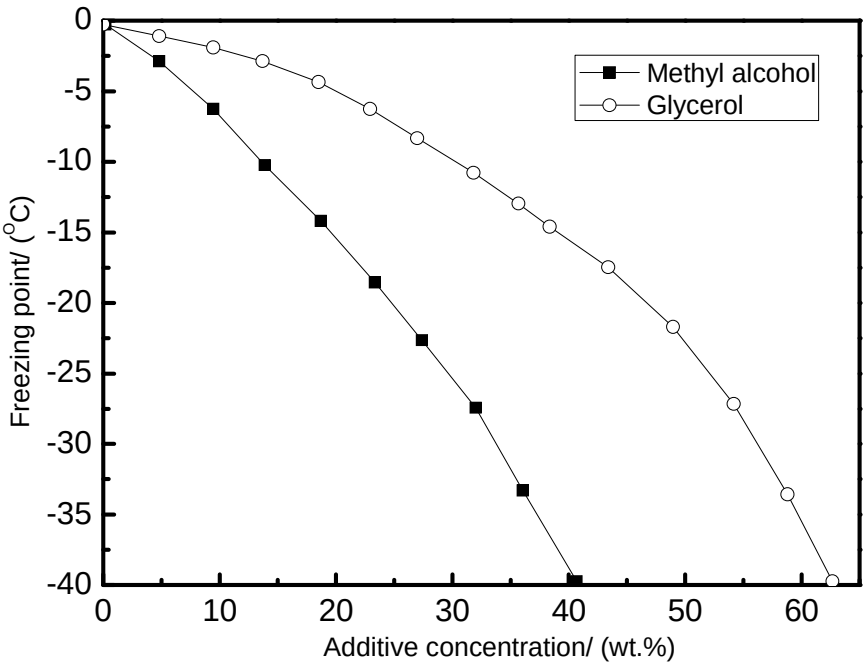

Figure 2.5 Freezing point as a function of the PCM concentration

Kumano et al [61] studied the effective latent heat of propylene glycol, ethylene glycol, ethanol, NaCl and $NaNO_3$ solutions using an energy balance equation, considering latent heat of pure ice, effects of freezing temperature depression and dilution in the calculation. Latent heat obtained by them are consistent with that reported in [60], as shown in Figure 2.6. An increase in the alcohol concentration decreases the latent heat of the solution and the freezing temperature. The cold storage capacity is therefore reduced but the cold grade is improved.

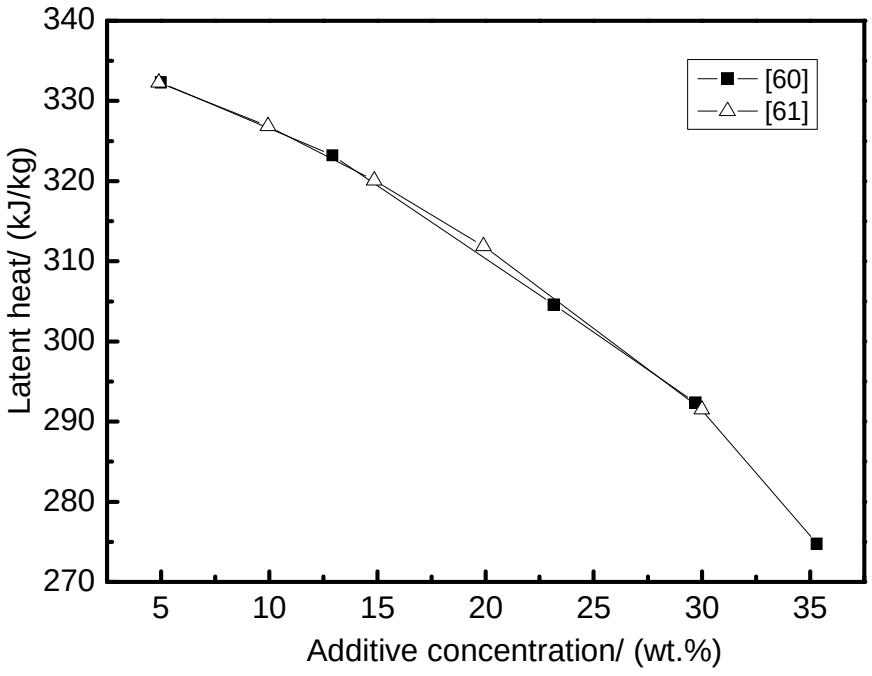

Figure 2.6 Latent heat distribution with addictive concentration

(2) Paraffins

For cold storage over a temperature range of -5~-10 ^{o}C (e.g. air conditioning), ice or ice slurries, hydrated salts and paraffins are main storage materials. Paraffins have a high energy efficiency due to the small temperature gap with the environment during phase change process and hence are a popular option [62].

Paraffins are mixtures of saturated hydrocarbons, which can be produced from petroleum refining process. Compared with inorganic based PCMs, paraffins have a high cyclic life and good chemical stability with little or no super cooling and phase separation. The main drawback of paraffins is their relatively low thermal conductivity, leading to low cold charge/ discharge kinetics. Butala et al [63] integrated RT20 into an air heat exchanger to store cold from low temperature air during night time. Although cold storage density of paraffins can be as high as 172 kJ/kg within a temperature range of 11~26 ^{o}C , the cold discharging rate was limited by the low thermal conductivity. Ukrainczyk et al [64] studied thermal properties of different paraffins and found that the thermal conductivity was in the range of 0.15 $W/(m\cdot K)$ (solid paraffin wax, melting point of 53 ^{o}C) and 0.358 $W/(m\cdot K)$ (solid C18, melting point 27.5 ^{o}C). Table 2.3 presents some thermo physical properties reported in their study.

Table 2.3 Thermal properties of paraffin wax (data from [63])

State of Paraffins	Number of carbon atoms	ρ (g/cm^3)	Melting (^{o}C)	Heat fusion (kJ/kg)	λ ($W/(m\cdot K)$)	C_p ($W/(kg\cdot K)$)
solid	>15	0.766~0.93	27.5~68	147~244	0.15~0.358	2.6~3.0

To enhance the thermal conductivity of paraffins, two methods have been studied. One is the use of composite materials containing high thermal conductivity materials. The other is to encapsulate PCM solutions to obtain an increased heat transfer area and reduced thermal diffusion distance.

Compared alcohol solutions with paraffins, alcohol solutions are advantageous for their higher latent heat and large density, but paraffins takes the advantage of the cyclic and chemical stability.

2.1.3.2 Multi-component PCMs

(1) Multi-component organic PCMs

Storage temperature is an important criterion for PCM selections. This requires a tuneable freezing temperature and can be achieved by the use of multi-component organic PCMs[65].

Guo [66] studied thermal properties of multi-component PCMs consisting of ethylene glycol, sodium formate, sodium lactate, ethacetic acid, glycerol, sodium propionate, ethylene glycol and water. Different freezing points were achieved. Michaud et al [67] investigated the phase change behaviour of mixtures of chlorobenzene and bromobenzene. They showed complete solubility in solid state can be achieved due to isomorphous crystallizing structures of the two components. The phase change temperature of the mixture was measured for different concentrations and the results are reproduced in Figure 2.7. It can be seen that the freezing point of the multi-component organic PCM is in the temperature range between -31 ^{o}C and -45 ^{o}C.

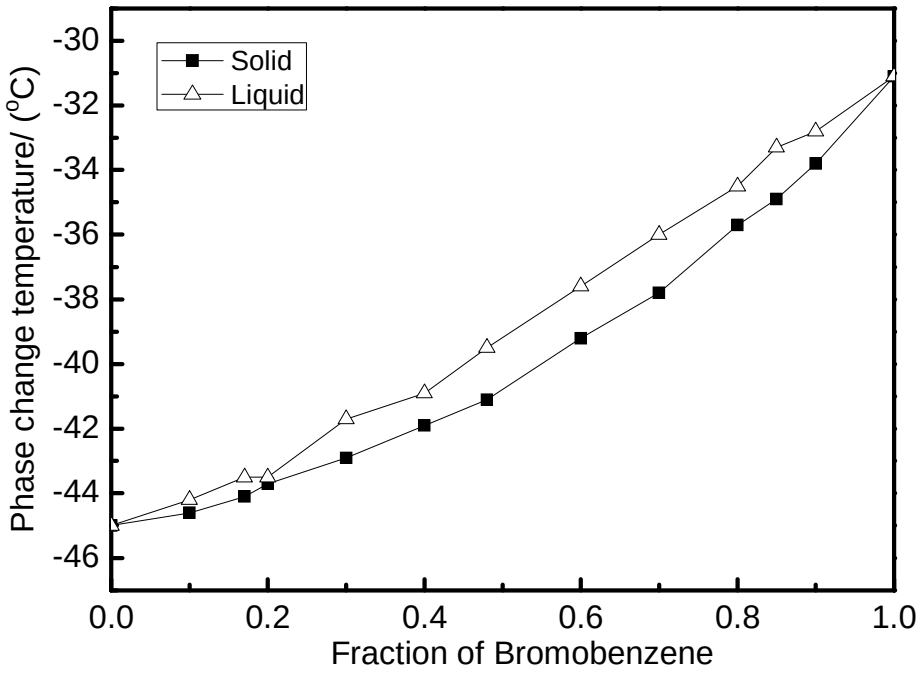

Figure 2.7 Phase change temperatures of multi-component organic PCM (a mixture of chlorobenzene and bromobenzene)

A big issue to the use of multi-component organic PCMs is that phase change process is not thoroughly understood so that the desired freezing points of the PCM mixtures have to be obtained by trial and error [65].

(2) Inorganic-organic composite PCMs

In most cases, the latent heat of inorganic PCMs (e.g. inorganic salt solutions) is higher than organic PCMs (e.g. alcohol solutions). However,

phase separation and corrosion of inorganic PCMs are key issues which affect the cyclic and chemical stability of the materials. These issues can be largely alleviated by mixing organic and inorganic PCMs because chemical corrosion can be inhibited by organic compounds or their derivatives (e.g. Gece [68]).

Bouayed et al [69] investigated the corrosion inhibition of organic molecules (thiophenol, phenol and aniline) on iron surfaces. They used gravimetric and electrochemical methods and found that thiophenol had the best effect on inhibition. To increase the inhibition effectiveness, Lebrini et al [70] prepared a new organic macrocyclic polyether based compound. They found that the inhibition effect could be improved by extending the polyethylene glycol unit. Other factors that affects the corrosion inhibition include the organic compound properties, such as steric effects, electronic density of donor atoms and orbital character of donating electrons [71-72] and the formation of a physical or chemical adsorbing film on the metal surface [73-74].

2.1.3.3 Eutectic solutions

Lots of PCM cold storage studies have been concentrated on the use of non-eutectic water-salt solutions and multi-compound PCMs [75]. These solutions may get phase separation as the component with the lowest melting point solidified first. The use of eutectic solutions can prevent the above happening and enables high grade of cold to be stored since eutectic solutions have a lower melting point than that of the compounds [76].

The eutectic solutions can be divided into binary and multi-compound eutectics consisting of either organic or inorganic compounds, including hydrates, salts and fatty acids. Due to favourable thermal physical properties, they are better options for high grade cold storage.

Amongst various investigations on the eutectic solution based cold storage, the following three have been the focus: characterization of thermal physical properties, investigation into heat transfer behaviour, and study on cyclic and chemical stabilities. As the chemical and cyclic stabilities have been discussed in Section 2.1.3.2, a brief review is given on the first two aspects.

(1) Characterization of thermal physical properties.

Zhang et al [77] investigated phase change behaviour of fatty acids in binary eutectics made of either lauric, palmitic or stearic acids (LA, PA,SA, respectively), using differential scanning calorimetry (DSC). The eutectic temperature was found to be 32.9 ^{o}C with an eutectic composition of 23% PA and 77% LA. Sari et al [78] studied the eutectics of lauric acid (LA) and

stearic acid (SA) encapsulated in an annular space of a concentric pipe. A mass ratio of LA to SA at 75.5%:24.5% was found to be the eutectic composition, leading to the eutectic point at 37 ^{o}C. The latent heat data of LA-PA and LA-SA are presented in Table 2.4.

Table 2.4 The latent heat of LA-PA and LA-SA mixtures

LA-PA		LA-SA	
PA (wt.%)	ΔH (kJ / kg)	SA (wt.%)	ΔH (kJ / kg)
0	185.5	0	186.4
19.41	146.5	19.2	180.5
22.95	150.6	22.7	185.4
28.45	153.8	27.4	186.2
39.12	168.9	39.7	189.8
100	202.9	100	198.6

Cedeno et al [79] studied phase transitions of both binary and ternary mixtures of three fatty acids (palmitic, stearic and oleic). They found that the latent heat of the ternary eutectics decreased with increasing of oleic concentration. Tayeb [80] investigated thermal properties of eutectics consisting of Glauber's salt and stearic acid. Energy storage density was observed to be the largest with a concentration ratio of Glauber's salt to stearic acid 60% to 40%.

Feichenfeld et al [81] studied tuneable freezing temperature of calcium chloride hexahydrate (CCH) and calcium bromide hexahydrate (CBH) mixture. They claimed that the mixture could behave as pure PCM in the condition of eutectic composition, in which case the lowest melting point was found to be adjusted in the range of 15~33.5 ^{o}C. The advantages of eutectic solutions were highlighted.

Although lots of studies have been carried out, the database for this category of PCMs need to be enlarged.

(2) Investigation of heat transfer behaviour

Jotshi et al [82] studied the heat extraction of a binary system consisting of ammonium alum and ammonium nitrate. They encapsulated the eutectic and exposed it to an air flow for heat extraction. The thermal extraction efficiency (defined as the actual heat extraction over the thermal energy storage in

PCMs) was observed as 89%. For sensible heat extraction, the Stanton number (the ratio of heat transferred into a fluid to the thermal capacity of fluid, formulated as $\frac{h}{\rho_f \cdot u_f \cdot Cp_f}$) was found to be improved by 74%. Sassi and Siffrini et al [83-84] established a simplified model for simulating the melting process of binary systems. Due to the assumption of uniformity of temperature distribution, their results could only predict the range or trend of the temperature of the whole sample. Jamil et al [85] developed a two dimensional model for heat transfer of ammonium chloride solution during melting. The model was based on the enthalpy method, using the fraction of local liquid to follow the melting front. It was concluded that the kinetics of the eutectic melting could be clearly understood by applying this model to DSC.

2.2 Enhancement of cold extraction processes

Stored cold is used either for cooling or for power applications. Effective extraction of cold energy from the storage media plays an important role for both of the applications. This is determined by the heat transfer process. Consequently, this section will give a review on this aspect.

2.2.1 Introduction of heat transfer in PCMs

Phase change heat transfer is characterised by the so-called moving boundary [86]. Such a process is transient and non-linear. Shape, position and speed of the moving boundary all contribute to the complexity of the heat transfer problem [87-88].

Phase change heat transfer during charge/ discharge processes can be regarded as a combination of heat conduction and convection [89-94]. Sparrow et al. [89], Bathelt et al. [90] and Gobin [91] are among the earliest who investigated the convective heat transfer of PCM melting process. Previous studies on phase change heat transfer mechanism of PCM are listed in Table 2.5. Dincer et al [92] analyzed the heat transfer behaviour of PCM around isothermal finned cylinders. The issue of big thermal resistance in melting process was reduced. Hirata el al. [93] compared the melting behaviour of octadecane and ice in rectangular PCM capsules under isothermally heated condition. The aspect ratio (defined as height over width, written as $\frac{H}{W}$) of the capsules had not significant effect on the melting process. Ho et al [94] investigated the influence of the air volume flow rate and recycling ratio on the heat transfer efficiency and energy consumption.

In all of the above studies, combined effect of heat conduction and convection has been considered.

Table 2.5 Summarization on heat transfer mechanism of melting process

Concentrated on	Authors	Main conclusions
heat transfer mechanism	Sparrow et al. [89], Bathelt et al. [90], Gobin [91]	conduction dominates only during the early stages of the melting process; but natural convection comes into play and ultimately gives rise to a steady value of the heat transfer coefficient

Methods for studying phase change heat transfer can be classified as the following three categories.

(i) Experimental methods. Heat transfer properties of PCM can be investigated by using DSC, while the shape, position and moving of the interface can be traced by measuring the temperature profile or by monitoring the visual images. However, measurement of volume variation of PCM should be addressed due to its significant effect on the data deviation.

(ii) Analytical methods. Most of the analytical methods are based on one dimensional moving boundary problem, including precise solution (e.g. Stefan problem) and approximate solution using quasi-stationary approximation, perturbation methods, the Megerlin method and the Heat-balance-integral method [87]. The drawbacks of the analytical methods lies in the assumptions of semi-infinite or infinite storage and constant freezing point [86].

(iii) Numerical methods. Based on the enthalpy method and the effective heat capacity method, heat transfer behaviour can be studied by using finite difference method (FDM) or finite element method (FEM). In principle, enthalpy method substitutes temperature with enthalpy in the energy equations since the enthalpy is directly related to the state of PCMs. Voller et al [95] obtained an explicit formation of the energy equation using enthalpy method; while Costa et al [96] developed a fully implicit formation based on FDM. However, the calculation by this method is likely to ‘”jump” the phase change temperature range. Therefore, the effective heat capacity method has been proposed, which uses heat capacity (defined as derivative

of enthalpy h to PCM storage temperature T_{PCM} , written as $\frac{\partial h}{\partial T_{PCM}}$) in the energy equation [97]. As a result, the above drawback can be overcome.

2.2.2 Heat transfer enhancement in cold extraction unit (CEU)

As the phase change heat transfer is an combination of the heat conduction and convection, heat transfer enhancement can be achieved by improving thermal conduction, convection and surface area. Methods for improving the cold extraction capacity of PCM based cold energy storage are reviewed in this part.

2.2.2.1 Improving thermal conductivity

Thermal conduction is enhanced by improving the thermal conductivity of a PCM, which can be effectively increased through structures or particles addition into the PCM.

(1) Inserting structures with high conductivity (PCM side).

According to different structures, the inserted materials can be classified as simple structures and complex structures.

- Simple structures. Metal fins embedded in PCM are commonly used due to the advantages in simplicity, fabrication and cost of the construction. Erek et al. [98] studied fluid flow and heat transfer of finned tubes in thermal energy storage (TES) systems, using water as the storage material. They found that the energy charging rate was improved with the increase of fin radius and the decrease of fin space. This improvement was attributed to the increased effective thermal conductivity.
- Complex structures. These include metal structures, such as matrix, fibre, rings and foams and non-metal structures made of carbon or graphite. Cabeza et al. [99] investigated the effect of stainless steel pieces, copper pieces and a graphite matrix impregnated with water in a small TES system. They concluded that the fin effect was significant when a highly conductive matrix (e.g. graphite) was used. Kazmierczak et al [100] developed a heat conducting enhancement device (HCED) by using porous copper mesh on the external surface of a tube. The freezing rate of water surrounded the tube was found to be increased by 50%~90% in the case that rolled copper screen mesh was used in the HCED. Tong et al. [101] studied the thermal conductivity improvement of materials consisting of PCMs and a high porosity metal matrix. They reported that the heat transfer rates were enhanced by one order of magnitude. Fan [102] reviewed numerous studies on enhancing the thermal conductivity

of PCMs over the past few decades. They concluded that the above methods were feasible since the conducting pathways or thermal resistance could be minimized by inserting structures with high thermal conductivity. Typical structures adopted in previous studies are summarized in Table 2.6.

Table 2.6 Structures added into PCMs for improving thermal conductivity (data from [102])

Structures	Authors	Investigation methods
metal powder	Hoover [103]	DSC measurements
metal pieces	Knowles and Webb [104]	Transient lumped model;
metal fins	Henze and Humphrey [105]	2D transient model
metal fibers	Bentilla [106]	experiments
Metal foams	Hoover [103]	DSC measurements
honeycomb	De Jong and Hoogendoorn [107]	Caloric method
Metal thin-strip matrix	De Jong and Hoogendoorn [107]	Enthalpy method
Lessing rings	Valraj [108]	Enthalpy method
Carbon fibers	Fukai [109]	Parameter estimation
Graphite matrix	Cabeza [110]	Parameter estimation

(2) Adding particles with high conductivity.

The thermal conductivity of PCMs can be improved by inserting metal structures. However, the use of the above structures is restrained by the large volume of structures which reduces the cold storage density; these structures are also restricted to be applied in the consideration of safety issues and compatibility of the structures with the storage medium [111–113]. As a result, adding particles with high conductivity has been used and studied.

Hirasawa et al [114] experimentally studied the transport characteristics of heterogeneous composite materials consisting of conductive solids and water. They reported that the melting rate during phase change was improved by increasing the volume ratio of high conductive solids in the composite materials. Calvet et al [115] developed a method for heat transfer enhancement in PCMs. They impregnated an isotropic matrix of expended natural graphite with a commercial paraffin for achieving a higher thermal conductivity of the composite materials. The equivalent thermal conductivity

was found to be in the range of 4 and 70 $W/(m\cdot K)$, which is approximately 15~290 times bigger than the pure paraffin (about 0.24 $W/(m\cdot K)$). Yu [116] investigated the effect of micro or nano particles on the heat transfer improvement of a liquid PCM. They reported that the thermal conductivity of the composite materials was improved since particles with higher conductivity in micro or nano size changed the structure of the base liquid and increased the micro convection between the particles and the liquid PCM, leading to the enhanced heat transfer in charge/ discharge processes.

The equivalent thermal conductivity of materials composited by particles and a base liquid PCM can be calculated according to the liquid-solid model proposed by Maxwell [117], as shown in Eq.(2.1):

$$\frac{k_{eff}}{k_f}=\frac{k_p+2\cdot k_f-2\cdot\varphi\cdot(k_f-k_p)}{k_p+2\cdot k_f+\varphi\cdot(k_f-k_p)} \tag{2.1}$$

2.2.2.2 Extending heat transfer surface area

Extending the surface area can enhance the charging/ discharging rate of PCMs in terms of Newton's cooling equation. The surface area can be increased by using metal fins (HTF side), multi tubes and PCM encapsulation.

(1) Metal fins (HTF side)

Theoretically, it is more effective to enhance heat transfer on the PCM side where the thermal resistance is dominant during phase changer process. However, as discussed before, the use of metal structure on PCM side is restricted by applicable environment. Alternatively, metal fins with different shapes and sizes can be installed on the HTF side [118].

Studies on heat transfer enhancement by using metal fins on PCM side have been reviewed in Section 2.2.2.1; similar studies with a focus on HTF side have been done by different groups. They highlighted the significance of using metal fins on HTF side in the considerations of safety and compatibility issues.

(2) Multi tubes

The benefit of using multi tubes in PCM is achieved due to the increased specific surface area (defined as area per volume). These multi tubes can be applied for the design of a compact heat exchanger.

The heat transfer characteristics in multi tubes have been extensively studied [119-122]. Hendra et al [119] studied the phase change heat transfer

characteristic of a staggered multi-tube PCM. A two-dimensional model for analyzing heat transfer behaviour was developed. They claimed that with increasing of the melted fraction, the heat transfer mechanism was converted from conduction-dominated to convective-dominated. Agyenim et al [120] investigated the thermal characteristics of multi tubes in energy storage system by using isothermal contour plots and temperature time curves. They reported that two-dimensional model was feasible due to the negligible temperature gradient in the PCM along the axial direction. Compared with the single-tube system, the heat transfer rate in the multi-tube system was improved due to the increased surface area and the improved convection resulting from the multiple convective cells [120]. However, sub cooling issue in the multi-tube system became explicit and need to be addressed.

The research methods for investigating heat transfer behaviour in multi-tube based PCM can be summarized as the following two :

- Equivalent single tube. A representative single-tube unit is studied. Quantity of the single-tube units is considered for calculating the heat transfer in the multi-tube system. Parameters calculation for a typical single-tube unit was demonstrated by Trp et al [121].
- Cross-section domain. Based on a two-dimensional model, heat transfer behaviour in the cross-section domain of the multi-tube PCM system is investigated. Both of the tube-tube pitch and tube-PCM pitch were considered in the study [122].

(3) PCM encapsulation

Heat transfer behaviour of PCM in charge/ discharge processes can be improved by encapsulating the PCM in different shapes and sizes. The improvement is due to the increase of the specific surface area for heat transfer and the inhibition of solid layer formation on fluid side.

The solidification layer formed during the charge/ discharge processes is demonstrated in Figure 2.8. One can see that the solid layer is formed on the PCM side during cold charging, while it appears on the fluid side in discharge process. The thermal resistance is therefore increased with the growing of the solid layer along both radial and axial directions, resulting in reduced overall heat transfer coefficient. However, this negative effect of solid layer can be minimized by PCM encapsulation.

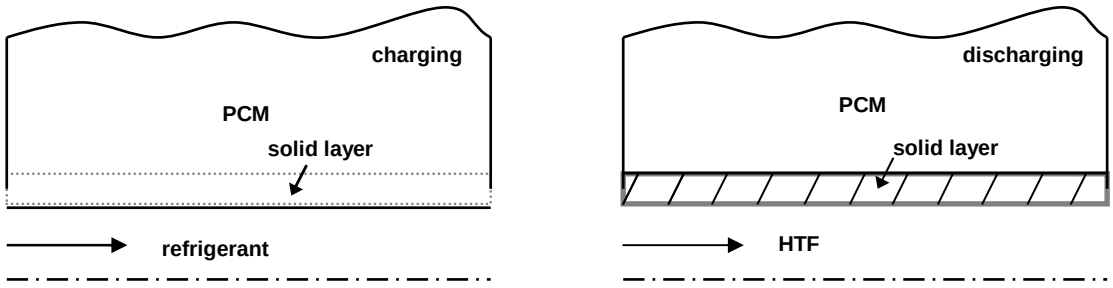

Figure 2.8 Solid layer formation during charge/ discharge processes

Numerous studies on PCM encapsulation have been done. According to the encapsulated size, these studies can be divided into macro encapsulation and micro encapsulation.

- Macro encapsulation

In this scale, different shapes of PCM capsules have been investigated. Laybourn et al [123] studied the cold storage using rectangular PCM capsules. The thermal resistance in such shape of capsules was analysed. Chen et al [124-125] investigated the thermal performance of PCM in cylindrical capsules located in a cold storage tank. The inlet temperature and flow rate of the coolant was measured. Arnold [126] observed the heat transfer behaviour of spherical capsules in charge/ discharge processes. Compared with other shapes of PCM capsules, the heat transfer with spherical-shape capsules has the largest charging/ discharging rate. This is due to the biggest specific heat transfer area and the best flow disturbance in such spherical PCM capsules.

Consequently, lots of studies have been focused on spherical PCM capsules [127-131]. Adref et al [127] analyzed dynamic behaviours of a single spherical-shape capsule in ice storage systems. Ismail et al [128-129] studied the effects of sizes and materials of PCM spherical capsules on heat transfer rate by using numerical model. While Hawlader et al [130] investigated the characteristics of the encapsulation ratio, hydrophilicity and energy storage capacity of PCM (paraffin) capsules in TES system. They found that a higher ratio coating of paraffin led to a higher paraffin encapsulation ratio but lower hydrophilicity. The encapsulated PCM (paraffin) had a storage capacity of 20~90 kJ/kg. The variation of storage capacity of the PCM was mainly dependent on different ratios of paraffin to coating. Cheralathan et al [131] studied the effect of porosity variation of the encapsulated PCM on heat transfer behaviours in CES system. With increasing of capsules porosity, charging/ discharging rate was improved.

- Micro encapsulation

The common usage of micro encapsulation of PCM is the microencapsulated PCM slurries by incorporating capsules into conventional HTF, which has a high potential to be applied for refrigeration and air-conditioning (RAC).

Schossig et al [132] studied the heat transfer rate in micro capsulated PCMs. They reported that the enhancement on the heat transfer rate was due to the largely increased heat transfer surface in such a capsule of micrometer-level diameter. Farid [133] researched the heat transfer improvement in micro channel heat exchangers by incorporating suspension of microcapsules into liquid as the heat transfer fluid. Hu et al [134] established an effective specific heat capacity model for considering the convective heat transfer enhancement in PCM slurries. Both of the studies concluded that the heat transfer enhancement could also be attributed to the latent heat effect and the increased effective thermal conductivity.

Other factors that affect the heat transfer enhancement in PCM slurries were summarized in [135-139]. These include the diameter and volumetric concentration of the microcapsules, the bulk Stefan number, the dimensionless phase change temperature range and initial degree of sub cooling. Besides, in the point of view of field coordination principle, increasing the fullness of dimensionless velocity and/or temperature profiles, or the included angle between the dimensionless velocity and temperature gradient vectors are effective ways for enhancing heat transfer [134]. However, the mechanism for heat transfer enhancement in PCM slurries has not been well illustrated in previous studies [134].

2.2.2.3 Enhancing convective heat transfer performance

As discussed above, convection in PCM heat transfer is crucial in the study of phase change thermal performance. The methods for improving convective heat transfer inside PCMs mainly include increasing flow disturbance by bubble agitation and direct contact of PCM and HTF.

(1) Increasing flow disturbance by bubble agitation

For improving the cold discharging capacity of PCM, methods for enhancing the heat transfer at solid-liquid interface need to be investigated, as mentioned by Mohamed [140].

One feasible method is using air bubbles in the PCM for increasing flow disturbance. Generating air bubbles were used to speed up the ice layer growth at the solid–liquid interface during the charging process [140]. The

solidification front velocity and ice layer growth rate increased by 20%~45% with the using of air bubbles. As a result, the cold charging rate was largely improved. It was reported that the cold storage capacity increased by 55%~115% due to the consequence of air bubbles.

(2) Direct contact of PCM and HTF

In the case of the direct-contact of PCM and HTF, PCM capsules were packed in a larger storage container, while HTF flowed in the void between the capsules. As a result, the large latent heat of PCM can be efficiently extracted. The limitations of this methods lies in the negative effect of packaging on heat transfer performance, due to the large thermal resistance between the PCM and package caused by volume variation during phase change of PCM [11].

A feasible solution for addressing this issue is using micro-capsule slurries of PCM. However, this method is restricted to be used since the cost of micro-encapsulation is significant [141]. Alternatively, the above direct contact method has been proposed, as presented in Figure 2.9. Insolubility and large density difference of PCM and HTF are required. In this case, a porous layer is formed between the PCM layer and the fluid layer during the charge/ discharge processes. The convective heat transfer is therefore enhanced due to the prolonged contact time of the PCM and heat transfer fluid. The advantages of the direct contact method include simplified system design, low construction cost , and improved heat transfer performance.

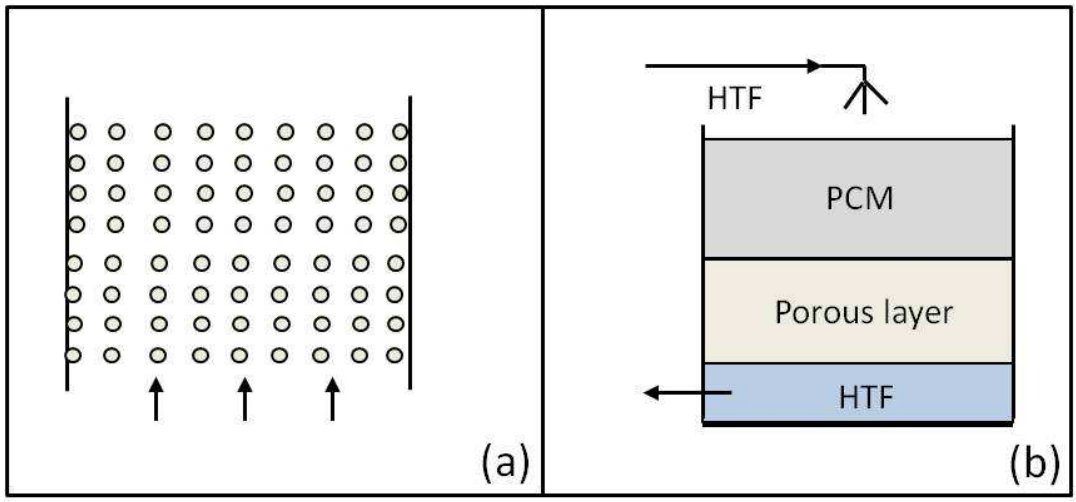

Figure 2.9 Convective heat transfer enhancement between PCM and HTF by: (a) micro capsule PCM; (b) direct contact of PCM and HTF.

Previous researchers have studied the heat transfer behaviours through direct contact of PCM and HTF for achieving longer residence time of droplets and better formation of porous layer in such a direct contact system. For instance, Asashina et al. [142] studied the influence of long residence time of HTF (oil droplets) in PCM (molten salt hydrate) on promoting the heat transfer rate; while Saito et al [143] investigated the effect of porous layer on heat transfer behaviours in a direct contact PCM (n-eicosane) system.

More heat transfer behaviours in direct contact PCM storage system have been investigated [144-145,11]. Saito et al [144] investigated the time-dependency of the charge heat flux using n-octadecane as the PCM. A non-dimensional heat flux during phase change was formulated on the basis of their previous results. They claimed that the average heat flux was affected by both the thermal physical properties of PCM and the geometric parameters of capsules. Kiatsiriroat et al [145] investigated the heat transfer characteristics in the direct contact system using sodium thiosulphate pentahydrate as PCM system and oil as HTF. The volumetric heat transfer coefficient was reported as high as 2000 $W/(m^2 \cdot K)$. They suggested that lumped analysis could be regarded as an effective method for analysing the temperature and solid fraction of PCM in the direct contact system. Martin et al [11] established a theoretical model for a direct contact PCM-water system in. They used the heat transfer unit method (HTU method) based on energy balance of PCM and HTF to assess the cold discharging rate, which was found to be over 1500 $W/(m^2 \cdot K)$ under the set conditions.

As claimed by Martin et al [11], several drawbacks need to be considered in the direct contact PCM cold storage system as follows:

- Expansion of the PCM-HTF bed. With increasing of flow rate of HTF, PCM might come out of the system due to bed expansion.
- Collapse of PCM-HTF bed. The porous layer consisting of frozen PCM and HTF may collapse during charge/discharge process. In this case, the passage for the HTF passing through the porous layer is blocked.
- Enclosure of liquid PCM/ HTF in the porous bed. Liquid may be trapped and enclosed in the porous layer, due to the rapid freezing under high temperature difference. As a result, the cold discharge rate is significantly affected.

2.3 Improvements of cold utilisation

Cold exergy can be extracted through discharge process, as discussed in section.2.2. In another aspect, cold exergy can also be utilized for power or electricity generation, which is based on thermal dynamic cycles and engine systems. Therefore, in this section, studies on design of thermal dynamic cycle and engine development are reviewed.

2.3.1 Thermal dynamic cycles

Generally, there are three methods of utilizing cold exergy for dynamic purposes: (i) direct expansion; (ii) based on Brayton cycle; (iii) based on Rankine cycle. The drawback of the direct expansion is the small heat efficiency and net power generation due to the low fluid temperature before expansion. Therefore, numerous studies have focused on cold utilisation based on thermal dynamic cycles.

2.3.1.1 Brayton cycle

The Brayton cycle can be divided into open cycle with fuel gas and close loop with idealized air for expanding in turbine. In both of the cycles, the working fluid is pressurized by the compressor and heated up without phase change. The heat efficiency of the Brayton cycle can be improved by incorporating Brayton cycle with compressor inlet cooling, reheating, and regeneration.

(1) Inlet cooling

In Brayton cycle, Gas turbine makes use of pressurized mixture consisting of fuel gas and air for power generation. The power generation by the gas turbine is restricted by the air temperature at the inlet of compressor in the cycle, which becomes more significant in hot seasons when the ambient temperature is higher. Numerous methods of inlet cooling have been proposed for improving the performance of turbine in Brayton cycle. These include the use of water chillers, evaporative coolers, thermal storage systems, absorption chillers and mechanical chillers [146-153].

- Water chillers. Commonly used methods include the controlled water spray and water fogging for inlet cooling, by which the power generation increased by 10%~20% [147-149].
- Evaporative coolers. Johnson et al [150] presented a parametrical study on the performance of an evaporator cooler. They discussed technical details for operating the coolers, for instance, installation, operation, feed water quality and water carry-over. Kim et al [151] used liquefied natural

gas (LNG) heat sink to cool the inlet air of the compressor. They found that the power generation in the combined system (Brayton cycle with the evaporative cooler using LNG) was also affected by the ambient air temperature and the relative humidity. The power generation was improved by 8% under dry air conditions (relative humidity lower than 30%), while the increase of the power generation was less than 6% under usual humidity conditions (relative humidity higher than 60%).

- Thermal storage systems. Ondryas et al [152] investigated the overall economic benefit of the power augmentation by using thermal storage systems for inlet cooling under high ambient temperature conditions. They reported that the thermal storage systems are worth investing since the benefits from the power augmentation in peak time outweighed the cost. Mercer et al [153] compared thermal storage systems to evaporative coolers. They reported that the maximum enhancement by thermal storage systems was 25%, while the benefit by evaporative coolers was approximately 10%~15%.
- Absorption chillers and mechanical chillers. Compared with water chillers and evaporative coolers, the power augmentation by using absorption chillers or mechanical chillers is larger. However, due to the higher initial capital cost and longer delivery and installation time, absorption and mechanical chillers are not suggested as better options for inlet cooling in Brayton cycle.

(2) Multi-stage compression or expansion based on regeneration

Due to the reduced heat absorption in Brayton cycle, regeneration is a favourable approach for increasing the heat efficiency of the Brayton cycle. Isothermal processes in regenerator have been studied by different groups [154-156]. Hernandez at al [154] used a regenerative heat exchanger in combustion gas turbine to achieve higher heat efficiency in the Brayton cycle. They showed that although the heat efficiency could be improved by regeneration, the heat absorption in the combustion chamber was an isobaric process. Consequently, the Converging combustion chamber (CCC) for achieving idealized isothermal heat addition has been proposed [155-156]. Vecchiarelli et al [155] reported the heat efficiency improved by 4% through heat addition in an approximate isothermal process. The heat efficiency can be further improved. Goktun et al [156] investigated the effects of two isothermal heat additions in a regenerative Brayton cycle. They used isentropic efficiency for figuring out fluid friction losses in the compressor and turbine. Compared with single isobaric heat addition, the

heat efficiency in such a Brayton cycle with two isothermal heat additions was found to be improved by 10%.

Based on the effectiveness of regeneration, the heat efficiency can be further improved by multi-stage compression with inter-cooling or multi-stage expansion with reheating. The effects of regenerating, inter-cooling and reheating on optimized power generation have been investigated [157-158]. Woods et al [157] studied the power generation in a regenerated Brayton cycle. They found that the power generation was independent on the regenerating effectiveness, which was due to the significant effect of internal irreversibilities on the power generation. Frost et al [158] analyzed regenerative, inter-cooling and reheating cycles with internal irreversibilities considered. The maximum power output and heat efficiency under different combined conditions consisting of simple cycle, regenerative, multi-stage inter-cooling and reheating were obtained. They claimed that both power generation and heat efficiency need to be optimized in consideration of the effects of the above approaches. From all the studies, it is highlighted that for optimizing the effectiveness of multi-stage compression with inter-cooling or multi-stage expansion with reheating, stage compression ratios and overall compression ratios need to be adjusted appropriately in terms of different thermal dynamic conditions.

2.3.1.2 Rankine cycle

Although the heat addition and heat rejection processes in Rankine cycle are isobaric, these processes happen with relatively small temperature variation due to the phase change of the working fluid. As a result, the heat efficiency in Rankine cycle is high and can be close to that in Carnot cycle. However, the heat efficiency of a Rankine cycle is restrained by properties of working fluids. Typical methods for improving the heat efficiency are discussed in the following section.

(1) Waste heat recovery

Organic Rankine cycle (ORC) uses an organic fluid instead of water as the working fluid and is advantageous for heat recovery with a low to medium temperature.

Hung et al. [159] and Larjola et al [160] investigated the exhaust heat recovery (EHR) in an ORC. They reported that the thermal exergy in the exhaust gas could be recovered by up to 50%. As a result, the dynamic power from the engine increased by 10% while the overall engine efficiency improved by approximately 10%. Cummins et al. [161-162] also studied the

heat recovery using Rankine cycle system. They found that the engine efficiency of Class 7–8 highway trucks could increase by more than 50%. Lee et al [163] presented a study in ORC using R-113 as the working fluid. The effects of condensing and evaporating temperatures on the economic benefits were investigated. They concluded that it was feasible to use waste steam recovery in ORC for moderate capacity plants.

Solar energy, geothermal energy, and waste heat from condensers in steam power plants or other industrial processes can be utilized for heat recovery. As a result, energy consumption and CO_2 emission can be reduced.

(2) Working fluid selection

The heat efficiency is largely affected by the types and properties of working fluids and irreversibilities in different thermal dynamic processes in the systems [164-166]. For improving the heat efficiency and power generation in a Rankine cycle, working fluid selection is crucial.

The working fluids can be classified as dry fluids, wet fluids, and isentropic fluids in terms of the slope of the saturation vapour curves in the T-S diagrams. Dry fluids have positive slope and normally have high molecular weights (e.g. R113 and Benzene); while wet fluids have negative slope of the saturation vapour curve and usually have low molecular weights (e.g. water and ammonia); isentropic fluids have infinite slope and hence can maintain saturated gas state during the expansion (e.g.R11 and R12) [164-166].

Theoretically, the optimum working fluids in Rankine cycle should have high enthalpy drops, low critical pressure, low saturated temperature before pumping and high chemical stability, as discussed below.

- High enthalpy drops. Compared with wet fluids, the dry or isentropic organic fluids usually have much lower enthalpy drops across the turbine than wet fluids. From this point of view, wet fluids are better options as the working fluid in the Rankine cycle. However, multi-stage steam turbine is required for fully using the enthalpy drop of wet fluids due to the appearance of liquid in the expanding process. The cost and complexity of the system are therefore increased.
- Low critical pressure. Most organic fluids (dry or isentropic fluids) have low critical pressures, which makes them easy to be operated under critical or super critical pressures in Rankine cycle. The working fluids under critical state have better heat transfer characteristic, leading to reduced irreversibilities of the heat transfer processes . Chen et al [167]

compared CO_2 and R123 as the working fluid in the Rankine cycle. They found that CO_2 had better temperature glide matching in a heat exchanger.

- Low saturated temperature before pumping. Organic fluids have relatively lower saturated temperature before pumping in the Rankine cycle, resulting in a reduced average exothermic temperature.
- High chemical stability. Chemical decomposition and deterioration are the big issues for most of organic fluids under high temperatures and pressures. These requires the operations in the Rankine cycle below those chemically unstable points of working fluids.

Based on these criterions for proper working fluid selection, Hung et al [166] studied the parametric effects on the system efficiency using cryogens such as benzene, ammonia, R11, R12, R134a and R113. With the increase of turbine inlet temperature, the system efficiency increased for wet fluids but decreased for dry fluids. For isentropic fluids, the effect of inlet temperature was not obvious under the condition of lower pressure. These effects by different types of working fluids on heat efficiency were attributed to the distinct slopes and shapes of these fluids in the saturation vapour curves. It was suggested that the isentropic fluids (R11 and R12) were selected as the working fluids for recovering low-temperature waste heat under 350 ^{o}C. Kaushik et al [168] investigated the system efficiency and overall system performance using and single fluids and dual fluids consisting of R12, R22, R113 and R114. It was reported that efficiency and overall system performance in dual-fluid systems were generally higher than that in single-fluid system. Dual fluids consisting of R113 and R114 was found to have the highest system performance and should be selected in the Rankine cycle.

Other methods that increase the average endothermic temperature and reduce the average exothermic temperature can be used. It is emphasised that multi-stage compression or expansion, reheating and regeneration in Rankine cycle are all feasible for improving the heat efficiency.

2.3.2 Technical considerations of engine

Methods of isothermal expansion in engine and designs of engine with technical details are reviewed in this section.

2.3.2.1 Isothermal expansion engine

Based on the thermal analysis of isothermal, adiabatic and polytropic processes, it is found that isothermal expansion in the engine has the largest

power generation, as claimed in Figure 2.10. In reality, feasible solutions for expansion with approximate isothermal process in engine or turbine have been proposed.

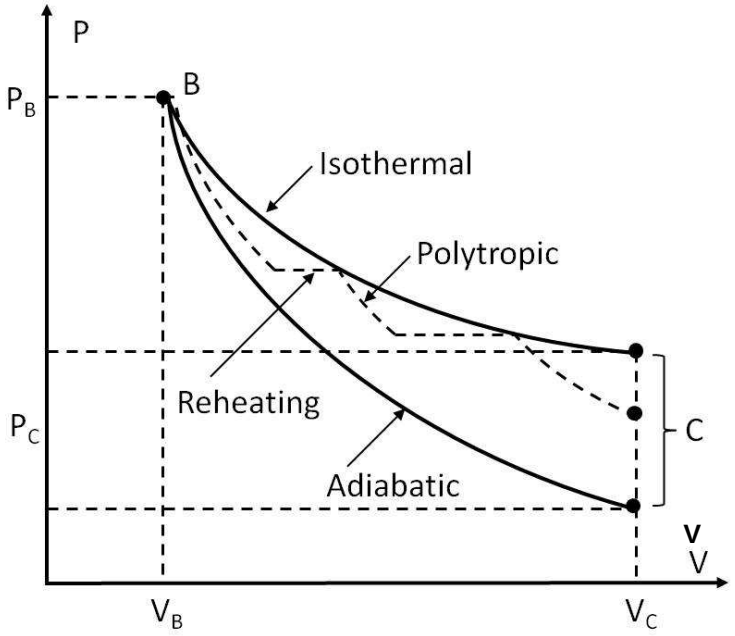

Figure 2.10 Comparison of different expanding processes for power generation

(1) Utilisation of ambient heat

Manning et al [169] developed a direct drive system using multi-stage expansions with reheating prior to the final stage of expansion in Brayton cycle. A regenerative device was proposed to improve the heat efficiency. West et al. [170] used a double acting piston expander to improve the efficiency of the working fluid. For using environmental heat, Negre [171] (MDI company in France) firstly designed multistage engine system, as described in Figure 2.11. Due to the utilisation of ambient heat, the expansion in the system was approximately an isothermal process. Marquand [172] (University of Westminster) developed a two-stage turbine with a heat pipe before the inlet of engine to make use of environmental heat. The heat transfer area of the heat pipe was up to 1.4 m^2, while the heat transfer efficiency was 85%. It was reported that when the inlet pressure was 4.5 MPa, and engine speed was 1000 rpm, the power generation was as high as 25 kW.

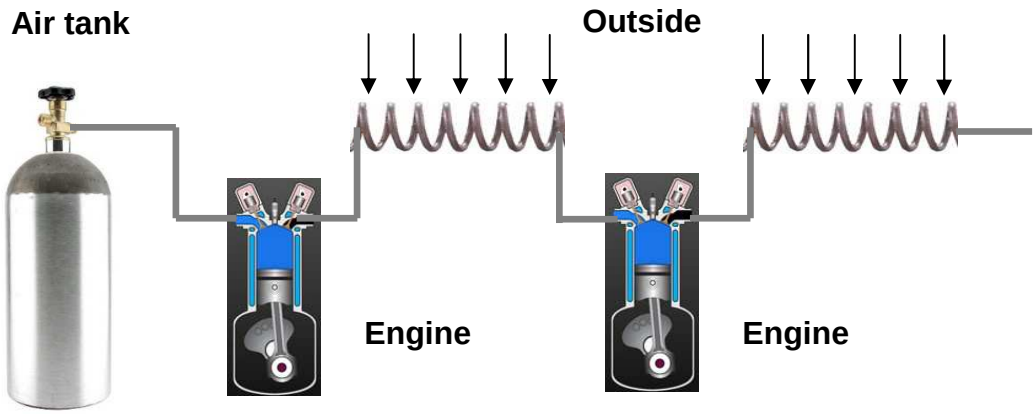

Figure 2.11 Schematic diagram of multistage engine in MDI

In the above studies, the processes in engine were considered as multi-stage adiabatic expansion with middle reheating using the ambient heat. This is favourable for improving system efficiency and power generation by engine. However, since the inlet temperatures in the expansion stages of the engine are lower than ambient temperature, system efficiency and power capacity are significantly restrained.

(2) Combination of ambient and combustion heat

Oxley et al [173] utilized combined heat from both ambient and combustion in a Stirling engine. Oxygen from the liquefaction and separation of air was used to enhance the efficiency of fuel combustion. Latter et al [174] used liquid air as the working fluid in the Rankine cycle. They utilized ambient heat to increase the liquid air temperature in the multi-stage expansion process. Additional fuel was subsequently injected to make use of the combustion heat in an internal combustion engine. Comparing with no utilisation of combustion heat, it was reported that the power generation increased by 50%.

2.3.2.2 Parametric design of engine

Apart from utilisation of environmental heat and combustion heat during the multi-stage expansion processes, other methods for improving system efficiency and power generation have been proposed as follows.

(1) Control of injecting time of high pressure gas

Negre et al [171] developed an engine system, with high pressure gas injected into the engine intermittently. In the system, air is absorbed into the chamber of engine when the piston goes down from top dead centre (TDC) to bottom dead centre (BDC). The absorbed air is then compressed to 20 bar under 400 ^{o}C during the movement of piston in the BDC to TDC

process, when the high pressure gas is injected. As a result, the temperature of the mixture gas is improved, leading to an increased power generation by the engine. However, due to the short injecting time, the thermal energy from the high pressure gas is insufficiently absorbed in the mixing process.

Consequently, Negre [171] designed a special crank published in patent to control time for mixture. With the new connecting rod, the piston can stay near the top for about 70^{o} of the shaft rotating. The components from two different injections are fully mixed. As a result, the power capacity of the engine system can be largely improved.

(2) Parametric optimization of engine

Group of Knowlend in University of Washington has done lots of work on this part. As claimed by Knowlend et al [175], parametric optimization of engine was also feasible for improving power generation under the same conditions. Working processes in engine with different size under different speed were simulated. It was pointed out that small radius of chamber, long length of stroke and low engine speed were all favourable for improving power generation and system efficiency of the engine. Based on the above parametric optimization, high pressure gas tended to expand in an approximate isothermal process, leading to enhanced power capacity of the engine.

Knowlend et al [175] also designed jagged surfaces for both cylinder block and piston with heater core imbedded inside expansion chamber. In the design, heat transfer agent was used to increase temperature of HTF, as shown in Figure 2.12. Knowlend et al [176] analyzed the enhancement of heat transfer rate by this novel piston-head configuration. They claimed that by imbedding a heater core within the expansion chamber, the expansion efficiency in the engine was performed as 85% of the ideal isothermal process. Therefore, the power generation by the designed engine was largely improved.

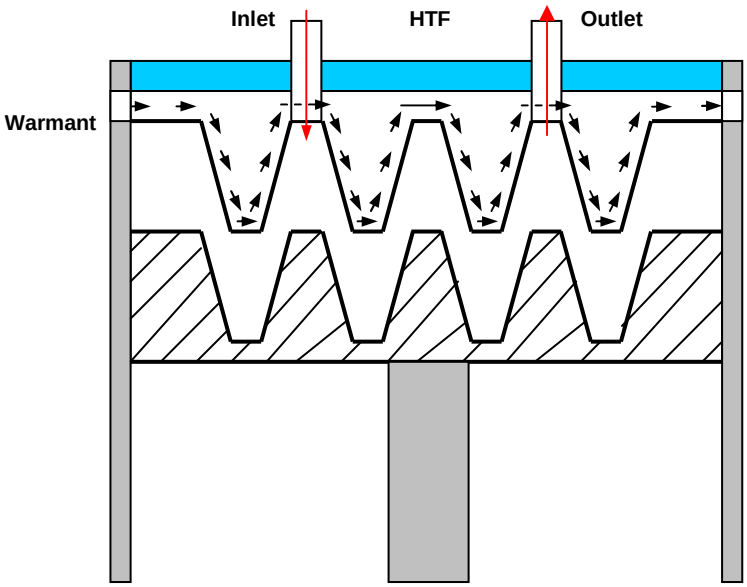

Figure 2.12 Schematic diagram of the designed engine in Washington University

2.4 Summary of the literature review

Numerous published papers focusing on methods and technologies for improving performance of a CES system are presented in this chapter.

Since refrigerator is a crucial device for storing cold energy according to the definition of the CES technology, methods for improving cold energy storage efficiency are categorized as PCM based refrigerators, design of evaporators and PCM cold storage in the refrigerator.

A PCM based refrigerator in a CES system is aimed to reduce temperature fluctuations of PCM during the charge and discharge processes. In consideration of the effects of natural heat loss, door opening, defrost operations and electrical energy failures, the PCM based refrigerator can improve COP of refrigerators by 10%~30% while reduce energy consumption by 7%~8%.

Evaporator is one of the most important components in the refrigerating cycle. Design of evaporators is aimed to increase the heat transfer area, or enhance the size effect on heat transfer performance, or reduce the irreversibility of the evaporation process. Heat transfer performance of the evaporation process is improved by at least 13%~15% by using internally finned evaporators, while it can be enhanced by up to 100% by applying micro finned evaporators due to the small scale effect. Dual evaporators can reduce the irreversibility caused by temperature difference between the

storage medium and refrigerant in the evaporators. The COP can be improved by approximately 20%.

PCM cold storage is aimed to lower the storage temperature with tuneable characteristics. This can be achieved by the use of multi-component PCMs and eutectic PCM solutions. Due to the possible phase separation issue caused in non-eutectic water-salt solutions and multi-compound PCMs, eutectic solutions is suggested to be a better option for high grade cold storage. Amongst various investigations on the eutectic solution based cold storage, thermal physical properties, heat transfer behaviour, and cyclic and chemical stabilities of the eutectic PCM solution are worthwhile to be investigated.

Effective extraction of cold energy from the storage media is determined by the performance of heat transfer during charge/discharge process, which can be improved by increasing thermal conductivity, extending heat transfer surface area and enhancing convective heat transfer. Structures or particles addition with high thermal conductivity, PCM encapsulation, flow disturbance enhancement by bubble agitation and direct contact of PCM and HTF are all effective methods that is recommended for improving extraction of cold energy.

In the point of view of cold to power conversion, cold exergy can be utilized for power or electricity generation, based on thermal dynamic cycles and engine systems. Brayton cycle or Rankine cycle with multi-stage compression or expansion, compressor inlet cooling, reheating and regeneration are typical methods for improving heat efficiency and power generation based on thermal dynamic cycles. It is highlighted that organic Rankine cycle (ORC) is advantageous for waste heat recovery with a low to medium temperature. But only the fluids with high enthalpy drops, low critical pressure, low saturated temperature before pumping and high chemical stability should be selected as the working fluids.

Cold to power conversion of a piston-based engine system can be improved by approaching isothermal expansion process in engine by means of utilisation of environmental heat and combustion heat. Control of injecting time of high pressure gas and parametric optimization of engine are also significant for affecting system efficiency and power generation.

Chapter 3
Cold energy storage using eutectic PCM solutions

3.1 The principle of cold energy storage

3.1.1 High cold storage density and cold grade

Cold energy storage technologies can make use of sensible heat, reversible chemical heat of the reactants or latent heat of PCM. The sensible heat based cold storage method gives a low energy storage density and the temperature during charge/ discharge changes with time, whereas the chemical based cold storage can have a high energy storage density but it is least developed and difficult to control and is an expensive option.

Latent heat cold storage technology is well developed and allows for a high energy density with a mostly constant phase change temperature. Especially, CES technology based on eutectic PCM solutions provides a high cold grade, since the eutectic point of the PCM solution is lower than that of pure component in the system.

For a cold charge process, PCM is cooled down from ambient temperature T_a to the objective temperature T_{PCM}, with phase change phenomena happening at freezing point T_r. The cold storage density in PCM can be defined as in Eq.3.1:

$$E_d = \begin{cases} \int_{T_{PCM}}^{T_a} Cp_l \cdot dT & T_{PCM} > T_r \\ \int_{T_{PCM}}^{T_r} Cp_s \cdot dT + \Delta H_{ls} + \int_{T_r}^{T_a} Cp_l \cdot dT & T_{PCM} \le T_r \end{cases} \tag{3.1}$$

In which E_d represents the cold storage density; Cp_l, Cp_s are specific heat capacity of liquid and solid PCM; while ΔH_{ls} is the latent heat of the PCM.

Reference temperature T_{cold} is proposed to demonstrate the concept of cold storage grade. The partial cold energy stored in PCM below the reference temperature is regarded as valuable energy. Consequently, cold storage grade is defined as the ratio of deep cold energy (stored energy in the temperature range of T_{PCM} and T_{cold}) to the whole stored cold energy, as described in Eq.3.2:

$$E_g = \begin{cases} \dfrac{\int_{T_{PCM}}^{T_{cold}} Cp_l \cdot dT}{\int_{T_{PCM}}^{T_a} Cp_l \cdot dT} & (T_{PCM} > T_r) \\ \dfrac{\int_{T_{PCM}}^{T_r} Cp_s \cdot dT + \Delta H_{ls} + \int_{T_r}^{T_{cold}} Cp_l \cdot dT}{\int_{T_{PCM}}^{T_r} Cp_s \cdot dT + \Delta H_{ls} + \int_{T_r}^{T_a} Cp_l \cdot dT} & (T_{PCM} \le T_r) \end{cases} \quad (3.2)$$

In which E_g is cold storage grade, which is apparently higher when PCM temperature is lower than the freezing point.

According to these definitions, the effects of the main thermal properties (e.g. Cp_l , Cp_s , L_{heat} , T_{PCM}) on cold storage density and cold storage grade are briefly analyzed. Temperature-energy (T-E) diagram is used to demonstrate the relation between the stored cold energy and media temperature, as shown in Figure 3.1~3.4. The vertical and horizontal axis denote temperature of the PCM and the stored cold energy. The slopes of curves in three stages of the cold energy storage are $\frac{1}{Cp_l}$,0 and $\frac{1}{Cp_s}$, respectively; while the length of the horizontal line in the middle stage represents the latent heat (ΔH_{ls}) during the phase change process. It is pointed out that each thermal property is the only variable in the analysis of its influence on cold energy storage under each case.

The effect of specific heat capacity of liquid (Cp_l) is shown in Figure 3.1. PCM with different Cp_l are cooled down from the same initial temperature T_1 to the same final temperature T_2 below the freezing point. Under the reference temperature T_0 , the stored cold energy is assumed to be zero. Consequently, the cold storage densities in the two cooling processes from T_1 to T_2 can be represented by $(oe-oa)$ and $(of-ob)$, respectively. Both CE and DF denote the latent heat of the PCM, so $CD = EF$. From the curve, it is seen that $ab = AB < CD = EF = ef$, therefore, $ae < bf$, which means PCM with bigger Cp_l (as OBD in the curve) results in larger cold storage density. However, it is seen that the cold storage grade is not improved by the increase of heat capacity of the liquid PCM, since the stored energy is increased but at the temperature level higher than freezing point of the PCM.

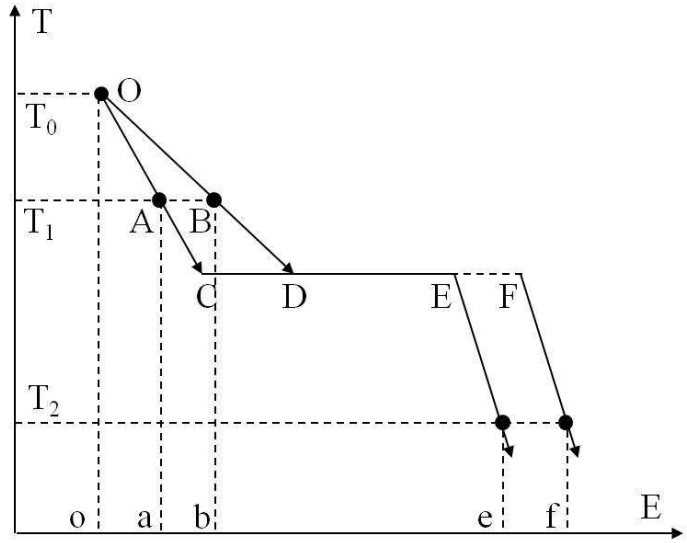

Figure 3.1 Effect of specific heat capacity of liquid

Figure 3.2 demonstrates the effect of specific heat capacity of solid PCM. Assumed that PCM is cooled down from T_1 to T_2 along the curve $ACDE$, the cold storage density can be expressed as ae. With higher solid heat capacity (smaller slope as DF in the curve), the cold storage density is obviously enlarged to be af. Compared with the cold energy storage in AD, the stored energy in section DE or DF is more useful since the media temperature is lower than the freezing point of PCM. With higher solid heat capacity, more cold energy ($df > de$) is stored in low temperature solid PCM, therefore, the cold storage grade is improved. In comparison, it is found that solid heat capacity (Cp_s) has more significant effect for the sake of high grade cold storage.

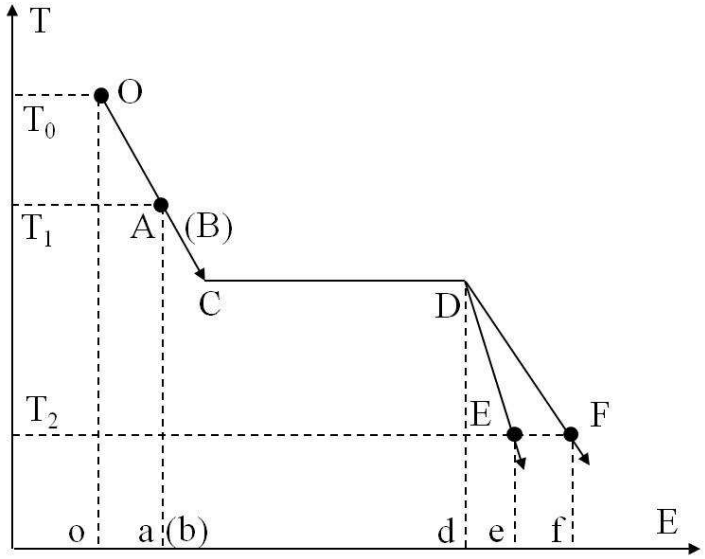

Figure 3.2 Effect of specific heat capacity of solid

Figure 3.3 describes the effect of latent heat of the PCM solution. With larger latent heat (BD compared to BC), it is seen that cold storage density is significantly increased (ae compared to af). Cold storage grade is improved since more latent heat cold energy is stored. However, it is worthwhile to point out that cold storage grade is mainly dependent on the level of freezing point. With lower freezing temperature of PCM, increase of latent heat is more valuable on the improvement of cold storage grade.

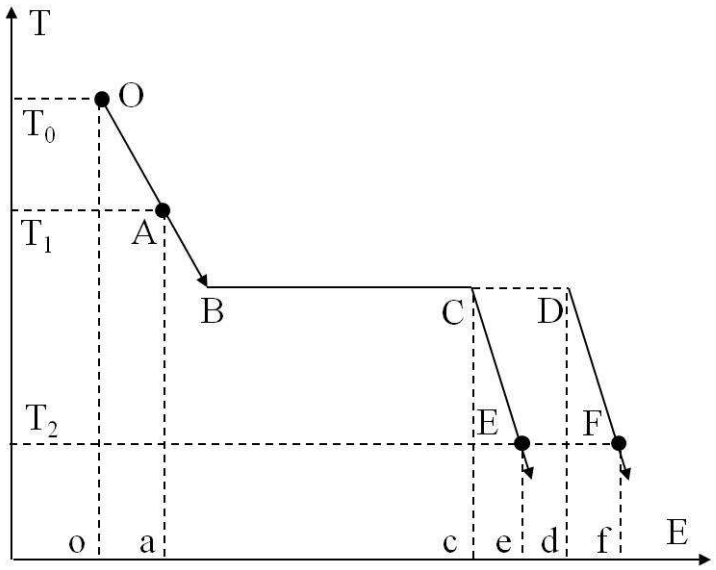

Figure 3.3 Effect of latent heat of the PCM

Figure 3.4 presents the effect of freezing point of the PCM. For most PCMs, solid heat capacity is smaller than that of liquid. As a result, the absolute value of the slope for DE and FG is bigger. In consideration of the same latent heat ($CD = BF$), PCM with lower freezing temperature has a larger cold storage density ($ag > ae$). In addition, due to phase change happens under a lower temperature, the cold storage grade for lower freezing point PCM is largely improved.

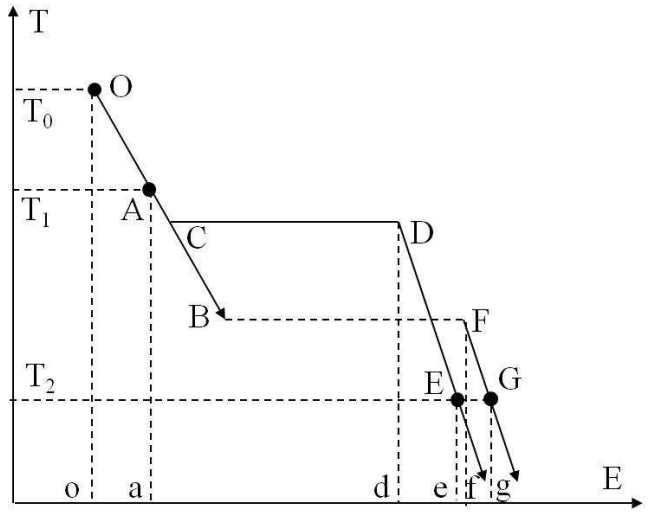

Figure 3.4 Effect of freezing point of the PCM

To sum up, for enlarging cold storage density, big specific heat capacity of liquid and solid, large latent heat of PCM and low freezing point are required. However, for improving the cold storage grade, low freezing point and large solid heat capacity of PCM are the prior criterion to be considered.

3.1.2 Adjustable freezing temperature of PCM

One of the attractive features of PCM cold storage is the quasi-isothermal process during charge/ discharge [177]. For most of PCM, the temperature keeps constant or varies in a small range. Due to the larger temperature difference between PCM and applying environment, the charging/ discharging rate is higher during phase change process.

However, the maintained temperature of PCM is restricted to be slightly lower than the environment in some applications, such as in transport of sensitive temperature products. Under these cases, the quasi-isothermal discharge process closing to the required temperature is of great concern since too low or too high cold temperature results in damaged products. Therefore, adjustable freezing temperature of PCM in cold storage should be proposed in accordance with applications.

One feasible approach is using eutectic salt-water solution in a binary or ternary cold energy storage system. According to Schroder's equation, the eutectic point of PCM in binary or ternary solutions can be determined, as described in Eq. (3.3):

$$\ln x_i = -\frac{\Delta H_{ls}}{R_{ideal}} \cdot \left(\frac{1}{T} - \frac{1}{T_{f,i}}\right) \tag{3.3}$$

In which x_i and $T_{f,i}$ are the molar fraction and freezing temperature of the compound i. T is the freezing point of the solution. R_{ideal} is the gas factor. Based on the Schroder's equation, the distribution of freezing temperature under different composition in binary system can be obtained, as shown in Figure 3.5.

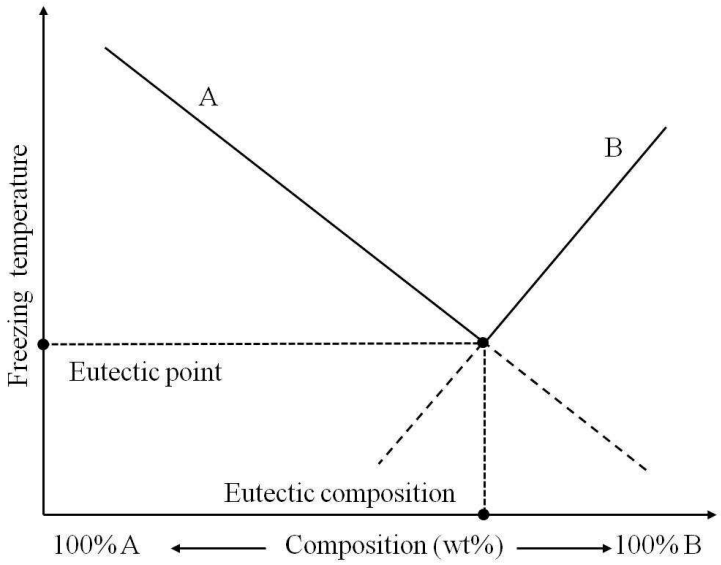

Figure 3.5 Adjustable freezing temperature based on application

From Figure 3.5. one can see that the PCM in the binary system has the lowest freezing temperature with the eutectic composition which can be determined by latent heat and freezing point of single PCM component. PCM solution with composition of either higher or lower value than the eutectic one has a temperature range in the phase change region. The variation of temperature in phase change process is dependent on the composition of the PCMs in the binary system. For example, with PCM A much more than that in the eutectic composition, the temperature variation during phase change becomes significant. This may prevent the use of the PCM solution in a cold storage system. Therefore, the applicable PCM composition is limited to a small range around the eutectic value. For specific applications, in case the required temperature is within the temperature range of the PCM solution in phase change process, salt addition to the binary system can be used to achieve a ternary system with adjustable freezing temperature. This will be discussed specifically in the following section.

In summary, the main principles of cryogenic energy storage using eutectic salt-water solution can be described as: (1) high cold storage density; (2) high-grade cold storage; (3) adjustable freezing temperature according to different applications.

Other requirements for cryogenic energy storage include high thermal conductivity, small volume change on phase transformation, low sub cooling, no phase separation, good cyclic and chemical stability and economics, etc [169].

3.2 Selection of PCM component in binary system

3.2.1 Calculation model of PCM properties

With the variation of composition in a binary PCM solutions, phase change phenomenon is distinguished by different phase change temperatures with diverse crystallization. For characterizing the charge/ discharge process, thermal properties of the PCM, such as freezing temperature, specific heat capacity and latent heat of PCM need to be further investigated.

(1) freezing temperature/ temperature range

According to the ideal solution model, the freezing temperature of the binary solution is lower than either of the pure component in the system. Therefore, binary or ternary PCM solution can be used for obtaining PCM with lower phase change temperature for high grade cold energy storage.

The phase diagram of ethylene glycol (EG) and water solution is presented in Figure 3.6. The liquid curve and solid curve represent the upper limit and lower limit of phase change temperature under different mass fractions of EG. By using Schroder's equation on ethylene glycol and water respectively, the liquid curves are obtained. The intersection point of the two liquid curves is the eutectic point of the binary system, through which with a horizontal line the solid curve is formed. Therefore, the integral section can be divided into three phase zones: (a) liquid zone above the liquid curve; (b) phase change zone between the liquid curve and solid curve; (c) solid zone below the solid curve.

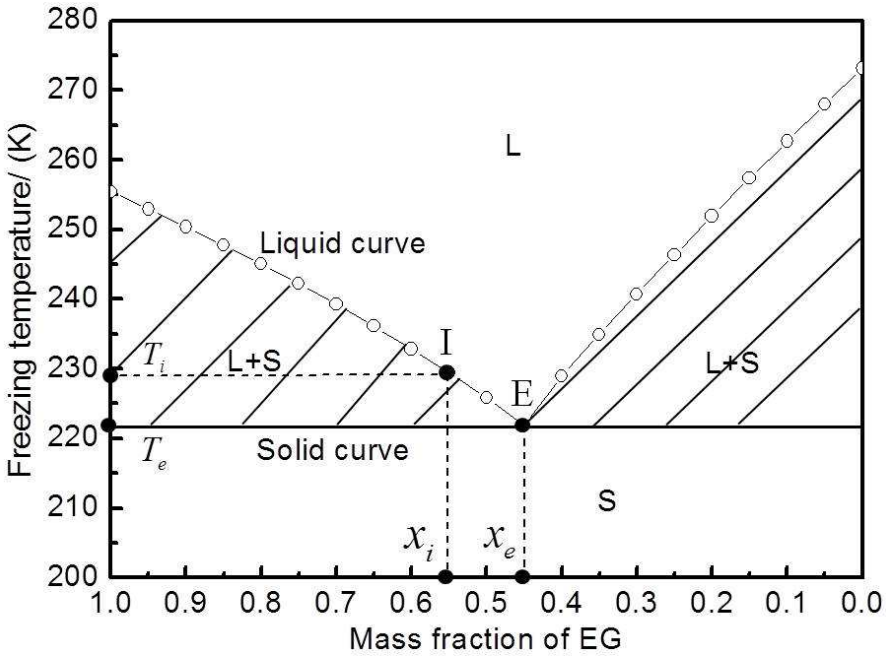

Figure 3.6 Phase diagram of EG water solution in CES system

The eutectic point (point E) is the lowest temperature for phase change in binary or ternary system, which can be obtained with the eutectic composition of PCM. Phase change temperature range (at point I) is caused under non-eutectic composition. As demonstrated in Figure 3.6, the eutectic temperature for EG and water solution (at point E) is approximately 221.9 K . Correspondingly, the eutectic composition (at point E) is 45% of mass fraction of EG. However, under non-eutectic compositions, for example, 55% of mass fraction of EG in the mixture, the phase change temperature range is from 229.4 K to 221.9 K. The thermal properties of EG and water used in the calculation are listed in Table.3.1.

Table 3.1 Thermal properties of EG and water

PCM	mass fraction (%)	latent heat (kJ/kg)	freezing point (K)	gas factor ($J/(mol \cdot K)$)
ethylene glycol	70	181	255.35	8.314
water	30	334	273.15	8.314

Based on the calculation for the phase diagram, it is suggested that binary system under the eutectic composition should be achieved for ideal cold energy storage, since the lowest and unchanged phase change temperature

improves the cold storage grade and charging/ discharging rate of the energy storage system. Especially, for temperature-sensitive applications, PCM with non-eutectic compositions is supposed to abandoned due to the variation of phase change temperature, as discussed in section 3.1.2.

Furthermore, the eutectic temperature in binary system should be approximately consistent to the required temperature in accordance with specific applications. Therefore, approach for the selection of eutectic salts as optimal PCM is of great significance and has been developed. As the fundamental step, DSC measurements on freezing temperature and latent heat for single PCM component are experimentally carried out. Based on the DSC data, the eutectic composition and eutectic temperature can be calculated according to the Schroder's equation for a featured PCM binary system. Subsequently, PCM solution with the calculated eutectic composition is produced and measured by DSC. The phase change temperature of the PCM solution obtained from the DSC measurement is used to verify the calculation. The selection criteria for the PCM binary system is using PCMs that have slightly lower eutectic temperature than the temperature required in the specific application. As a consequence, PCMs that cause an eutectic temperature higher than the requirement is to be rejected. The selection procedures for PCM are demonstrated in Figure 3.7.

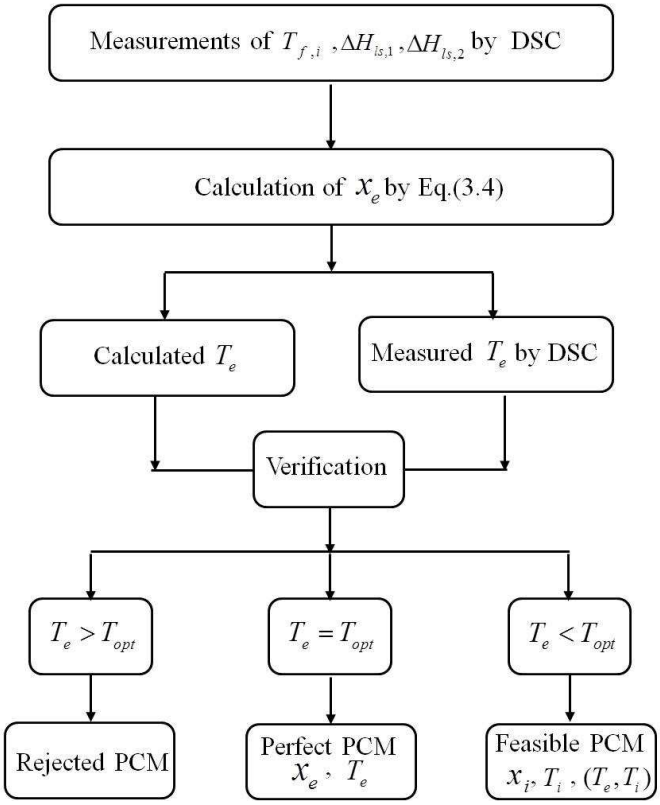

Figure 3.7 Selection procedures for PCM components in binary system

(2) specific heat capacity

The effective heat capacity (Cp_e) can be evaluated according to the thermal equilibrium model proposed in [178-179] for binary PCM storage system, which is defined as in Eq. (3.4a):

$$Cp_e = \frac{\phi_1 \cdot \rho_1 \cdot Cp_1 + \phi_2 \cdot \rho_2 \cdot Cp_2}{\overline{\rho}} \tag{3.4a}$$

In which $\phi_1, \phi_2, \rho_1, \rho_2, Cp_1, Cp_2$ are volume fraction, density, and specific heat capacity of component 1 and 2, respectively. However, this formula is restricted to be applicable when temperature is higher than the largest freezing temperature of component or the temperature is lower than the eutectic point.

In particular, for PCM solutions with lower temperature than the eutectic point, the effective solid heat capacity is calculated as:

$$Cp_{es} = \frac{\phi_1 \cdot \rho_1 \cdot Cp_{1s} + \phi_2 \cdot \rho_2 \cdot Cp_{2s}}{\overline{\rho}} \tag{3.4b}$$

In which $\overline{\rho}$ represents the averaged density, which can be described as in Eq. (3.5):

$$\overline{\rho} = \phi_1 \cdot \rho_1 + \phi_2 \cdot \rho_2 \tag{3.5}$$

It is obvious that the effective solid heat capacity is the mass average value of the solid heat capacity of pure PCM, the value of which is between Cp_1 and Cp_2, denoted as: $Cp_e \in (Cp_1, Cp_2)$ (suppose $Cp_1 < Cp_2$).

Due to the distinguished freezing point for PCM 1, PCM 2 and the binary system, effective liquid heat capacity is calculated based on the temperature of the binary PCM system. Since both of the components keep in liquid state even when the mixture temperature is below the freezing point of each component, as long as it is higher than eutectic point, the concept of artificial liquid heat capacity is proposed. The model of artificial liquid heat capacity for pure PCM component in the binary system is established, as demonstrated in Eq. (3.6):

$$Cp'_{1l} = \frac{Cp_{1l} \cdot (T_0 - T_1) + \beta \cdot \Delta H_{ls,1} + Cp_{1s} \cdot (T_1 - T_4)}{T_0 - T_4} \tag{3.6a}$$

$$Cp'_{2l} = \frac{Cp_{2l} \cdot (T_0 - T_2) + \beta \cdot \Delta H_{ls,2} + Cp_{2s} \cdot (T_2 - T_4)}{T_0 - T_4} \tag{3.6b}$$

In which T_0, T_1, T_2, T_3 are the initial temperature, freezing point of water ($T_{r,w}$), EG ($T_{r,EG}$) and the mixture PCM ($T_{r,mix}$), respectively; T_4 represents the PCM

temperature after cooling (T_{PCM}). While the factor β represents the phase change of the PCM solution, described as:

$$\beta = \begin{cases} 0 & (\mathrm{T_4} > \mathrm{T_3}) \\ 1 & (\mathrm{T_4} \le \mathrm{T_3}) \end{cases} \tag{3.7}$$

On this basis, the effective liquid heat capacity of the component PCM in binary system is obtained, seen in Eq. (3.8):

$$Cp_{el} = \begin{cases} \dfrac{\phi_1 \cdot \rho_1 \cdot Cp_{1l} + \phi_2 \cdot \rho_2 \cdot Cp_{2l}}{\overline{\rho}} (T_4 > T_1) \\ \dfrac{\phi_1 \cdot \rho_1 \cdot Cp'_{1l} + \phi_2 \cdot \rho_2 \cdot Cp_{2l}}{\overline{\rho}} (T_2 < T_4 < T_1) \\ \dfrac{\phi_1 \cdot \rho_1 \cdot Cp'_{1l} + \phi_2 \cdot \rho_2 \cdot Cp'_{2l}}{\overline{\rho}} (T_3 < T_4 < T_2) \end{cases} \tag{3.8}$$

It is pointed out that for the calculation of liquid heat capacity, factor β is equal to zero ($\beta = 0$) since temperature of the PCM solution is higher than the eutectic point of the binary system, as described in Eq. (3.7).

According to the calculation model (Eq. (3.4b) and Eq. (3.8)), heat capacity of EG and water solution with 45% EG by mass fraction is evaluated, shown in Figure 3.8. Under temperature higher than the freezing point of water ($T_0 > T_1$), single component for either water or EG is in liquid state, therefore, the effective liquid heat capacity of the PCM solution can be calculated as 3357 kJ/kg according to Eq. (3.8). With a decrease of PCM temperature, the effective liquid heat capacity, the effective liquid heat capacity is reduced to be 2525 kJ/kg and 2502 kJ/kg in the temperature range of $T_2 < T_4 < T_1$ and $T_3 < T_4 < T_2$, respectively. It is shown that when PCM temperature is in the range of $T_3 < T_4 < T_1$, the effective liquid heat capacity drops by 25.5% than the value under temperature higher than the ice point. When temperature is further reduced to be lower than the eutectic point T_3, PCM solution is in solid state and thus the solid heat capacity can be calculated. According to Eq. (3.8), the solid heat capacity is equal to 2176 kJ/kg, which is an average heat capacity of solid PCM components in terms of mass fraction. The thermal properties for pure EG and water are presented in Table 3.2.

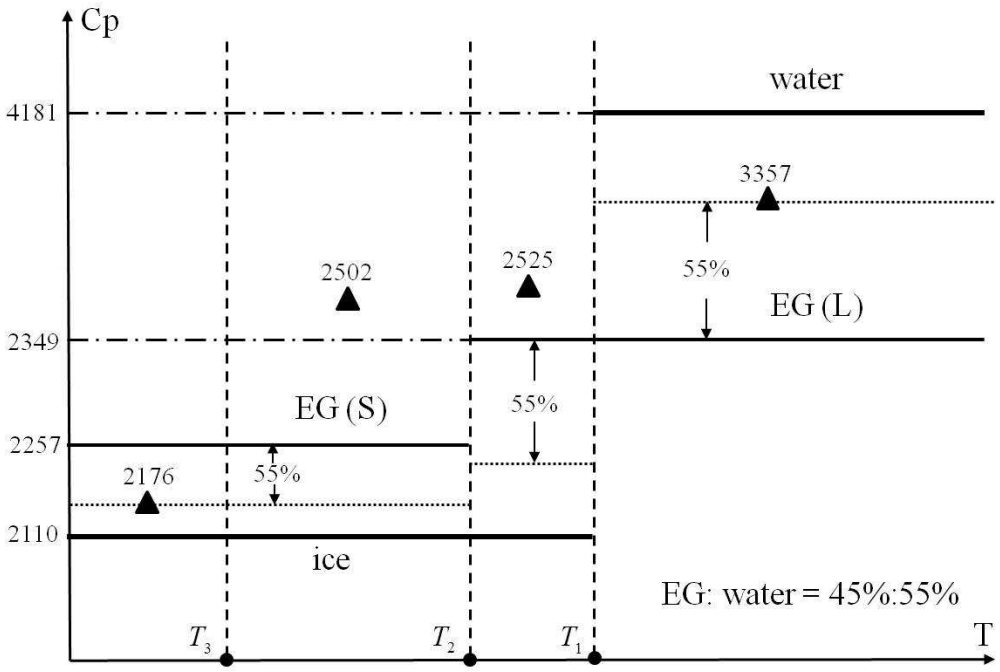

Figure 3.8 Heat capacity of EG water solution in CES system

Table 3.2 Thermal properties of EG and water for the calculation of Cp_e

m %	T_0	T_1	T_2	T_3	T_4	$Cp_{1,l}$	$Cp_{1,s}$	$Cp_{2,l}$	$Cp_{2,s}$	$\Delta H_{ls,1}$	$\Delta H_{ls,2}$
			K				$kJ/(kg \cdot K)$			$kJ/(kg \cdot K)$	
45	300	273	255	221	200	4181	2110	2349	2257	334	181

(3) latent heat

For analyzing the relation between the effective latent heat of the binary system and the latent heat of pure PCM component, a cold charge process from T_0 to T_3 is supposed. Therefore, the energy conservation equation for the cold charging process can be written as Eq. (3.9):

$$\overline{\rho} \cdot Cp_{es} \cdot (T_3 - T_4) + \overline{\rho} \cdot \Delta H_{ls,3} = \phi_1 \cdot \rho_1 \cdot Cp'_{1l} \cdot (T_0 - T_4) + \phi_2 \cdot \rho_2 \cdot Cp'_{2l} \cdot (T_0 - T_4) \quad (3.9)$$

In which, $Cp_{es}, Cp'_{1l}, Cp'_{2l}$ are the effective heat capacity of solid PCM, artificial heat capacity for pure liquid PCM 1 and 2, respectively; $\Delta H_{ls,3}$ are the latent heat of the binary PCM solution.

Since phase change happens, $\beta = 1$, the latent heat of pure component $\Delta H_{ls,1}, \Delta H_{ls,2}$ are considered. It is supposed that $T_0 = T_3 + dT$ and $T_4 = T_3 - dT$, using Eq.(3.4b), (3.6) and (3.8), the effective latent heat of the PCM solution is determined:

$$\Delta H_{ls,3} = \frac{1}{\overline{\rho}} \cdot \left\{ \phi_1 \cdot \rho_1 \cdot [\Delta H_{ls,1} + (Cp_{1s} - Cp_{1l}) \cdot (T_1 - T_3)] + \phi_2 \cdot \rho_2 \cdot [\Delta H_{ls,2} + (Cp_{2s} - Cp_{2l}) \cdot (T_2 - T_3)] \right\} \tag{3.10}$$

In the above formula, liquid heat capacity of pure component is equal to the solid heat capacity of that component PCM, since the initial temperature T_0 ($T_0 = T_3 + dT$) is lower than freezing temperature of pure component T_1, T_2. Consequently, Eq. (3.10) can be simplified as:

$$\Delta H_{ls,3} = \frac{1}{\overline{\rho}} \cdot (\phi_1 \cdot \rho_1 \cdot \Delta H_{ls,1} + \phi_2 \cdot \rho_2 \cdot \Delta H_{ls,2}) \tag{3.11}$$

Therefore, the effective latent heat of PCM binary system is equal to the weighted average value of the latent heat of pure component PCM 1 and 2. For instance, for EG water solution with 45% of EG by mass fraction, the calculated latent heat is approximately 265.2 kJ/kg.

3.2.2 Influence of PCM properties on cold storage

For increasing the cold storage density and improving the cold storage grade, the thermal properties in binary PCM system need to be furthered analyzed.

According to Eq.(3.3), derivative of eutectic temperature in binary PCM system can be written as in Eq. (3.12):

$$dT = -\frac{1}{T_{f,i}^{\ 2}} \cdot dT_{f,i} - \frac{1000 R_{ideal}}{M \cdot \Delta H_{ls} \cdot x_i} \cdot dx_i + \frac{1000 R_{ideal} \cdot \ln(x_i)}{(M \cdot \Delta H_{ls})^2} \cdot (\Delta H_{ls} \cdot dM + M \cdot d\Delta H_{ls}) \tag{3.12}$$

It is deduced that the reduction of eutectic point aimed for higher cold grade storage is restricted by variation of freezing temperature, latent heat and molecular weight of component PCM in the binary system.

From Eq. (3.12), it is obviously seen that for reducing the eutectic point, PCM with lower freezing temperature and smaller molecular weight should be selected as the components in the binary PCM system. However, selecting PCM having lower latent heat results in higher cold storage grade, at the expense of lowering the cold storage density which is caused by smaller effective latent heat.

Furthermore, the relation of the two PCM components in the binary system was considered by M.S. Ding et al [172]. Phase diagrams of seven binary carbonates for making the non-aqueous electrolytes for lithium batteries were investigated by DSC measurement. By comparison of the different phase diagrams, it was concluded that PCM having comparable melting temperatures and compatible molecular structures in the binary system tend

to be feasible for expanding the liquid region towards lower temperature level.

According to the differential equation, the reduction of mass fraction of component PCM is conceivable to lower the eutectic point, which can be achieved by extending the binary system to ternary system by salt addition. Ding et al [180] added different amount of lithium salt ($LiPF_6$) in the binary system composed by ethyl methyl carbonate and ethylene carbonate. It was found that the solid curve in the phase diagram became lower in the consequence of the lithium salt addition, which indicated the improvement of cold storage grade of the PCM system. The liquid curve dropped more remarkable than that of the solid curve, leading to much narrower phase change zone in the phase diagram. As has been noted, the quasi-isothermal feature during phase change is advantageous for improving the charging/ discharging rate of the storage system and is of particular significance under temperature-sensitive cold applications.

For the explanation of the positive effect of salt addition, the eutectic point in ternary system is deduced. Provided that component 3 (salt) is added into a binary system with a mass fraction of x_3, and there is no crystallization in the process. Therefore, an eutectic ternary system is formed. The new composition of 1 and 2 in the ternary system can be therefore expressed as:

$$x_1' = \frac{x_1}{1+x_3},\ x_2' = \frac{x_2}{1+x_3} \tag{3.13}$$

Based on the melting temperature, latent heat and mass fraction of single PCM component 1 and 2, the eutectic temperature and eutectic composition of the ternary system can be calculated according to Eq. (3.3) and Eq. (3.13). In this condition, the calculated mass of salt addition x_3 is equal to the mass required in the ternary composition. However, if salt addition is too much or little, non-eutectic ternary system is obtained, in which case temperature of PCM solution varies in a small range during phase change. And when the non-eutectic PCM solution is cooled down to a temperature lower than the ternary eutectic point, redundant amount of PCMs is separated by crystallization process. As can be seen in Figure 3.9, ternary eutectic point is even lower than the binary eutectic point. Therefore, salt addition can be used to adjust freezing temperature of the PCM solution.

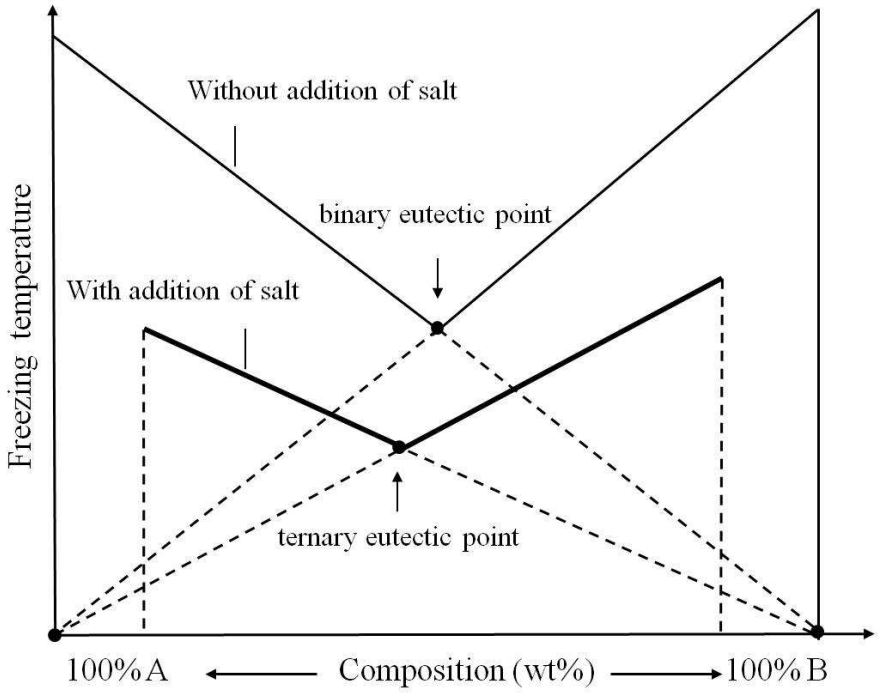

Figure 3.9 Phase diagram in ternary system

In summary, by selection of proper PCM components in binary system, cryogenic energy storage with large cold storage density and high cold storage grade can be achieved. It is pointed out that DSC measurements of PCM thermal properties is the fundamental work to be carried out prior to PCM selection.

3.3 Improvement of PCM cold storage by nanoparticles

Restriction for the application of PCM cold storage is caused by the low thermal conductivity of PCM, leading to small cold discharging rate of the cold storage system. One of feasible approaches is adding nanoparticles in PCM cold storage system, by which both of thermal conductivity and heat capacity of PCM can be improved.

3.3.1 Improvement of heat capacity

By adding nanoparticles in PCM solutions, the heat capacity can be further improved. The heat capacity can be predicted by formula shown below from [178-179]:

$$Cp_t = \frac{\phi_p \cdot \rho_p \cdot Cp_p + \phi_f \cdot \rho_f \cdot Cp_f}{\phi_p \cdot \rho_p + \phi_f \cdot \rho_f} \tag{3.14a}$$

$$Cp_t - Cp_f = \frac{\phi_p \cdot \rho_p \cdot (Cp_p - Cp_f)}{\phi_p \cdot \rho_p + \phi_f \cdot \rho_f} \tag{3.14b}$$

In which Cp_t , Cp_p , Cp_f are the effective heat capacity of PCM with nanoparticles, heat capacity of particle and original PCM solution, respectively. ρ_p and ρ_f , ϕ_p and ϕ_f represents the density and the volume fraction of the nanoparticle and the fluid, respectively. From Eq. (3.14b), the heat capacity is improved by the addition of nanoparticle in the condition that the heat capacity of the nanoparticle is higher than that of the base liquid. For example, by adding 1% of SiO_2 nanoparticles (0.93 $J/(g\cdot^oC)$) by volume in calcium chloride (0.65 $J/(g\cdot^oC)$), the heat capacity is improved by 2.6% (0.667 $J/(g\cdot^oC)$).

Nelson et al [181] studied variation of heat capacity by adding graphite nanoparticles in polyalphaolefin. It was found that 0.6% concentration of nanoparticles by weight results in enhanced heat capacity by 50%. Shin and Banerjee et al [182] studied the specific heat capacity in molten salt based silica nanofluid. It was reported that heat capacity increased by 26% for 1% of mass fraction of silica particles in the solution. However, heat capacity was reduced by 40%~50% in water based Al2O3 nanofluid at 21.7% volume concentration [183].

The mechanism for enhancement of heat capacity by nanoparticles were discussed in [179]. As was stated in [183], nanoparticles with larger heat capacity than the base fluid and able to be well dispersed in solution could improve the heat capacity of the PCM; otherwise, the heat capacity is decreased.

3.3.2 Improvement of thermal conductivity

Nanofluids were also reported for the enhancement of thermal conductivity [184-188]. The positive effect of copper nanoparticles [184-185], TiO2 nanoparticles [186] and carbon nanotube [187] in different base fluids were all investigated. It was explained that percolation network within the cluster of nanoparticles caused by particle aggregation was the main reason for thermal conductivity enhancement [188].

The effective thermal conductivity in the suspension was described by Maxwell [117] without consideration of the nanolayer impact, seen in Eq.3.15:

$$k_{Maxwell} = \frac{k_p + 2\cdot k_l + 2(k_p - k_l)\cdot \phi_p}{k_p + 2\cdot k_l - (k_p - k_l)\cdot \phi_p}\cdot k_l \tag{3.15}$$

Yu et al [189] developed a modified Maxwell model, with the effect of nanolayer considered, formulated in Eq.3.16:

$$k_e = \frac{k_p + 2k_l + 2(k_p - k_l)(1+\gamma)^3 \phi_p}{k_p + 2k_l - (k_p - k_l)(1+\gamma)^3 \phi_p} k_l \tag{3.16}$$

$$\gamma = \frac{\delta_{nano}}{r_{nano}} \tag{3.17}$$

Which γ represents the ratio of nanolayer thickness δ_{nano} to the particle radius r_{nano}. From Eq. (3.15)~(3.16), it is seen that the thermal conductivity can be improved when the nanoparticle has a thermal conductivity larger than that of the base fluid. Considering the effect of nanolayer, the influence of the nanoparticles on the thermal conductivity is further enhanced.

By Eq.(3.15), the presence of very thin nanolayers ($<10nm$) on improvement of thermal conductivity could be predicted. Two main conclusions were obtained: (1) when particle radius was smaller than 5nm, the calculated enhancement of thermal conductivity considering the effect of nanolayer was as 3~8 times as that calculated by conventional Maxwell model; (2) under the same mass fraction of particle, adding smaller nanoparticles was better than adding more particles.

From previous studies, it is demonstrated that adding nanoparticles into the eutectic salt water solution was verified as an efficient method for improving cold storage density due to increased heat capacity and cold discharging capacity due to improved thermal conductivity. It is concluded that added nanoparticles with higher heat capacity and thermal conductivity than the base fluid and have larger volume concentration but small particle size are beneficial to improve both cold storage and cold discharging capacity. However, good dispersion in solution is also required to avoid agglomeration of nanoparticles and degradation of the thermal properties.

3.4 Temperature-adaptive cold storage for cold protection

Binary or ternary PCM solutions have being extensively used for cold energy storage due to the significance of the lower eutectic point for improving the cold storage grade. However, for some of the applications, such as temperature-sensitive cold protection, phase change temperature of PCM is highly required to be approximate to the temperature of the protected items. Temperature out of the permitted small variation range is inclined to result in unacceptable consequence. On the other aspect, cold storage system should be temperature-adaptive in terms of different applications. Therefore, temperature-adaptive cold storage is proposed.

3.4.1 Introduction of adjustable cold storage technology

As discussed previously, it is stated that non-eutectic composition of PCM causes variable phase change temperature, therefore, is not suggested for general applications. However, partial-eutectic composition in ternary PCM system can be utilized to adjust the temperature level of phase change in the condition of having an unchanged freezing point.

The partial-eutectic temperature and partial-eutectic composition in ternary PCM cold storage system are demonstrated in Figure 3.10. The PCM A and B and salt C can be regarded as two subdivided systems AC and BC. Providing the proportion of A (or B) and C is in accordance with the mass fraction ratio in binary system AC (or BC), partial-eutectic of AC (or BC) is defined. Correspondingly, partial-eutectic temperature and partial-eutectic composition are determined. However, it is pointed out that in ternary system A, B and C, it is actually non eutectic composition due to the unmatched mass fractions.

Generally, there are two phase change surfaces under non-eutectic compositions. In terms of the above analysis, two partial-eutectic points can be found in the phase diagram, such as point AC and point BC in Figure 3.10. With the increasing of mass fraction of component 3, these partial-eutectic points are lowered down, seen in Figure 3.10. The eutectic point (ABC in Figure 3.10) exists in the condition of eutectic composition in ternary PCM system.

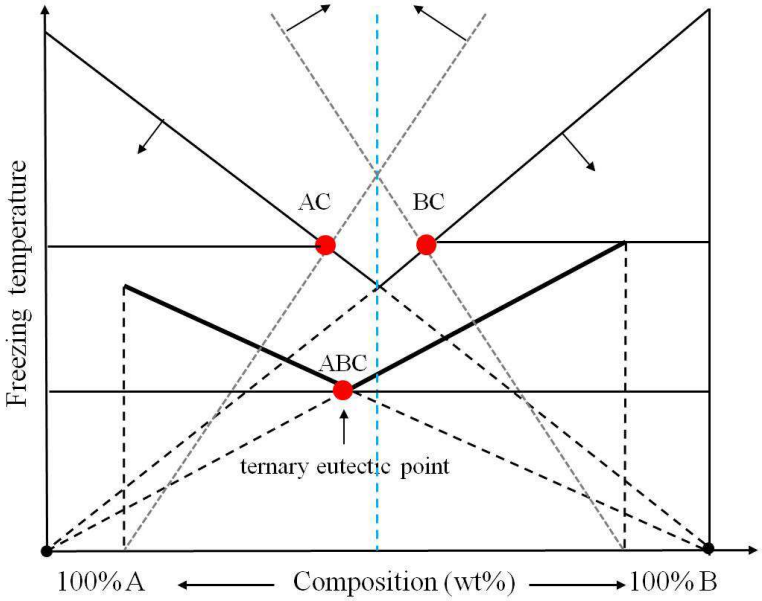

Figure 3.10 Description of eutectic point in ternary PCM cold storage system

The partial-eutectic compositions for 1 and 3, 2 and 3 are written as $x_{pe,1}$ and $x_{pe,2}$, which are distinguished from the eutectic composition for 1, 2 and 3, written as $x_{e,1}$, $x_{e,2}$ and $x_{e,3}$. The partial-eutectic compositions are the solutions of the following equations:

$$\frac{1}{T_{f,1}}-\frac{1000R_{ideal}\ln\frac{x_1}{1+x_3}}{M_1\Delta H_{ls,1}}=\frac{1}{T_{f,3}}-\frac{1000R_{ideal}\ln\frac{x_3}{1+x_3}}{M_3\Delta H_{ls,3}} \quad \text{(written as: } x_{pe,1}=f(x_3)\text{)} \quad (3.18)$$

$$\frac{1}{T_{f,2}}-\frac{1000R_{ideal}\ln\frac{x_2}{1+x_3}}{M_2\Delta H_{ls,2}}=\frac{1}{T_{f,3}}-\frac{1000R_{ideal}\ln\frac{x_3}{1+x_3}}{M_3\Delta H_{ls,3}} \quad \text{(written as: } x_{pe,2}=g(x_3)\text{)} \quad (3.19)$$

Based on the mathematical model, the cooling process of the ternary system under non-eutectic composition is analyzed by comparing the mass fractions to the partial-eutectic mass fractions:

When $x_1 > x_{pe,1}$, phase change temperature is varied in a small range with solid component 1 separated from the solution;

When $x_2 > x_{pe,2}$, the PCM solution freezes in another temperature range with crystallization of solid component 2;.

When $x_1 = x_{pe,1}$ or $x_2 = x_{pe,2}$, isothermal phase change is obtained. It is highlighted that the phase change temperature can be adjusted by varying the proportions of the other two components, which is theoretically in the range of the eutectic points in ternary system and in binary system.

To sum up, the partial-eutectic composition in ternary PCM system is a crucial feature for the temperature-adaptive cold storage. For cold protection applications, the main parameters of the cold storage system include:

(1) cold protection capacity. The parameter denotes the quantity of cold energy that can be discharged. Basically, it is determined by the latent heat and mass of the partial-eutectic PCM and salt.

(2) adjustable temperature range. The parameter represents the temperature-adaptive ability for cold protection. Assuming that $x_1 = x_{pe,1}$, then the partial-eutectic temperature is feasible for applications with precise temperature requirement of $T_{opt} = T_{pe,1}$. By changing the mass fractions of component 2 and 3 in the ternary system, the partial-eutectic temperature $T_{pe,1}$ varies in an adjustable range.

In the partial-eutectic ternary PCM solution, the phase change temperature of PCM 2 and salt is varied in a small range since the mass fractions of PCM 2 and salt are not under the eutectic composition. While PCM 1 and salt

have the eutectic temperature $T_{pe,1}$, which can be either higher or lower than the temperature range as mentioned above. Therefore, PCM cooling diagram for cold protection that requires higher or lower temperature than the phase change temperature range of subdivided 2 and 3 binary system are demonstrated in Figure 3.11 (a) and (b), respectively.

As can be seen in Figure 3.11, the cold protection capacity is quantified as the energy difference during phase change. This is determined by latent heat of the partial-eutectic PCM solution. The gap α is the adjustable temperature range of the ternary PCM system, which can be tuned by changing the mass fractions of component 2 and 3.

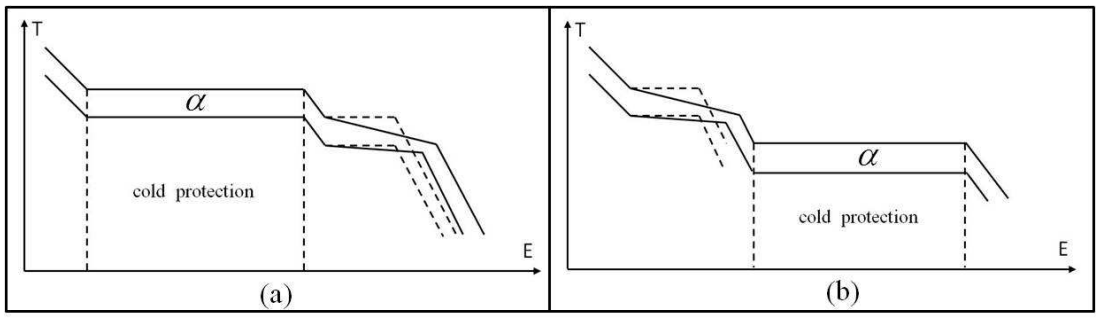

Figure 3.11 Cooling diagram of a ternary system for cold protection

3.4.2 A case study

Binary PCM system composed by EG and water solution is considered. A kind of paraffin is added into the binary system for obtaining adjustable cold temperature range for cold protection. For comparing the adjustable temperature range influenced by the salt addition, three different paraffin with different thermal properties are investigated. The thermal properties of three different paraffin are obtained from [12], listed in Table 3.3.

Table 3.3 Properties of adding paraffin in ternary system

Paraffin	formula	weight	Freezing point (K)	Latent heat (kJ / kg)
n-Undecane	$C_{11}H_{24}$	156	247.5	141.9
n-Decane	$C_{10}H_{22}$	142	243.4	201.8
n-Nonane	C_9H_{20}	128	219.5	120.6

It is assumed that PCM 1 (EG) and salt 3 (paraffin) is under the partial-eutectic composition in the ternary system. Therefore, phase change temperature is maintained at partial-eutectic point of PCM 1 and salt 3. For

simplification, total mass of EG and water is recorded as 1; while mass of the added salt is written as x_3, which can be any value theoretically.

For cold protection applications, the required cold temperature is supposed to equal to the partial-eutectic temperature. According to the Schroder's equation, the objective temperature can be expressed as in Eq. (3.20):

$$T_{opt} = T_{pe,1} = \frac{1}{\frac{1}{T_{f,3}} - \frac{1000 R_{ideal} \ln \frac{x_3}{1+x_3}}{M_3 \Delta H_{ls,3}}} \tag{3.20}$$

Correspondingly, the mass fraction of PCM 1 is determined:

$$x_{pe,1} = (1+x_3) \cdot e^{(\frac{1}{T_{f,1}} - \frac{1}{T_{pe,1}}) \cdot \frac{M_1 \Delta H_{ls,1}}{1000 R_{ideal}}} \tag{3.21}$$

Provided that the total mass of the binary system consisted of PCM 1 and 2 is one unit, the above formula indicates the mass of each component in the partial eutectic ternary system is $x_{pe,1}$, $(1-x_{pe,1})$ and x_3, respectively. Assuming that the required temperature for cold protection is slightly higher or lower than the eutectic temperature of EG and water solution (221.9 K). By changing the mass fraction of EG and salt, the phase change temperature is adjusted.

The partial-eutectic composition and temperature are shown in Figure 3.12~3.13. Figure 3.12 shows that the partial eutectic composition is changed with the addition of paraffin. With the increase of mass fraction of added paraffin, the corresponding partial eutectic composition increases gradually till the upper limit. The partial eutectic composition of PCM 1 and n-Nonane is obviously lower due to the smaller formula weight and latent heat as shown in Eq.(3.21).

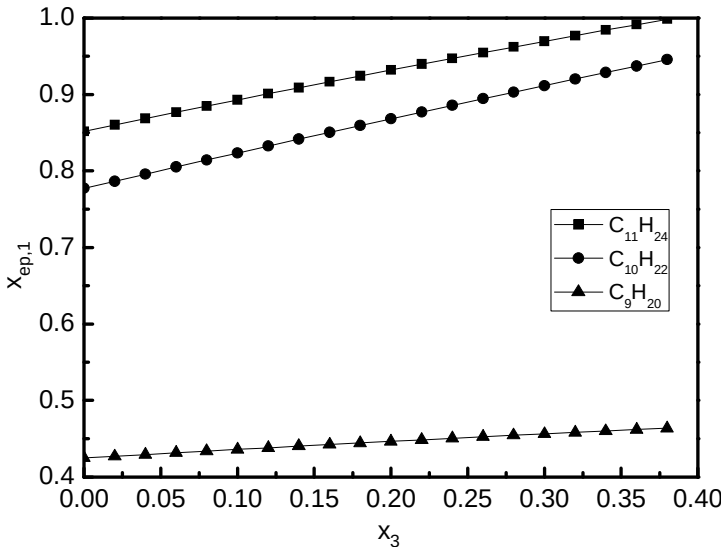

Figure 3.12 Variation of partial eutectic composition

Figure 3.13 shows that the partial eutectic temperature is tuneable with addition of paraffin. According to the calculation, the adjustable temperature range for n-Undecane, n-Decane and n-Nonane is equal to $7.2K$, $5.5K$ and $9.4K$, respectively. The binary solution of PCM 1 and n-Nonane has the largest phase change temperature range due to the smallest formula weight, latent heat and the lowest pure freezing temperature of n-Nonane, as discussed above.

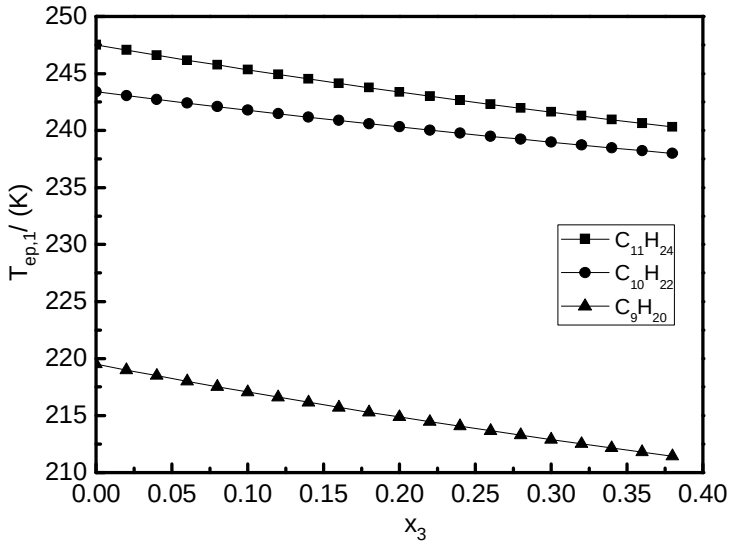

Figure 3.13 The adjustable temperature range in ternary system

The detailed PCM composition and concentration of a ternary system composed by EG, water and n-Nonane is demonstrated based on the above results. With 0.45 g of EG, 0.55 g of water and 0.2 g of n-Nonane in the ternary system, the mass fraction of EG, water and paraffin is 37.5%, 45.8% and 16.7%, while the concentration of the components is 5.89 mol/L, 24.80 mol/L, and 1.27 mol/L, respectively. In a binary system, since the mass fraction of each PCM is reduced than that in pure PCM system, the eutectic temperature is lower than either of the single component according to Eq. (3.3). With addition of the third PCM into the binary system, the eutectic temperature can be further lowered since the mass fraction of each component is relatively lower in the ternary system. Similarly, the partial eutectic temperature in the ternary system can be adjusted by adding PCM with different mass fraction, formula weight, freezing temperature and latent heat according to the Schroder's equation.

Based on the above calculation, in the condition that the phase change temperature of a binary PCM system is slightly higher or lower than required temperature for cold protection applications, it is feasible to achieve

adjustable eutectic point in a temperature range of several degrees by adding proper salt and changing the mass fraction of PCM in the formed ternary solution. Salts with smaller formula weight, lower freezing temperature but lower latent heat are suggested to be used for enlarging the adjustable temperature range.

3.5 Summary of this chapter

This chapter provides a fundamental study of the CES technology using eutectic PCM solution, with the principles of high cold storage density, high cold grade and adjustable phase change temperature.

The influence of thermal properties of single PCM on cold storage density is analyzed. Cold storage density of single PCM can be improved by selecting PCM component with large latent heat and heat capacity of liquid and solid. By adding nanoparticles with heat capacity bigger than the base PCM, specific heat capacity can be further improved.

The cold grade of the storage is defined as the ratio of deep cold energy (stored cold at a temperature lower than the freezing point of PCM) to the whole stored cold energy. It is mainly affected by the freezing temperature, the latent heat of PCM and the PCM storage temperature after charging. Binary eutectic PCM solutions can be used to improve the cold grade due to the further lowered freezing temperature. In a binary PCM system, the eutectic phase change temperature is determined by the formula weight, latent heat and the freezing temperature of single PCM.

However, PCM solution for cold storage should have a phase change temperature in terms of specific situation. Therefore, PCM cold storage with a low and adjustable freezing temperature in accordance with the applications is required. This can be achieved by addition of a third PCM to form a ternary PCM solution. A case study of adjusting freezing temperature for cold protection is conducted. By adding the third PCM with smaller formula weight, smaller latent heat and lower freezing temperature, the adjustable temperature range is bigger.

Chapter 4
Discharge behaviour of PCM based cold storage in a CES system

This chapter aims to answer the following two questions:

(1) How to improve the cold discharging rate?

(2) How to evaluate the cold discharging rate in consideration of combined effect of cold radiation and convection?

4.1 Introduction

4.1.1 Embedding metal foams in PCM for improving discharging rate

The advantages of PCM cold storage using eutectic solutions include high cold storage density due to the large latent heat and high cold grade caused by the lowered eutectic point of the solution [190]. However, there are two main disadvantages:

(1) Small thermal conductivity. The thermal conductivities of commonly used PCM are approximately 0.1~0.2 $W/(m.\mathrm{K})$ for paraffin, 0.4~0.6 $W/(m.\mathrm{K})$ for salt and salt hydrates and 0.3~0.5 $W/(m.\mathrm{K})$ for fatty acids.

(2) Reduced surface heat flux. The solid- liquid interface moves away from the heat transfer surface in the cold charging process. The heat flux on the contact surface decreases due to the increased thermal resistance of the PCM.

Therefore, improvement of discharge behaviour in the PCM cold storage is required. The feasible approaches for improving cold extraction of PCM are summarized as increasing thermal conductivity of PCM, extending heat transfer area and enhancing convective heat transfer between PCM and HTF, etc.

The conventional heat enhancement techniques mainly included the application of embedded fins into PCM and impregnation of metal matrix using materials with high thermal conductivity, e.g. carbon fiber, brushes and multitubes [191]. It was claimed that thermal conductivity was largely improved by both of the methods, since the solid/ liquid interface was observed with faster moving during the conduction-dominated regime. However, due to the lower porosity and lower permeability of the fins or

metal matrixes, the convective heat transfer was severely constrained, as pointed out by Zhao et al [192] and Boomsma et al [193]. Therefore, as a complex structures with high thermal conductivity, specific surface area (high porosity and pore density) and permeability, open-cell metal foams was proposed to be the perfect structure for improvement of cold discharging capacity.

Lots of the analytical methods are based on one dimensional moving boundary problem, with the assumption of semi-infinite or infinite storage geometry. This is inconsistent with the realistic volume or shape of the PCM used for cold storage. Therefore, in this chapter, a two dimensional model is developed for analytical investigation of discharge behaviour of PCM cold storage embedded with metal foams.

4.1.2 The combined effect of cold radiation and convection for evaluating discharging rate

4.1.2.1 Combination of cold radiation and convection

Lots of open literatures can be found on investigating the discharging behaviour in PCM cold storage system. However, to the author's knowledge, there is few literatures considering the effect of cold radiation. The motivation for considering the combined effect of heat convection and cold radiation is based on the following facts:

(1) Low PCM temperature. For high grade cold storage, the PCM is stored at a low temperature, for example, EG and water solution is cooled down to be lower than $-40^{O}C$. Especially, for cold protection applications, the temperature of PCM solution maintains constant at a low temperature level during the discharging period.

(2) Significant contribution of cold radiation on cold discharge for big PCM capsules. With increase of PCM capsule diameter, the convective heat transfer decreases gradually, resulting in increased ratio of cold dissipation by radiation relative to convection. According to [194], in the case of air flowing across the sphere capsule of $10mm$ radius with Re lower than 300, the convective heat transfer coefficient was less than $20W/(m^2 \cdot K)$. While it was reduced to be lower than $10W/(m^2 \cdot K)$ and $5W/(m^2 \cdot K)$ when the radius was as large as $20mm$ and $40mm$, respectively. In a case study of assuming fluid temperature as $300K$ and the PCM temperature as $200K$, the evaluated heat flux by convection under different radius were $2000W/m^2$, $1000W/m^2$ and $500W/m^2$. Since the heat flux by cold radiation was calculated as $368.5W/m^2$, the ratio of radiation relative to convection was

18.4%, 36.9% and 73.7%, respectively, indicating an increasing significance of the contribution of cold radiation on cold discharging.

4.1.2.2 Heat transfer model for a PCM capsule

As mentioned previously, thermal properties of PCM can be investigated by using DSC and tracing the shape, position and moving of the interface which is monitored through the temperature profile measurement or visual methods, etc. In another aspect, phase change heat transfer performance can be studied by numerical methods (FDM or FEM) combined with enthalpy method or effective heat capacity method. Temperature distribution and solid-liquid interface can be obtained by solving partial differential equations.

However, the limitation of the above experimental and numerical methods is the poor comparability of heat transfer characteristics derived by different researchers. This is due to the data deviation caused by different setups (e.g. experimental or numerical conditions) and different assumptions (e.g. neglected volume variation and limited mesh density) [11].

In comparison, one feature of the heat transfer model in this study is that it is fundamentally established in the view of energy balance of PCM capsule. By using this method, the averaged temperature and the overall heat transfer characteristics of PCM capsule during the discharging process can be precisely predicted.

Another feature of this model is using equivalent heat flux to consider the combined effect of cold convection and radiation. The concept of equivalent heat flux was originally used for characterizing the radiation transport process in open-cell metal foams for the thermal conduction problem by Zhao et al [195]. As claimed in [195], the equivalent radiation conductivity was calculated according to the definition of thermal conduction, considering the effects of emissivity, reflectivity and configuration factors for evaluating the net radiation heat flux. In current study of regarding the effect of thermal radiation on phase change heat transfer, the equivalent heat flux was proposed and calculated, based on the variation of internal energy of PCM capsule.

4.2 Discharging behaviour of PCM based cold storage system embedded with metal foams

4.2.1 Product solution method

Multi-dimensional problems are usually complicated to be solved. The common approach for simplification is the synthesis of two or three one-dimensional problems by using product solution method, which is composed of geometry combination and solution combination.

4.2.1.1 Geometry combination

For typical container of regular prisms used for PCM storage, it can be regarded as an infinite long prism perpendicularly intersected by an infinite plate. Figure 4.1 demonstrated the formation of an infinite long rectangular cylinder with a sectional dimension of $2\delta_1 \times 2\delta_2$ by intersection of two infinite plates with a thickness of $2\delta_1, 2\delta_2$, respectively. In this case, two-dimensional problem can be transformed as two one-dimensional problems.

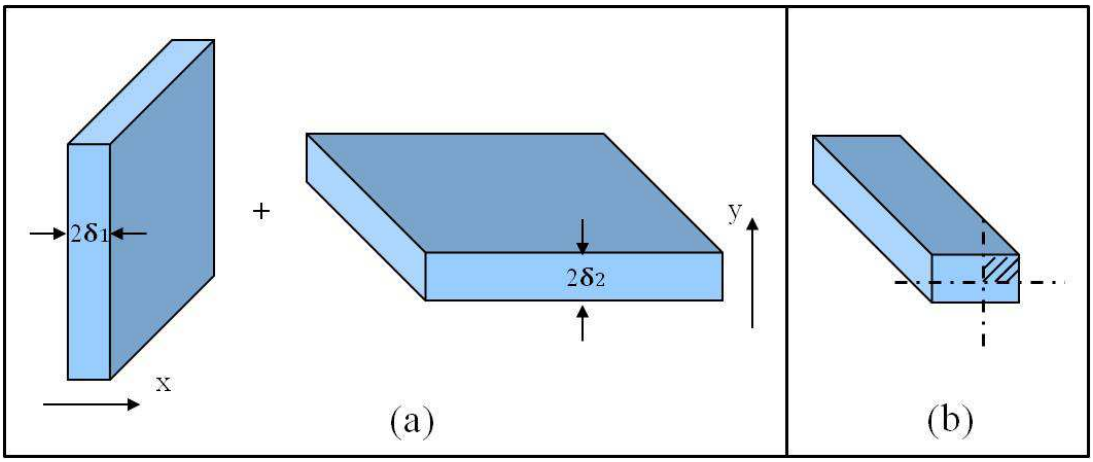

Figure 4.1 Infinite long rectangular cylinder with a sectional dimension of $2\delta_1 \times 2\delta_2$

Similarly, a short cylinder can be regarded as the intersection of an infinite plate of 2δ thick and an infinite long cylinder with a radius of R, seen in Figure 4.2. In this case, three-dimensional problem was transformed as one-dimensional problem in infinite plate and two-dimensional problem in a regular cylinder.

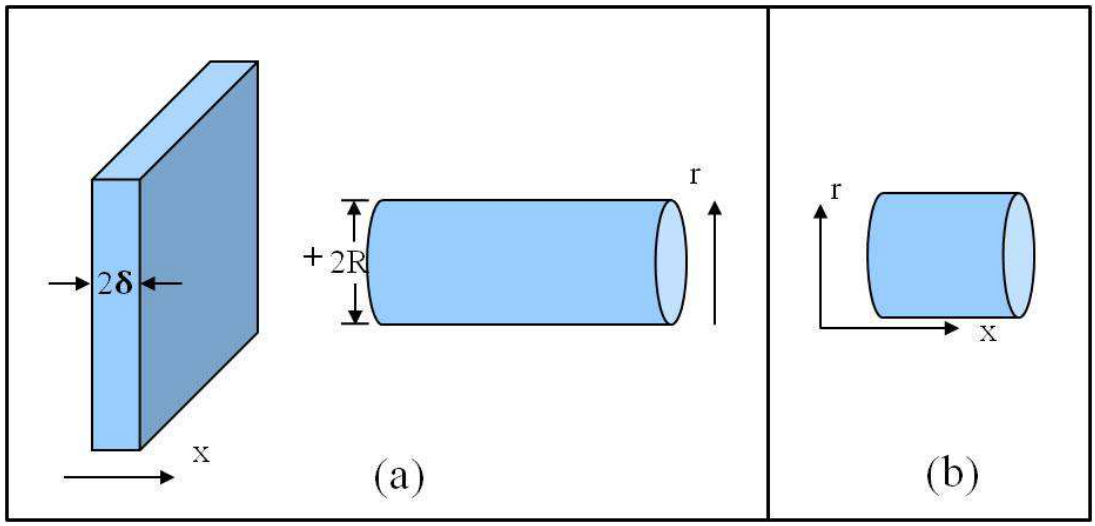

Figure 4.2 Formation of a short cylinder

4.2.1.2 Solution combination

Based on the geometry combination, two or three dimensional thermal conduction solution in typical geometries can be calculated by multiplying of two or three one-dimensional solutions, shown in Eq. (4.1):

$$\Theta(x,y,\tau)=\Theta_x(x,\tau)\cdot\Theta_y(y,\tau) \tag{4.1}$$

In which $\Theta(x,y,\tau)$ is the solution of two dimensional problem for short regular prisms; $\Theta_x(x,\tau)$, $\Theta_y(y,\tau)$ are the solution of infinite plate (x direction) and the solution of infinite long prism (r direction), respectively.

The following part is the verification of Eq. (4.1). Take the infinite long rectangular cylinder as an example, the computational domain is shown in Figure 4.3. Due to the symmetry of the geometry, section O-A-B-C is considered.

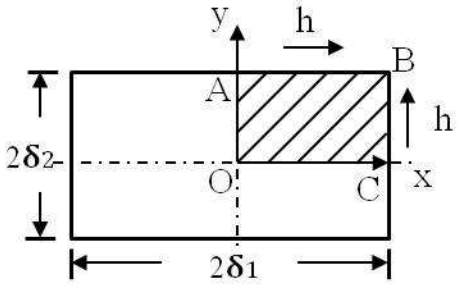

Figure 4.3 Computational domain of rectangular cylinder

The governing equation and the definite conditions are shown in Eq. (4.2) ~ (4.5):

$$\frac{\partial\Theta}{\partial\tau}=a\cdot\left(\frac{\partial^2\Theta}{\partial x^2}+\frac{\partial^2\Theta}{\partial y^2}\right) \tag{4.2}$$

$$\Theta(x,y,0)=1 \tag{4.3}$$

$$\Theta(\delta_1,y,\tau)+\frac{\lambda}{h}\cdot\frac{\partial\Theta(x,y,\tau)}{\partial x}\Big|_{x=\delta_1}=0 \tag{4.4a}$$

$$\Theta(x,\delta_2,\tau)+\frac{\lambda}{h}\cdot\frac{\partial\Theta(x,y,\tau)}{\partial y}\Big|_{y=\delta_2}=0 \tag{4.4b}$$

$$\frac{\partial\Theta(x,y,\tau)}{\partial x}\Big|_{x=0}=0 \tag{4.5a}$$

$$\frac{\partial\Theta(x,y,\tau)}{\partial y}\Big|_{y=0}=0 \tag{4.5b}$$

In which $\Theta(x,y,\tau)$ is the dimensionless excess temperature, which is defined as follows:

$$\Theta=\frac{T(x,y,\tau)-T_\infty}{T_0-T_\infty}=\frac{\theta}{\theta_0} \tag{4.6}$$

For one dimensional problem for infinite plate (seen Figure 4.1 (a)), $\Theta_x(x,\tau)$ is the solution of:

$$\frac{\partial\Theta_x}{\partial\tau}=a\cdot\frac{\partial^2\Theta_x}{\partial x^2} \tag{4.7}$$

$$\Theta_x(x,0)=1 \tag{4.8}$$

$$\Theta_x(\delta_1,\tau)+\frac{\lambda}{h}\cdot\frac{\partial\Theta_x(x,\tau)}{\partial x}\Big|_{x=\delta_1}=0 \tag{4.9}$$

$$\frac{\partial\Theta_x(x,\tau)}{\partial x}\Big|_{x=0}=0 \tag{4.10}$$

For one dimensional problem for infinite long rectangular cylinder (seen Figure 4.1 (b)), $\Theta_y(y,\tau)$ is determined by:

$$\frac{\partial\Theta_y}{\partial\tau}=a\cdot\frac{\partial^2\Theta_y}{\partial y^2} \tag{4.11}$$

$$\Theta_y(y,0)=1 \tag{4.12}$$

$$\Theta_y(\delta_2,\tau)+\frac{\lambda}{h}\cdot\frac{\partial\Theta_y(y,\tau)}{\partial y}\Big|_{y=\delta_2}=0 \tag{4.13}$$

$$\frac{\partial\Theta_y(y,\tau)}{\partial y}\Big|_{y=0}=0 \tag{4.14}$$

For verifying Eq. (4.1), both of the governing equation Eq. (4.2) and the definite conditions Eq. (4.3) ~ (4.5) need to be verified.

Firstly, for the governing equation Eq. (4.2), the left term and right term can be written as:

$$\frac{\partial \Theta}{\partial \tau}=\frac{\partial(\Theta_x\cdot\Theta_y)}{\partial \tau}=\Theta_x\cdot\frac{\partial \Theta_y}{\partial t}+\Theta_y\cdot\frac{\partial \Theta_x}{\partial t} \quad \text{(Left term)} \tag{4.15a}$$

$$a\cdot(\frac{\partial^2\Theta}{\partial x^2}+\frac{\partial^2\Theta}{\partial y^2})=a\cdot(\Theta_y\cdot\frac{\partial^2\Theta_x}{\partial x^2}+\Theta_x\cdot\frac{\partial^2\Theta_y}{\partial x^2}) \quad \text{(Right term)} \tag{4.15b}$$

Consequently, the difference of left and right terms is:

$$\Theta_x\cdot\frac{\partial \Theta_y}{\partial t}+\Theta_y\cdot\frac{\partial \Theta_x}{\partial t}-a\cdot(\Theta_y\cdot\frac{\partial^2\Theta_x}{\partial x^2}+\Theta_x\cdot\frac{\partial^2\Theta_y}{\partial x^2})=\Theta_y\cdot(\frac{\partial \Theta_x}{\partial \tau}-a\cdot\frac{\partial^2\Theta}{\partial x^2})+\Theta_x\cdot(\frac{\partial \Theta_y}{\partial \tau}-a\cdot\frac{\partial^2\Theta_y}{\partial y^2}) \tag{4.15c}$$

That is to say, in the condition that $\Theta_x(x,\tau)$, $\Theta_y(y,\tau)$ are the solutions of Eq.(4.7) and Eq.(4.11), solution of governing equation Eq. (4.2) can be written as combination of two one-dimensional solutions, as shown in Eq. (4.1).

Secondly, since the governing equation is verified, for the initial condition of Eq.(4.3), it becomes:

$$\Theta(x,y,0)=\Theta(x,0)\cdot\Theta(y,0)=1\times1=1 \tag{4.16}$$

While for the boundary conditions of Eq. (4.4a)~(4.5a), we have:

$$\Theta_x(\delta_1,\tau)\cdot\Theta_y(y,\tau)+\Theta_y(y,\tau)\cdot\frac{\lambda}{h}\cdot\frac{\partial \Theta_x(x,\tau)}{\partial x}\Big|_{x=\delta_1}=\Theta_y(y,\tau)\cdot[\Theta_x(\delta_1,\tau)+\frac{\lambda}{h}\cdot\frac{\partial \Theta_x(x,\tau)}{\partial x}\Big|_{x=\delta_1}]=0 \tag{4.17}$$

$$\frac{\partial \Theta(x,y,\tau)}{\partial x}\Big|_{x=0}=\frac{\partial \Theta_x(x,\tau)}{\partial x}\Big|_{x=0}\cdot\Theta_y(y,\tau)=0\cdot\Theta_y(y,\tau)=0 \tag{4.18}$$

Similarly, Eq.(4.4b) and (4.5b) can be validated.

From Eq. (4.16)~(4.18), it is demonstrated that, in the condition that $\Theta_x(x,\tau)$, $\Theta_y(y,\tau)$ are the solutions of Eq.(4.8)~(4.10) and Eq. Eq.(4.12)~(4.14), respectively, solution of definite conditions of Eq. (4.3)~(4.5) can be written as combination of two one-dimensional solutions, as shown in Eq. (4.1).

Therefore, the feasibility of product solution method is verified. This method can be used but not limited in the following definite conditions:

(1) The third thermal boundary conditions;

(2) Initial temperature remains constant.

It is pointed out that it also can be applied under the first thermal boundary conditions when temperature on the boundary is constant value.

4.2.2 Physical and mathematical models

4.2.2.1 Two dimensional heat transfer model

Through embedding metal foams in PCM, although the storage volume of PCM is slightly reduced, the effective thermal conductivity of the composite material is much higher than that of PCM. As a result, cold discharging rate of the cold storage system can be largely improved.

For establishing the heat transfer model for discharging behaviour in the composite materials, the characteristics of heat transfer performance were explicitly demonstrated:

(1) Internal natural convection neglected. In discharging process, convection between the melt PCM and metal foams was not considered, since the thermal resistance of thermal conduction was much smaller than that of convection caused by buoyancy force inside the composite materials. Without regard for the convective heat transfer at the interface of PCM and metal foams, single-equation model was feasible to be used for describing the heat transfer characteristics in PCM embedding with metal foams.

(2) External forced convection considered. Except for the multi-dimensional thermal conduction, forced convection caused by fluid discharging on the outside wall of the PCM module was also under consideration. This was clearly demonstrated in the boundary conditions. Due to the embedding of metal foams, the discharge capacity of the PCM module was enhanced under the condition of the same forced convection.

Consequently, the governing equation for a cylinder-shaped PCM module discharged by fluid flowing outside can be written as in Eq.(4.19):

$$(\rho \cdot Cp)_m \cdot \frac{\partial T}{\partial t} = k_m \cdot (\frac{\partial^2 T}{\partial x^2} + \frac{1}{r} \cdot \frac{\partial T}{\partial r} + \frac{\partial^2 T}{\partial r^2}) \tag{4.19}$$

In which k_m represents the effective thermal conductivity of the PCM module. Three-dimensional cellular morphology model for calculating effective thermal conductivity in metal foams can be found in [194-195]. $(\rho \cdot Cp)_m$ is the averaged cold storage density of the composite materials, which can be calculated by the formula in Eq. (4.20):

$$(\rho \cdot Cp)_m = (1-\varepsilon) \cdot \rho_s \cdot Cp_s + \varepsilon \cdot \rho_f \cdot Cp_f \tag{4.20}$$

Where ε is porosity of metal foams, usually in the range of $0.85 \sim 0.98$; ρ_s, ρ_f are density of metallic fibre and PCM, respectively; Cp_s, Cp_f are heat capacity of metal foams and PCM, respectively.

The PCM module was assumed to be surrounded by fluid flowing with a uniform heat transfer coefficient h. Therefore, the cold discharging capacity of the PCM system was dependent on the temperature difference of the fluid and PCM at the wall. On the boundary, energy balance by forced convection and thermal conduction within the PCM module can be established. However, due to the complexity of multi-dimensional thermal conduction, boundary conditions can not be easily described, so analytical model based on product solution method is carried out in the following section.

4.2.2.2 Analytical model

As discussed above, a short cylinder of 2δ long with a radius of R can be intersected by an infinite plate of 2δ thick and an infinite long cylinder with a radius of R, as shown in Figure 4.2.

For infinite plate, thermal conduction with forced convection on the boundary has the analytical solution that can be expressed as in Eq. (4.21):

$$\theta_x(x,t) = \theta_{xo} \cdot A_x \cdot e^{-\mu_{1x}^2 \cdot Fo_x} \cdot \cos(\mu_{1x} \cdot \frac{x}{\delta}) \tag{4.21}$$

In which θ_{xo} was the initial excess temperature of the plate; $\theta_x(x,t)$ represented the excess temperature of the plate at different position and time; Fo_x was Fourier number in the x direction, defined as:

$$Fo_x = \frac{k_m}{(\rho \cdot Cp)_m} \cdot \frac{\tau}{\delta^2} \tag{4.22}$$

A_x and μ_{1x} are two coefficients, calculated as:

$$A_x = 1.0101 + 0.2575 \cdot (1 - e^{-0.4271 \cdot Bi_x}) \tag{4.23}$$

$$\mu_{1x} = (0.4022 + \frac{0.9188}{Bi_x})^{-1/2} \tag{4.24}$$

Where Bi_x denoted Biot number in the x direction, defined as:

$$Bi_x = \frac{h \cdot \delta}{k_m} \tag{4.25}$$

While for infinite long cylinder, regarding the uniform heat transfer surrounding the cylinder, the problem can be simplified as one-dimensional thermal conduction coupled with the third-class thermal boundary condition. The analytical solution can be expressed as in Eq. (4.26):

$$\theta_r(r,t) = \theta_{ro} \cdot A_r \cdot e^{-\mu_{1r}^2 \cdot Fo_r} \cdot J_0(\mu_{1r} \cdot \frac{r}{R}) \tag{4.26}$$

In which θ_{ro} was the initial excess temperature of the infinite long cylinder; $\theta_r(r,t)$ represented the excess temperature of the infinite long cylinder along the radius direction at different time; Fo_r was Fourier number in the r direction, defined as:

$$Fo_x = \frac{k_m}{(\rho \cdot Cp)_m} \cdot \frac{4\tau}{R^2} \tag{4.27}$$

The Bessel function $J_0(x)$ is approximately calculated as:

$$J_0(x) = 0.9967 + 0.0354 \cdot x - 0.3259 \cdot x^2 + 0.0577 \cdot x^3 \tag{4.28}$$

Where x was substituted by $\mu_{1r} \cdot \frac{r}{R}$ as in Eq. (4.26).

While the coefficients A_r , μ_{1r} can be obtained by Eq.(4.29)~(4.30):

$$A_r = 1.0042 + 0.5877 \cdot (1 - e^{-0.4038 \cdot Bi_r}) \tag{4.29}$$

$$\mu_{1r} = (0.1700 + \frac{0.4349}{Bi_r})^{-1/2} \tag{4.30}$$

Where Bi_r represented the Biot number for the infinite long cylinder surrounded by flowing fluid, as expressed in Eq.(4.31):

$$Bi_r = \frac{h \cdot R}{2k_m} \tag{4.31}$$

Therefore, according to the product solution method, the temperature distribution of the PCM module under consideration can be written as the product of the solutions for infinite big plate and infinite long cylinder, formulated as:

$$\theta(x,r,t) = \frac{\theta_x(x,t) \cdot \theta_r(r,t)}{\theta_0} \tag{4.32}$$

In which θ_0 was the initial excess temperature of the PCM module before the discharge process.

4.2.3 A case study on PCM embedded with metal foams

A case study is carried out to investigate the enhancement of the discharging capacity by embedding high porosity metal foams in PCM of paraffin. The value of the effective thermal diffusivity and thermal conductivity of the composite materials is justified. The effect of heterogeneous nature of the open-cell metal foams in the real life on heat transfer performance is assessed.

4.2.3.1 Sample problem description

A paraffin module is regarded as the PCM in the sample problem and shaped as a short cylinder of L long ($L = 0.6m$)with a radius of R ($R = 0.2m$). Open-cell metal foams with a porosity of 0.8 ($\varepsilon = 0.8$) and a pore density of 20 ($PPI = 20$) is embedded in the paraffin module to form the PCM composite. It is assumed that the embedded metal foams has the same geometry as the paraffin module, therefore the volume-average method can be used to evaluate the thermal physical parameters of the PCM composite

materials. The specific parameters of the metal foams, paraffin and air were listed in Table 4.1.

Table 4.1 Specific parameters of PCM module in discharging

ρ_s kg/m^3	Cp_s $J/(kg\cdot K)$	k_s $W/(m\cdot K)$	ρ_f kg/m^3	Cp_f $J/(kg\cdot K)$	k_f $W/(m\cdot K)$	r kJ/kg	ε	h $W/(m^2\cdot K)$	L m	R m
2500	2000	200	855	2400	0.558	200	0.8	120	0.6	0.2

In the discharging process, air with a constant temperature of 20 ^oC flows across the PCM composite. The initial temperature of the PCM composite is -30 ^oC, which is 50 ^oC lower than the air temperature. The convective heat transfer coefficient h is supposed to be 120 $W/m^2\cdot K$. Due to cold extraction, temperature of the PCM composite will increase gradually until the energy balance is achieved.

The geometric origin of the PCM composite is defined as the point located at the centre of the PCM module, as shown in Figure 4.3. Therefore, the boundary conditions on the lines OA and OC satisfies the symmetric temperature condition due to the symmetry of the geometry. While temperature on the boundaries of AB and BC is set under the third-class thermal boundary condition. The initial conditions and boundary conditions of the cold extraction for the PCM composite materials are summarized in Table 4.2.

Table 4.2 Initial and boundary conditions

<table>
<tr><td rowspan="2">T_{air} ^oC</td><td rowspan="2">$T_{PCM,i}$ ^oC</td><td colspan="4">Boundaries of the geometry</td></tr>
<tr><td>OA</td><td>OC</td><td>AB</td><td>BC</td></tr>
<tr><td rowspan="2">20</td><td rowspan="2">-30</td><td rowspan="2">$\frac{\partial T_{PCM}}{\partial x}=0$</td><td rowspan="2">$\frac{\partial T_{PCM}}{\partial y}=0$</td><td colspan="2">$h\ W/(m^2\cdot K)$</td></tr>
<tr><td colspan="2">120</td></tr>
</table>

4.2.3.2 Temperature distribution during discharge

Based on the above conditions, the temperature distribution of the cylinder-shaped PCM composite is obtained.

The radial and axial distributions of excess temperature at different locations are demonstrated in Figure 4.4 and Figure 4.5. With time going, cold

discharging rate becomes smaller due to the reduced temperature difference between PCM module and the flowing air. After 2400 S , the excess temperature is less than 5 ^{o}C , indicating that more than 90% of cold energy is extracted by the convection of the air flowing. Compared with excess temperature on the boundaries of the PCM module, it is found that excess temperature on the right boundary ($x/\delta=1.0$) is lower that on the upper boundary ($r/R=1.0$). This indicated that cold discharge process along axial direction is faster for the designed PCM module.

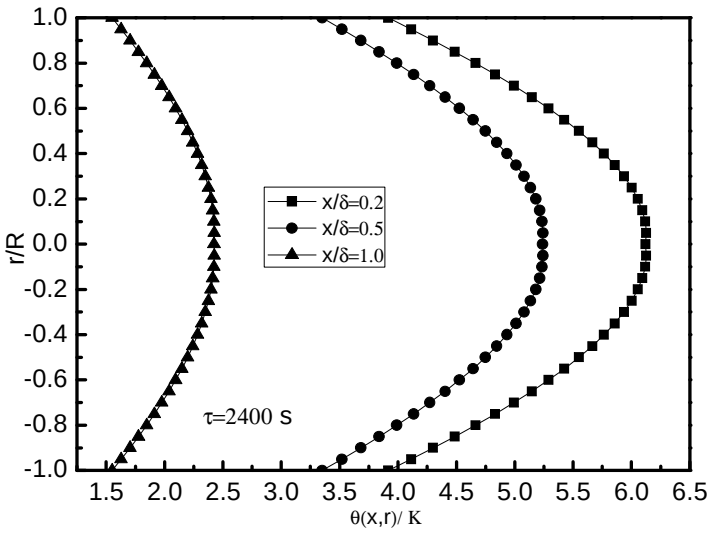

Figure 4.4 The radial distributions of excess temperature

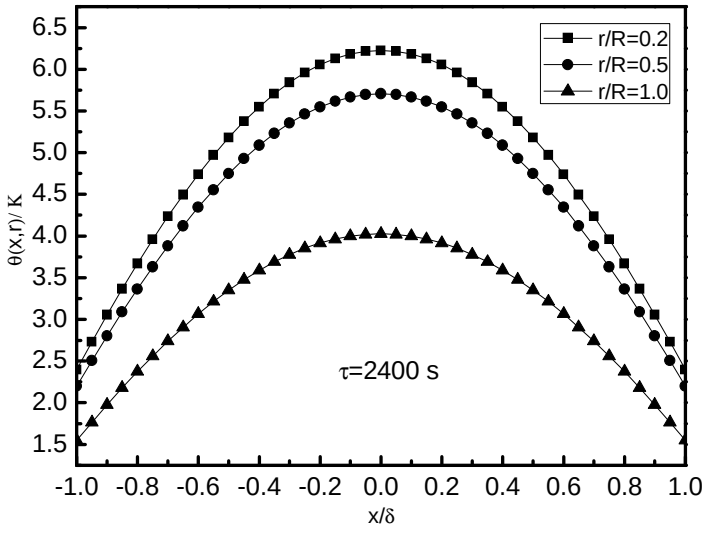

Figure 4.5 The axial distribution of excess temperature

Specifically, the time-dependent temperature distribution on typical points of the PCM module is shown in Figure 4.6. It is seen that point O (0,0) has the highest excess temperature, while point B (1,1) had the lowest. It is noted

that excess temperature at point C (1,0) is smaller than that at point A (0,1), demonstrating larger cold discharging along axial direction.

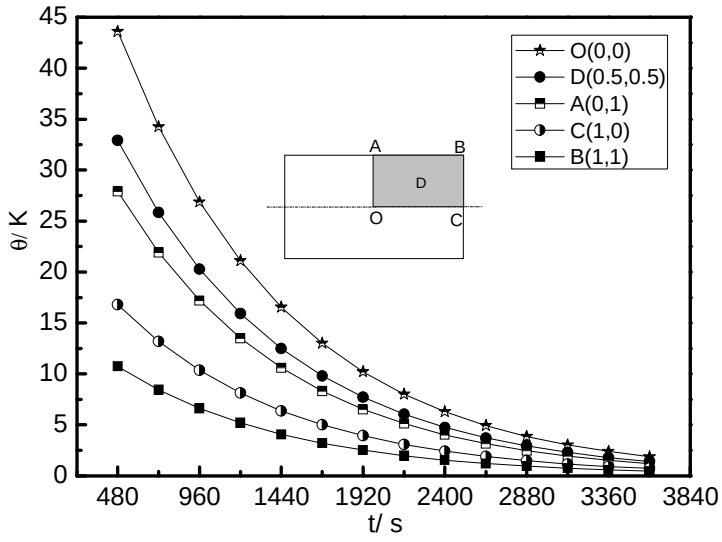

Figure 4.6 The time-dependent distribution on typical points

4.2.3.3 Effective thermal diffusivity and thermal conductivity

For demonstrating the effect of metal foams on enhancement of the cold discharging rate, temperature distributions of PCM modules with and without metal foams embedding are compared. As shown in Figure 4.7, the excess temperature distribution of the PCM without metal foams along the radial direction is much higher than that of PCM module embedded with metal foams. This indicates that the cold discharging rate of the PCM module is largely improved by embedding metal foams.

At the point of (0.5,0), temperatures of the two different PCM modules are compared. Without metal foams, the excess temperature of PCM module is reduced to 35 ^{o}C after 4800 s, while it is discharged to the same temperature level after only 600 s for the PCM module with metal foams. Therefore, it is indicated that with metal foams embedded, the cold discharging rate can be improved by approximately 8 times.

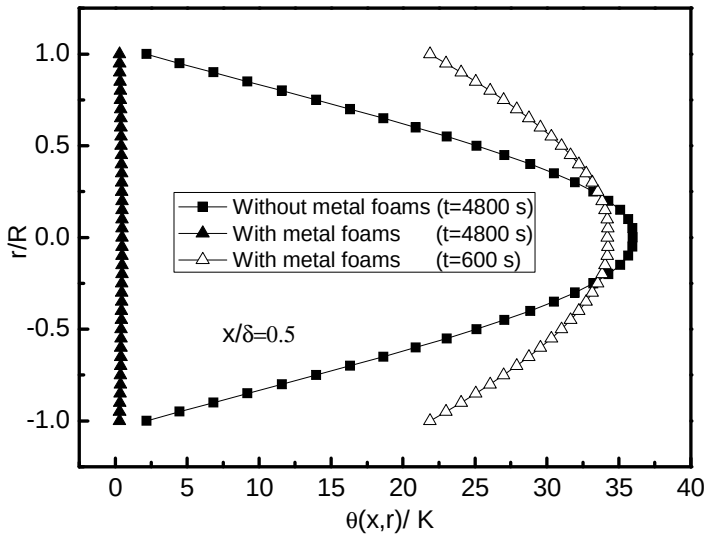

Figure 4.7 The effect of metal foams

The cold discharging rate of the PCM composite materials is enhanced due to the improvement of the effective thermal conductivity k_m. Based on a three-dimensionally structured model for open-cell metal foams [195], the effective thermal conductivity of the PCM composite materials can be obtained, as shown in Eq. (4.33):

$$k_m = \frac{\sqrt{2}}{2(R_A + R_B + R_C + R_D)} \tag{4.33a}$$

$$R_A = \frac{4\lambda}{(2e^2 + \pi\lambda(1-e))k_s + (4 - 2e^2 - \pi\lambda(1-e))k_f} \tag{4.33b}$$

$$R_B = \frac{(e-2\lambda)^2}{(e-2\lambda)e^2 k_s + (2e - 4\lambda - (e-2\lambda)e^2)k_f} \tag{4.33c}$$

$$R_C = \frac{(\sqrt{2}-2e)^2}{2\pi\lambda^2(1-2e\sqrt{2})k_s + (2\sqrt{2} - 2e - -\pi\lambda^2(1-2e\sqrt{2}))k_f} \tag{4.33d}$$

$$R_D = \frac{2e}{e^2 k_s + (2e - 4\lambda - (4-e^2)k_f} \tag{4.33e}$$

$$\lambda = \sqrt{\frac{\sqrt{2}(2 - (5/8)e^3\sqrt{2} - 2\varepsilon}{\pi(3 - 4e\sqrt{2} - e)}}, \ e = 0.339 \tag{4.33f}$$

In which k_s, k_f represents the thermal conductivity of metal foams and PCM, respectively. According to the above formulas, it is seen that the effective thermal conductivity of the PCM composite is determined by k_s, k_f and three dimensional structure and porosity of the open-cell metal foams.

In the case study, Al foams is embedded in paraffin materials. The thermal conductivity of Al foams (k_s) and paraffin (k_f) is 200 $W/(m\cdot K)$ and 0.558 $W/(m\cdot K)$, respectively; the effective thermal conductivity of the PCM composite is calculated as 12.6 $W/(m\cdot K)$ in terms of the above model. One can see that the thermal conductivity is as 22.6 times big as that of paraffin.

However, effective thermal conductivity is not the only factor that affects discharging rate of PCM composite. As can be seen from Eq. (4.19), effective thermal diffusivity ($\frac{k_m}{(\rho Cp)_m}$) is a critical property needed to be considered. Therefore, further discussion considering the effect of effective thermal diffusivity is done in the following.

Temperature distributions of different PCM (Paraffin and $NaCO_3$) with and without metal foams are compared in Figure 4.8 and Figure 4.9, respectively. Without metal foams embedding in PCM, cold discharging rate of $NaCO_3$ module is larger than that of paraffin module, which is attributed to the larger thermal conductivity of $NaCO_3$, as shown in Table 4.3. Hence, with Al foams embedded, it is sensible to use $NaCO_3$ as the PCM for getting a big discharging rate.

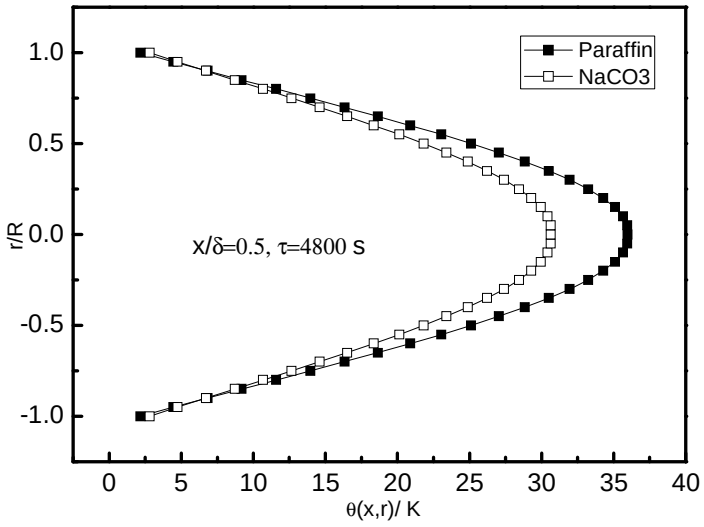

Figure 4.8 Temperature distributions of different PCM without metal foams

However, by embedding Al foams in different PCMs, it is observed in Figure 4.9 that the excess temperature of paraffin-Al module is smaller than $NaCO_3$ –Al foams module, indicating the former has bigger cold discharging rate under the same conditions. This is because paraffin-Al foams module has effective thermal diffusivity of $5.763\times10^{-6} m^2/s$, which is 42.5% higher than the value of $NaCO_3$ –Al foams module.

The calculated effective thermal conductivity and thermal diffusivity for single paraffin, single $NaCO_3$, paraffin-Al foams module and $NaCO_3$–Al foams module are shown in Table 4.3. One can see that although the paraffin-Al foams module has lower effective thermal conductivity but higher effective thermal diffusivity than those of $NaCO_3$–Al foams module. But since paraffin-Al foams has lower excess temperature distribution under the same conditions, it is concluded that effective thermal diffusivity has more significant value for improving the cold discharging rate of the PCM composite.

Table 4.3 Calculated thermal properties of different materials

Materials	k_m $W/(m\cdot K)$	$(\rho\cdot Cp)_m$ $10^{-6}J/(m^3\cdot K)$	$\frac{k_m}{(\rho\cdot Cp)_m}$ $10^6 m^2/s$	Bi_x	Bi_r	Fo_x	Fo_r
Paraffin	0.558	2.1375	0.261	64.5	21.5	0.384	3.132
NaCO3	0.83	2.4444	0.339	43.4	14.5	0.453	4.077
Paraffin+ Al foams	12.6	2.186	5.763	2.86	0.95	7.69	69.21
NaCO3+Al foams	13.1	3.239	4.044	2.75	0.92	5.39	48.51

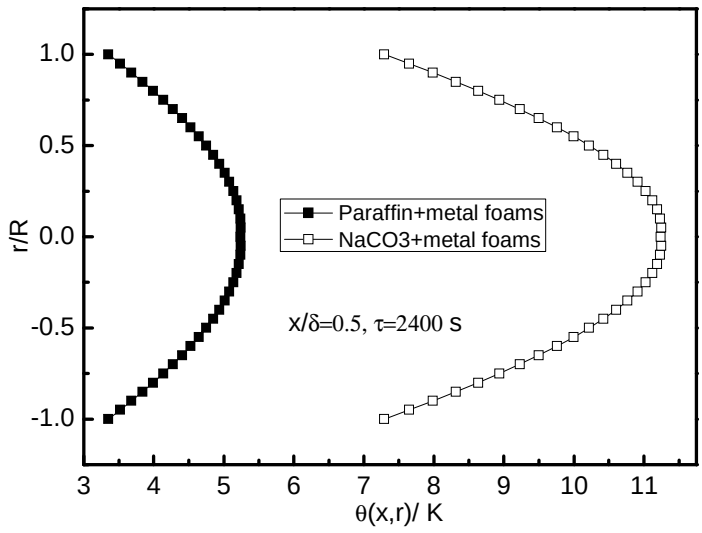

Figure 4.9 Temperature distributions of different PCM embedding with metal foams

4.2.3.4 Further discussions on real-life featured model

For the above simplified heat transfer model, the real-life open-cell metal foams is not considered. In reality, the solid matrix of metal foams has a three dimensional and heterogeneous interior microstructures, leading to a hard capture of the heat transfer phenomena with accuracy.

The general solution regarding the heterogeneous nature of the open-cell metal foams is the use of volume-average method. The typical diagram of a porous media is shown in Figure 4.10. The controlled volume V is composed by both α phase (solid matrix) and β phase (fluid region). The volume for solid matrix and fluid region is written as V_α and V_β, respectively. The microscopic fluid flow in the porous media is significant and can be related to macroscopic physical quantities in a small volume. For example, the averaged value of PCM temperature T_{PCM} can be expressed as:

$$T_{PCM} =< T_\beta >= \frac{1}{V}\int_{V_\beta} T_\beta \cdot dV \tag{4.34}$$

In which $< T_\beta >$ represents the average kinetic power of PCM molecular in β phase.

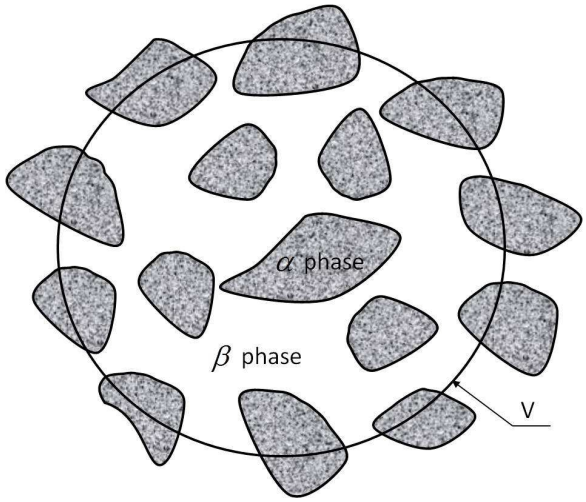

Figure 4.10 Controlled volume in a typical porous media

In terms of the volume-average method, the detailed information within a controlled volume is neglected while the influence of heterogeneous interior microstructures can be reflected in geometric properties (i.e. porosity and pore density) of metal foams and effective thermal properties of the PCM composite (i.e. thermal conductivity and thermal diffusivity). For more complicated situation such as forced convection in metal foams, more real-life characteristics of open–cell metal foams including flow disturbance by

the solid matrix and inertial effect under non-Darcy flow are to be considered.

4.3 Discharge behaviour in PCM capsules considering the combined effect of cold radiation and convection

4.3.1 Single-particle heat transfer model

The following heat transfer model is based on the concept of average temperature, with phase change phenomena considered. However, the influence of neglecting the detailed temperature difference in the PCM capsule is assessed under both small and large Biot number.

4.3.1.1 Heat transfer model without phase change

Provided that cold PCM capsule is discharged by air flowing through, the heat transfer model during discharging can be established. Without melting of solid PCM, the energy balance during discharging can be express as in Eq. (4.35):

$$\int_0^t [h\cdot(T_f - T_s(t)) + \varepsilon_s\cdot\sigma\cdot({T_f}^4 - {T_s}^4(t))]\cdot 4\pi R^2 dt = \int_0^t \rho\cdot C_p\cdot\frac{dT_s(t)}{dt}\cdot\frac{4}{3}\pi R^3\cdot dt \quad (4.35)$$

In which $T_s(t)$, T_f represent the temperature of PCM and fluid, respectively; h is the heat transfer coefficient; ρ, C_p, R are density, heat capacity, and radius of PCM capsules; ε_s is the radiation emissivity, σ is Bolzman constant (5.67×10^{-8}).

The derivative of the above equation with respect to t is,

$$-h\cdot T_s(t) - \varepsilon_s\cdot\sigma\cdot{T_s}^4(t) + \varepsilon_s\cdot\sigma\cdot{T_f}^4 + h\cdot T_f = \rho\cdot C_p\cdot\frac{dT_s(t)}{dt}\cdot\frac{R}{3} \quad (4.36)$$

The terms on the left hand of the above equation is the total heat transfer through radiation and convection, while the term on the right hand represents the reduce of internal energy of the PCM capsule. Eq. (4.36) describes the energy balance of one PCM capsule before or after phase change in the discharging process.

4.3.1.2 Heat transfer model with phase change

For establishing heat transfer model regarding phase change during discharge process, the basic idea is: (1) analyzing phase change process separately; (2) finding out the relation of the two cases (with and without phase change during discharging) in terms of overall energy balance. Provided that melting point is T_r, the staring time and final time of melting

are t_{rs} and t_{re}, respectively. Hence, the energy equation for the melting process is written as:

$$\int_{t_{rs}}^{t_{re}} [h \cdot (T_f - T_r) + \varepsilon_s \cdot \sigma \cdot ({T_f}^4 - {T_r}^4)] \cdot 4\pi R^2 dt = \int_{t_{rs}}^{t_{re}} \rho \cdot \Delta H_{ls} \cdot \frac{d\varepsilon_r(t)}{dt} \cdot \frac{4}{3} \pi R^3 dt \quad (4.37)$$

In which ε_r represents the volume ratio of melt PCM in the module. Eq. (4.37) can be used to calculate the melting time. After melting, energy equation is:

$$\int_{t_{re}}^{t} [h \cdot (T_f - T_s(t)) + \varepsilon_s \cdot \sigma \cdot ({T_f}^4 - T_s(t)^4)] \cdot 4\pi R^2 dt = \int_{t_{re}}^{t} \rho \cdot C_p \cdot \frac{dT_s(t)}{dt} \cdot \frac{4}{3} \pi R^3 dt \quad (4.38)$$

Comparing Eq. (4.35) to Eq. (4.38), the relation of the discharge time of the PCM module under different models (with or without phase change considered) was established in terms of different PCM temperature after the discharge process, as in Eq. (4.39):

$$t' = \begin{cases} t & T_{final} < T_r \\ t + (t_{re} - t_{rs}) \cdot \varepsilon_r & T_{final} = T_r \\ t + t_{re} - t_{rs} & T_{final} > T_r \end{cases} \quad (4.39)$$

Therefore, the heat transfer behaviour during discharging is described by Eq. (4.35) and Eq. (4.39).

4.3.1.3 Feasibility of the heat transfer model

(1) With small Biot number

Lump-capacitance method is an analytical approach for obtaining the average temperature of an object that is in the third-class thermal boundary condition. Biot number (Bi_V) is a critical dimensionless parameter in the lump-capacitance method, which can be defined as in Eq. (4.40):

$$Bi_V = \frac{h(V/A)}{\lambda_o} \quad (4.40)$$

V, A and λ_o are the volume, surface and thermal conductivity of the object, while h is the convective heat transfer coefficient on the boundaries. In fact, Bi_V compares the thermal resistance of thermal conduction within the volume of the object ($(V/A)/\lambda_o$) and the thermal resistance of convection on the boundaries of the object ($1/h$). According to [194], the lump-capacitance method can be used in the condition that the following condition is fulfilled.

$$Bi_V = \frac{h(V/A)}{\lambda_o} < 0.1M \quad (4.41a)$$

For spherical object,

$$\frac{V}{A}=\frac{\frac{4\pi R^3}{3}}{4\pi R^2}=\frac{R}{3} \tag{4.41b}$$

$$M=\frac{1}{3} \tag{4.41c}$$

From Eq.(4.41a)~ Eq.(4.41c), for spherical object, the limitation for using the lump-capacitance method can be written as:

$$Bi_V=\frac{hR}{3\lambda_o}<0.1/3 \tag{4.41d}$$

This indicates that when Bi_V is less than 0.033, the thermal conduction of the spherical object can be neglected. As a result, the temperatures with the volume of the object can be regarded as the same temperature, as described in the heat transfer model in the above sections.

In a case study, a PCM capsule under a low temperature is discharged by air flowing across the outer surface of the capsule. Assuming that the capsule diameter is 5 mm, while the thermal conductivity of the PCM is 0.55 $W/(m\cdot K)$. The convective heat transfer coefficient keeps constant as 20 $W/(m^2\cdot K)$. The Bi_V is calculated as 0.030, which is smaller than the maximum value for spherical object. Therefore, the feasibility of the lump-capacitance method is justified.

(2) With large Biot number

With large Biot number, the thermal resistance of the PCM capsule can not be neglected. Although PCM is shaped as spherical capsule with small diameter, the temperature difference exists within the volume of the capsule. However, from the point view of energy, cold discharging rate is dependent on the overall effect of heat convection by the fluid flow and the thermal radiation between the PCM capsule and the environment. Accordingly, the average temperature of the PCM capsule is more significant than the detailed temperature distribution within the volume of the PCM capsule. Therefore, average temperature of the PCM capsule is used in the heat transfer model.

In cold discharge process, wall temperature of the PCM capsule should be used to evaluate the heat flux by heat convection and thermal radiation. As a result, the following part will assess the deviation of the average temperature and the wall temperature under large Biot number.

In reality, temperatures at different locations in PCM capsule are variable due to different heat transfer coefficients at different angles.

Provided that air flows across the PCM capsule for discharging purpose. Figure 4.11 demonstrates the distribution of local Nusselt number for this case. With increase of angle in the range of $0^0 \sim 80^0$, the local Nusselt number decreases since the boundary layer becomes thicker. However, due to the flow transition to a turbulent flow, it goes up again beyond the range. At the angle of 140^0, a second round of rising up for the local Nusselt number is observed, which is attributed to the separation of the flow to the cylinder.

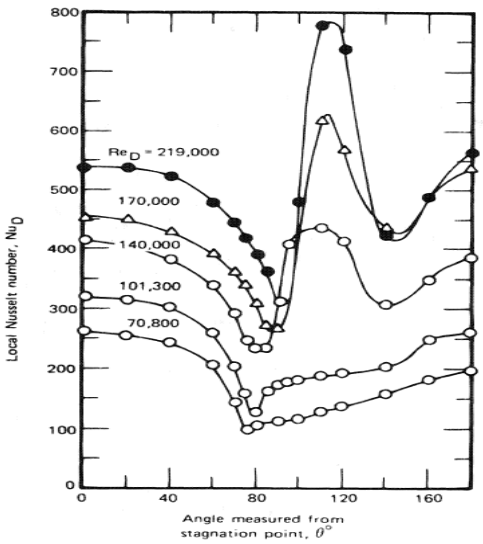

Figure 4.11 Distribution of local Nusselt for a cylinder with fluid flowing across (data from [194])

As the heat transfer coefficients varied with angle, its effect on discharge behaviour is analysed. With increasing of time, the solid-liquid interface moves towards the centre of the PCM capsule. The internal energy equation in PCM capsule is written as:

$$-\rho_l \cdot L \cdot \frac{d\delta(t)}{dt} = k_l \cdot \frac{\partial T_l(\delta,t)}{\partial x} \tag{4.42}$$

The external energy balance at the boundary is described as:

$$h \cdot (T_{air} - T_w) = \lambda \cdot \frac{\partial T_l}{\partial r} \tag{4.43}$$

The parameters of the PCM capsule in this case are shown in Table 4.4.

Table 4.4 The parameters of the PCM capsule in the case study

Cp_l $kJ/(kg\cdot K)$	T_{si} K	D m	ρ_l kg/m^3	T_{air} K	u m/s	Re
2500	233	0.02	1100	300	56.5	70800

By solving the above equations, the position of solid-liquid interface is obtained. Figure 4.12 shows the interface positions at different angles for the cylinder-shaped PCM capsule after 10 minutes' discharging by air flowing. It is shown that the melt PCM at 0^0 is 7.4 mm thick, while it is 6.8 mm thick at 76^0. Hence, after 10 minutes, the biggest difference of interface location deviated from the border of the PCM capsule is only 0.6 mm. Furthermore, with time going, the difference is even smaller due to the reduced temperature potential between the air and PCM border. Therefore, it is indicated that the temperature difference along the circumferential direction of the PCM capsule can be neglected.

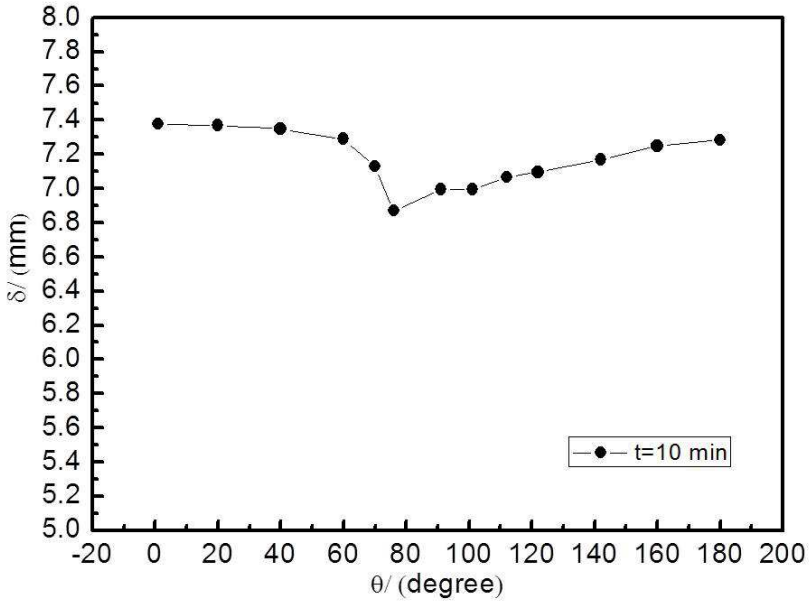

Figure 4.12 Interface positions at different angles during discharging

As a result, the average temperature of the PCM capsule can be regarded as the temperature at $R/2$, which is expressed as:

$$\overline{T} = \frac{T_w + T_{inside}}{2} \tag{4.44}$$

In which T_w and T_{inside} represent the wall temperature and the centre temperature of the PCM capsule, respectively. The deviation of the average temperature and the wall temperature of the PCM capsule is evaluated as:

$$T_w - \overline{T} = \frac{h_e R_{PCM} (T_{air} - T_w)}{2\lambda_{PCM}} = \frac{3Bi_{v,e}}{2}(T_{air} - T_w) \quad (4.45)$$

In which h_e is the equivalent heat transfer coefficient considering the combined effect of heat convection and thermal radiation. One can see that in that condition that Biot number is less than 0.2 ($Bi_{v,e} \leq 0.2$), the temperature difference can be ignored. In the case study, PCM has a thermal conductivity of 0.5 $W/(m \cdot K)$ and is encapsulated in a sphere with a diameter of 40 mm; the heat convection by air flow has a convective heat transfer coefficient of 15 $W/(m^2 \cdot K)$; the Biot number is calculated as 0.2, indicating that the using of the average temperature concept is reasonable. However, when Biot number is large, a significant temperature deviation is caused by using the concept of average temperature. But it becomes much smaller and is negligible after certain time in the cold discharge process.

4.3.2 Analytical solution

The above heat transfer model is established on the basis of energy conservation of a single PCM capsule in the discharge process. Due to the low temperature of the PCM capsule, cold radiation towards the relatively warm atmosphere through the border of the PCM capsule is considered. Hence, the combined effect of thermal radiation and convection on the cold discharging rate is to be figured out.

For the first-order nonlinear non-homogeneous equations (4.35) and (4.38), it is difficult to get the solutions by mathematical transformation. Consequently, thermal resistance method is used for regarding the combined effect on the contributions to cold discharging rate. Specifically, heat transfer model with only thermal radiation or convection is established separately. The partial effects of radiation and convection on cold discharging rate are combined based on thermal resistance diagram developed for the discharge process.

By using the thermal resistance method, the combined effect on cold discharging is analyzed, as seen in the following section.

4.3.2.1 Without phase change

As pointed out above, cold discharge behaviour of PCM capsule can be equivalently regarded as discharge behaviour of PCM without phase change,

followed by evaluation of melting time in terms of the final PCM temperature after the discharge process. On this basis, the combined effect is studied through thermal resistance analysis.

(1) Thermal radiation

Provided that only the thermal radiation is taken into account during cold discharge, Eq.(4.35) was written as:

$$\varepsilon_s \cdot \sigma \cdot [T_f{}^4 - T_s^4(t)] = \rho \cdot C_p \cdot \frac{dT_s(t)}{dt} \cdot \frac{R}{3} \tag{4.46}$$

The differential equation describes the PCM temperature variation caused by cold energy radiation to atmosphere. By numerical iteration, the solution of the above equation is obtained. For a specific case assuming initial temperature of PCM as $T_{si} = 193\ K$ and emissivity of surface as $\varepsilon_s = 0.8$ (usually 0.97~0.7), the calculated PCM temperature is shown in Figure 4.13. It is seen that smaller radius of PCM capsules results in faster temperature rising. Therefore, in consideration of cold radiation, smaller PCM capsule is beneficial for improving the cold discharging rate. With the discharge process going, cold radiation becomes smaller due to the reduced temperature difference of the PCM capsule and the air flow.

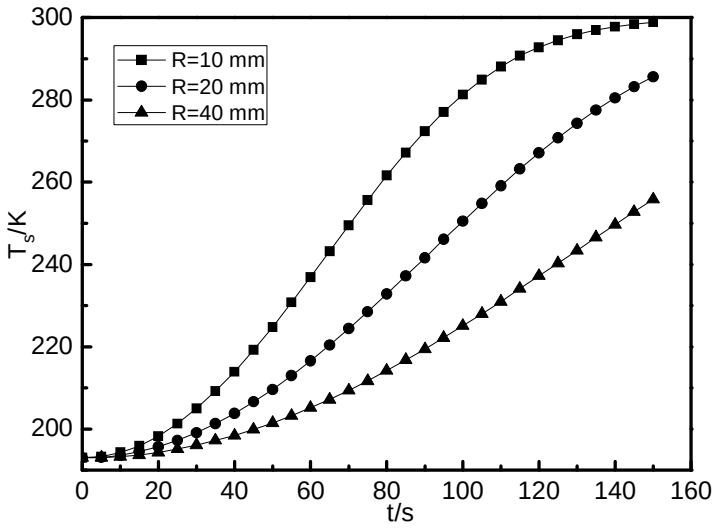

Figure 4.13 Temperature distribution with only thermal radiation considered

(2) Heat convection

Similarly, provided that only heat convection is considered in cold discharging, Eq.(4.35) can be written as:

$$h \cdot (-T_s(t) + T_f) = \rho \cdot C_p \cdot \frac{dT_s(t)}{dt} \cdot \frac{R}{3} \tag{4.47}$$

The differential equation demonstrates the energy balance of internal energy variation and cold energy loss through convection. The solution is:

$$T_s(t) = T_f - \frac{T_f - T_{si}}{e^{\frac{3 \cdot h \cdot t}{\rho \cdot C_p \cdot R}}} \tag{4.48}$$

In which h represents the convective heat transfer coefficient. According to [194], the experimental correlation for convective heat transfer across cylinder is formulated as:

$$Nu = 0.3 + \frac{0.62 \cdot \mathrm{Re}^{1/2} \cdot \mathrm{Pr}^{1/3}}{[1+(0.4/\mathrm{Pr})^{2/3}]^{1/4}} \cdot [1+(\frac{\mathrm{Re}}{282000})^{5/8}]^{4/5} \tag{4.49}$$

Assuming that $T_f = 300K$, the characteristic temperature of fluid is, $T_c = \frac{T_{si} + T_f}{2} = 246.5K$. The thermal conductivity is $\lambda = 0.0220W/(m \cdot K)$, while Prantl number is set as $\mathrm{Pr} = 0.713$. Hence, the relation of heat transfer coefficient and Re was calculated, as shown in Figure 4.14.

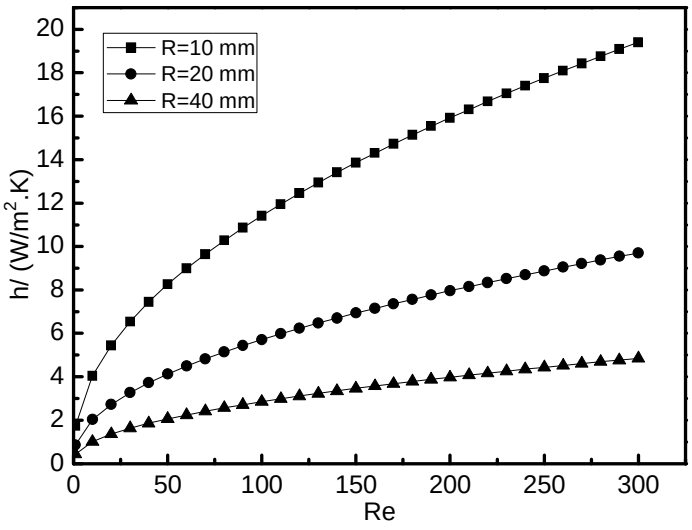

Figure 4.14 Relation of heat transfer coefficient and Re

With increasing of Re, convective heat transfer coefficient becomes larger. Under the same flowing conditions, it is shown that small size PCM capsule results in enhanced convection between air flow and PCM. The variation of PCM temperature under $\mathrm{Re} = 270$ is shown in Figure 4.15. For PCM capsule with 10 mm radius, the temperature increases faster compared to bigger size PCM capsule. The benefit of decreased radius is more significant in the beginning of the discharge process.

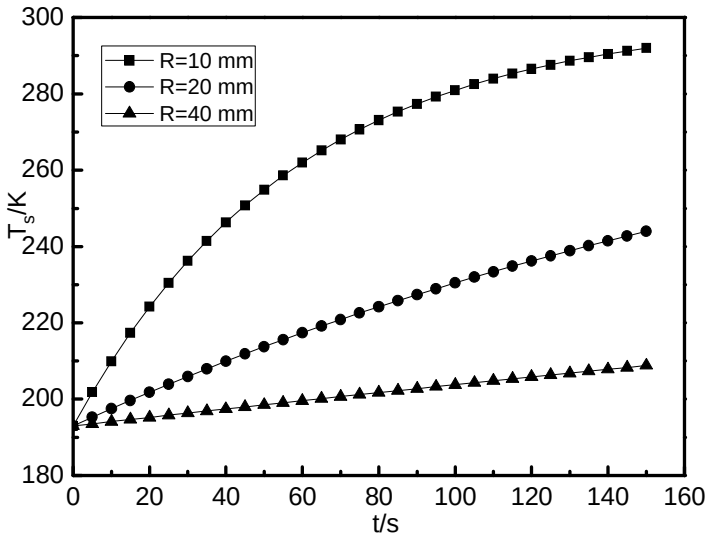

Figure 4.15 Temperature distribution with only convection considered

For heat convection, cold discharging rate is affected by heat transfer coefficient and the temperature difference between PCM and air flow. While for cold radiation, cold discharging rate is determined by both of temperatures of PCM and air. In the cases of heat convection and cold radiation, cold discharging rates are calculated in terms of energy balance described in Eq.(4.47) and Eq.(4.46), respectively. The comparison is presented in Figure 4.16. The larger heat flux by convection indicates that heat convection plays a dominant effect on discharging for the regarded case. However, the effect of cold radiation was significant for PCM sealed in bigger capsule. By comparing Figure 4.13 to Figure 4.15, It is found that the temperature rising rate of PCM capsule by cold radiation is faster than by heat convection. This is caused by the high order effect of temperature in the case of cold radiation, as seen in Eq. (4.46).

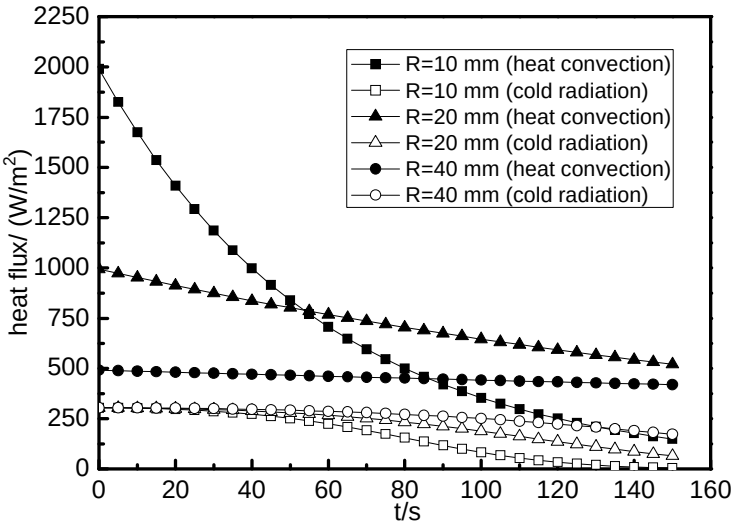

Figure 4.16 Cold discharging rate of PCM

Figure 4.17 compares the heat flux caused by radiation and convection. For PCM capsule with radius of 10 mm, 20 mm and 40 mm, the highest ratio of heat flux contributed by cold radiation to that by heat convection is 30%, 34% and 62%, respectively. This implies an increasing significance of regarding the combined effect of both radiation and convection for PCM capsule with larger size.

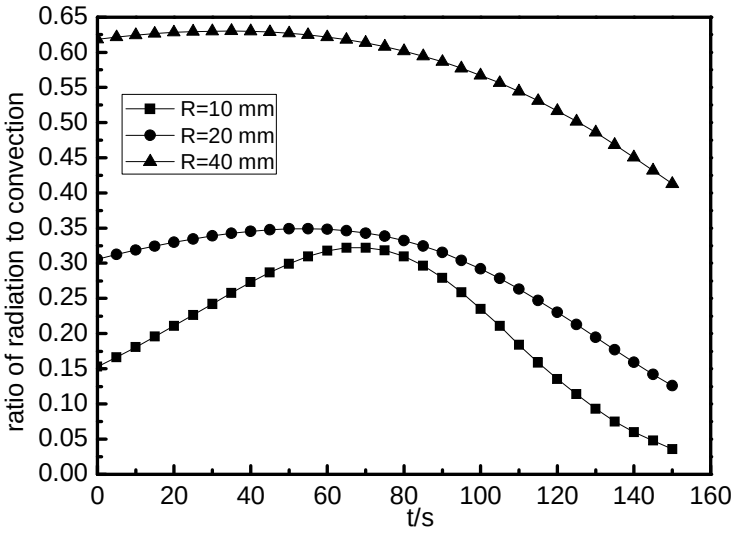

Figure 4.17 Distribution of ratio of radiation to convection

(3) Combination of cold radiation and heat convection

Conjunction effect of cold radiation and heat convection is considered by using thermal resistance method. In the regarded case, the temperature potential is determined by the cold discharging rate between PCM capsule and air flow. Under the same temperature potential, both of cold radiation and heat convection have significant effect on the cold discharging rate. Hence, thermal resistances for radiation and convection are regarded as shunt resistance in the resistance diagram, as demonstrated in Figure 4.18.

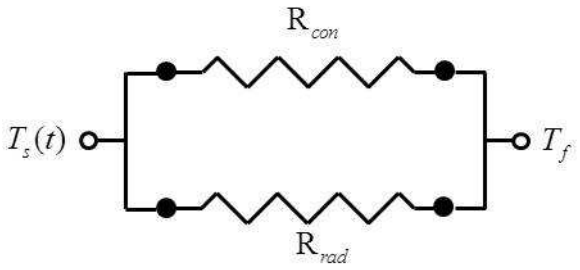

Figure 4.18 Thermal resistance diagram

Consequently, the equivalent thermal resistance for cold discharging is described as in Eq. (4.50):

$$\frac{1}{R_{equ}} = \frac{1}{R_{con}} + \frac{1}{R_{rad}} \tag{4.50}$$

In which R_{equ} , R_{con} , R_{rad} are equivalent resistance, resistance by convection and resistance by radiation, respectively. According to the above analysis, the equivalent heat flux of the discharging process is formulated as:

$$q_{equ} = q_{con} + q_{rad} \tag{4.51}$$

Where q_{equ} , q_{con} , q_{rad} are equivalent cold discharging rate and heat flux contributed by convection and radiation, respectively. The partial contribution of convection and radiation are analyzed separately as the above. Hence, the equivalent heat flux is obtained by using Eq.(4.51).

As presented in Figure 4.19, the equivalent heat flux decreased with discharge time going. This is attributed to the reduced temperature potential in the discharging process. For smaller size PCM capsule, the equivalent heat flux decreases more significantly with time. The faster temperature rising for PCM capsule with smaller radius is caused by the enhanced contribution of radiation and convection for smaller-radius PCM capsule, as is claimed in the above section.

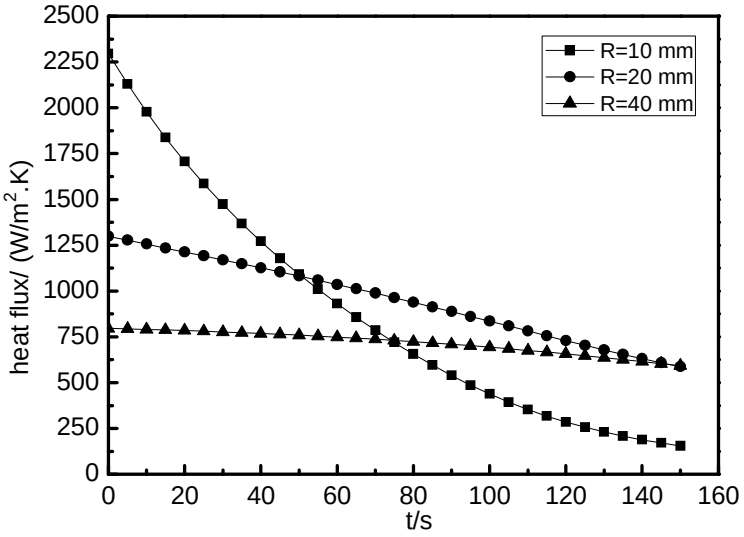

Figure 4.19 Distribution of the equivalent heat flux

In consideration of both radiation and convection, energy balance in discharging process is rewritten as in Eq. (4.52):

$$q_{equ}(t) = \frac{\rho \cdot C_p \cdot R}{3} \cdot \frac{dT_s(t)}{dt} \tag{4.52}$$

Therefore, the temperature of the PCM capsule is determined:

$$T_s(t) = \frac{3}{\rho \cdot C_p \cdot R} \int_0^t q_{equ}(t) \cdot dt \tag{4.53}$$

From Eq. (4.51) and Eq. (4.53), the distribution of PCM temperature is obtained, as shown in Figure 4.20. It is emphasised that the PCM temperature is calculated based on thermal resistance diagram. Compared PCM temperature under conjunction effect to the case with only convection considered, the former temperature increases faster due to the improved cold discharging rate.

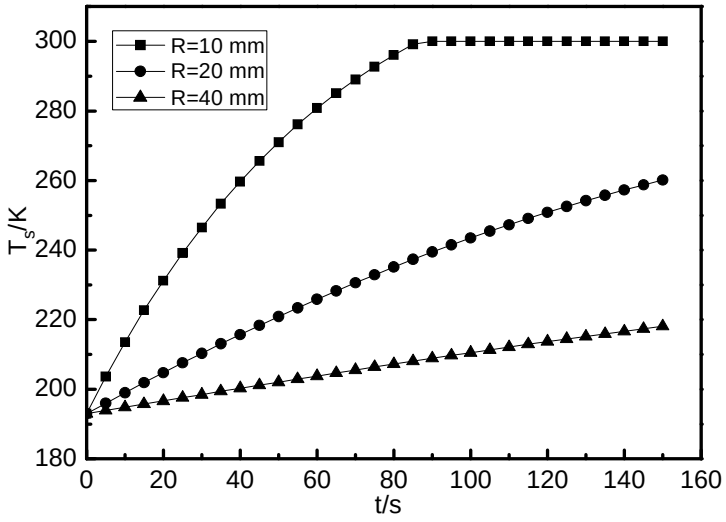

Figure 4.20 PCM temperature distribution

4.3.2.2 With phase change

Provided that the melting point of PCM is T_r, the starting time for freezing is t_{rs},while the ending time for freezing is t_{re}. Based on the established heat transfer model, the liquid fraction of the PCM during phase change ratio can be expressed as:

$$\varepsilon_r(t) = \frac{3 \cdot \left\{ [h \cdot (T_f - T_r) + \varepsilon_s \cdot \sigma \cdot ({T_f}^4 - {T_r}^4)] \cdot t - [h \cdot (T_f - T_r) + \varepsilon_s \cdot \sigma \cdot ({T_f}^4 - {T_r}^4)] \cdot t_{rs} \right\}}{\rho \cdot r \cdot R} \tag{4.54}$$

The initial liquid fraction is set as $\varepsilon_r(t_{rs}) = 0$. Consequently, for phase change process, the ending time is calculated as in Eq. (4.55):

$$t_{re} = t_{rs} + \frac{\rho \cdot r \cdot R}{3 \cdot [h \cdot (T_f - T_r) + \varepsilon_s \cdot \sigma \cdot ({T_f}^4 - {T_r}^4)]} \tag{4.55}$$

In which r is the latent heat of PCM. From Eq. (4.55), it is found that PCM with lower freezing point and latent heat packed in smaller-radius capsule is beneficial to shorten the melting time.

The heat transfer model with phase change has been established in Section. 4.3.1.2. According to Eq. (4.35), Eq. (4.39), Eq.(4.54) and Eq. (4.55), cold discharge including phase change process can be theoretically determined.

Using EG water solution (60% EG by volume) with 10mm and 20 mm radius as PCM module, a case study of cold discharging is carried out. With regarding to the conjunction effect of radiation and convection, variation of PCM temperature is calculated, as shown in Figure 4.21. It is shown that melting process for 10 mm and 20 mm radius EG water are 496 s and 1728 s, respectively. The longer melting time for bigger radius PCM is attributed to the increased total PCM latent heat in the capsule with increase of the capsule radius.

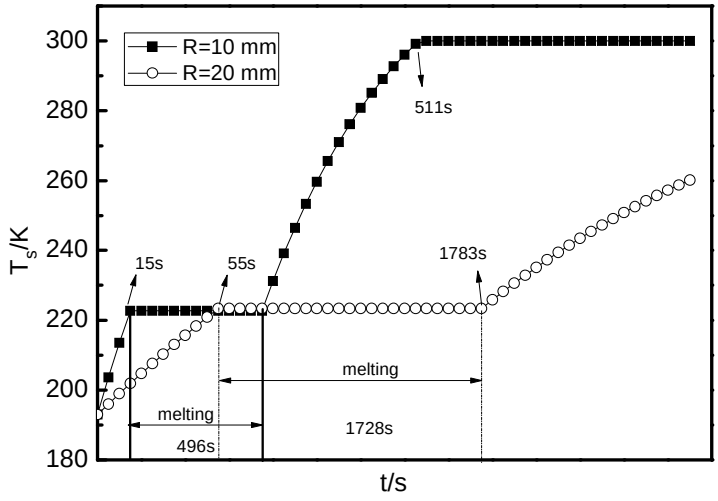

Figure 4.21 EG water melting process (60% EG by volume)

In the above study, the combined effect of cold radiation and heat convection is considered based on thermal resistance diagram for the discharge process. It is concluded that the significant effect of cold radiation on the cold discharging rate of PCM capsule should be considered under the following conditions:

(1) Lower PCM temperature: bigger temperature potential between PCM and fluid increases the heat flux by cold radiation;

(2) Larger radius PCM capsules: according to the above result, the ratio of radiation to convection becomes bigger with increase of radius of PCM capsule;

(3) Smaller Re number: ratio of radiation to convection is improved due to the reduced heat flux by convection.

The former two are consistent with the requirements for high grade and high density cold storage, as discussed in chapter 3. Therefore, combined effect

of cold radiation and heat convection is highlighted for investigating the discharge behaviour in PCM based cold storage.

4.3.3 Further discussions on real-life featured model

4.3.3.1 Influence of moving solid-liquid interface

The above heat transfer model is established based on energy balance of the PCM capsule with consideration of phase change phenomena. In reality, except for the latent heat during the phase change, the solid- liquid boundary moves towards the centre of the capsule. Therefore, the following part is to analyse the influence of the moving solid –liquid interface on the discharging rate of the whole PCM capsule.

With moving of the solid-liquid interface, discharging rate by air flowing across the PCM capsule is changed due to the varied temperature at the border of the PCM. The movement of the solid-liquid interface can be mathematically analysed, as shown in Eq. (4.42). By considering the effect of moving interface, the calculated temperatures on the boundary are compared to that without consideration of the moving interface, as listed in Table 4.5.

Table 4.5 Comparison of calculated temperature under different models (with only convection considered)

	Time	2 min	3 min	4 min
Temperature at the border (K)	With consideration	287	290	292
	Without consideration	278	293	299

It is seen that the difference of the calculated temperatures by the two methods is within 9 ^{o}C in all time. The minimum difference is 3 ^{o}C which appears at the 3rd minute. However, the time-averaged temperature on the border with consideration of moving interface is equal to that without consideration. This indicates an approximately equivalent discharging rate for the PCM capsule.

4.3.3.2 Influence of capsulation materials

In reality, PCM is shaped and encapsulated by materials which is thin and highly thermal conductive. This section is to assess the influence of the capsulation materials on the cold discharging rate of the PCM capsule.

Assuming that the thickness of the capsulation materials is 1 mm ($\delta_{ca} = 1mm$) and the thermal conductivity of the materials is 50 $W/m \cdot K$ ($\lambda_{ca} = 50W/m \cdot K$). The PCM capsule is a spherical shape with a diameter of 40 mm ($R_{PCM} = 20mm$). The thermal resistance of the capsulation materials can be expressed as:

$$TR_{ca} = \frac{\delta_{ca}}{4\pi\lambda_{ca} R_{PCM}(R_{PCM} + \delta_{ca})} \tag{4.56}$$

Which is calculated as 0.0038 K/W. Therefore, in the condition that the capsulation materials is thin and has a high thermal conductivity, the influence of the capsulation materials can be neglected.

However, the thermal resistance between the capsulation materials and the PCM capsule is large and becomes more significant during phase change due to the variable volume of the PCM. By improving the volume ratio of PCM within the encapsulated volume, the resistance can be largely reduced. Another issue is the leakage problem caused by the deformation of the capsulation materials. This can be addressed by using micro-capsulation technology by which capsules can be manufactured with a diameter of 1~100 μm. It is worth mentioning that with small diameter of PCM capsule, the concept of average temperature is feasible to be used in the energy equation.

4.4 Summary of this chapter

The chapter concerns the improvement and assessment of the discharge behaviour of a PCM based cold storage.

For improving the cold discharging rate of the PCM based cold storage, open-cell metal foams is embedded in PCM to form a PCM composite. Two dimensional heat transfer model is established, which can be analytically solved by using product method. A case study is demonstrated to show the improvement of the discharging rate by embedding high porosity metal foams in paraffin. The results shows that the improvement of the cold discharging rate is due to the enhancement of the effective thermal diffusivity and thermal conductivity of the PCM composite, which is justified in the case

study. The influence of the heterogeneous nature of the open-cell metal foams on cold discharge behaviour is discussed. By using volume-average method in metal foams, the influence of the specific structure of the solid matrix has been considered in the energy equation.

Discharge behaviour in PCM capsules is assessed in consideration of the combined effect of cold radiation and convection. The heat transfer model is established based on the average temperature of the PCM capsule. However, the temperature difference within the volume of the PCM capsule is assessed under both small and large Biot number. Real-life features of the heat transfer model including the moving solid-liquid interface and the influence of the capsulation materials are further discussed. Thermal resistance method is used to analyse the combined effect of cold radiation and heat convection. It is concluded that the effect of cold radiation on the cold discharging rate of PCM capsule becomes significant for PCM capsules with low temperature and large radius, or under small Re number.

Chapter 5
Cold utilisation through carbon dioxide based Rankine cycle

Cold utilisation can be defined as use of cold exergy based on a thermal dynamic cycle in the purpose of generating dynamic power or electricity. Cold utilisation through a Rankine cycle has been experimentally and theoretically studied and results are presented in this chapter. Through the study, it is hoped:

(1) to demonstrate the feasibility of small scale CES systems; and
(2) to understand how to make improvement on cold utilisation efficiency.

5.1 Introduction

5.1.1 The principle of cold storage and utilisation

An overall block diagram of CES system is shown in Figure 5.1. The CES system includes CO_2 cycle, refrigerator cycle and water cycle. The CO_2 cycle includes a CO_2 tank, a cryogenic pump, several heat exchangers, an engine and numerous pipes and valves. Liquid CO_2 with low temperature stored in the CO_2 tank is sucked by the cryogenic pump to get a higher pressure of CO_2. Regenerator (HEX 3), hot heat exchanger (HEX 1) and super heater are used to improve the temperature of the working fluid, which will be expanded in the engine for power generation. The water cycle is designed to supply heat to CO_2 by using the hot heat exchanger. Ambient heat will be absorbed by water in the water tank during off-peak time. The refrigerator cycle is an accessorial system for cooling the CO_2 after expansion. This can be done by pumping the liquid EG and water mixture with low temperature to the other side of the cold heat exchanger.

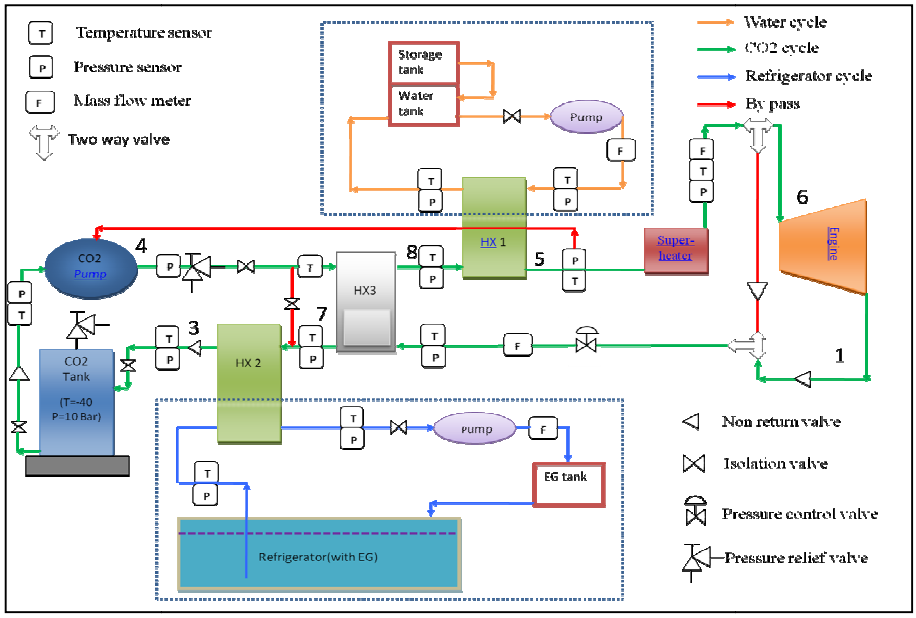

Figure 5.1 An overall block diagram of CES system

The principle of the CES system for peak-shifting is presented in Figure 5.2. The prototype CES system for peak-shifting is composed by cold storage unit (CSU) and cold conversion unit (CCU). The CSU mainly includes a refrigerator (deep freezer) and cold storage media (EG and water mixture). During off-peak time, the CSU stores cold energy in freezer for producing coolant with low temperature (-40~-50 ^{O}C) by consuming cheap electricity. The stored quantity of cold energy is dependent on cheap electricity that need to be stored during the off peak time. The CCU contains cryogenic pump, components in Rankine cycle, engine and cold heat exchanger, etc. In peak time, cold energy stored in PCM in the CSU is utilized for power generation through Rankine cycle based on critical carbon dioxide. Through cold storage and cold utilisation, peak-shifting of electricity grid based on CES system can be achieved.

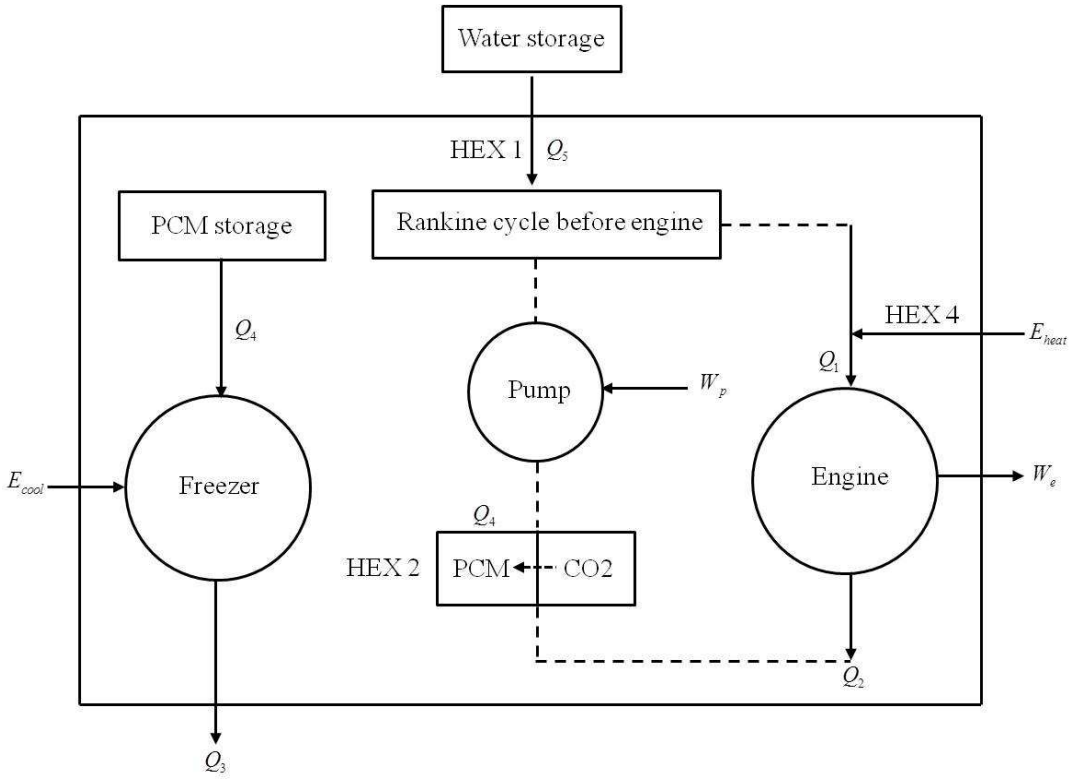

Figure 5.2 Principle diagram of the CES system

Specifically, the flow chart of carbon dioxide in the prototype CES system was shown in Figure 5.3. Saturated liquid carbon dioxide is pumped out from CO_2 tank. For recovering heat of CO_2 after expanding, regenerator (HEX 3) is located before the pre-heating process in HEX 1. After heating up in hot exchanger, CO_2 flows in engine for expanding. Following heat recovery in regenerator, CO_2 is cooled down to saturated liquid by PCM and return the CO_2 tank. Based on the thermal dynamic cycle, the cold energy stored in PCM during off-peak time is utilized and converted into dynamic power.

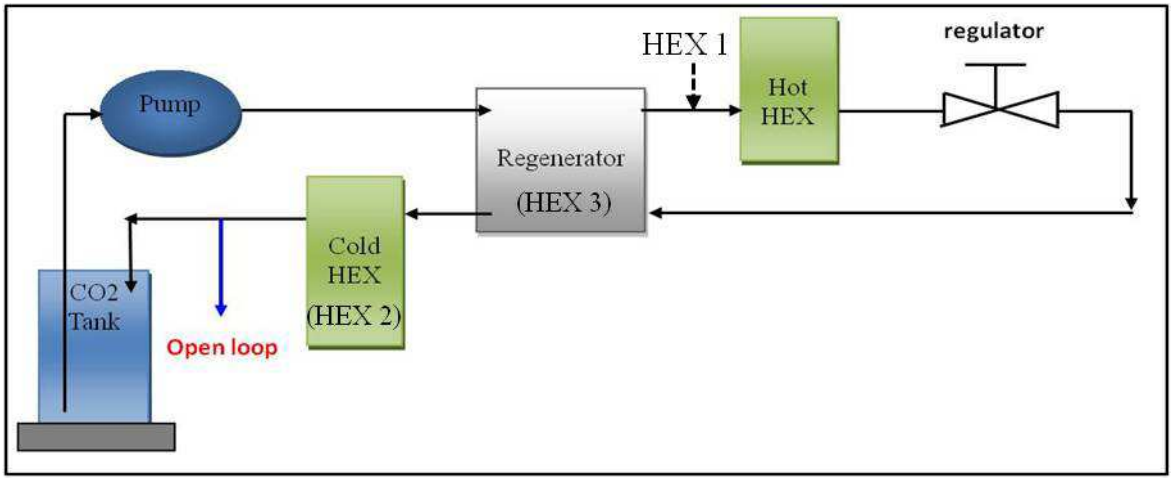

Figure 5.3 Flow chart of CO2 in the prototype CES system

5.1.2 Cold storage efficiency

Cold storage efficiency for CES is actually the exergy efficiency of the system, defined as the net power generation divided by electricity consumption. It is not affected by the released heat from engine (Q_2) and freezer (Q_3), as a result, can be formulated as in Eq. (5.1):

$$\eta_{CES} = \frac{W_s}{E_{cons}} \tag{5.1}$$

The power generation by engine is W_e, while the electricity consumption by pump is W_p. Therefore, the net power generation is expressed as :

$$W_s = W_e - W_p \tag{5.2}$$

The consumed electricity for producing cold PCM in freezer is E_{cool}. In the Rankine cycle, water under ambient temperature is used to pre-heat carbon dioxide, while cold PCM is used to cool down the exhausted gas from engine. However, no extra electricity is consumed in the above heat exchanging processes. Before expanding in engine, carbon dioxide is heated up for improving the power capacity. The energy consumed in the heating process is E_{heat}. It is worth mentioning that both of waste heat and electricity can be utilized. As a consequence, the net electricity consumption is formulated as:

$$E_{cons} = \begin{cases} E_{cool} & (\text{waste heat used}) \\ E_{cool} + E_{heat} & (\text{electricity consumed}) \end{cases} \tag{5.3}$$

The thermal physical processes of the revised Rankine cycle is described in the T-S diagram (T is temperature, S denotes entropy), as presented in Figure 5.4. Process 3-4 is the pumping of liquid carbon dioxide from the CO_2 tank. Process 4-8 and 1-7 represent the heating and cooling processes of carbon dioxide in the regenerator; while processes 8-5 and 5-6 are the heating processes by hot heat exchanger and super heat exchanger, respectively. Process 6-1 is the expanding process of CO_2 in engine. Process 7-2-3 is the cooling process of CO_2 by cold EG and water solution in the cold heat exchanger, by which CO_2 can be cooled to saturated liquid.

From the T-S diagram, it is seen that the pressure of the saturated liquid carbon dioxide is improved after pumping (shown as 3-4). Provided that the pump efficiency is taken into account, the process is presented as from 3 to 4_{act}. After heating up in heat exchangers, high temperature and high pressure carbon dioxide expands in engine for power generation (from 6 to

1). Considering the actual efficiency of engine, the expanding process is described as from 6 to 1act. Therefore, the net power generation in the revised Rankine cycle is formulated as:

$$W_s = \eta_{engine} \cdot (h_6 - h_1) - \eta_{pump}^{-1} \cdot (h_4 - h_3) \tag{5.4}$$

In which h_6, h_1, h_4, h_3 are the enthalpy of carbon dioxide at point 6, 1, 4 and 3, respectively. While $\eta_{engine}, \eta_{pump}$ represent the efficiencies of engine and pump, which are given before the analysis.

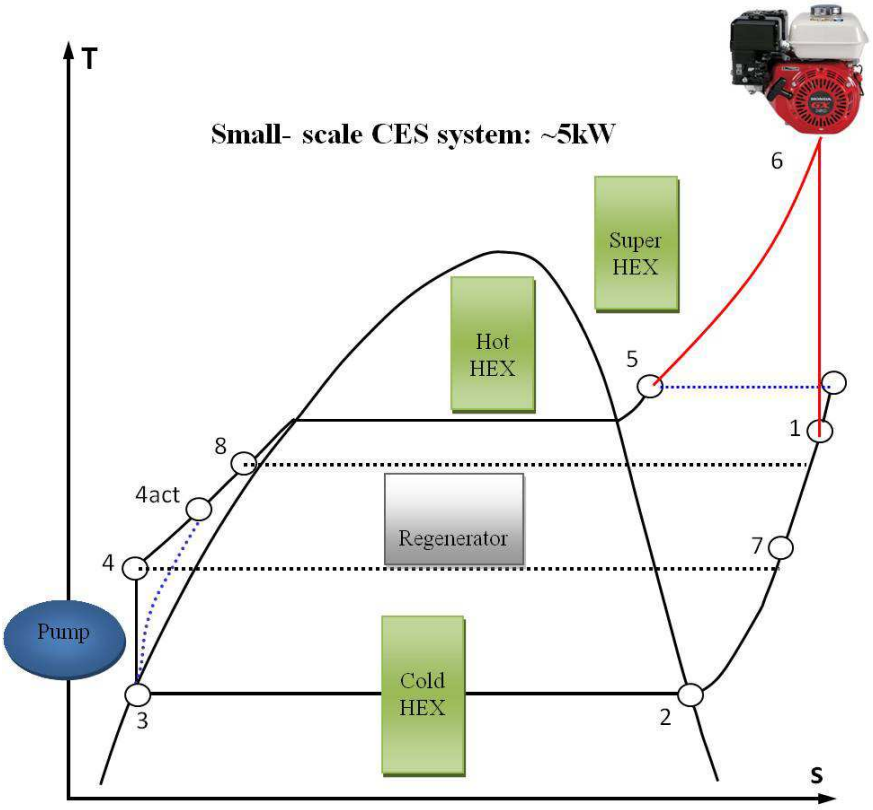

Figure 5.4 T-S diagram for Rankine cycle in CES system

According to the definition, electrical consumption by cool storage is easily obtained, shown in Eq. (5.5):

$$E_{cool} = \frac{Q_4}{COP_{act}} \tag{5.5}$$

In which Q_4 is the released heat from PCM in the refrigerating cycle. The coefficient of performance (COP) of the refrigerator is calculated by Eq. (5.6a):

$$COP_{act} = \eta_{refrig} \cdot \frac{1}{\frac{T_{envi}}{T_{PCM}} - 1} \tag{5.6a}$$

Where η_{refrig} is the efficiency of refrigerator; T_{envi} , T_{PCM} represent environmental temperature, and PCM temperature in the freezer, respectively. As discussed before, the working fluid is cooled down by stored cold PCM solution through cold heat exchanger (HEX 2). Provided that heat transfer efficiency in HEX 2 is 100%, the temperature of CO_2 at point 2 in the cycle can be assumed to be equal to PCM temperature, therefore, Eq. (5.6a) can be written as:

$$COP_{act} = \eta_{refrig} \cdot \frac{1}{\frac{T_{envi}}{T_2} - 1} \tag{5.6b}$$

In the refrigerating cycle, the released heat from PCM is written as Q_4. Considering the heat transfer process in HEX 2, the absorbed heat by PCM from carbon dioxide is Q_c. This heat transfer process in the CES system under steady case is demonstrated in Figure 5.5. In steady condition, temperature of PCM module keeps constant, therefore, the former is equivalent to the released heat of CO_2 in HEX 2, thus,

$$Q_4 = Q_c \tag{5.7}$$

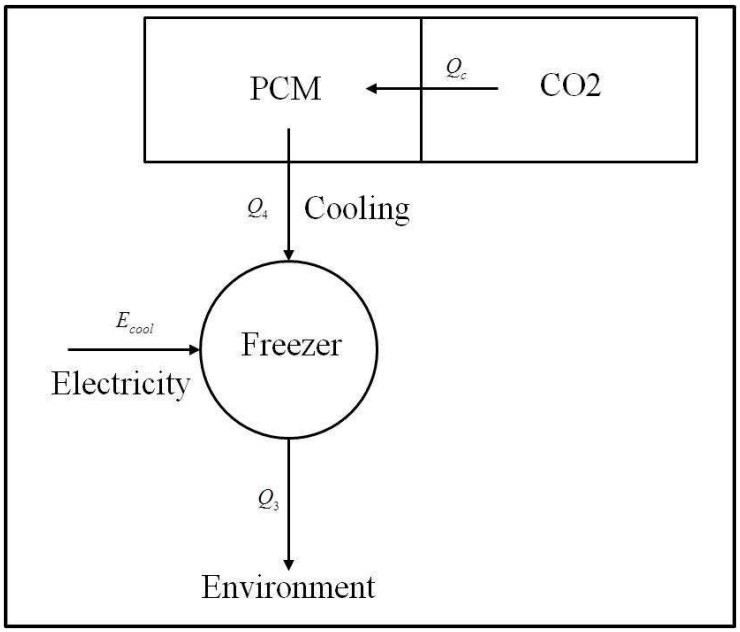

Figure 5.5 Equivalent refrigerating cycle in CES system

Due to the effect of regenerator, it is noted that the real exothermal process in HEX 2 is from point 7 to point 3 (7-3) rather than from point 1 to point 3 (1-3), therefore, the calculation for Q_c is described in Eq. (5.8):

$$Q_c = \dot{m}_{CO2} \cdot (h_7 - h_3) \tag{5.8}$$

From Eq. (5.5) ~ (5.8), the electricity consumption for cold production is obtained:

$$E_{cool} = \frac{\dot{m}_{CO2} \cdot (h_7 - h_3)}{\eta_{refrig} \cdot \frac{1}{\frac{T_{envi}}{T_2} - 1}} \tag{5.9}$$

Carbon dioxide is pre-heated and super-heated in HEX 1 (from point 8 to 5) and hot heat exchanger (from point 5 to 6), respectively. Consequently, the capacity of CO_2 for dynamic power generation is significantly enhanced. In pre-heater, water under ambient temperature is used to warm up carbon dioxide. While in super heater, as discussed before, both of waste heat and electricity can be used for heating, therefore, the electrical consumption in super heater (hot heat exchanger) can be differently described, as shown in Eq. (5.10):

$$E_{heat} = \begin{cases} 0 & (\text{waste heat used}) \\ \dot{m}_{CO2} \cdot (h_6 - h_5) & (\text{electricty consumed}) \end{cases} \tag{5.10}$$

In which m_{CO2} is the mass flow rate of CO_2 in the system; h_6 and h_5 are the enthalpy of carbon dioxide at point 6 and 5, respectively.

According to the above equations, the storage efficiency can be written as:

$$\eta_{ces} = \frac{\eta_{engine} \cdot (h_6 - h_1) - \eta_{pump} \cdot (h_4 - h_3)}{\frac{\dot{m}_{CO_2} \cdot (h_7 - h_3)}{\eta_{refrig} \cdot \frac{1}{\frac{T_{envi}}{T_2} - 1}} + \dot{m}_{CO_2} \cdot (h_6 - h_5)} \quad \text{(waste heat used in HEX 1)} \tag{5.11a}$$

$$\eta_{ces} = \frac{\eta_{engine} \cdot (h_6 - h_1) - \eta_{pump} \cdot (h_4 - h_3)}{\frac{\dot{m}_{CO_2} \cdot (h_7 - h_3)}{\eta_{refrig} \cdot \frac{1}{\frac{T_{envi}}{T_2} - 1}}} \quad \text{(electricity consumed in HEX 1)} \tag{5.11b}$$

The storage efficiency is the ratio of power generation to the total electricity used for storing cold in PCM solution and heating carbon dioxide in Rankine cycle. In comparison, heat efficiency represents the efficiency of a thermal dynamic cycle for obtaining power W_s at the expense of heat absorption $Q_5 + Q_1$, which can be expressed as:

$$\eta_h = \frac{\eta_{engine} \cdot (h_6 - h_1) - \eta_{pump} \cdot (h_4 - h_3)}{h_6 - h_8} \tag{5.12}$$

The storage efficiency and heat efficiency will be further discussed in the following section. It is pointed out that storage efficiency can be bigger than 100% in the condition that waste heat is used for heating up CO_2 to a high temperature level. In that case, dynamic power generation is more than the electricity consumption by the CES system. It is reasonable since the contributions of waste heat in pre-heater (HEX 1) and the super heater (hot heat exchanger) are not accounted as consumptions.

5.2 Investigation on feasibility of small scale CES system

5.2.1 Introduction of the small scale CES system

A prototype CES system with $5\,\mathrm{kW}$ power capacity has been designed and constructed. This section introduces the experimental system with specifications of all the system components, the experimental procedures for cold energy storage and power generation, and the experimental parameters in typical measurements.

5.2.1.1 Experimental system

The CO2 system is a Rankine cycle which mainly contains tank, pump, regenerator, pre-heater, super heat and engine. The CO2 tank hired from BOC is a tank-in tank design which can resist 23.5 bar pressure, as shown in Figure 5.6. The specific parameters of the tank are listed in Table 5.1.

Figure 5.6 Picture of CO_2 tank in CES system

Table 5.1 Specifications of the selected CO_2 tank

Name	Cryogenic tank (Dewar vessel)
Supplier	Wessington Cryogenics Ltd (Via BOC)
Product Code	GT-120HP
Capacity(Litre)	~120
Structure	Tank-in-tank
Dimension (mm)	506 (diameter)×1200(height)
Weight (kg)	~100
Working pressure (bar)	23.5
Daily boil-off (%)	<2.6%

The CO_2 pump used in the small scale CES system is a cryogenic pump from CAT Pump (UK) Ltd, as shown in Figure 5.7. The cryogenic pump can work under a temperature of -40 ^{o}C and can improve the pressure of the working fluid to be in the range of 20~73 bar. The tuneable outlet pressure of the working fluid can be achieved by adjusting the frequency on the panel of the inverter of the pump. The specific parameters of the cryogenic pump are listed in Table 5.2.

Figure 5.7 CO_2 pump used in the CES system

Table 5.2 Specifications of the cryogenic pump

Name	Cryogenic pump
Working Fluid	Liquid carbon dioxide/air
Inlet Pressure (bar)	~12
Inlet temperature (^{o}C)	~ -40
Outlet Pressure (bar)	20~73
Flow rate (*kg/s*)	0.1~1
Efficiency (%)	>70

Regenerator is a heat exchanger used to increase the temperature of CO_2 out of the cryogenic pump, by recovering the waste heat of CO_2 after expansion. As a result, the heat efficiency of the Rankine cycle is improved. The selected regenerator in the CES system is a plate-fin heat exchanger from SWEP International Ltd, as shown in Figure 5.8. The specifications of the regenerator is listed in Table 5.3.

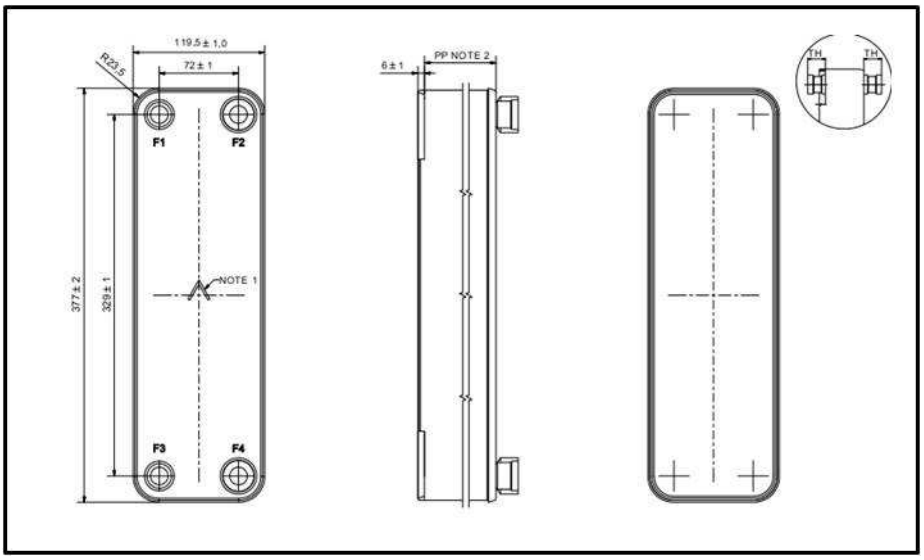

Figure 5.8 Selected regenerator in the CES system

Table 5.3 Specifications of the selected regenerator

Designer	SWEP International Ltd
Type	Plate-fin
Model	B16DWx12H/1P
Working fluid	Carbon dioxide
Designed pressure (bar)	140 (under 150 ^{o}C)
Working temperature (^{o}C)	-40~150
Flow rate (kg/s)	0~0.11

The hot heat exchanger (HEX 1) and cold heat exchanger (HEX 2) are used to heat up and cool down the working fluid (CO_2), respectively. The maximum design pressure of the heat exchangers is as high as 140 bar under the fluid temperature of 150 ^{o}C. The structural diagram and the specifications of the selected heat exchangers are shown in Figure 5.9 and Table 5.4, respectively.

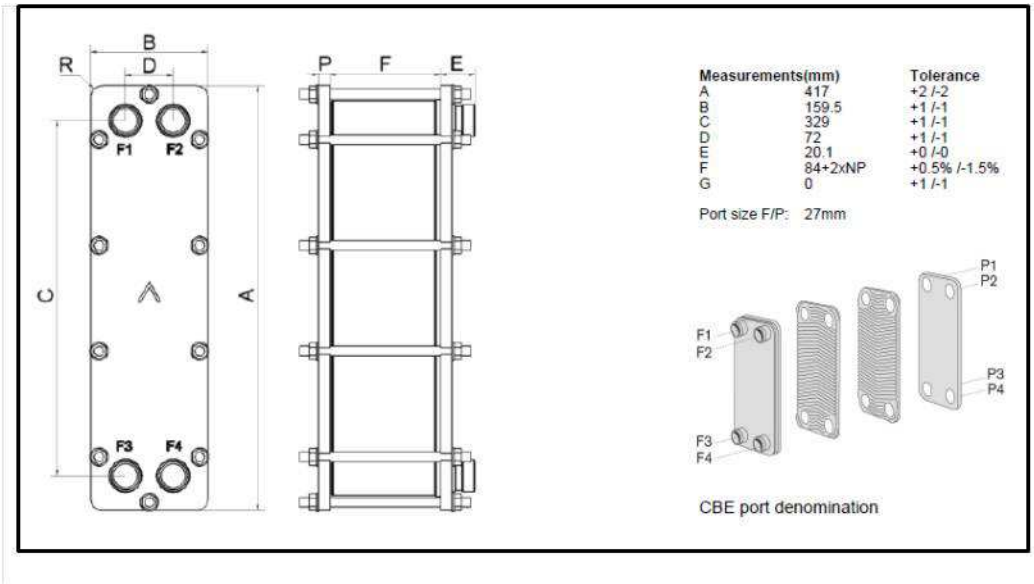

Figure 5.9 Selected heat exchangers in the CES system

Table 5.4 Specifications of heat exchangers (HEX 1 and 2)

Designer	SWEP International Ltd
Type	Plate-fin
Model	B16DWx60H/1P
Working fluid	Carbon dioxide
Heating/ cooling fluid	Water / EG Solution
Design pressure of (cold) working fluid	140bar (150 ^{o}C)
Pressure of heating/ cooling Fluid (bar)	1.3
Working temperature (^{o}C)	-40~150
Flow rate of working fluid(kg/s)	0.0-0.11
Flow rate of heating fluid (kg/s)	~0.2

The super heater (HEX 4) is used to get super-heated working fluid. For simulating the waste heat of diesel engine, CO_2 is heated up to 200~300^{O}C before entering the engine. The picture and the specifications of the selected super heater are shown in Figure 5.10 and Table 5.5.

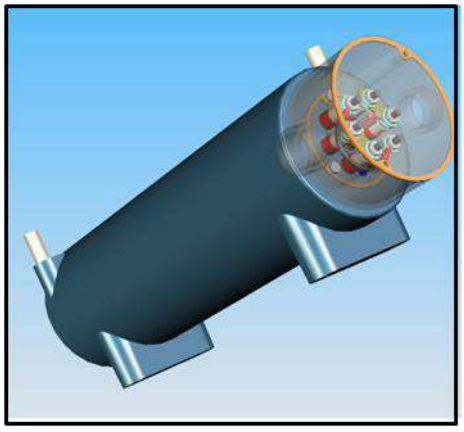

Figure 5.10 Selected super heater in the CES system

Table 5.5 Specifications of the selected super heater

Designer	Watlow Ltd
Type	Circulation heater
Model	CAST X 3000
Working Fluid	Carbon dioxide
Heat load	28.4 kW
Design pressure of working fluid (bar)	70
Maximum working temperature (^{o}C)	~300
Flow rate of working fluid(kg/s)	0.0-0.10

Engine is one of the most important components in the CES system. The outlet pressure of the engine is designed to be around 12 bar for obtaining a saturated carbon dioxide temperature of -40 ^{o}C. When the inlet pressure in experiments is as high as 70 bar, the expansion ratio is required to be up to 5.8, which is a challenge for lots of the commercial engines. More details of the engine system will be discussed in chapter 6. The technical requirements of the engine in the CES system are listed in Table 5.6.

Table 5.6 Parameters of the selected engine

Type	Piston based
Inlet pressure (bar)	20-70
Inlet temperature (^{o}C)	200-300
Outlet pressure (bar)	12-20
Volume	162 cm^3 or 1900 cm^3
Flow rate (kg/s)	0.02-0.1

Refrigerator is used to store cold energy in the cold carrier (EG and water solution) during off-peak time. The picture and specifications of the selected refrigerator in the CES system are presented in Figure 5.12 and Table 5.7, respectively.

Figure 5.11 Selected refrigerator in the CES system

Table 5.7 Specifications of the selected refrigerator

Name	Refrigerator
Supplier	Progen Scientific Direct
Type	Chest
Model	ULTF420
External size (mm)	885×1560×695
Gross capacity (L)	383
Temperature range (^{o}C)	-40/-85
Ambient temperature (^{o}C)	+10 - +32
Power consumption (kWh)	12.4 (per 24h)
Voltage supply (V)	230

Water pump and EG pump are also selected. The specifications of these two pumps are summarized in Table 5.8 and Table 5.9.

Table 5.8 Specifications of water pump for hot heat exchanger (HEX 1)

Supplier	London pumps
Model No.	Clear water pump SV218F034T
Power supply	Three phase/50HZ/400V
Power rate (kW)	0.37
Flow rate (m^3/h)	1.2
Working fluid temperature (^{o}C)	-20~30

Table 5.9 Specifications of EG pump for cold heat exchanger (HEX 2)

Name	EG pump
Supplier	London Pumps
Model Code	SV 220F034T
Pressure head (m H_2O)	40.9
Flow rate (m^3/h)	1.08
Working fluid temperature (^oC)	>-20
Rated power (kW)	0.37
Motor electricity	50HZ/3ph/400V

From the above, key components in the CES system are specified. These include a CO_2 tank, a cryogenic pump, a regenerator, two heat exchangers, a super-heater and an engine in the CO_2 cycle, a refrigerator and an EG pump in the refrigerator cycle, and a water pump in the water cycle. More work about the selection of components can be found in [196].

5.2.1.2 Experimental procedures and parameters

This section demonstrates the specific procedures for operating a CES system, followed by an introduction of typical parameters in the small scale CES system.

As discussed above, cold storage unit (CSU) works during off-peak time for storing cold energy. The specific procedures are as follow:

- Preparation of cold carrier. 90 L of water and 110 L of EG is poured and mixed in the refrigerator. Then cover the lid of the refrigerator.
- Running the refrigerator. Switch on the power supply for the refrigerator and set the target temperature of the coolant (i.e. -40~-50 ^oC).
- Record the power consumption. A power meter is connected to measure the electricity consumption.

The refrigerator will run during the night until the set temperature is achieved. This indicates that the cheap electricity in off-peak is converted into cold energy and stored in the EG and water solution under a low temperature. In peak time, CO_2 system is operated according the following procedure:

- Check the pressure of CO_2 tank. If pressure of CO_2 is higher than 12 bar, release some amount of gas CO_2 by open the releasing valve of the vessel;

- Switch on CO_2 monitor and run the ventilation fan;
- Pre-cool the pipe system. Make sure all the valves connected to the ventilation pipe is open. Slightly Open the outlet valve of the CO_2 tank so CO_2 goes out of the system through the pipes. when liquid CO_2 can be observed, close the valves connected to the ventilation pipe.
- Switch on the cryogenic pump to increase the pressure of liquid CO_2. Record the outlet pressure of the pump. Adjust the frequency on the panel of the inverter to change the outlet pressure if needed;
- Switch on the water pump immediately and record the flow rate of water. Issue of frozen water should be avoided;
- Switch on the EG pump and record the flow rate of EG and water solution, inlet and outlet temperature at the cold heat exchanger;
- Adjust the regulator to get a proper inlet pressure of the engine;
- Run the engine system and record the torque and power from the hand panel;

After the experiments, the following procedures should be obeyed:

- Make sure to switch off the outlet valve of the CO_2 tank firstly;
- Switch off the cryogenic pump;
- Switch off engine system;
- Open the valves connected to the ventilation pipe.
- Switch off the water pump and EG pump.

Since the CES system is running under high pressure, the operation of the experimental system should be careful to get rid of risks.

In the constructed small-scale CES system, the typical mass flow rate of CO_2 is between 0.01~0.1 kg/s, which can be adjusted by setting the mass flow rate or pressure of the cryogenic pump. The saturated liquid CO_2 is under a temperature of -40 ^{o}C and a pressure of 12 bar. This value varies in specific operations since the CO_2 in the Rankine cycle is sometimes not in saturated state or over cooled when it returns to be the tank.

Considering the safety issues, the actual operating pressure of CO_2 is lower than 70 bar, which is typically in the range of 15~40 bar. In the case that the super heater is used, the temperature of CO_2 after heating is lower than 150 ^{o}C.

Although components have been selected by previous researcher, there are lots of works that haven't been done. My contributions on the CES system lies in the following:

- Thermal analysis for validating the selection of the components. Based on the proposed 5 kW CES system, all key components are theoretically analyzed;
- Integration of the CES system. This includes calculations for geometric and physical parameters in the system and engineering considerations for the designed rig diagram.
- Operations of the complicated experiments. These include basic tests for single components and operations of the whole CES system.
- Labview program. Critical parameters in the system is recorded and analyzed.
- Computer program for count setting. This is used to modify the p-crank angle of the engine for obtaining optimal power generation under specific conditions.
- Development of the piston based engine system. This include contributions on the expansion analysis and experiments with small and large engines.

5.2.2 Feasibility of the small scale CES system

5.2.2.1 Feasibility of cold storage

The PCM temperature, charge time and electricity consumption rate of the constructed CES system are discussed in this section.

Cold storage in a deep freezer is experimentally studied. Electricity is consumed to lower the air temperature inside the refrigerator. Temperature of the air in the refrigerator is measured, shown in Figure 5.12. Air temperature decreases sharply in the beginning and slowly in the subsequent time. It is found that the air can be cooled down to the lowest temperature of -85 ^{o}C in 250 minutes. For reaching the designed saturated temperature of -40 ^{o}C , time of 70 minutes is required.

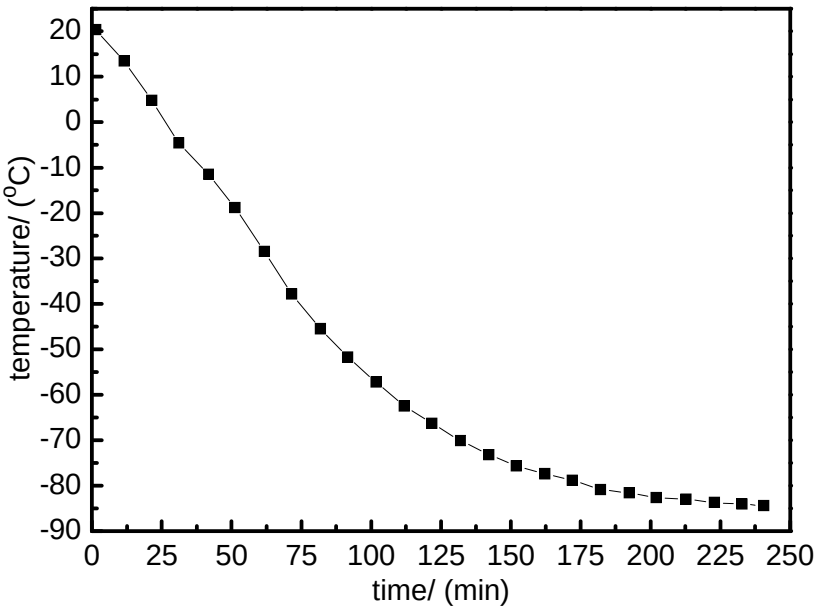

Figure 5.12 Temperature variation with time in the refrigerator

Experiment with PCM filled in the freezer is also carried out, as presented in Figure 5.13. Ethylene glycol is mixed with water in different proportions for obtaining the lowest freezing temperature. As the PCM for cold storage, 300 L of the solutions with 70% of ethylene glycol by volume is filled in the freezer. It is reported that ethylene glycol and water solution is cooled down from ambient temperature to -40 ^{o}C within 48 hours. Although the cooling time is much longer than the normal charging time of 8 hours per day, cold storage for the CES system is still feasible. The reason is that the actual cold energy recharged for the PCM is much smaller. For example, after cold discharging, the PCM solution was as high as -30 ^{o}C, therefore, the electricity consumption for recharging the PCM is 15.6% of that for charging PCM from ambient temperature (24 ^{o}C) to -40 ^{o}C. As a result, the cold discharge time is approximate 7.5 hours. This indicates that PCM cold storage at -40 ^{o}C is feasible to be completed in the night time by using cheap electricity.

In cold charge process, energy equation can be written as below:

$$Q_c' = COP \cdot E_{cool}'(t) \tag{5.13}$$

In which, Q_c', $E_{cool}'(t)$, COP are cold charging rate, electricity consumption rate and coefficient of performance of the refrigerator, respectively.

COP of refrigerator is calculated by Eq.(5.6a). The electricity consumption rate by the refrigerator is measured, as seen in Figure 5.6. It is shown that electricity consumption rate fluctuates in the range of 400~600 W during the testing time. This is attributed to the changing of the refrigerator efficiency. In

this case, provided that charging time is 8 hours, the utilized electricity can be evaluated as 3.2~4.8 $\mathrm{kW}h$. From the point of view of energy saving, cold production in off-peak time by consuming cheap electricity is feasible for later usage.

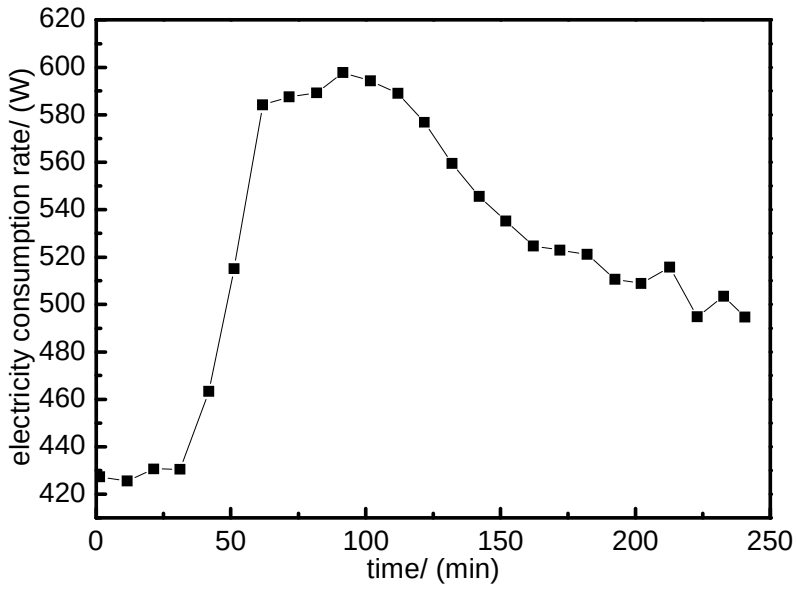

Figure 5.13 Electricity consumption rate by the refrigerator

5.2.2.2 Feasibility of cold utilisation in open cycle

Due to the complexity of the engine system, at the first stage, regulator is used instead in an open Rankine cycle. The experimental study of engine in the CES system will be presented in chapter 6.

The schematic diagram of the open Rankine cycle system is shown in Figure 5.2. A regulator is used to simulate the pressure drop of CO_2 during expanding in engine. The constructed system of the open Rankine cycle is mainly composed by CO_2 tank, cryogenic pump, regenerator (HEX 3), hot heat exchanger, regulator and cold heat exchanger (HEX 2), as seen in Figure 5.14.

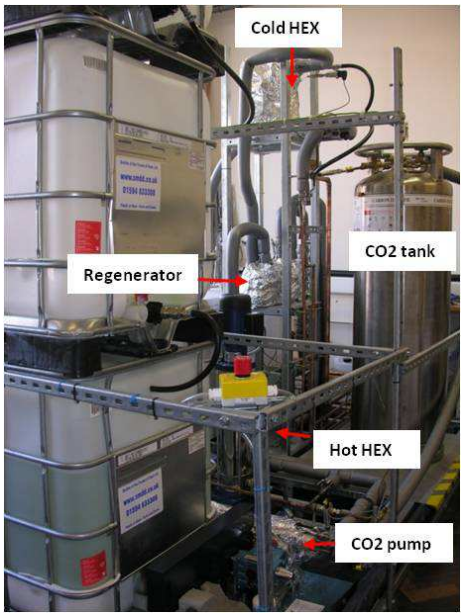

Figure 5.14 The constructed system of the open Rankine cycle

Cryogenic pump is used to circulate the EG and water solution for heat transfer in the cold heat exchanger (HEX 2). In the refrigerator system, flow rate and temperature of the PCM are the main factors that influence the cooling process in HEX 2. Consequently, both of the above are experimentally studied.

Flow rate of EG pump is tested under different conditions. The results are shown in Figure 5.15 and Figure 5.16. It is found that the EG pump has limited flow rate of about 1.28 m^3/h. The critical current and frequency are 0.0156 A and 38 Hz, respectively. Before the maximum value, the flow rate of EG and water are proportional to current and frequency in the pump.

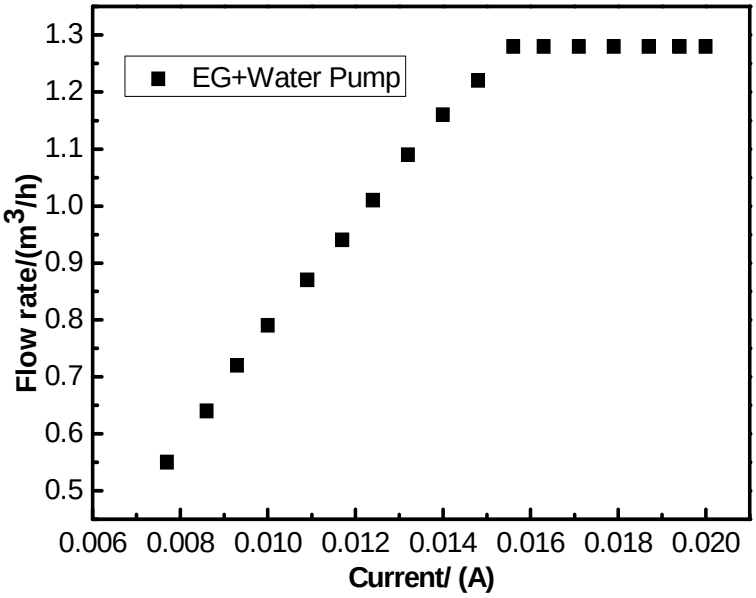

Figure 5.15 Relation between flow rate and current for EG pump

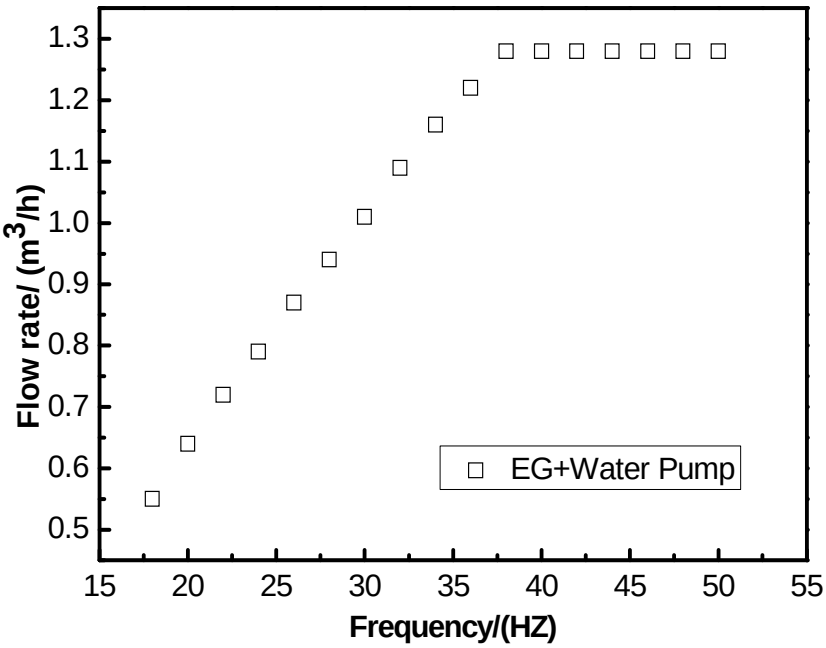

Figure 5.16 Relation between flow rate and frequency for EG pump

The temperatures of EG water solution are also measured. Without CO_2 flowing through at the other side of the plate heat exchanger, PCM temperature at both inlet and outlet of the cold heat exchanger are recorded. The measured temperatures are shown in Figure 5.17. It is found that with the increase of pump frequency, both of the inlet and outlet temperatures are lower. It is explained by the increased mass flow rate of cold PCM. After 35 Hz of the EG pump, inlet and outlet temperatures maintain constant at -33.0 ^{o}C and -15.4 ^{o}C, respectively, since the mass flow rate of PCM solution reaches the maximum value. It is noted that both of the temperatures are higher than -40^{o}C. This is due to the loss of cold energy in pipes and cold heat exchanger.

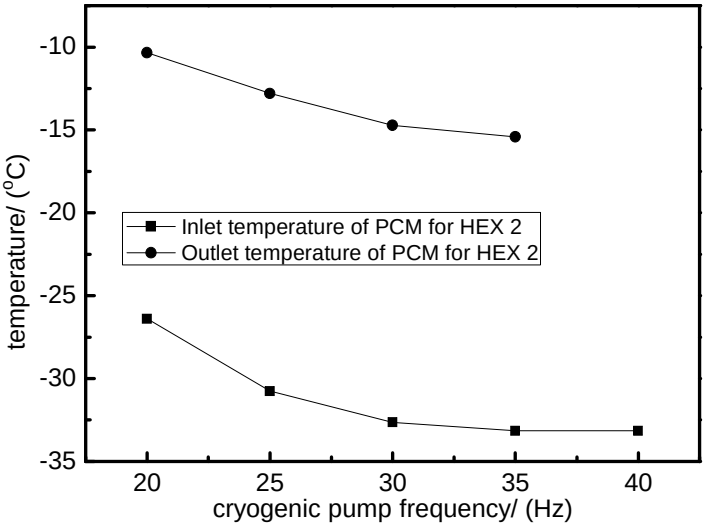

Figure 5.17 Measured temperatures at the inlet and out of HEX2

However, the purchased cryogenic pump has the lowest temperature limitation for working fluid as -20 ^{O}C. Consequently, more requirements for the PCM temperature at the outlet of HEX 2 are proposed. In the HEX 2, the outlet PCM temperature is approximate to the inlet temperature of CO_2 on the other side of the cold heat exchanger (point 7, CO_2 side), hence, both of inlet and outlet temperature of HEX 2 on CO_2 side are investigated.

The results are presented in Figure 5.18 and Figure 5.19. It is found that the inlet and outlet temperatures are mainly affected by saturated pressure in CO_2 cycle and efficiency of regenerator. From Figure 5.18, it is concluded that the saturated pressure of CO_2 can't be lower than 12 bar, otherwise, CO_2 temperature at point 7 will be lower than -20 ^{O}C. This is consistent with the designed saturated pressure for the CES system. From Figure 5.19, it is shown that with higher regenerator efficiency, temperature of CO_2 at point 7 becomes lower, since more heat was released in the regenerator. According to the measured result, when the regenerator efficiency is higher than 93%, the inlet temperature on CO_2 side (point 7) is lower than -20 ^{O}C. In this case, the cryogenic pump will probably be damaged.

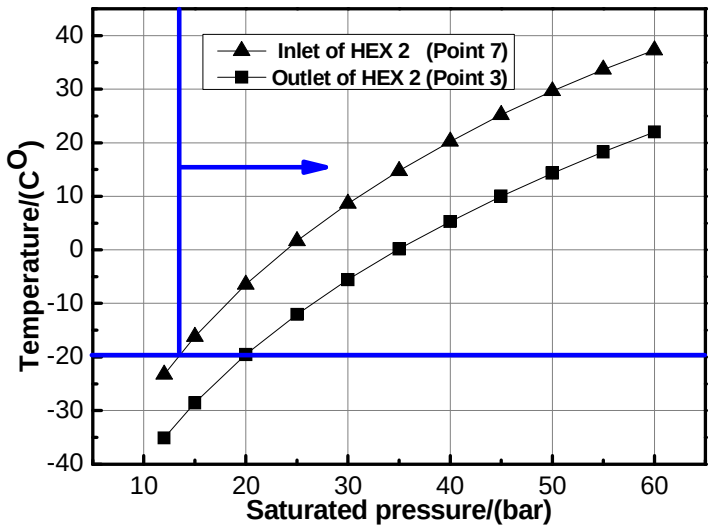

Figure 5.18 Effect of low pressure on temperature

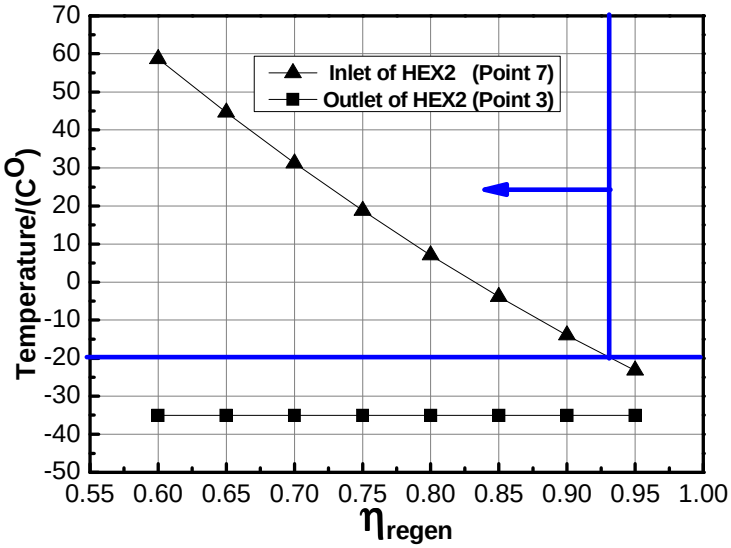

Figure 5.19 Effect of regenerator efficiency on temperature at point 7

5.3 Improvement of cold utilisation efficiency of CES system

5.3.1 Methods of parametric analysis

The following parametric analysis on cold storage efficiency in CES system is based on Rankine cycle. This is due to its similarity to Carnot cycle and the wide applications in industry.

For thermal dynamic analysis, both of the saturated pressure and temperature at engine inlet are given before the calculation. In the analysis, saturated pressure of carbon dioxide is designed as $12\,bar$. For simulating heat recovery from diesel engine, temperature of CO_2 at inlet of engine is in the range of 200~300 ^{O}C. Besides, actual efficiencies for pump, regenerator

and engine are all considered, as mentioned previously. These parameters are listed in Table 5.10.

Table 5.10 Given parameters before the thermal dynamic analysis

Saturated pressure	12 bar
Inlet temperature of engine	200~300 ^{O}C
Pump efficiency	80%
regenerator efficiency	90%
Engine efficiency	90%

With the given parameters, thermal parameters at different state points in Rankine cycle was analyzed based on the T-S diagram as shown in Figure 5.4. The methodology of the analysis was demonstrated in Table 5.11.

Table 5.11 Calculation procedure in Rankine cycle

State point	Method description	
3	P_{low}	Saturated liquid
2	P_{low}	Saturated gas
4	$s_4 = s_3$	$P_4 = P_{high}$
6	$P_6 = P_{high}$	T_6 given
1	$s_1 = s_6$	$P_1 = P_{low}$
7	Regenerator efficiency given	$P_7 = P_{low}$
8	Iteration	
5	$P_5 = P_{high}$	calculation for HEX
1act	Engine efficiency given	definition
4act	Pump efficiency given	definition

Point 3 and 2 represents saturated liquid and vapour of CO_2 under the designed saturated pressure, respectively. The temperature, enthalpy and entropy are easily obtained since the saturated pressure is given as 12 bar. For single phase fluid, the state is determined by two independent parameters of temperature, pressure, enthalpy and entropy. For point 4,

entropy is equal to that of point 3, while the pressure is obtained by measuring the outlet pressure of the cryogenic pump. so all the other state parameters can be obtained. For point 6, both temperature and pressure are given, hence, the enthalpy and entropy at point 6 can be calculated. Similarly, for point 1, pressure is given as 12 bar, while the entropy is equal to that at point 6.

For point 7, due to the isobaric process in heat exchanger, pressure is 12 bar , but the temperature is calculated in terms of the regenerator efficiency. By heat recovering of CO_2 in regenerator, the average temperature for heat absorption increases, resulting in an improved heat efficiency of the Rankine cycle and storage efficiency for the whole CES system (shown as 1-7-4-8). The regenerator efficiency is defined as:

$$\eta_{regen} = \frac{T_{1act} - T_7}{T_{1act} - T_{4act}} \tag{5.14}$$

In which, T_{1act} , T_{4act} are the temperatures at point 1 and 4 with actual efficiencies of engine and pump considered. The actual enthalpy for point 4 and 1 can be calculated by the definitions of pump and engine.

$$h_{4,act} = h_3 - \eta_{pump}^{-1}(h_3 - h_4) \tag{5.15}$$

$$h_{1,act} = h_6 - \eta_{engine}(h_6 - h_1) \tag{5.16}$$

Therefore, T_{1act} and T_{4act} can be determined by the given pressure and calculated enthalpy.

Point 5 represents the state after pre-heating by water. In the case of using electricity for heating CO_2 in super heater, the temperature at point 5 is essential for the calculation of storage efficiency. The reason is that the more heating is obtained from water, the less electricity is consumed in super heater. However, when waster heat is used in super heater, temperature at point 5 has no effect on the storage efficiency in the CES system.

In the pre-heater in the constructed CES system, carbon dioxide flows through on one side while counter-flow of hot water is pumped through on the other side. Heat transfer unit method is adopted since phase change happens in the heat exchanger. The performance of the heat exchanger (ε) and the number of transfer unit (NTU) is calculated according to the flow conditions on both side of the heat exchanger. Based on these two parameters, the temperatures of CO_2 at the inlet and outlet (point 5) of the

heat exchanger are obtained. The flow chart for the calculation is shown in Figure 5.20.

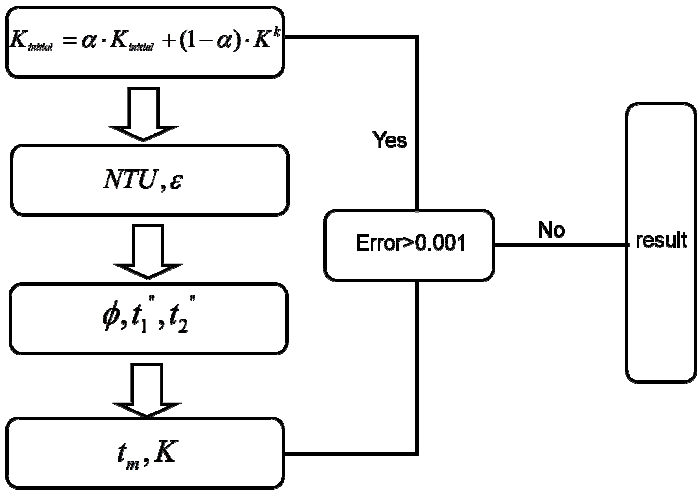

Figure 5.20 Flow chart for heat transfer calculation using heat transfer unit method

For point 8, pressure is equal to the outlet pressure of the cryogenic pump. The enthalpy can be calculated based on energy conservation in the regenerator, as expressed in Eq. (5.17):

$$h_8 = h_1 + h_4 - h_7 \tag{5.17}$$

However, by pressure and enthalpy, state of CO_2 at point 8 is not determined. It is probable that carbon dioxide is sub-cooled liquid or saturated liquid-vapour with certain vapour quality. The state of CO_2 at point 8 is determined by comparison of the calculated enthalpy at point 8 to the saturated liquid enthalpy under the pressure after pumping.

5.3.2 Thermal properties of CO_2

For obtaining state parameters at each point in the cycle, thermal properties of CO_2 covering sub-critical and super critical states need to be calculated.

Critical temperature and pressure for CO_2 are 31.1 ^{O}C and 73 bar, respectively. Therefore, super critical region covers the area with pressure higher than 73 bar and temperature more than 31.1 ^{O}C. Thermal properties of CO_2 in super critical region were largely studied by previous researchers. Lots of studies was based on the state equations of CO_2. Silva et al [197-198] developed equations for both vapor pressure and liquid density. Eslami et al [199] proposed accurate equations for liquid and liquid-mixture refrigerants, in which statistical-mechanical perturbation theory was adopted. The results were consistent with experimental data. However, all of these equations were unavailable in the condition that phase change happened.

Subsequently, Huang et al [200] developed accurate state equations for carbon dioxide. All of sub-critical and super critical states were covered in the model. Therefore, thermal properties under different states can be precisely predicted.

Due to the complexity of the proposed equations, commercial software (such a REFPROP) is used instead for obtaining thermal properties of CO_2. However, regarding the interaction of thermal properties at different state points in Rankine cycle, software is less efficient and not suitable for dealing with iteration processes (e.g. point 8). Therefore, computer codes based on CO_2 properties were developed for finding the parameters. T. Honda and R. Akasaka developed codes in terms of CO_2 equations for predicting thermal properties of carbon dioxide. On the basis of their codes, program for the CES based on Rankine cycle has been developed by the author. Specifications of the program can be seen in the appendix.

5.3.3 Parametric study

In the above, methodology for parametric analysis and calculation of thermal properties of carbon dioxide are discussed. On the basis of these, parametric study on cold storage efficiency is carried out. In the following study, optimal parameters for obtaining higher storage efficiency in the CES system are theoretically analyzed.

5.3.3.1 Effect of high pressure

High pressure represents the pressure at the outlet of cryogenic pump. The effects of high pressure on heat efficiency, storage efficiency and the dynamic power are investigated, as presented in Figure 5.21 and Figure 5.22. It is seen that the heat efficiency (η_h) and the dynamic power generation increased with the improving of the high pressure after pumping. For the storage efficiency (η_{EES}) in CES system, it increases before the pressure reaches 65 bar but decreases subsequently with further increasing of pressure. The decreased storage efficiency is explained by the largely increased demand of energy consumption in the super heater after the pressure of 65 bar . According to the calculation, the maximum capacity of the system for power generation in peak time is about 4.36 kW . This is at the expense of consuming off-peak electricity of 13 kW . Therefore, the largest cold storage efficiency in this case is 33.3%.

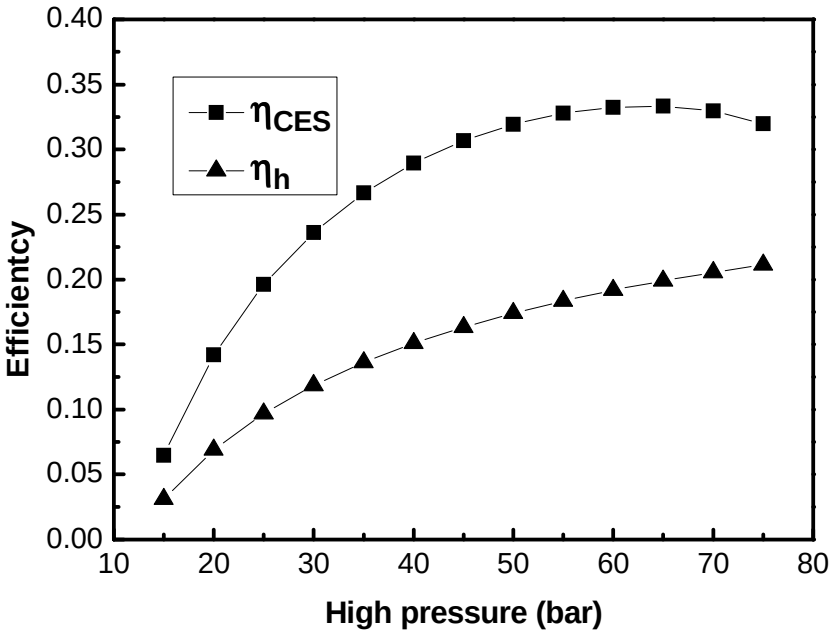

Figure 5.21 Effect of the high pressure on efficiencies

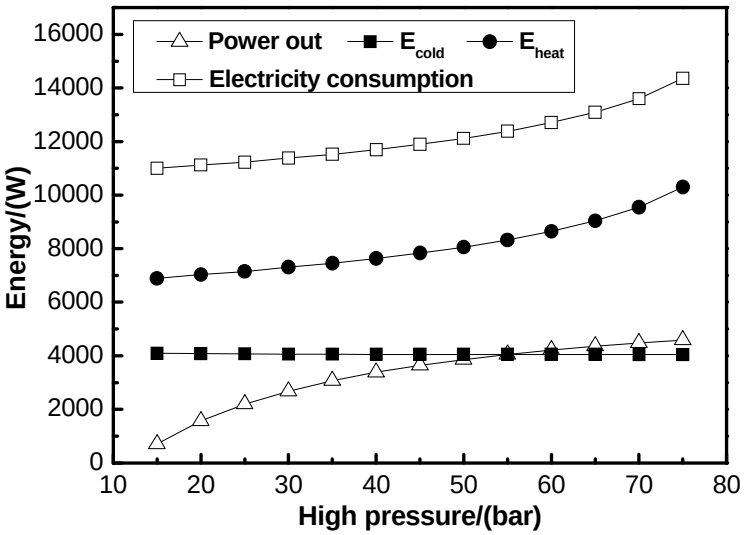

Figure 5.22 Effect of the high pressure on energy input and output

The above results are based on the hypothesis of utilizing electricity for heating up CO_2 in the super heater. However, as mentioned before, when waste heat or solar energy is utilized instead of off-peak electricity in the super heater, the predicted efficiency and power will be different.

The results under two different cases are compared in Figure 5.23 and Figure 5.24. It is found that the storage efficiency for CES system with waste heat utilized in super heater is much bigger than that in the previous case. In the condition of consuming electricity in super heater, with increasing of pressure, electricity consumption in refrigerator (E_{cool}) remains constant, while electricity consumption in super heater (E_{heat}) increases largely, as

shown in Figure 5.24. However, the amount of electricity consumption can be equivalently obtained from waste heat or solar energy. Since waste heat for heating up CO_2 is not taken into account for the calculation, the storage efficiency is largely improved.

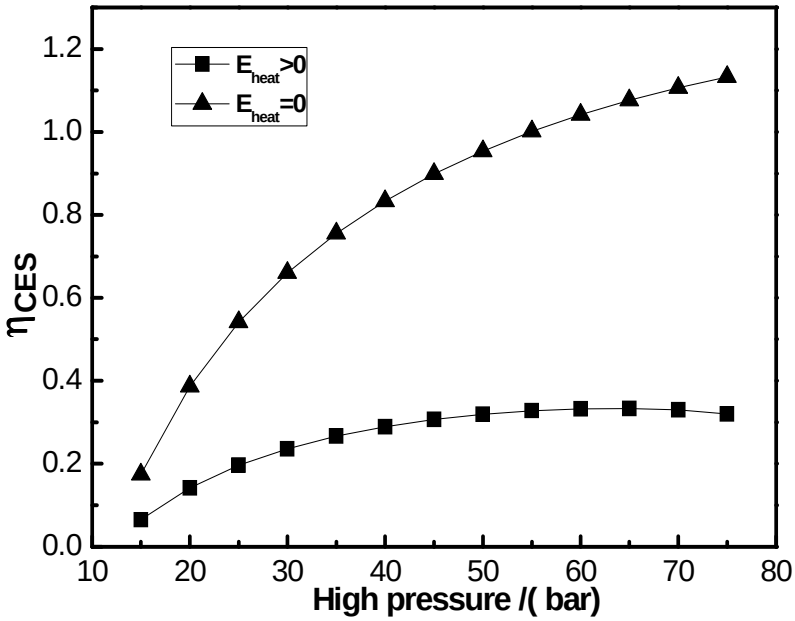

Figure 5.23 Comparison of storage efficiency under different heat source in super heater

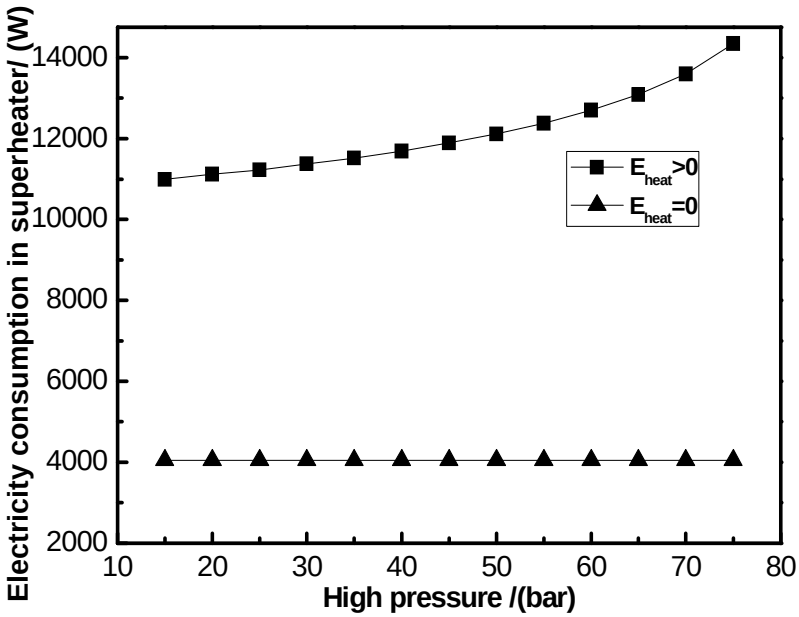

Figure 5.24 Comparison of electricity consumption under different heat source in super heater

5.3.3.2 Effect of saturated pressure

Saturated pressure is the liquid-vapour pressure of carbon dioxide in the designed vessel. Similarly, results under two different cases are compared, as shown in Figure 5.25~5.28.

When electricity is used in super heater, the results are presented in Figure 5.25~5.26. It is shown that lower saturated pressure results in higher heat efficiency and storage efficiency. This is due to the lowered endothermic temperature in the Rankine cycle. From Figure 5.26, it is seen that dynamic power is reduced with the increase of saturated pressure. This is explained by the increased energy consumption by the cryogenic pump in the Rankine cycle.

However, according to the phase diagram of CO_2, liquid carbon dioxide appears with pressure higher than 10 bar. Therefore, the lowest saturated pressure in the CES system should be restricted to be higher than 10 bar, for guaranteeing the cryogenic pump not being damaged.

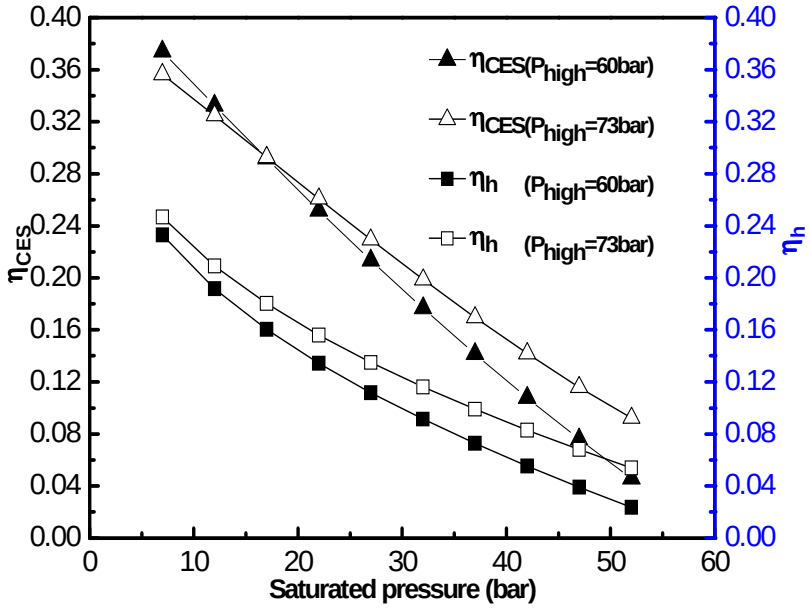

Figure 5.25 Effect of saturated pressure on efficiencies

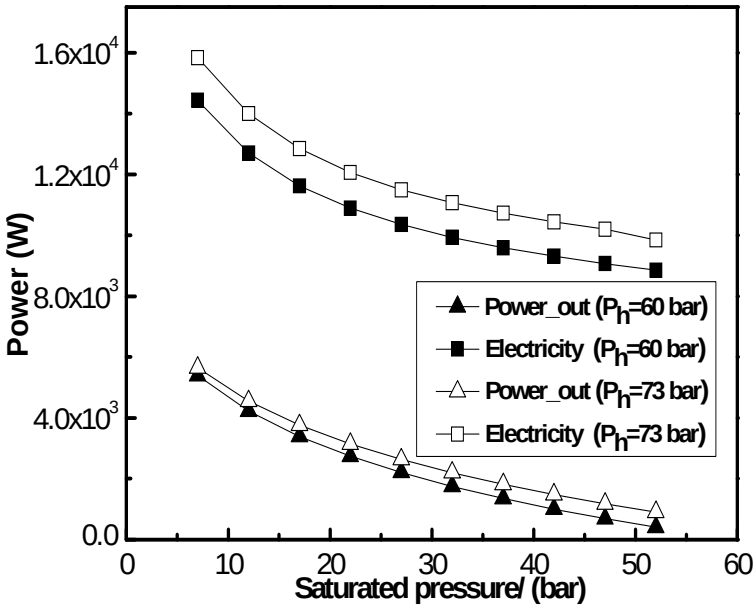

Figure 5.26 Effect of saturated pressure on dynamic power

In comparison, provided that waste heat or solar energy is utilized in super heater, the predicted results are shown in Figure 5.27~5.28. It is found that heat efficiency of Rankine cycle decreases with increasing of the saturated pressure, but it is not affected by heat sources used in the super heater.

However, the storage efficiency increases with the increase of saturated pressure. The trend is opposite to that in the previous case. Because without accounting for the electricity consumption in super heater (E_{heat}), effect of electricity consumption by freezer (E_{cool}) becomes significant. With increasing of the saturated pressure, CO_2 temperature at point 2 (T_2) is increased. Regarding the caused increasing of COP of the freezer, E_{cool} is largely reduced.

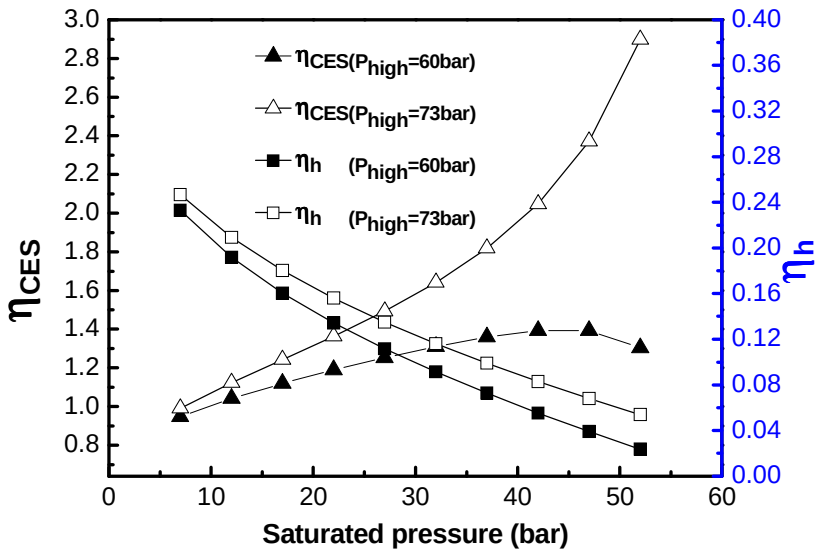

Figure 5.27 Effect of saturated pressure on efficiencies ($E_{heat} = 0$)

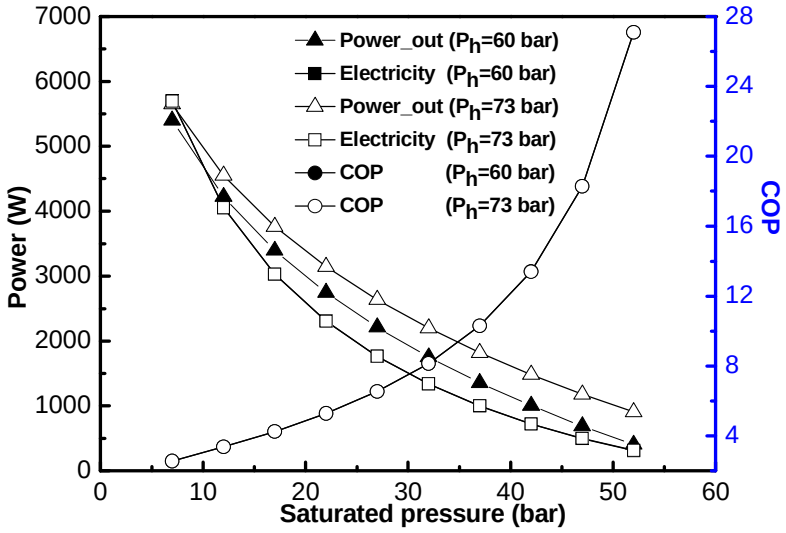

Figure 5.28 Effect of saturated pressure on power output ($E_{heat} = 0$)

The discussion above shows the distinguished results under different heat sources in super heater. For simplifying the discussion, the following analysis is based on the assumption that electricity in off-peak time is utilized in the super heater ($E_{heat} \neq 0$).

5.3.3.3 Effect of temperature at the inlet of engine

Temperature at the inlet of engine is the temperature of CO_2 before entering engine. The power generation by the engine mainly depends on the inlet pressure and temperature. Under a given pressure (equal to the pressure after pumping), the effect of inlet temperature of engine is investigated, as presented in Figure 5.29~5.30. It is seen that the heat efficiency of the Rankine cycle and the power generation in the CES system increases with improving of the inlet temperature. However, the cold storage efficiency decreases with inlet temperature increasing, as seen in Figure 5.29. It is explained that electricity consumption in super heater is largely increased, as demonstrated in Figure 5.30.

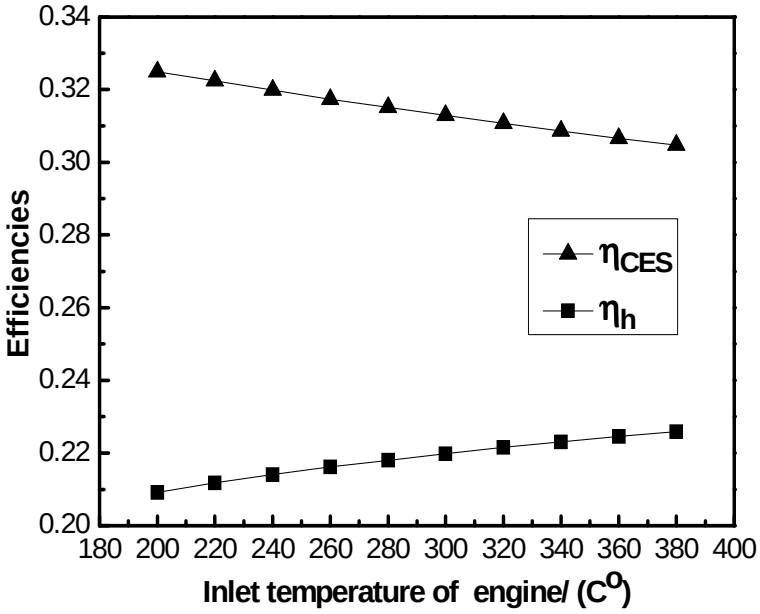

Figure 5.29 Effect of inlet temperature on efficiencies

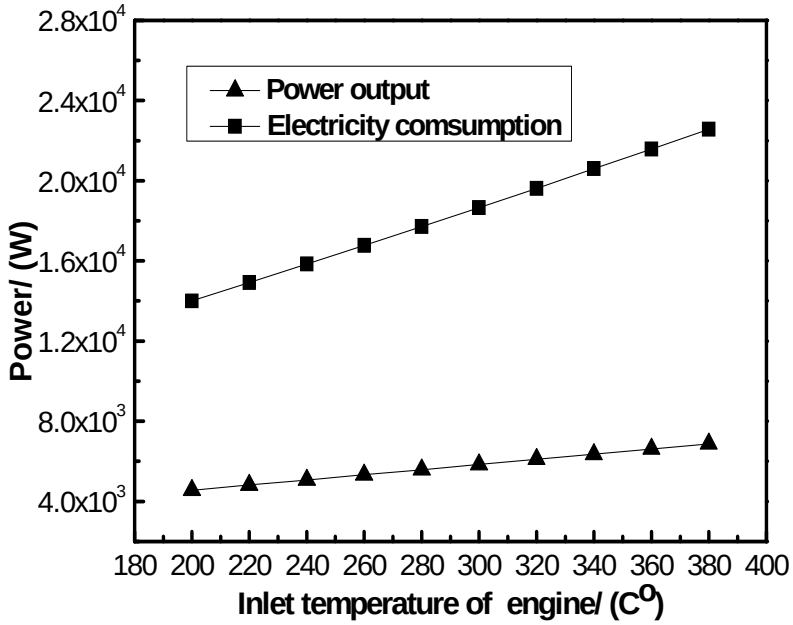

Figure 5.30 Effect of inlet temperature on power output

5.3.3.4 Effect of mass flow rate of CO_2

The effect of mass flow rate of CO_2 is also investigated. The results are shown in Figure 5.31 and Figure 5.32. The heat efficiency is not relevant to the mass flow rate of CO_2. However, it is noted that with an increase of the mass rate, the outlet temperature of hot heat exchanger (HEX 1) is decreased, leading to more electricity consumption under the same inlet temperature of engine, as shown in Figure 5.32. It is seen that with the increase of mass flow rate, increased electricity consumption is bigger than

increase of power output. Therefore, the storage efficiency is lowered, as shown in Figure 5.31.

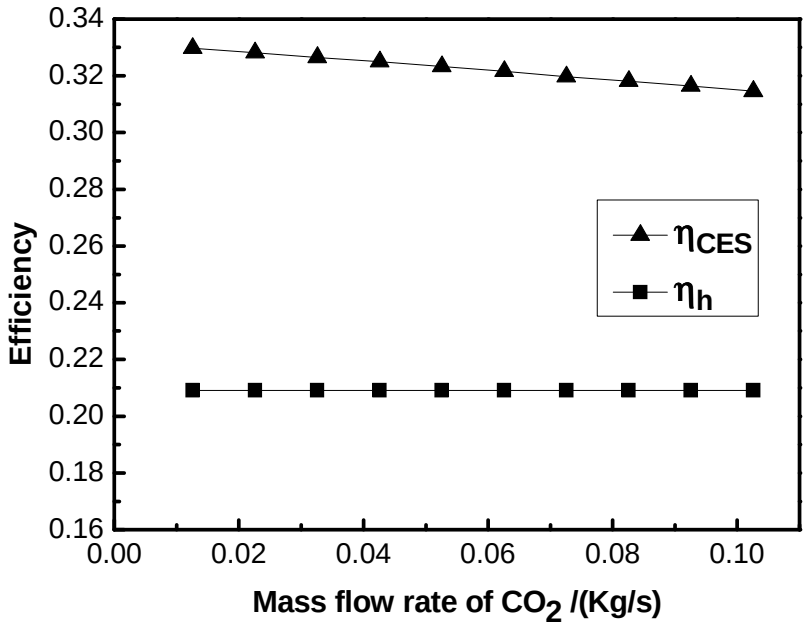

Figure 5.31 Effect of mass flow rate on efficiencies

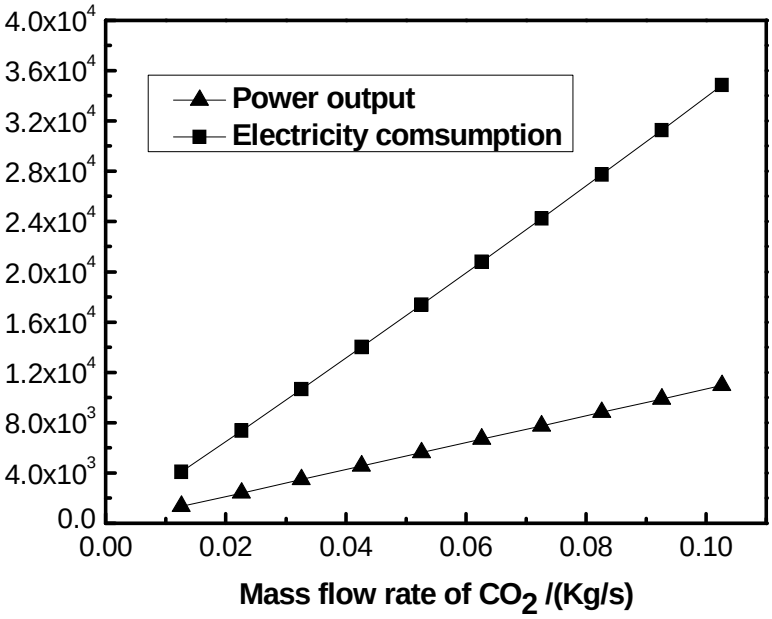

Figure 5.32 Effect of mass flow rate of CO_2 on power output

5.3.3.5 Effect of efficiencies of components in Rankine cycle

The actual efficiencies of pump, regenerator and engine are considered in the calculation. The investigations on the effect of these efficiencies in the CES system are presented in Figure 5.33~5.40.

From Figure 5.33 and Figure 5.34, it is seen that the effect of pump efficiency becomes less significant when the pump efficiency is higher than

20%. For cryogenic pump that is widely used, the pump efficiency is generally in the range of 70% ~ 85%. Therefore, the effect of pump efficiency on the calculation of storage efficiency can be neglected in reality.

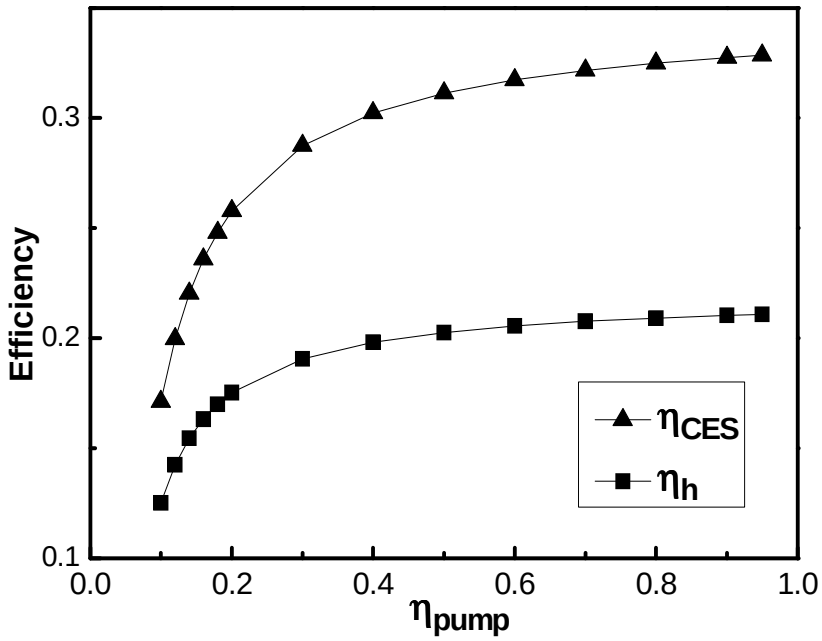

Figure 5.33 Effect of pump efficiency on storage efficiency

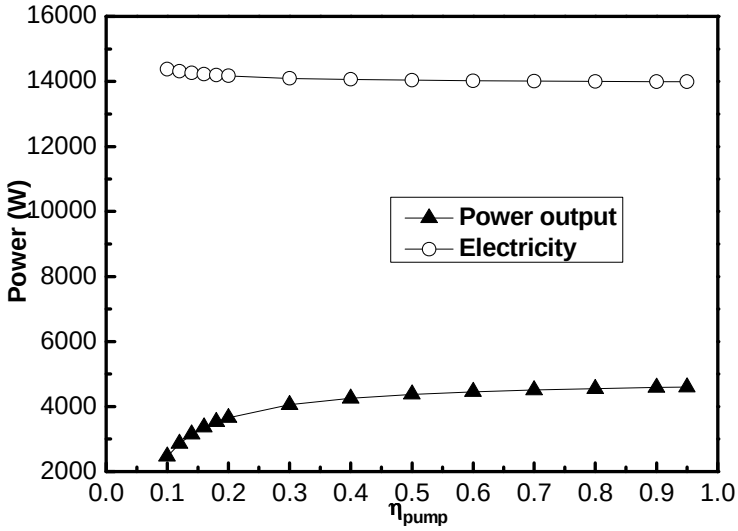

Figure 5.34 Effect of pump efficiency on power output

The effect of regenerator is demonstrated in Figure 5.35 and Figure 5.36. It is found that the regenerator has no effect on heat efficiency of the Rankine cycle and the dynamic power generation in the CES system. However, higher regenerator efficiency results in increased storage efficiency. The reason is that quantity of electricity consumption in super heater is reduced due to heat recovery of CO_2. It is concluded that higher regenerator

efficiency increases the capacity of heat recovery of the CES system, leading to reduced demand of electricity consumption in super heater.

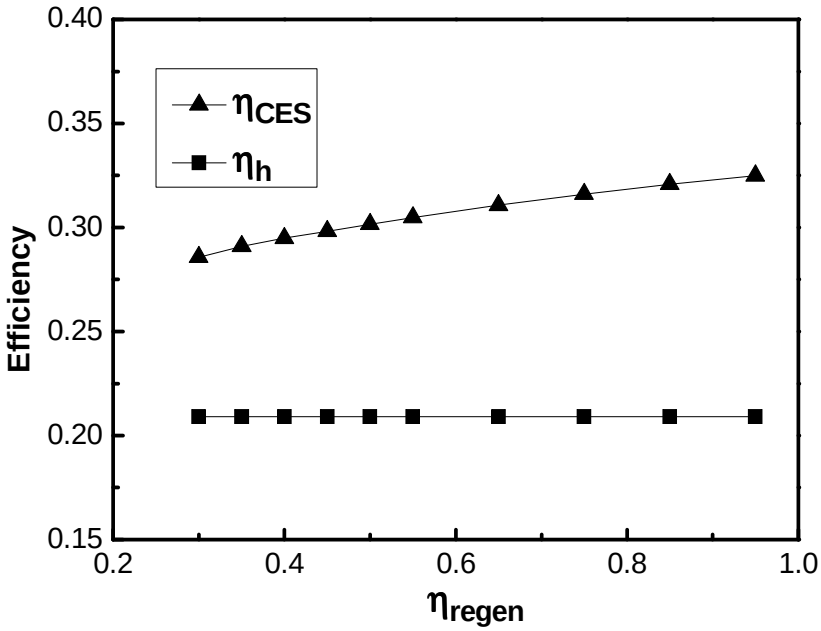

Figure 5.35 Effect of regenerator on efficiencies

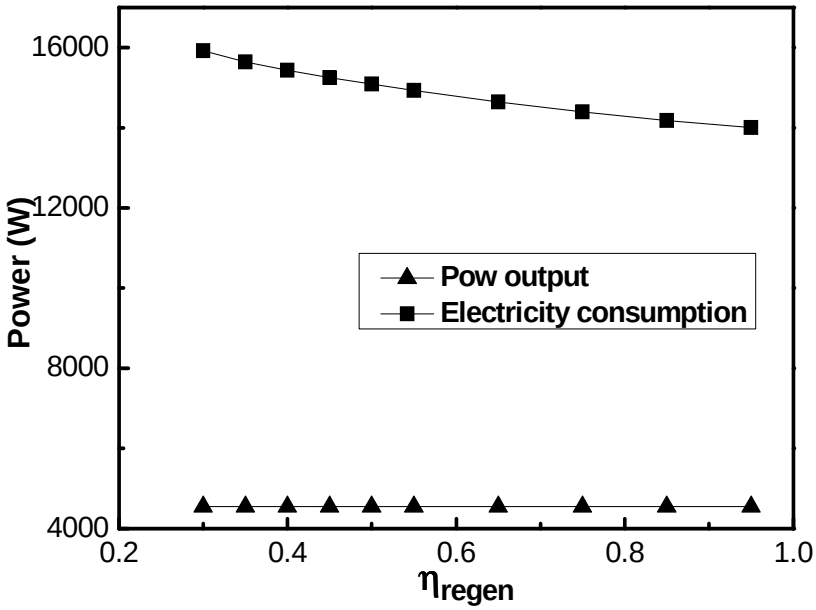

Figure 5.36 Effect of regenerator on power output

The effect of the engine efficiency is demonstrated in Figure 5.37 and Figure 5.38. It is seen that all of the heat efficiency, storage efficiency and the dynamic power generation increase with the improving of engine efficiency. The consumed electricity in super heater (E_{heat}) is not relevant to the change of engine efficiency. However, electricity consumption by freezer (E_{cool}) is

slightly affected by the engine efficiency, since the enthalpy at point 7 (h_7) is varied according to Eq. (5.9).

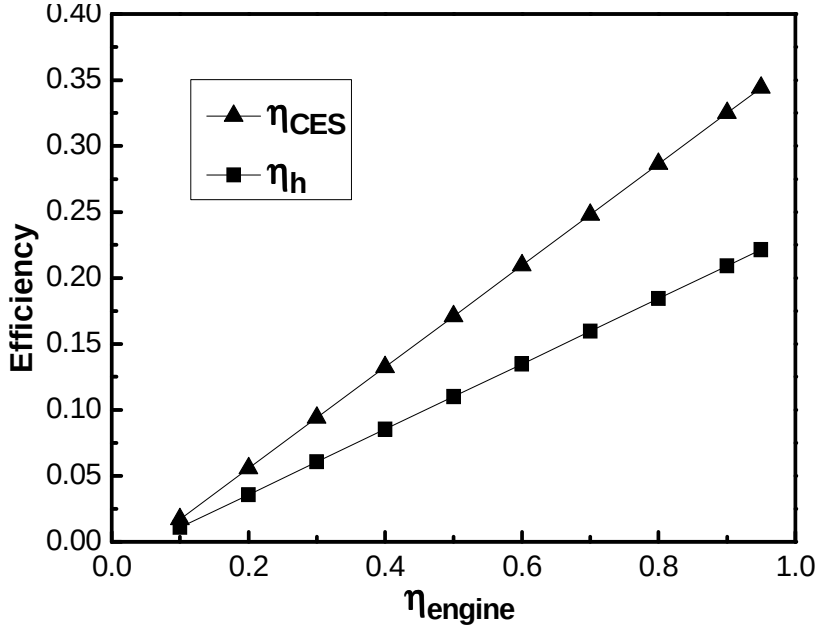

Figure 5.37 Effect of engine efficiency on efficiencies

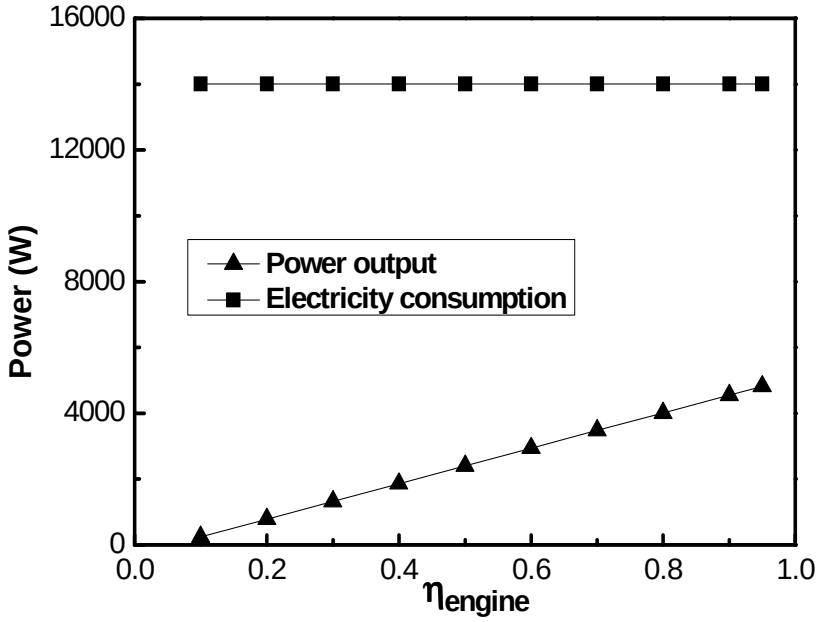

Figure 5.38 Effect of engine efficiency on power output

The effect of the refrigerator efficiency is presented in Figure 5.39 and Figure 5.40. It is found that the refrigerator efficiency has no influence on heat efficiency and power generation. However, the storage efficiency increases while the electricity consumption is reduced with the increase of the refrigerator efficiency.

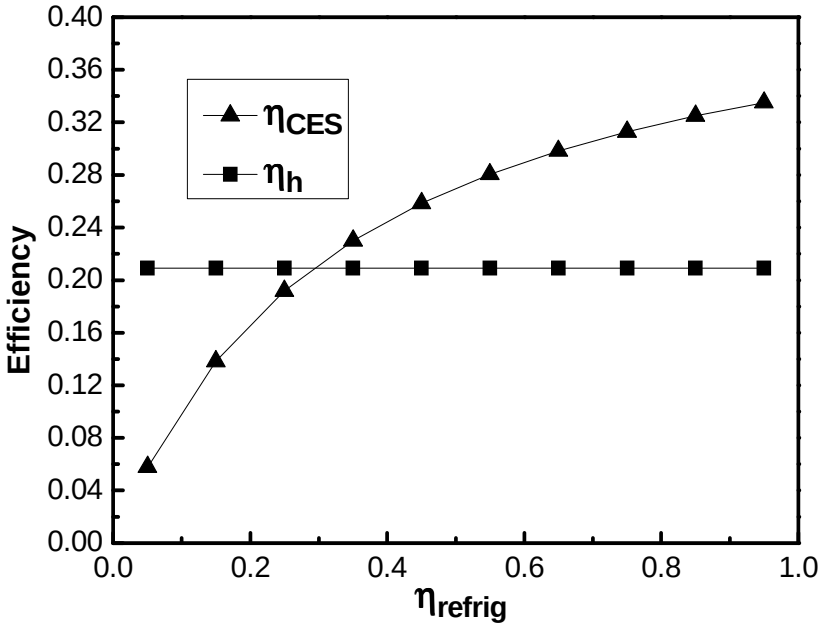

Figure 5.39 Effect of refrigerator efficiency on efficiencies

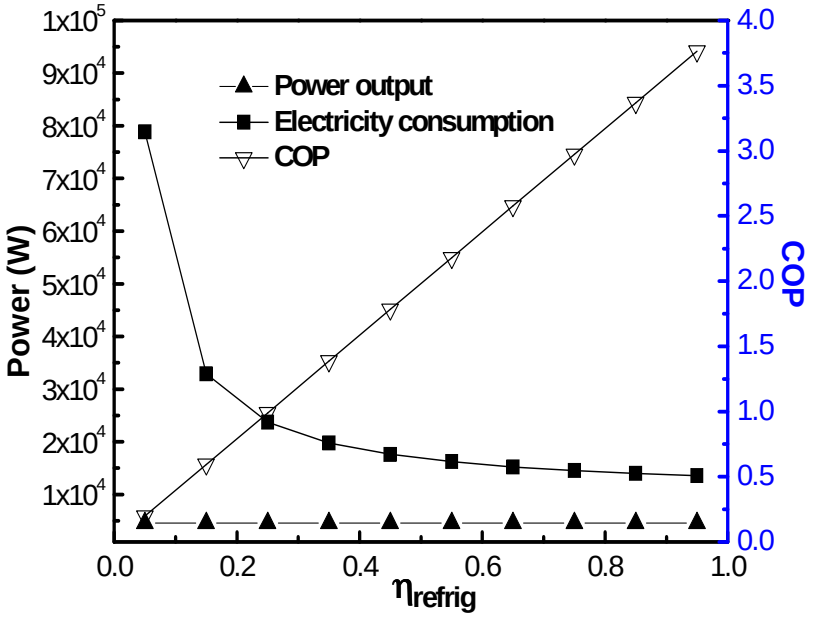

Figure 5.40 Effect of refrigerator efficiency on the power output

The effect of environment temperature is also conducted, as shown in Figure 5.41 and Figure 5.42. It is indicated that improved environment temperature results in a decreased storage efficiency of CES, as seen in Figure 5.41. This is because more off-peak electricity is consumed in the freezer due to the sharply decreased COP, shown in Figure 5.42. However, it is obvious that both the heat efficiency and dynamic power generation in the CES system are not affected.

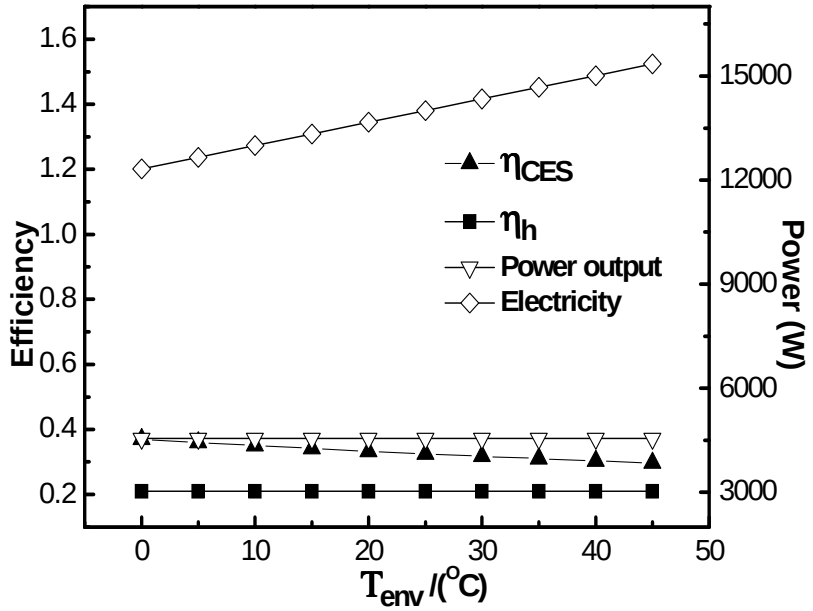

Figure 5.41 Effect of environment temperature

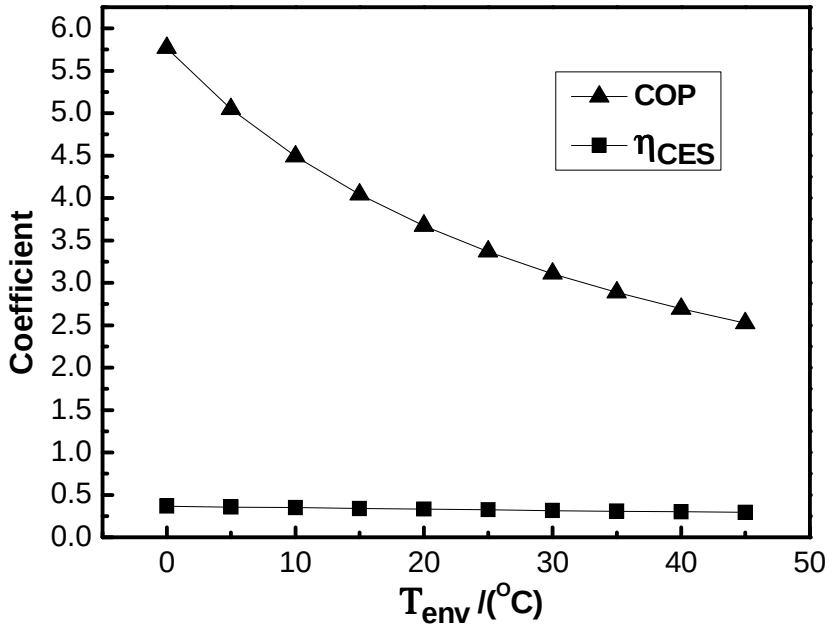

Figure 5.42 Performance of refrigerator (COP) affected by environmental temperature

The default parameters for the calculation are listed in Table 5.12.

Table 5.12 Basic parameters used in the parametric study

$P_h = 73bar$	$P_l = 12bar$	$T_{engine} = 200C^O$	$m_{co2} = 0.0426kg/s$
$\eta_{pump} = 0.8$	$\eta_{regen} = 0.95$	$\eta_{engine} = 0.9$	$\eta_{refig} = 0.85$
$T_{envi} = 25C^O$	$T_{H2O} = 37^oC$	$m_{H2O} = 0.1kg/s$	$C_P = 4200\ J/(kg \cdot K)$

5.4 Summary of this chapter

This chapter is focused on the cold utilisation through Rankine cycle. The feasibility of small-scale CES system is experimentally studied. PCM temperature, charge time and electricity consumption rate during the charge period are discussed. For analyzing the feasibility of cold utilisation in an open-cycle Rankine cycle, the flow rate of cryogenic pump and temperatures at the inlet and outlet of the cold heat exchanger (HEX 2) are studied.

Methodology for the thermal analysis in the Rankine cycle is particularly explained. Subsequently, thermal properties of carbon dioxide covering the sub-critical region are introduced. Based on these, parametric study for obtaining higher storage efficiency in the CES system is carried out.

It is concluded that the efficiencies and power generation are significantly affected by utilizing different heat sources in the super heater. Compared to the case of using off-peak electricity in super heater, the predicted storage efficiency is much bigger when waste heat or solar energy is utilized.

Besides that, it is found that the with operating pressure of 65 bar after pumping, the storage efficiency is as the largest as 43.9%, in the condition that the efficiencies of pump, regenerator, engine and refrigerator are all equal to 100%. The results are shown in Figure 5.37. However, with consideration of the actual efficiencies, the storage efficiency is generally between 30%~40%.

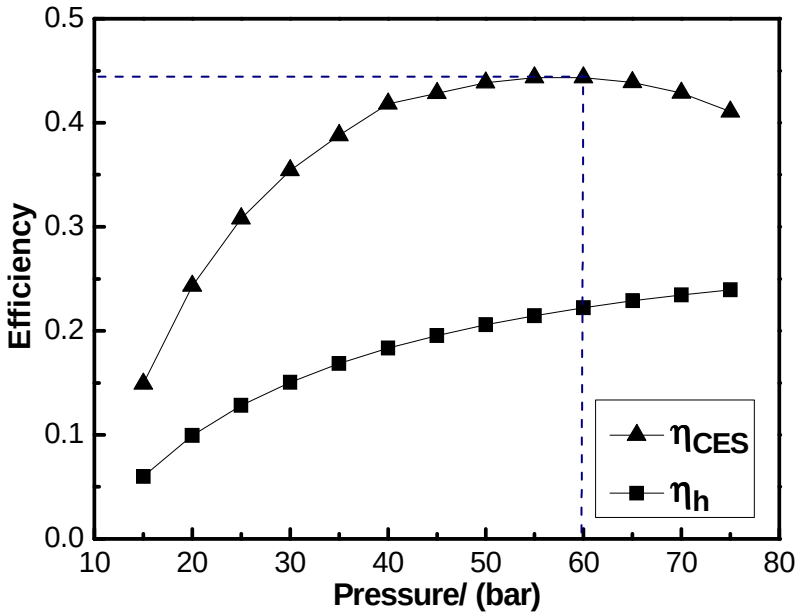

Figure 5.43 CES efficiencies in an ideal situation

It is also concluded that by increasing the operating pressure and efficiencies of pump, regenerator, engine and refrigerator, or by decreasing the saturated pressure, mass flow rate of CO_2, temperature at the inlet of engine and environmental temperature, the cold storage efficiency in the constructed CES system can be improved.

Chapter 6
Cold to power conversion using a piston based engine system

Engine is an essential component for cold to power conversion in a CES system. This chapter presents a new valve scheme in a piston based engine system with a new valve-control method demonstrated. Power generations by two engines with different size are compared. The influence of the efficiency of engine on the overall energy storage efficiency is further discussed.

6.1 An engine system for cold to power conversion

6.1.1 Introduction of the engine system

The block diagram of the CO_2 cycle in CES system is presented in Figure 6.1. After being pumped and heated up, CO_2 is under high operating pressure and temperature and will expand in engine for power generation. The proposed CES system has a designed electricity output of 5 kW and can run for more than 1 hour. Since the CES system can store electricity of more than 12 kWh, the storage efficiency of the CES system is evaluated as around 40%. The basic parameters of the constructed CES system is as shown in Table 6.1.

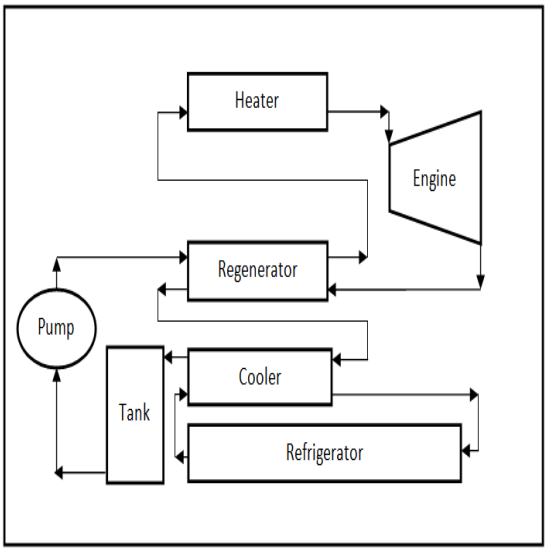

Figure 6.1 Schematic diagram of the experimental system

Table 6.1 Basic parameters of the CES system

CES system	Designed value
Designed electricity output	5 kW
Storage off-peak electricity	More than 12 kWh
Duration of operation (peak time)	~ 1 hour
Engine inlet temperature	200 – 300 degree
cold temperature	-40 degree

As the critical part in the designed CES system, an piston based engine system is proposed, as shown in Figure 6.2. The new engine system is mainly composed by an engine, a motor, a new valve scheme and the controlling modules.

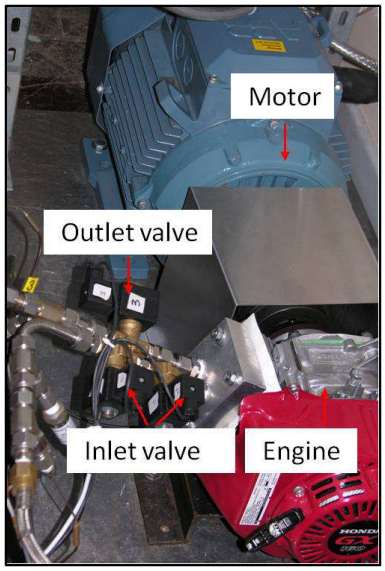

Figure 6.2 Picture of the new engine system

ABB motor drive is selected as the torque and speed measurement unit in the engine system, as shown in Figure 6.3. It is a digital controlled servomotor system that can precisely control the rotation of the motor. The principle of the motion control is as follows:

- Monitoring position of the rotor. The rotor of the motor drive is directly connected to the operating drive shaft. A position sensor in the motor is used to continuously monitor the rotor's position.
- Feeding back the position information to the control unit, where the measured position is compared to the position required at that instant by the pre-programmed travel curve.

- Sending out control signals to the converter unit. These signals will drive the motion of the circuit breaker and therefore control the rotation of the motor.

The torque and speed of the motor are measured and shown on a hand panel connected to the ABB motor drive. The specifications of the ABB motor drive are listed in Table 6.2.

Figure 6.3 Picture of the ABB motor drive system

Table 6.2 Specifications of the ABB motor drive in engine system

Name	Motor Drive
Supplier	ABB AB
Product Code	Motor Drive ™ ACS800
Type	Digital one point alarm
Encoder	90HA-25-080C1BRU-1024
Power (kW)	7.5
Working temperature (^{o}C)	-50~40
Voltage of power Supply (V)	110 or 240

The engine used in the CES system is a conventional engine with modifications and the use of a valve scheme that can control the process of gas entering the chamber. The picture of a conventional engine is shown in Figure 6.4. Mechanical valves are used at the inlet and outlet of the chamber. Through the movement of cam linking to the shaft of the engine, these valves are opened and closed periodically. In this case, high pressure

gas can enter the chamber for power generation, while the exhaust gas can be exhausted from the system after expanding.

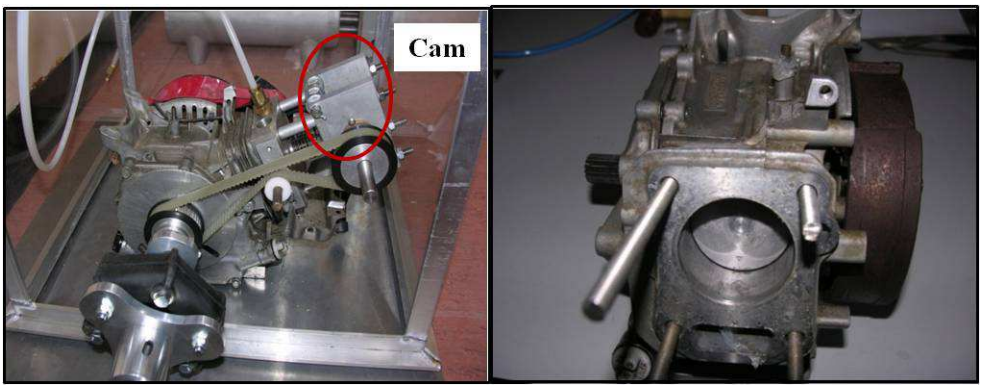

Figure 6.4 A conventional piston based engine

The shape of the shaft is specially designed for controlling the opening and closing time of the valves. However, this type of engine has two major problems:

(1) Gas leakage. The working process in engine can be divided into three stages: gas entering, expansion process and gas exhausting. These stages can be demonstrated by Figure 6.5. During the gas entering, V1 is open but V2 is close; subsequently, in the expansion process, both V1 and V2 are close; but during the gas exhausting process, V1 is close but V2 need to be open. However, the tightness of the chamber is not as good as required by mechanical operation of the valves. This causes leakage of high pressure gas, leading to reduced power generation.

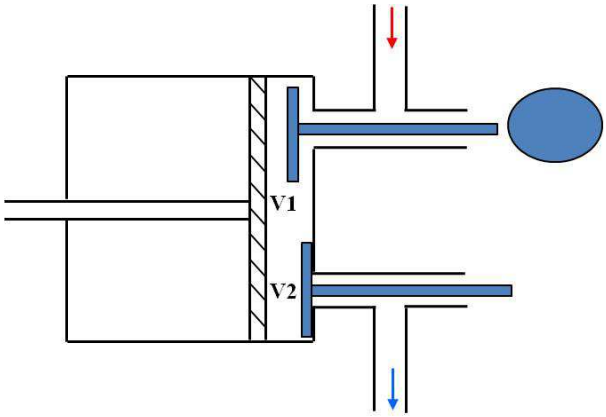

Figure 6.5 Gas leakage in conventional engine

(2) Inflexible time control. As mentioned above, the time for gas entering, expansion and exhausting is dependent on the particular shape of the shaft. As long as the shaft is designed, the opening and closing operations on valves are at definitive time. However, time adjustment in terms of different

dynamic conditions of high pressure gas (e.g. pressure, temperature and mass flow rate, etc) is required.

However, both the leakage issue and inflexible time control for gas entering the engine can be addressed by the engine with a new valve scheme. The valve scheme and the valve control method will be introduced in the following section.

6.1.2 A new valve scheme and valve control method

The solenoid valves are installed at the inlet and outlet of the engine. The specific structure is presented in Figure 6.6. This kind of valve is widely used for shutting off, releasing, dosing, distributing or mixing fluids. The advantages of the solenoid valves include fast switching, high reliability without leakage, long service life, good medium compatibility of the materials, low control power and compact design.

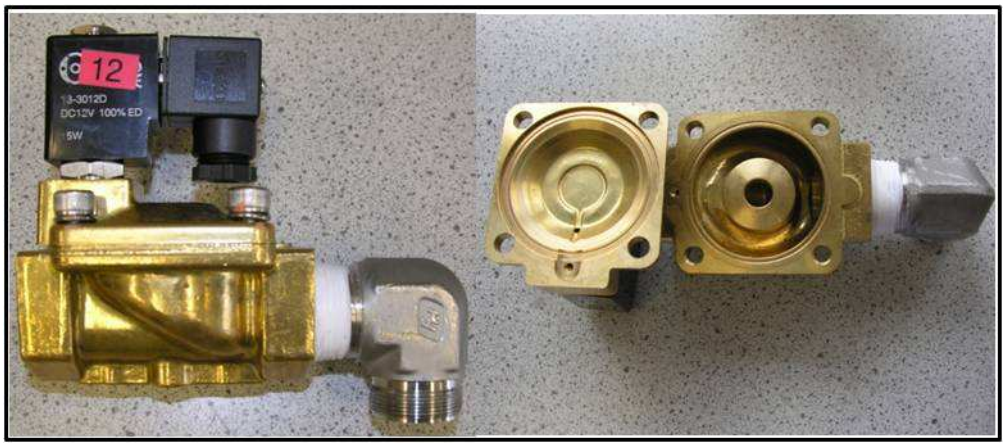

Figure 6.6 The specific structure of the solenoid valve

Two types of solenoid valves are tested. For small valve of 1.8 mm diameter, the reflection time for opening and closing are 15 ms; while for large valve with diameter of 12 mm, the reflection time is improved to 50 ms. It is indicated that single valve is not able to be used for time controlling of gas entering the chamber under high motor speed. For instance, for motor speed under 240 rpm, the round time is 25 ms, but the total reflection time for one-round opening and closing operations on the small and large valves is 30 ms and 100 ms, respectively. Consequently, in that case, time controlling on gas entering and leaving the chamber through the solenoid valves becomes invalid.

As a result, in order to flexibly control the gas behaviours, two solenoid valves are connected in series at the inlet of the engine. In the multi-valve

system, states of valves are tracked by recording the supplied electrical voltage. When voltage is 0 $\mathrm{V}$and $4\,\mathrm{V}$, the valve is regarded as in close and open state, respectively. The supplied electrical voltage is recorded by Labview program for tracking the states of the valve. Actions of valves in one cycle with motor speed of 60 rpm are shown in Figure 6.7. V1 and V2 are connected in series at the inlet, while V3 is connected at the outlet. By controlling the actions of V1 and V2, the entering time and expanding time of the gas can be controlled. It is noted that in one circle's time (1 s), the total opening time is about 140 ms, while the expanding time is approximately 400 ms.

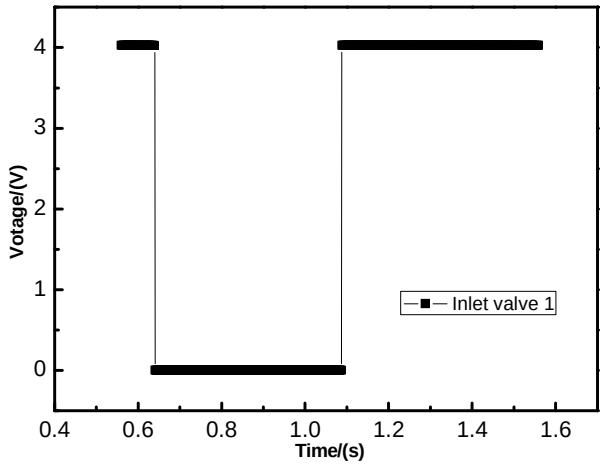

(a) Inlet valve 1

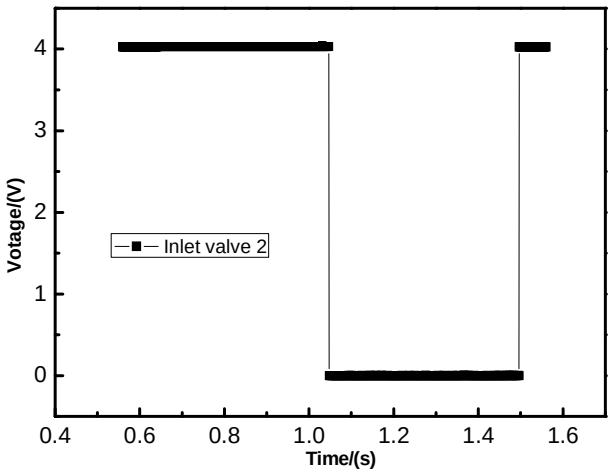

(b) Inlet valve 2

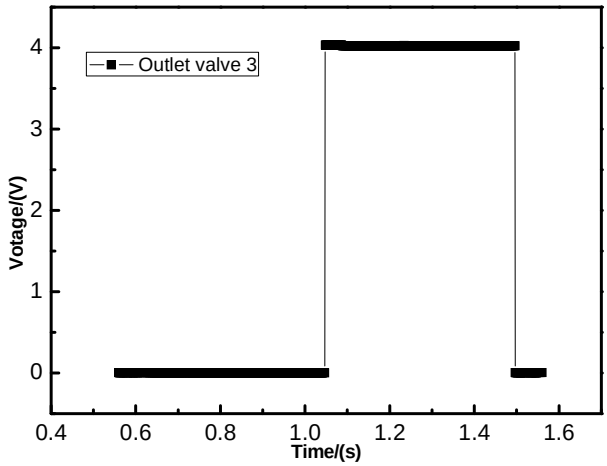

(c) Outlet valve 3

Figure 6.7 Actions of valves in one cycle with motor speed of 60 rpm: (a) Inlet valve 1; (b) Inlet valve 2; (c) Outlet valve 3

For precisely controlling opening and closing time, count setting method is used. Specifically, the circle of the shaft in engine is equally divided into 320 parts. Each part is called one count. When the piston is at the top dead centre (TDC), an index is marked at the bottom of the shaft where the 0th count is scheduled. In the controlling modules, opening and closing operations on valves are associated with counts by initiating electrical voltage for all of the 320 counts in the circle of the shaft. Consequently, by resetting the electrical voltage on different counts, the opening and closing time for each valve can be controlled.

In the multi-valve system, provided that two solenoid valves at the inlet are open simultaneously during certain period, the corresponding rotating angle of the shaft during this period is called p-crank angle. For instance, V2 is set open from 0th count to 180th count, while V2 is set open from 210th count to 30th count, as a result, the p-crank angle is $30\times\frac{360}{320}\approx 33.8^{o}$ (30 counts from 0th count to 30th count). The concept of p-crank angle is demonstrated in Figure 6.8.

As shown in Figure 6.8, in the opening time (t_1), piston moves from the TDC to the shown location (x); while at the time of half circle ($t/2$), the piston reaches the bottom dead centre (BDC). Consequently, the relation of time and piston location can be approximately formulated as in Eq. (6.1):

$$\frac{t_1}{t/2}=\frac{x}{L}=\alpha \tag{6.1}$$

In which, α is the proportion of opening time to half circle time of the engine. In this case, p-crank angle can be expressed as:

$$p-crank\ angle = 180^{o} \cdot \alpha \tag{6.2}$$

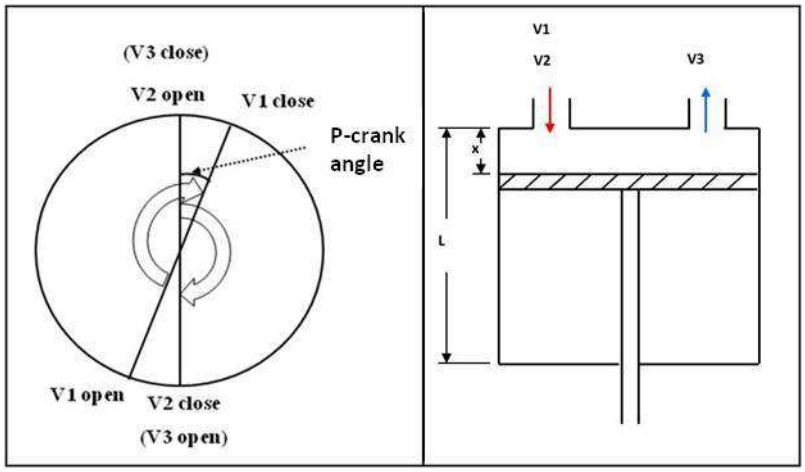

Figure 6.8 Formation of p-crank angle by count setting

It is pointed out that with the increase of p-crank angle, the opening time of the inlet is longer. This indicates more mass of gas enters the chamber. However, due to the reduced volume for expanding, the specific power (power generation per unit mass) is reduced. Due to the significant effect on power generation, p-crank angle controlling in terms of thermal dynamic conditions of gas needs to be investigated. In the following parts, both experimental and theoretical studies are carried out.

6.2 Torque and power analysis based on the engine system

6.2.1 Basic understanding of torque and power

The relation of the electricity, motor/ generator and engine is demonstrated in Figure 6.9. One can see that the motor/ generator can be driven by both of the electricity and engine. As a result, when the electricity consumption (EC) is larger than the engine power (EP), the rotating device acts as a motor; while when EC is smaller than EP, it becomes a generator in the system.

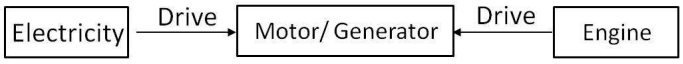

Figure 6.9 The motor-driven mode in the engine system

The block diagram of the engine and ABB motor drive system is shown in Figure 6.10. Due to the special motor driving mode, the net power consumption or generation of the motor/ generator can be regarded as the combined contribution of electricity consumption (EC, written as Pow_1), and engine power (EP, written as Pow_2). Assuming that there is no energy loss on the motor/ generator, the net electricity output of the motor (EM) can be calculated as $Pow_1 - Pow_2$. It is noted that when the value of EM is negative, the engine and ABB motor drive system will have a net electricity generation.

Correspondingly, the torque on the motor from electricity and engine can be written as Tor_1 and Tor_2, respectively. The net torque on the motor is expressed as $Tor_1 - Tor_2$.

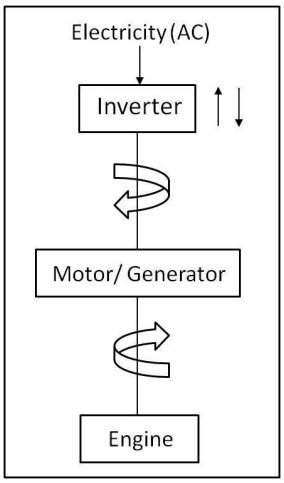

Figure 6.10 The block diagram of the engine and ABB motor drive system

6.2.2 Method for torque and power analysis

In the experiments, the data shown in the hand panel is torque percentage, which is defined as the ratio of the torque on the motor in current conditions to the maximum torque ($Tor_{\max}$) on the motor. The rated power of the ABB motor drive system ($Pow_{\max}$) is 11 kW, under which the motor has the maximum speed ($\omega_{\max}$) of 2900 rpm. Therefore, the maximum torque on the motor can be calculated as:

$$Tor_{\max} = \frac{Pow_{\max}}{\omega_{\max}} = 36.2N \cdot m \tag{6.3}$$

Based on the definition of torque percentage, the absolute torque on the motor can be obtained.

In terms of the understanding of the torque on the motor in the previous section, the torque on the motor in the condition that motor is not driven by engine can be regarded as the torque by electricity consumption (Tor_1).

Three different experiments for obtaining Tor_1 are conducted under the following situations:

- Case 1: motor is disconnected with engine;
- Case 2: motor is connected with engine but the outlet of engine keeps open;
- Case 3: moter is connected with engine and both of the inlet and outlet of the engine are closed. The start torque and end torque in a cycle time is recorded under this situation.

The results are shown in Figure 6.11. One can see that the measured torque percentage on the motor by electricity consumption (Tor_1) has an approximate value in case 1 and case 2. With the increase of motor speed, the value of Tor_1 decreases slightly. The measured Tor_1 has the maximum value of 14.3% during the experiments.

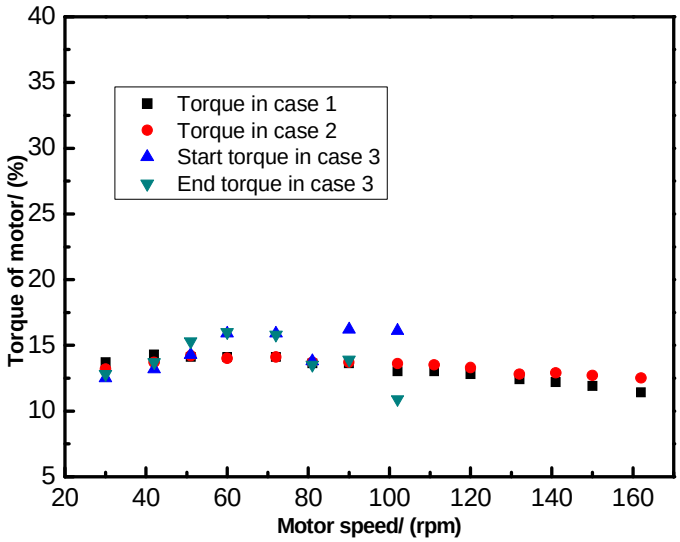

Figure 6.11 The measured torque of motor (T1) in different cases

However, when motor is driven by both electricity and engine power, for example, in the case that high pressure gas is supplied to the engine, the torque on the motor can be regarded as the net torque ($Tor_1 - Tor_2$). In these experiments, the torque percentage shown on the hand panel is ($Tor_1 - Tor_2$), leading to the net electricity consumption or generation of the engine and ABB drive system.

When Tor_1 and ($Tor_1 - Tor_2$) are obtained by the above experiments, the torque by engine power (Tor_2) can be calculated. This represents the contribution of engine for driving the motor seperately.

Based on the above torque analysis, power can be calculated by Eq. (6.4):

$$Pow = Tor \times \frac{\omega}{\omega_{\max}} \tag{6.4}$$

In which Pow and Tor are power percentage and torque percentage, respectively. ω is the motor speed in operation. As a result, Pow_1, $Pow_1 - Pow_2$, Pow_2 can all be calculated. The absolute power can be obtained by multiplying the power percentage with the rated power of the ABB motor drive system.

For validating the relation of torque percentage and power percentage, experiments in both case 1 and case 2 are conducted. Calculated torque percentage by the correlation is compared with that by experiments. The results are shown in Figure 6.12 and Figure 6.13. It is found that the predicted torque percentage is consistent with the measured value, with the maximum deviations of 5.1% under case 1 and 5.9% under case 2. Consequently, the power percentage can be expressed as the product of torque percentage and speed percentage of the motor.

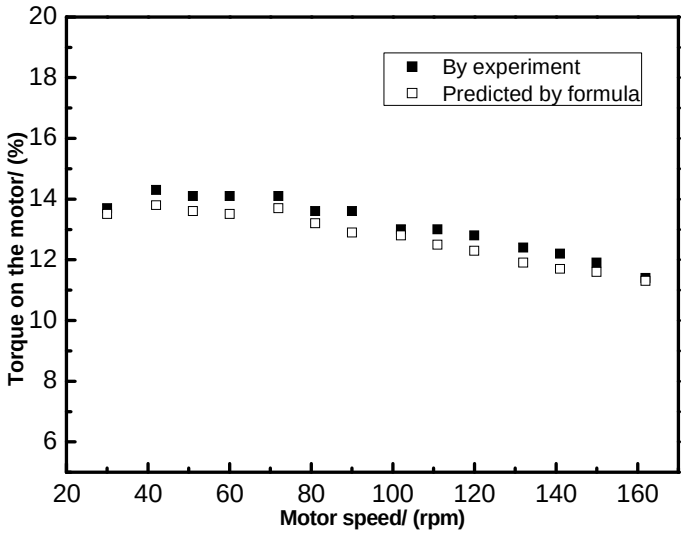

Figure 6.12 Validation of relationship of torque percentage and power percentage (under case 1)

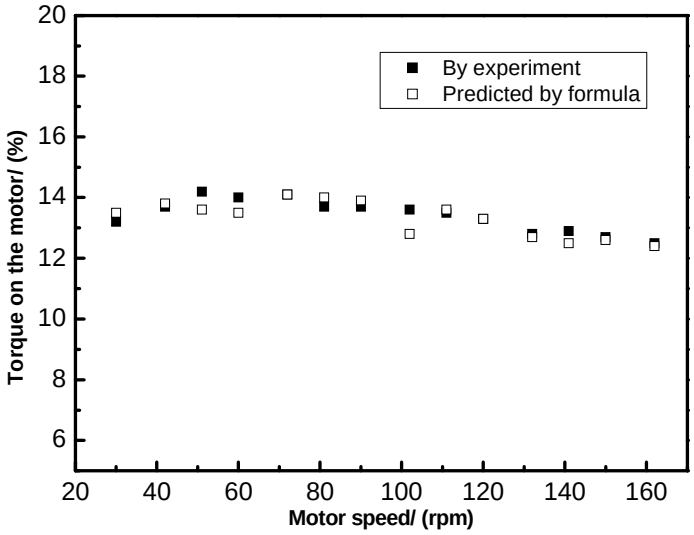

Figure 6.13 Validation of relationship of torque percentage and power percentage (under case 2)

6.3 Measurement of power generation in CES system

6.3.1 Experimental procedures and parameters

In the consideration of safety issue, power generation tests are firstly done in an open cycle, with exhausted gas eliminated to the environment directly. These include experiments with compressed air and high pressure CO2 under different operating conditions.

The block diagram for compressor air experiments is shown in Figure 6.14. The system is composed by a compressed air tank, a regulator, a non-return valve, a super heater, an engine and some accessorial pipes.

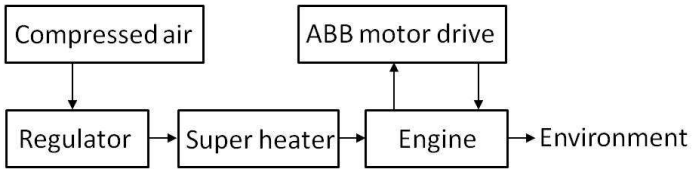

Figure 6.14 The block diagram of the compressed air experimental system

The experimental procedures in the open cycle test with compressed air as the working fluid is as following:

- Adjust the outlet pressure of the compressed air tank to a certain pressure higher than the operating pressure (i.e. 20 bar);
- Connect the air tank with the copper pipes for gas supply. A soft tube that can resist high pressure will be used;
- Reduce the pressure to the operating pressure by turning the valve on the regulator;

- Make sure the non-return valve after the regulator is closed;
- Start the ABB motor drive system and set the motor speed;
- Open the valve before the super heater;
- Slightly open the non-return valve;
- Record the torque and power from the hand panel.

The CO_2 experimental system is the constructed CES system as mentioned previously. The experimental procedures in the open cycle test with CO_2 as the working fluid is as below:

- Adjust the outlet pressure of the CO_2 tank to the operating pressure;
- Start the ABB motor drive system and set the motor speed;
- Switch on the super heater to heat up CO_2 to the required temperature;
- Slightly open the hand valve before the inlet of engine;
- Record the torque and power from the hand panel.

For both experiments, in case the high pressure gas is blocked in the system, the outlet valve of the tank should be turned off firstly to avoid risks.

During the experiments, the operating pressure is set lower than 50 bar while the temperature of the working fluids are limited to a value less than 150 ^{o}C. This is due to the possible hazards caused by high pressure and high temperature. The mass flow rate varies in the range of 0.1~1 kg/s. Although the motor speed can be as high as 2900 rpm, it is set below 200 rpm during the experiments. For studying the influence of the p-crank angle on power generation, p-crank angle is set in a big range in the control program. The typical experimental parameters of the engine system are summarized in Table 6.3.

Table 6.3 Experimental parameters of the engine system

Parameters	Compressed air	CO_2
Operating pressure (bar)	5~40	10~50
Working fluid temperature (^{o}C)	20~150	20~100
Mass flow rate (kg/s)	0.1~1	0.1~1
Motor speed (rpm)	30~200	30~200
P-crank angle (degree)	<60	<60

6.3.2 Experimental results

6.3.2.1 With a small engine

Small engine (162 cm^3) connected with either small valves (1.8 mm diameter, 15 ms responding time) or large valves (12 mm diameter, 50 ms responding time) is experimentally studied. The methodology of continuous and effective working for the engine system is explored.

As discussed previously, engine power (EP, written as Pow_2) can be obtained by the electricity consumption (EC, written as Pow_1) and the net electricity output of the motor (EM, written as ($Pow_1 - Pow_2$)). The effect of motor speed on the power is presented in Figure 6.15. Compressed air under 10 bar pressure is supplied to the engine. The p-crank angle of the engine is set as 18^o. It is found that with the increase of motor speed, power contribution by engine increases and then becomes approximately constant when motor speed is higher than 160 rpm. It is explained that the movement of piston from TDC to BDC takes less time with larger motor speed, leading to a larger power generation per unit time. However, volume flow rate of high pressure gas is suppressed due to the limited pipe diameter and gas velocity. The critical motor speed is observed as 160 rpm for the small engine.

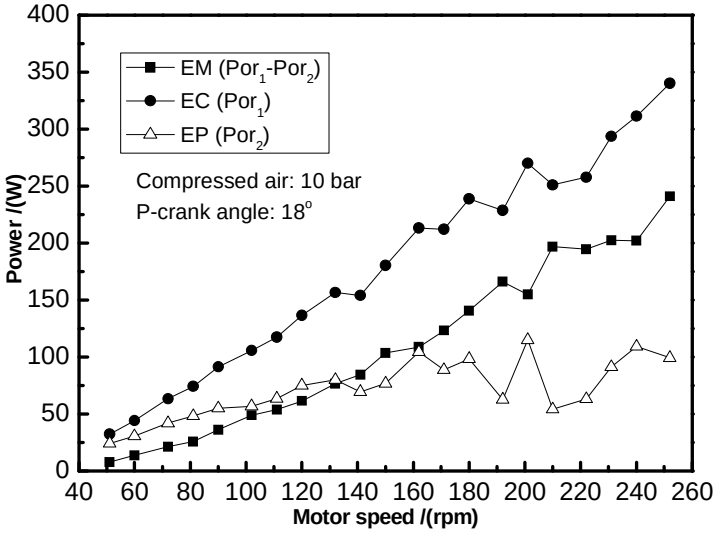

Figure 6.15 Effect of motor speed (with small valves)

P-crank angle can be changed by parameter setting on the PIC panel during experiment. However, for complicated situations of valve opening/ close, p-crank angle of the engine is pre-set by count setting in the Labview program before the experiment. The effect of p-crank angle in the range of 0^o~62^o is shown in Figure 6.16. It is seen that the engine power is improved with the increase of the p-crank angle.

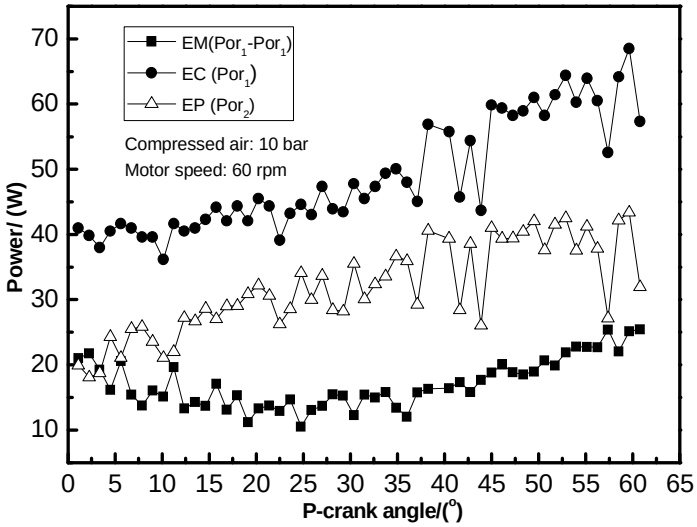

Figure 6.16 Effect of p-crank angle (with small valves)

Theoretically, optimal p-crank angle exists for obtaining the maximum engine power under certain conditions. For carbon dioxide or air, the optimal p-crank angle is found to be in the range of 70^o~80^o. The effect of optimal p-crank angle on the egnine power generation is demonstrated by comparative experiments. Results under 18^o and optimal p-crank angle (80^o) are compared, as shown in Figure 6.17. It is seen that engine power under the optimal p-crank angle is significantly bigger than that under a p-crank angle of 18^o. The maximum engine power generation is obtained with a motor speed of 160 rpm. Under the optimal p-crank angle, the maximum engine power is improved from 80 W to 150 W. It is expected that the improvement will be more significant when high pressure gas is utilized for expanding in the engine.

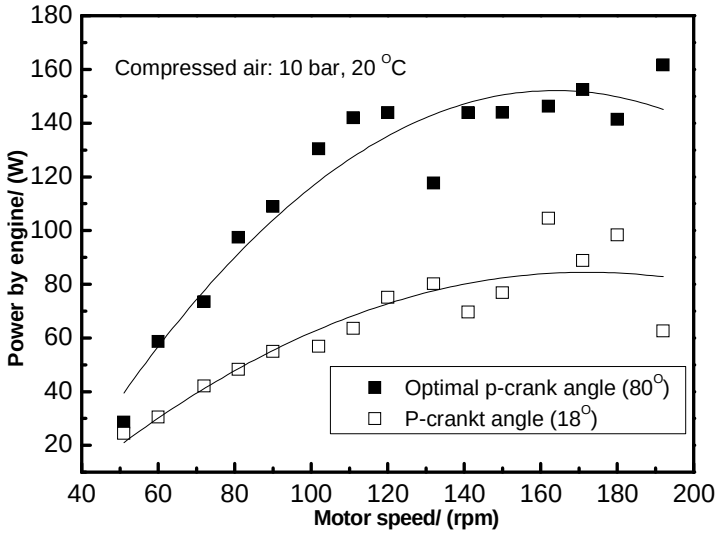

Figure 6.17 The effect of optimal p-crank angle on engine power generation

However, in the experiments with a small engine, the optimum p-crank angle is difficult to be found. This is because the engine has a small power capacity due to the small volume of the engine chamber (162 cm^3), and the gas supply with a lower pressure (10 bar).

The power generation of engine under different gas pressure is studied, as shown in Figure 6.18. Compared with the result under the pressure of 10 bar, it is found that engine power is improved. The power improvement becomes significant with a motor speed of higher than 80 rpm.

During the experiments, valves connected to the engine are opened for filling compressed gas. However, they are subsequently shut down for measuring the electricity consumption on motor (EC). As a result, EC increases with improving of the gas pressure, as can be seen in Figure 6.18.

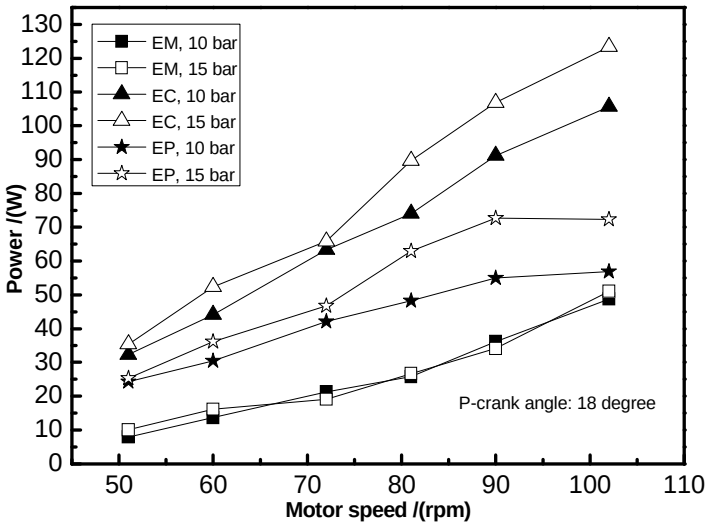

Figure 6.18 The power generation of engine under different gas pressure

The effect of gas temperature is also investigated. The p-crank angle is set as 18^o while the motor speed is 120 rpm in the experiments. Compressed air with a pressure of 10 bar is heated up to be more than 50 ^{o}C. The results are shown in Figure 6.19. It is seen that engine power (EP) is in the range of 75~90 W. However, in this low temperatuer level, it is found that the effect of temperature is not significant.

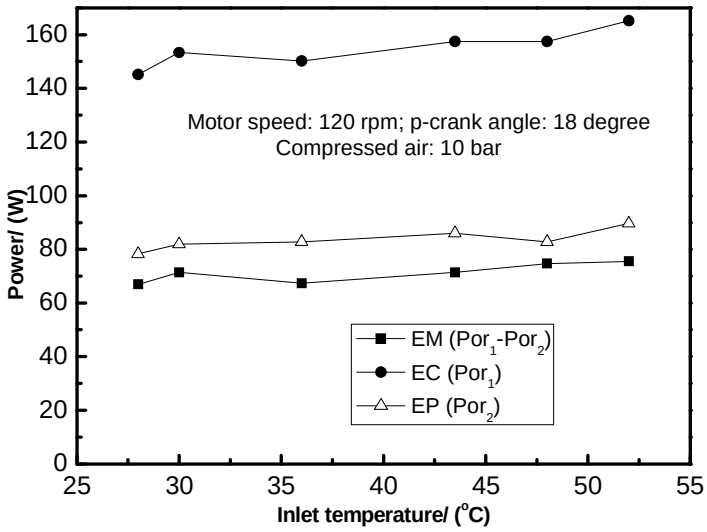

Figure 6.19 The effect on temperature on power generation

Further experiments with compressed air under a specific higher temperature (~100 ^{o}C) is carried out. And for getting more engine power, the supplied gas pressure is improved to be 15 *bar* while the p-crank angle is set as 36^{o}. The reuslt is presented in Figure 6.20. It is found that with the increase of motor speed, the maximum engine power (EP) is improved to be around 150 W . This is about 66.7%~ 100% higher than that under ambient temperature. It is also seen that EP increases firstly and becomes constant subsequently with a critical motor speed of 160 rpm.

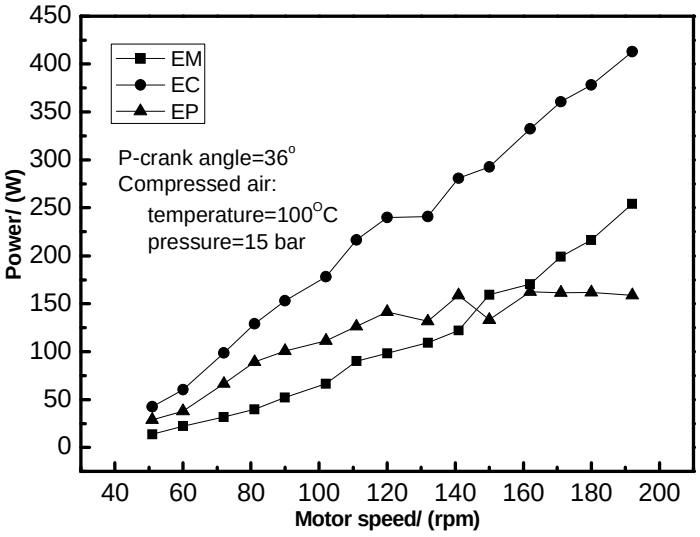

Figure 6.20 Power generation under higher temperature

Since it is the working fluid in Rankine cycle in the CES system, experiments with CO_2 are conducted under the same operating conditions as compressed air. Specifically, the gas pressure is 10 bar, while the p-crank angle of engine is equal to 18^{o}. Comparative results by CO_2 and air are

shown in Figure 6.21. It is found that the engine power (EP) by CO_2 is larger than that by the compressed air under the same operating conditions. The reason is that carbon dioxide has larger molecular weight, resulting in bigger mass flow rate of high pressure gas in the engine chamber.

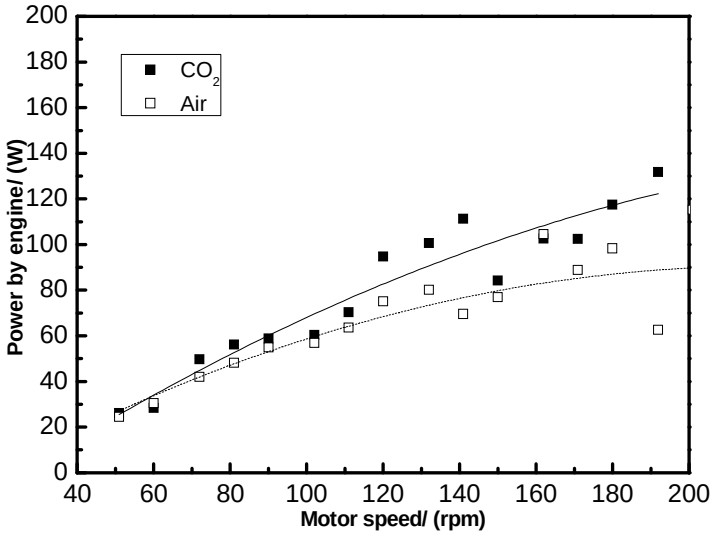

Figure 6.21 comparison of CO_2 and air as the working fluid

In the above, study of engine power (EP) in the small engine is conducted. The effects of motor speed, optimal p-crank angle, gas pressure, gas temperature and the selection of the expanding gas are all experimentally investigated.

From all the above results, the net electricity consumption (EM) on the motor is positive under different conditions. This indicates an overall electricity consumption by the small engine and ABB motor drive system.

6.3.2.2 With a large engine

A large engine with a volume of 1900 cm^3 is experimentally tested for obtaining negative electricity output of the whole system. The engine has four cylinders, which can be divided into two groups in terms of the movements of piston. There are three valves for each cylinder, two of which are at the inlet and the other one is at the outlet. Due to the symmetry of the cylinders, one group of cylinders is presented in Figure 6.22.

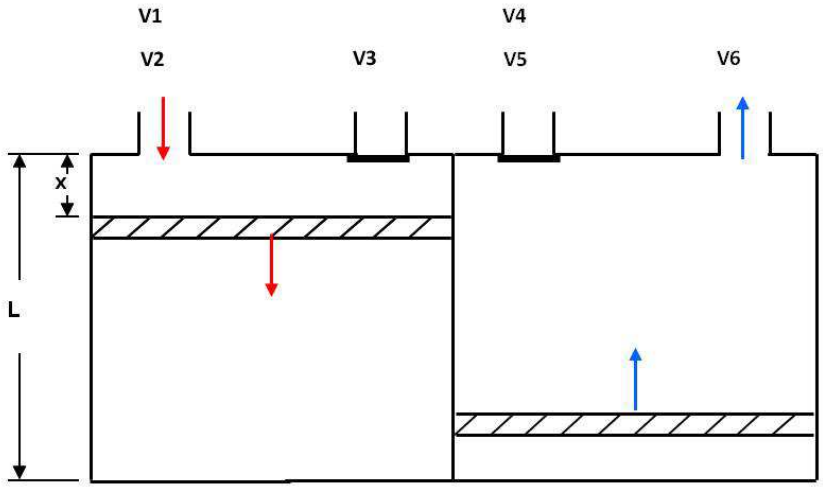

Figure 6.22 One group of cylinders of the large engine

Theoretically, the outlet pressure of engine is equal to the ambient pressure. However, in the actual expanding and exhausting processes, outlet pressure is largely affected by the performance of solenoid valves due to the reflection time for opening and closing the inlet and outlet. The outlet pressure of the engine affected by large valves (50 ms as the reflection time) is shown in Figure 6.23. It is found that the outlet pressure fluctuated periodically. The averaged pressure is slightly higher than ambient pressure. This is caused by the insufficient expansion due to reflection time of valves.

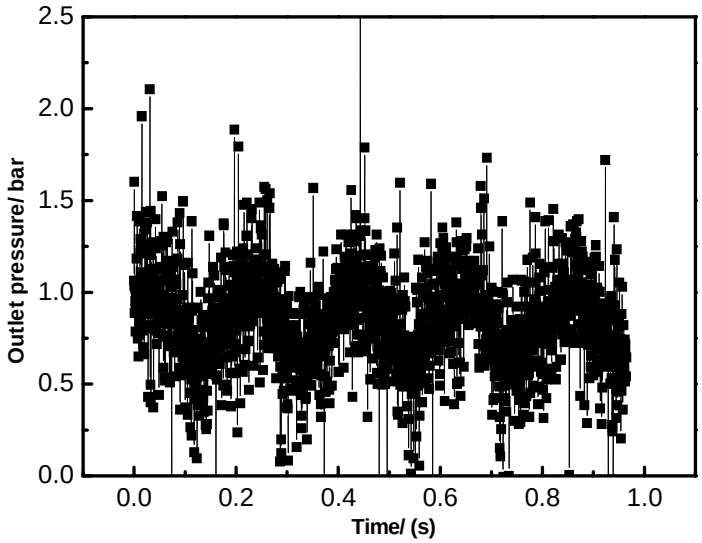

Figure 6.23 The fluctuation of outlet pressure of the engine

It is evaluated that bigger valves have more significant influence on eliminating process of the exhaust gas. In large engine system, since large valves are used at both inlet and outlet, the effect on outlet pressure need to be diminished. Feasible method is resetting the initial counts for the valves in the controlling module, as claimed in Figure 6.24.

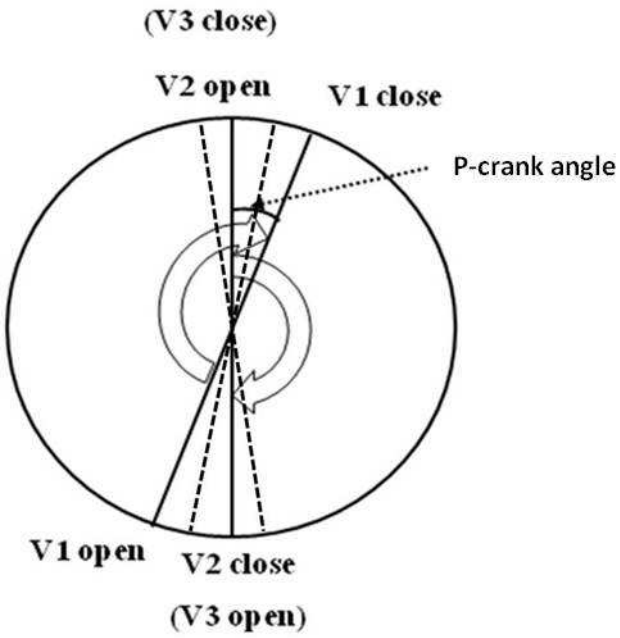

Figure 6.24 Count resetting in the consideration of time delay of valves

The electricity consumption (EC) for driving the motor is measured without supply of high pressure gas to the engine. The results are presented in Figure 6.25. It is seen that EC increased linearly with the increase of motor speed. This indicates that the torque on the motor is approximately constant during the measurements. Based on torque analysis, electricity consumption can be calculated. The experimental data agrees well with the predicted value, as presented in Figure 6.25.

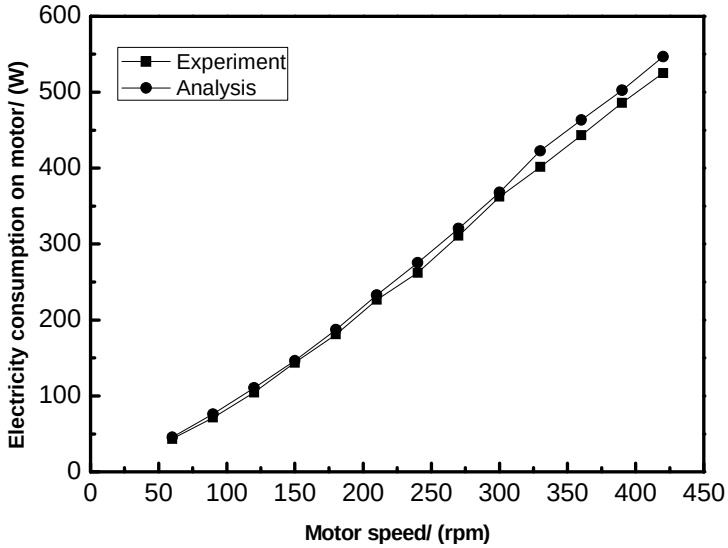

Figure 6.25 The energy consumption by ABB without gas supply

In the experiment, motor is connected with large engine without compressed air. Due to the resistance of the engine, the torque consumption in the system (Tor_1) is largely increased. Torque percentage of the large engine is

compared with that in small engine, as shown in Figure 6.26. It is found that torque percentage consumed by the large engine system is much bigger than that in small engine system. With the increase of motor speed, torque percentage in small engine system decreases gradually. This is due to the reduced friction in the condition of higher motor speed. While in large engine system, with improving of motor speed, torque percentage increases sharply before motor speed of 350 rpm. In this case, resistance of compressed gas enclosed in the chamber has dominant effect on preventing the movement of piston.

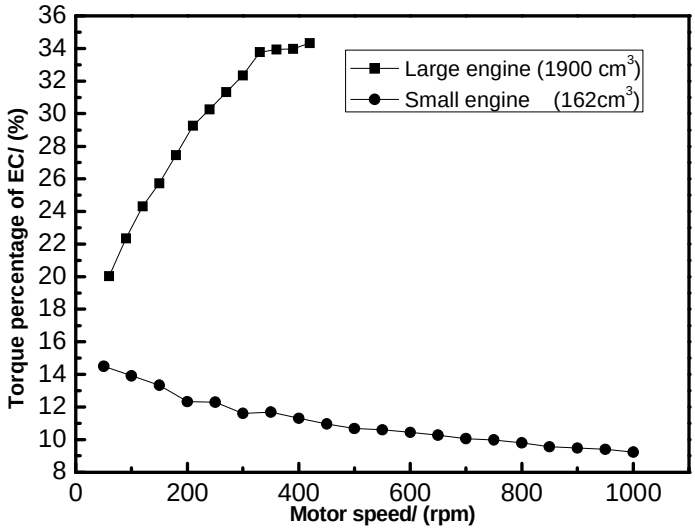

Figure 6.26 Comparison of the torque consumption in different engines

The corresponding electricity consumptions (EC) in the case are shown in Figure 6.27. With increasing of motor speed, electricity consumptions in both situations are improved due to the increased speed percentage. However, the energy consumption with the large engine is more than 450 W with a motor speed of more than 350 rpm, which is much bigger than that with the small engine.

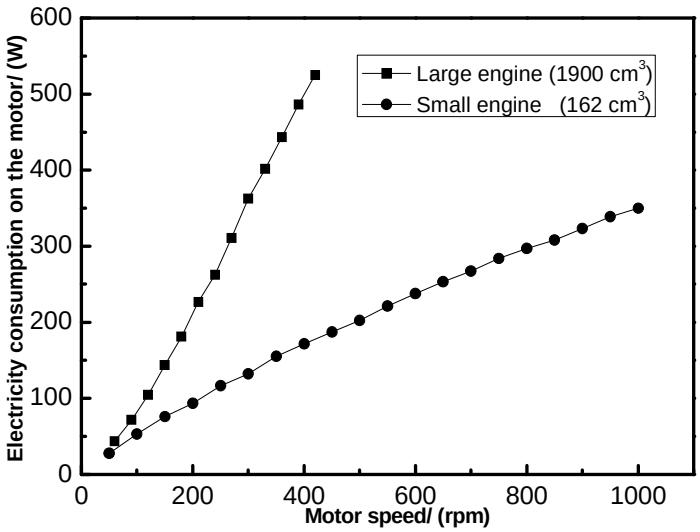

Figure 6.27 Energy consumptions in system without gas supply

Torque ratio is defined as the proporation of torque from the contribution of engine (Tor_2) in the total torque by electricity consumption (Tor_1). Comparative experiments for the torque ratio in the two different engines are conducted. In the experiments, compressed air of 10 bar is supplied to the engine. Thie inlet angel is initialized as 18^o. The resluts are shown in Figure 6.28. It is seen that torque ratio in large engine system is over 80% after motor speed of 350 rpm, while it is less than 40% in small engine system.

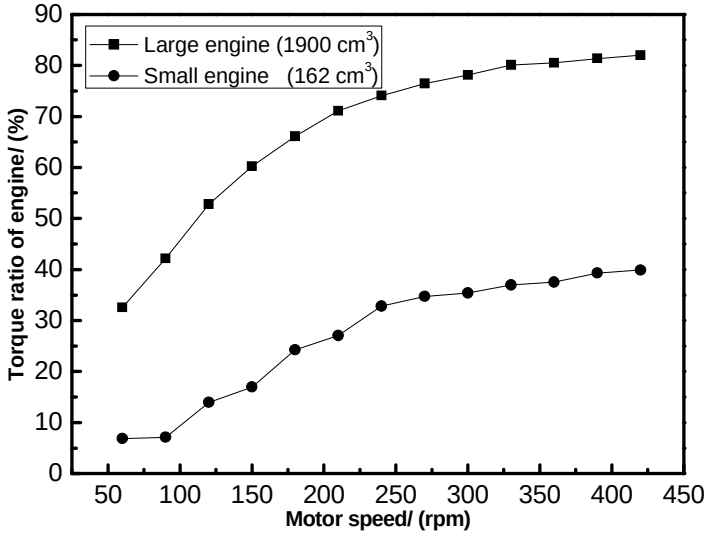

Figure 6.28 Variation of the torque ratio in different engines

Similarly, power ratio is is defined as the proporation of engine power (Pow_2) in the total electricity consumption (Pow_1). The power ratio in two engines under the same conditions are compared, as presented in Figure 6.29. It is seen that the power contribution by large engine occupies 72.4% of the electricity consumption with a motor speed around 400 rpm, while with the

small engine, the power ratio of engine is reduced to 42.6% under the same motor speed.

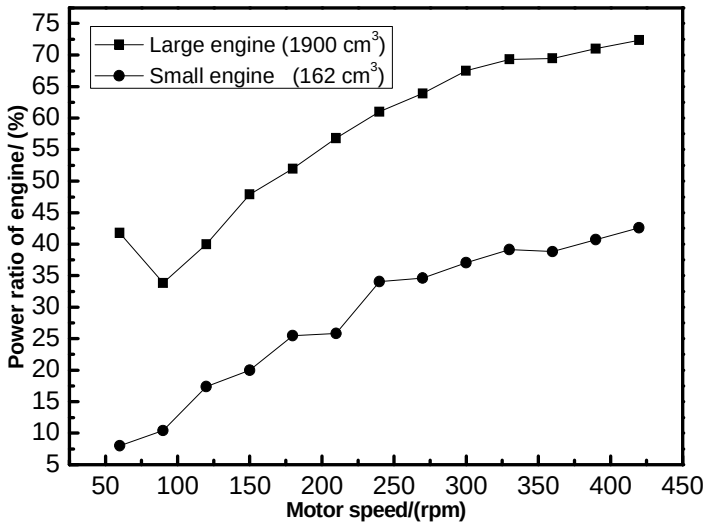

Figure 6.29 Energy consumption ratio of engine without gas supply

The comparisons of torque ratio and power ratio in the large engine and small engine system indicate that the large engine has a high proportion of contribution on electricity generation under the same operating conditions including gas pressure, p-crank angle and motor speed. This is due to the increased volume of the large engine, leading to an improved volume flow rate in the engine chamber under the same motor speed.

Volume flow rate at the outlet of the engine is measured. The results are shown in Figure 6.30. More gas is supplied to the engine chamber, since the density of gas is increased under an improved pressure; while the opening time of the engine inlet keep the same under the set p-crank angle and motor speed. This amount of gas will be eliminated from the outlet of the engine. Therefore, the volume flow rate at the outlet increases with the improving of the inlet pressure.

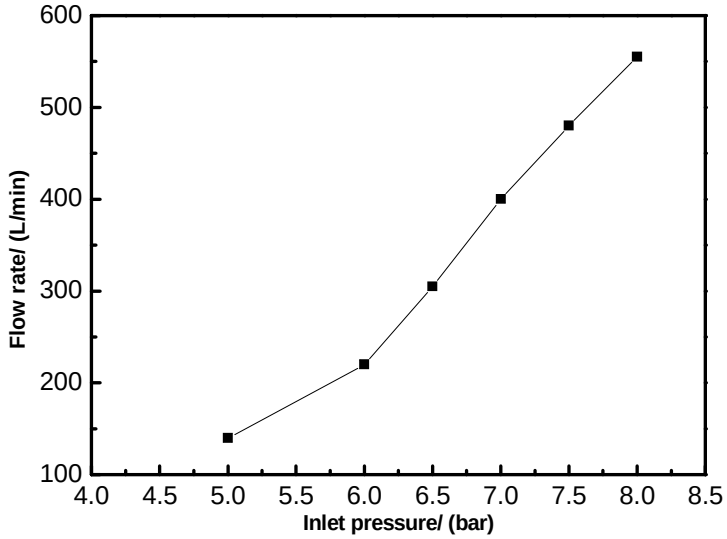

Figure 6.30 Measurement of mass flow rate of exhaust gas through large valves

However, in realistic engine experiments, part of the exhaust gas will be enclosed within the engine chamber at the end of the eliminating process. The remained gas increases the resistance for gas entering the chamber and prevents the movements of the piston in the engine. As a result, the performance of the engine will be reduced.

The improvement of engine performance can be achieved by the following methods: (1) improving the limit value of flow rate by enlarging the flowing passage inside the valve; (2) reducing the numbers of valves connected with engine by abandoning one valve at each inlet of engine. However, the former has less significant effect while the latter is confined to lower motor speed, in the consideration of the time delay for opening and closing the valves.

Both methods are used in the following engine tests. In the experiments with the large engine, the motor speed and p-crank angle are set as 60 rpm and18^{o}, respectively. The inlet pressure of the compressed air is 10 bar. The results are shown in Figure 6.31.

The previous results shows that the overall effect of the engine and ABB motor drive system is consuming electricity. However, after the improvement of the engine performance, the net electricity consumption is negative, which indicates a net electricity output by the whole engine system. This can be regarded as electricity supply to the grid during peak time. Therefore, the value of the CES system is demonstrated.

Furthermore, one can see that under the best engine performance that can be actually achieved by using the above methods, the net electricity output can be improved to be as high as 160 W. The results are also compared with the predicted power generation, as can be seen in Figure. 31.

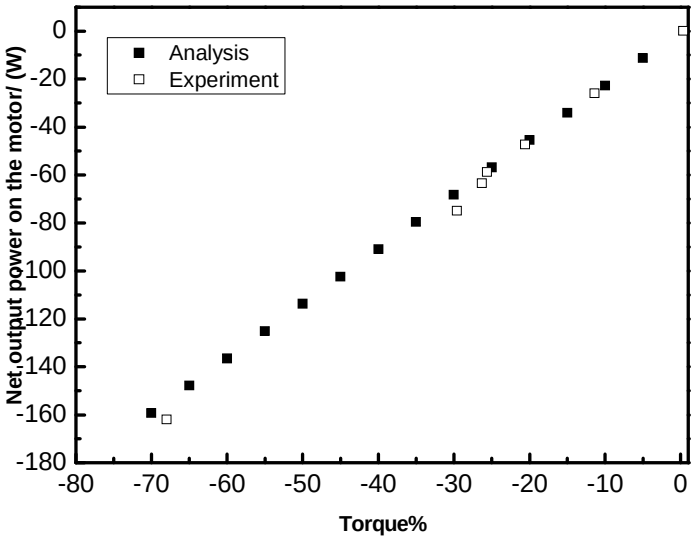

Figure 6.31 Power improvement of engine with a motor speed of 60 rpm

6.4 Prediction of power generation in the engine

6.4.1 Theoretical model

Thermal dynamic cycle of a piston based engine is demonstrated as process A-B-C-E, as presented in Figure.6.32. The process A-B is the gas injection into the engine chamber, during which mass of gas increases with time. The process B-C represents the expansion process. Since the valves at both inlet and outlet of the engine are closed, gas mass keep constant during the process. While the process C-E is the gas elimination process, when the gas mass in the chamber is reduced with time. One can see that there is no compression process for the engine driven by high pressure gas. As a result, the specific engine power (J/kg) is generated in the process B-C, which can be expressed as in Eq. (6.5):

$$w = \int_{P_B}^{P_C} -v \cdot dP \tag{6.5}$$

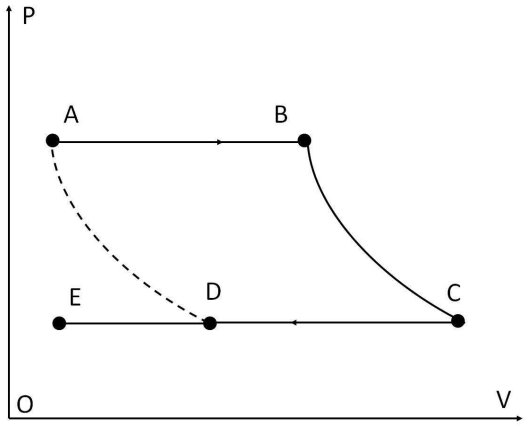

Figure 6.32 Thermal dynamic cycle of the piston-based engine

The gas expansion in the piston based engine can be either isothermal process or adiabatic process. As claimed in chapter 2, expansion in an isothermal process results in the maximum power output, compared with other thermal processes in the engine. However, the temperature condition is difficult to achieve in actual engine tests, especially with a high motor speed. Therefore, the specific engine power in the adiabatic expanding process will be analyzed in the following.

6.4.1.1 Specific power

The expanding process in the engine is irreversible due to the pressure difference between the chamber and environment. However, it is regarded as approximate adiabatic process since the expanding happens very fast. As a result, few amount of heat is transferred out of the engine system. Consequently, the process equation for air can be written as:

$$P_B v_B^{\,k_{po}} = P_C v_C^{\,k_{po}} \tag{6.6}$$

In which k_{po} is the Possion factor, which is defined as,

$$k_{po} = \frac{C_{p,g}}{C_{V,g}} \tag{6.7}$$

In which $C_{p,g}$, $C_{V,g}$ are the heat capacity of gas at constant pressure and volume, respectively. The diagram of the revised engine is shown in Figure 6.30. The whole length of the chamber is L. The volume of the chamber is 162 or 1900 cm^3. Valves at the inlet are open before piston reaches the position of x. During this opening time, mass of gas increases with piston moving from location of 0 to x. Valves are all closed subsequently. As a result, mass of gas maintains constant value in the expanding process.

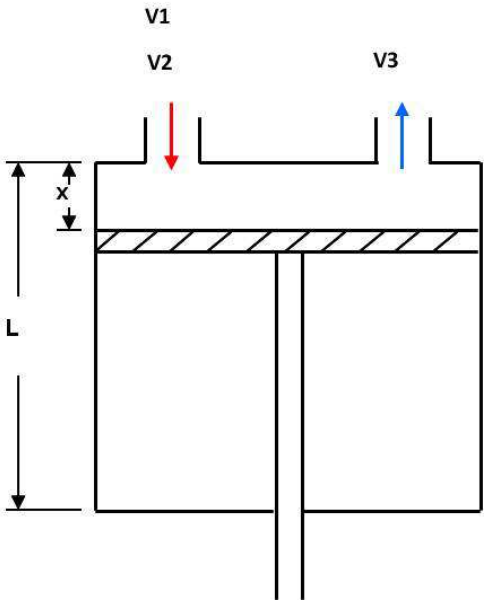

Figure 6.33 Schematic diagram of revised engine

For adiabatic process of ideal gas, the specific power is calculated as:

$$w = \frac{1}{k_{po} - 1} \cdot R_g \cdot T_{in} \cdot [1 - (\frac{P_c}{P_{in}})^{\frac{k_{po}-1}{k_{po}}}] \tag{6.8}$$

In which R_g is gas constant ($J/(kg \cdot K)$); P_{in} and T_{in} are pressure and temperature of gas at the inlet of engine, respectively; P_c is the pressure after expansion.

In ideal situation, P_c is equal to the ambient pressure ($P_c \approx P_o$). For gas expanding, equation of ideal gas can be described as Eq.(6.9)~(6.10):

$$P_{in} x^k = P_c L^k \tag{6.9}$$

$$\frac{x}{L} = (\frac{P_c}{P_{in}})^{\frac{1}{k}} \tag{6.10}$$

As discussed previously, the opening time for gas entering the engine can be controlled by setting the value of p-crank angle. The relation of p-crank angle and locations of piston in the engine can be formulated in Eq. (6.11):

$$\frac{x}{L} = p - crank\ \ angle / 180 = \alpha \tag{6.11}$$

According to Eq.(6.9)~(6.11), provided that the gas pressure is equal to the ambient pressure, the p-crank angle should be set as:

$$p - crank\ \ angle = 180(\frac{P_o}{P_{in}})^{\frac{1}{k}} \tag{6.12}$$

6.4.1.2 Mass flow rate

State equation for ideal gas at the engine inlet is described as:

$$P_{in} \cdot V = m \cdot R_g \cdot T_{in} \tag{6.13}$$

Assuming that piston of engine moves simultaneously with motor due to the solid linkage between them. Therefore, gas mass entering the chamber during opening time can be calculated as:

$$m = \frac{P_{in}}{T_{in}} \cdot \frac{1}{R_g} \cdot \omega \cdot r \cdot A \cdot t_1 \tag{6.14}$$

In which ω is motor speed, r is radius of shaft, A is the section area of chamber and t_1 represents opening time for gas entering the engine, respectively. Therefore, the mass flow rate at the inlet is obtained:

$$\dot{m}_{in} = \frac{m}{t_1} = \frac{P_{in}}{T_{in}} \cdot \frac{1}{R_g} \cdot \omega \cdot r \cdot A \tag{6.15}$$

In one circle time, piston moves from TDC to BDC and back to TDC, therefore,

$$\omega \cdot r \cdot \frac{2\pi}{\omega} = 2 \cdot L \tag{6.16}$$

According to Eq.(6.15)~(6.16), mass flow rate at the engine inlet is formulated:

$$\dot{m}_{in} = \frac{1}{\pi} \cdot \frac{P_{in}}{T_{in}} \cdot \frac{1}{R_g} \cdot \omega \cdot V \tag{6.17a}$$

The average mass flow rate in a cycle is:

$$\overline{\dot{m}}_{in} = \frac{1}{\pi} \cdot \frac{P_{in}}{T_{in}} \cdot \frac{1}{R_g} \cdot \omega \cdot V \cdot \alpha \tag{6.17b}$$

In which V is the volume of chamber (162 cm^3 for small engine and 1900 cm^3 for large engine). It is pointed out that the mass flow rate at the outlet of engine is not equal to the inlet mass flow rate, since part of exhausted gas still remains in the engine chamber after the elimination process.

From Eq. (6.8) and Eq. (6.17), the engine power can be calculated:

$$W = \frac{1}{k_{po} - 1} \cdot \frac{1}{\pi} \cdot P_{in} \cdot \omega \cdot V \cdot [1 - (\frac{P_c}{P_{in}})^{\frac{k_{po}-1}{k_{po}}}] \tag{6.18a}$$

Correspondingly, the average engine power in a cycle is expressed as:

$$\overline{W} = \frac{1}{k_{po}-1} \cdot \frac{1}{\pi} \cdot \alpha \cdot P_{in} \cdot \omega \cdot V \cdot [1-(\frac{P_c}{P_{in}})^{\frac{k_{po}-1}{k_{po}}}] \quad (6.18b)$$

From this formula, one can see that by using CO_2 as the working fluid instead of compressed air, mass flow rate is increased, resulting in an improved engine power under the same operating conditions.

From Eq. (6.17b), the average volume flow rate is obtained:

$$\overline{\dot{V}_{in}} = \frac{1}{\pi} \cdot \omega \cdot V \cdot \alpha \quad (6.19)$$

From the above equation, it is indicated that volume flow rate is determined by the motor speed, engine volume and the p-crank angle of the engine. In the large engine, the average volume flow rate increases massively, compared with that in the small engine. As a result, the electricity generation by engine is improved.

As discussed before, volume flow rate is restricted by the maximum diameter of the flowing passage before entering the engine. Therefore, the formula for calculating the engine power can be used for the small engine and the large engine with a motor speed less than 160 rpm and 350 rpm, respectively.

6.4.2 Power capacity of engine

6.4.2.1 Influence of p-crank angle

The effect of p-crank angle is investigated, as shown in Figure 6.34. With the increase of the p-crank angle, the power contribution by engine increases firstly and decreases subsequently. The highest power by engine is obtained under the optimum p-crank angle. It is found that under different Possion factor, the optimum p-crank angle is changed. For instance, at lower temperature when $k_{po} = 1.4$, the optimal value of α is 0.440, while at higher temperature when $k_{po} = 1.3$, this value is reduced to 0.389. Accordingly, p-crank angle decreases from 80^o to 70^o. It is concluded that the best piston location at the end of opening time is slightly smaller than half way of the chamber length.

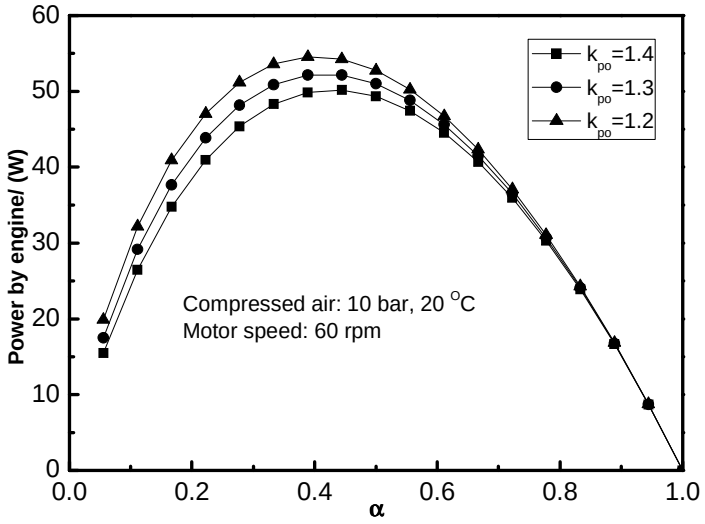

Figure 6.34 The effect of p-crank angle by theoretical prediction

6.4.2.2 Power generation under high operating parameters

The effect of motor speed is studied under optimum inlet angle, as presented in Figure 6.35. When motor speed is lower than160 rpm , power generation increases linearly with increasing of motor speed. The power generation by engine is restricted by the smallest section area of the flowing passage in the system.

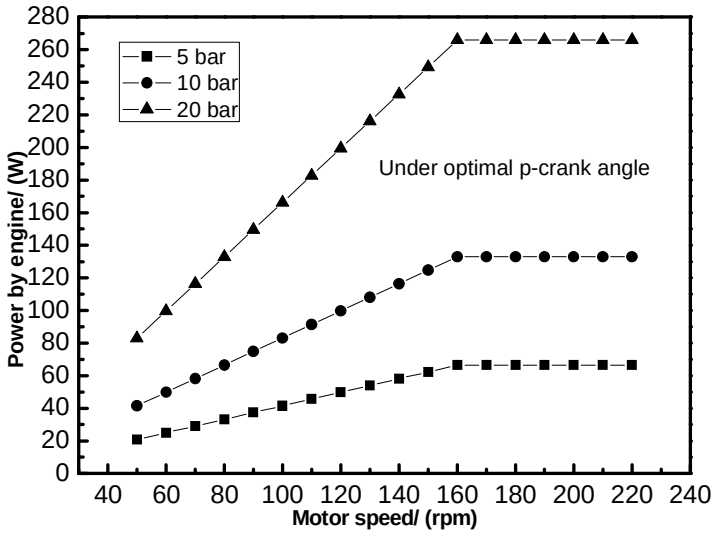

Figure 6.35 Effect of motor speed by theoretical prediction

The effect of pressure under optimal inlet angle is presented in Figure 6.36. With the increase of pressure, power generation increases linearly. It is noted that the effect of pressure is more significant when speed is higher.

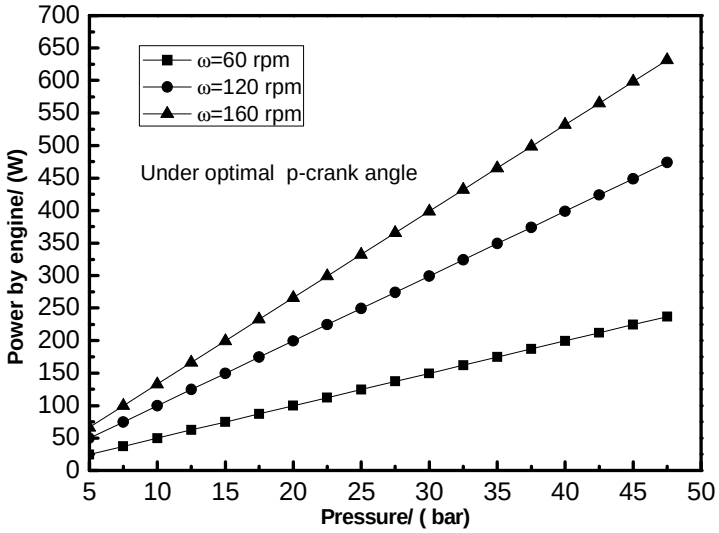

Figure 6.36 Effect of pressure by theoretical prediction

The effect of gas temperature is carried out, as seen in Figure 6.37. Both of CO_2 and air are tested. With the increase of CO_2 temperature, power by engine increases gradually. However, the effect of temperature is less significant when air is expanded in the engine. Consequently, CO_2 is better than air for generating power in the engine system.

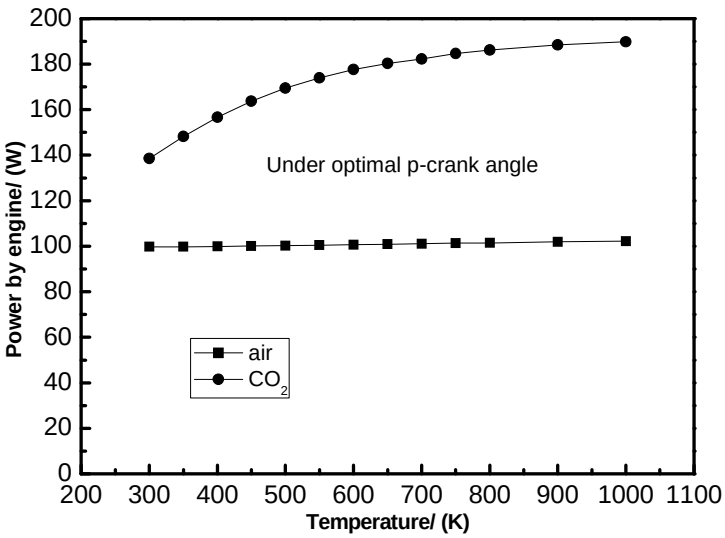

Figure 6.37 Effect of temperature by theoretical prediction

As discussed previously, power generation by engine is restricted by the minimum inner diameter of the valves. Theoretically, the velocity of gas is less than the sound velocity 340 m/s. Therefore, the minimum diameter of the valve can be calculated, as expressed in Eq. (6.20):

$$d_{\min} = \frac{2}{\pi} \cdot \sqrt{\frac{\omega \cdot V}{340}} \tag{6.20}$$

The results are shown in Figure 6.38. The minimum diameter of small valves is 1.8 mm. From the figure, it is seen that the critical motor speed is160 rpm. When motor speed is higher than the critical value, power generation keeps constant. This is consistent with the previous experimental results. Similarly, for large valves with the minimum diameter of 12 mm, the critical motor speed is found as 600 rpm. As claimed previously, higher motor speed results in larger power generation. Therefore, for large engine systems, large valve is used for enlarging the power capacity of the engine system.

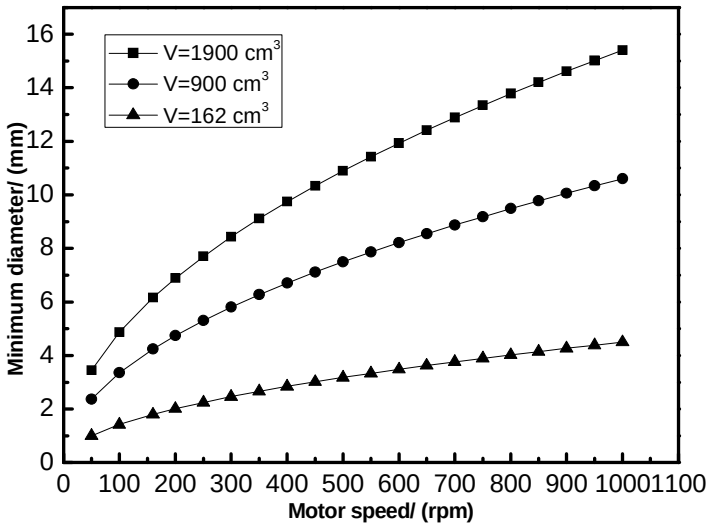

Figure 6.38 Relation of minimum diameter of the valve and the motor speed

The power capacity of large engine connecting with large valves is predicted, as shown in Figure 6.39. Compressed air with pressure of 5, 10 and 20 *bar* is expanded in the engine respectively. It is found that the maximum power generations in different cases are as high as $3\,\mathrm{kW}$, $6\,\mathrm{kW}$ and $12\,\mathrm{kW}$, respectively. The maximum power is restricted by the minimum diameter of 12 mm in the valves. Therefore, with larger valves used, more power can be generated. However, in that case, time delay for opening and closing the valves becomes more significant.

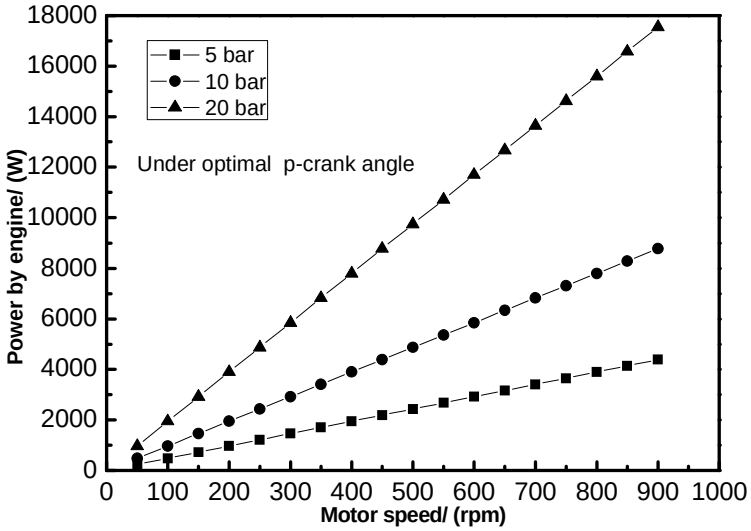

Figure 6.39 The prediction of power capacity of large engine

6.5 Further discussions on the piston-based engine

In the above section, engine performance in the piston based engine is investigated by both experimental study and theoretical analysis. Apparently, compared with the small engine, more power can be generated in the large engine due to the increased chamber volume of the engine.

However, the engine power is also significantly affected by the performance of engine in the gas expansion process, therefore, this section concerns the efficiency of the engine, followed by further discussions on the effect on the storage efficiency of the CES system.

6.5.1 Improvement of engine efficiency

The engine efficiency in this section refers to the exergy efficiency, which is defined as the ratio of actual power output to the theoretical engine power based on thermal analysis.

As discussed above, the engine efficiency can be formulated:

$$\eta_{engine} = \frac{36.2 \times Tor_2 \cdot \omega}{\frac{1}{k_{po}-1} \cdot \frac{1}{\pi} \cdot \alpha \cdot P_{in} \cdot \omega \cdot V \cdot [1-(\frac{P_c}{P_{in}})^{\frac{k_{po}-1}{k_{po}}}]} \quad (6.21a)$$

In which Tor_2 represents the torque percentage by engine contribution. In the experiments, electricity consumption (EC) and electricity output on the motor (EM) can be obtained, therefore, the engine efficiency can be expresses as:

$$\eta_{engine} = \frac{EC - EM}{\frac{1}{k-1} \cdot \frac{1}{\pi} \cdot \alpha \cdot P_{in} \cdot \omega \cdot V \cdot [1 - (\frac{P_c}{P_{in}})^{\frac{k-1}{k}}]} \quad (6.21b)$$

A case study is presented as below. In this case, the inlet pressure of the compressed air is 10 bar; the inlet angle is set as 18^o; the motor speed is 60 rpm.

With a large engine, the electricity consumption (EC) on the motor is 60 W, as seen in Figure 6.27; while the net electricity output of the motor (EM) with better performance of engine can be as high as -160 W, as shown in Figure 6.31. Therefore, the engine power (EP) is as 220 W. The theoretical engine power is calculated as approximately 572 W. Consequently, the engine efficiency in terms of the above definition is about 38.5%.

With a small engine, EC on the motor is 45 W while EM is found as 15 W, as presented in Figure 6.15. As a result, the engine power is equal to 30 W. The theoretical engine power is calculated as 49 W. According to Eq. (6.20), the efficiency of the small engine is 61.2%.

By using a large engine in the CES system, the engine efficiency is reduced. One of the significant factors for lowering the engine performance is that more exergy loss is caused due to the inadequate gas expansion in the large engine chamber under. For the piston based engine with a new valve scheme, more work should be done to address the time delay issue of the large valves for opening and closing operations.

6.5.2 Influence of engine efficiency on overall storage efficiency

Although the efficiency of the large engine is reduced, large engine is still recommended to be used in a CES system. This is because large engine supported by ABB motor drive system can result in a net power generation that can be sent back to the electrical grid for peaking shifting purpose.

In the point view of energy storage and utilisation, the contribution of the engine system lies in the net output power by the system. Therefore, the actual engine efficiency can be expressed as:

$$\eta'_{engine} = \frac{-EM}{\frac{1}{k_{po}-1} \cdot \frac{1}{\pi} \cdot \alpha \cdot P_{in} \cdot \omega \cdot V \cdot [1 - (\frac{P_c}{P_{in}})^{\frac{k_{po}-1}{k_{po}}}]} \quad (6.22)$$

As a result, in the above case study, the large engine system has an efficiency of 28.0%. However, for the small engine system, the actual engine efficiency for power generation in the CES system is -30.6%.

As presented in chap 5, the storage efficiency of the CES system can be formulated as:

$$\eta_{CES} = \frac{W_e - W_p}{E_{heat} + E_{cool}} \tag{6.23}$$

In which, W_e represents the power generation in the engine system. From the above analysis, the storage efficiency is written as:

$$\eta_{CES} = \frac{-EM - W_p}{E_{heat} + E_{cool}} \tag{6.24}$$

A case study is presented below to show the influence of the actual engine efficiency on the overall storage efficiency. Since the gas pressure at the inlet of engine is as high as the saturated pressure (10 ~12 bar), pump is not used in the actual operation. Therefore, the electricity consumption by pump is zero. With a mass flow rate of 0.0426 kg/s, the theoretical engine power is:

$$EP_{theo} = 0.0426 \times \frac{1}{k_{po} - 1} \cdot R_g \cdot T_{in} \cdot [1 - (\frac{P_c}{P_{in}})^{\frac{k_{po}-1}{k_{po}}}] \tag{6.25}$$

Which is calculated as 8659 W under the above operating conditions. According to the above engine efficiency of 38.5%, the actual engine power (EP) for the large engine is 3334 W. However, in consideration of the electricity consumption on the motor, the net output of the ABB motor drive and engine system is further reduced to 2425 W.

From Figure 5.22, the electricity consumption by the refrigerator for cold storage is 4000 W, while the electricity consumption in the super heater for heating the working fluid to 200 ^{o}C is 7000 W. According to Eq. (6.23), the storage efficiency of the CES system is approximately 22%. Theoretically, this indicates that for storing 10 kW of cold energy by consuming cheap electricity in off-peak time, the constructed CES system have a 2.2 kW of net output electricity that can be later used in peak time. However, the efficiency of the large engine system will still be a big challenge in actual engine tests.

6.6 Summary of this chapter

A piston based engine and ABB motor drive system for cold to power conversion is investigated in this chapter.

A new valve scheme by using solenoid valves at the inlet and outlet of the engine has been developed. As a result, a flexible control of the gas injection

and elimination processes in terms of different operating conditions in the engine can be achieved.

Since the motor is doubly driven by both engine and ABB motor drive system, the net electricity consumption of the motor (EM, written as $Pow_1 - Pow_2$) can be regarded as the combined contributions of electricity consumption on motor (EC, written as Pow_1), and engine power (EP, written as Pow_2). When the value of EM is negative, the whole engine and ABB motor drive system will have a net electricity generation.

Based on the above understanding, power consumptions/ generations in a small engine and a large engine are experimentally investigated under different conditions. The experimental results shows that the net electricity consumption on the motor (EM) in the small engine system is a positive value, indicating an overall electricity consumption by the system.

With the large engine, engine power (EP) is apparently larger due to the increased chamber volume. But the engine performance is reduced due to the block of the exhaust gas in the chamber. However, this issue can be effectively addressed by improving the limit value of flow rate and reducing the numbers of valves at the engine inlet. Consequently, EM in the large engine system can achieve a negative value as high as -160 W in the case study (i.e. gas pressure is 10 bar, inlet angle is 18^o while the motor speed is 60 rpm). This indicates a net electricity supply to the grid during peak time, which demonstrates the value of the CES system.

The theoretical value of the engine power (EP) is predicted by establishing a model based on thermal analysis. Power capacity of the engine for developing a large scale CES system is evaluated by using the theoretical model.

Further discussions on the piston-based engine concerns the improvement of the engine efficiency and its influence on the overall storage efficiency. In the presented case study, the efficiency of the small engine is 61.2%, while it is reduced to 38.5% for the large engine. However, in the point view of net electricity output, the actual efficiency of the small engine for power generation in the CES system is -30.6%, while the actual efficiency of the large engine system is 28.0%. Therefore, large engine system is still recommended for CES system.

Theoretically, with an increase of the engine efficiency, the storage efficiency of the whole CES system will be improved. In the presented case study, with the large engine that has an actual efficiency of 28.0%, the storage

efficiency of the CES system is approximately 22.0%. However, this low storage efficiency can be improved by further investigation on the improvement of engine efficiency in future engine experiments.

Chapter 7
Conclusions and recommendations for future work

This chapter summarises the main conclusions of the PhD study. Recommendations for the future work are also given on the basis of this work.

7.1 Summary of main conclusions

Study of cold energy storage in this thesis is structured in the order of background, literature review, cold storage, cold extraction, cold utilisation, cold conversion and system application. In the above CES research, the following conclusions are summarized:

(A) Cold energy storage (CES) is attractive due to its ability of providing high energy storage density and high cold storage grade. This can be achieved by using eutectic PCM solution with a PCM temperature lower than its freezing point. A third PCM can be added into the binary eutectic PCM for obtaining the tuneable characteristics of the CES.

PCM selection in a binary or ternary system is crucial due to its significant effect on cold energy storage caused by their thermal physical properties. PCM with low freezing temperature, large latent heat and small molecular weight should be selected as the component in the binary system. However, PCMs that have comparable melting temperatures and compatible molecular structures are required.

(B) The cold discharging rate can be largely improved by embedding metal foams in PCM solutions, due to the enhancement of the effective thermal diffusivity and thermal conductivity of the PCM composite. In a case study, compared with single paraffin, the thermal diffusivity and thermal conductivity of the PCM composite (paraffin embedded with Al foams) is improved by 20 times and 20.6 times, respectively.

For evaluating the cold discharging capacity, combined effect of cold radiation and convection is considered. The calculation for a spherical PCM capsule shows that the effect of cold radiation on the cold discharging rate of PCM capsule is significant in the conditions of lower PCM temperature, larger radius PCM capsules and smaller Re number.

(C) The feasibility of a small scale (5kW) CES system is justified by

experimental study in the constructed system based on an open Rankine cycle (without engine). This is because the EG and water solution in the CES system can be charged to be -40 ^{o}C within approximate 7.5 hours and the stored cold can be pumped to the cold heat exchanger (HEX 2) with a sufficient mass flow rate and a low temperature (-33 ^{o}C). However, the cold energy loss in the pipes and cold heat exchanger should be further reduced.

(D) Cold utilisation through a CO2 based Rankine cycle is theoretically studied. It is found that the operating pressure of 65 bar results in the largest storage efficiency, which can be as high as 43.9%. However, with consideration of the actual efficiency of cryogenic pump, regenerator, engine and refrigerator, the storage efficiency is generally between 30%~40%.

The storage efficiency of the CES system can be improved by increasing the operating pressure, and efficiencies of pump, regenerator, engine and refrigerator, or decreasing the back pressure, mass flow rate of CO_2, inlet temperature of engine and environmental temperature.

(E) Experimental results on power consumption/ generation in a piston based engine and ABB motor drive system show the feasibility of a large engine coupled with the new valve scheme for cold-to-power conversion in the CES system. This is because the the net electricity consumption on the motor (EM) in the large engine system is a negative value, indicating an overall electricity generation by the system.

With the large engine, engine power (EP) is apparently larger but the engine efficiency is lower due to poor engine performance caused by the block of the exhaust gas in the chamber. However, it is recommended to use a large engine in the CES system. This is because from the point view of net power generation, the actual efficiency of the small engine is -30.6% while it is 28.0% for the large engine system. As a result, in the presented case study, the large engine with the above actual efficiency leads to a storage efficiency of approximately 22.0% in the CES system.

7.2 Recommendations for the future work

Fundamentals of cold energy storage have been studied in this thesis. These include high density and high grade cold storage, high discharging rate, analysis of storage efficiency, feasibility of small scale CES system, and engine technology for cold-to-power conversion. Nevertheless, there are a few challenges that need to be addressed:

(A) DSC measurements for properties of PCM. As claimed in the thesis,

eutectic PCM solution is adopted for high density, high cold grade and temperature-adaptive storage. Freezing temperature, specific heat capacity and latent heat of PCM need to be measured by DSC. For each case of two PCM solutions in binary system, based on the calculated eutectic composition, DSC measurements for verification of eutectic temperature should be carried out. This is essential for PCM selection for satisfying the requirement of optimal temperature in the specific application.

(B) Study on PCM phase separation and super cooling. For eutectic water-salt solutions, cold storage density is reduced by phase separation and super cooling. By adding water with gelling or thickening, phase separation can be restricted in some degree. Further experimental investigation need to be carried out for obtaining suitable addition for the specific PCM solutions. By adding nucleating agents or exerting physical fields, super cooling degree can be effectively restrained. Experiments with carbon nanofibers, copper and titanium oxide, potassium sulphate and borax are suggested for reducing the super cooling degree.

(C) Experimental study of PCM embedded with metal foams. The effect of metal foams on improving cold discharging rate of PCM modules has been theoretically investigated in chapter 4. However, experimental study is needed for validation of the analytical model. Furthermore, PCM temperature, liquid phase ratio and shape and velocity of the front of interface need to be investigated.

(D) Heat transfer model based on multi-particles. Although combined effect of cold radiation and cold convection is considered for evaluating the cold discharging capacity of PCM capsules, heat transfer model is based on single particle, ignoring the interaction of particles. For cold storage with PCM capsules, multi-particles should be considered in the established model. Cold radiation between particles and thermal conduction through contact of different capsules is suggested to be studied.

(E) Experimental investigation with super critical carbon dioxide. The optimum working fluids in Rankine cycle should have higher enthalpy drops, lower critical pressure and lower boiling point. Based on these criterions, CO_2 is one of the best choices as the working fluids. CO_2 under super critical or super critical pressure is suggested for further investigation due to the better heat transfer characteristic and reduced irreversibility of the heat transfer processes.

(F) Investigation of engine performance with high pressure and high temperature gas under high motor speed. Due to the low pressure and temperature of the gas source, the power generation by the engine system is very limited. However, the improvement of the actual engine efficiency will be a challenge because the gas with high pressure and temperature will have more negative influence on movement of piston and operations of the valves. Furthermore, experiments with higher motor speed are challenged due to the time delay of valves in the system. Therefore, it is suggested that solution of time delay of solenoid valves should be addressed before experiments under higher motor speed.

APPENDIX A Program codes for CES

A1: Parametric study of cold storage efficiency in Rankine cycle based on sub critical carbon dioxide

```
!*****************************************************************
!  ------------------------MAIN PROGRAM----------------------------
!*****************************************************************
   PROGRAM MAIN
   implicit double precision(a-h,o-z)
   implicit integer(i-k,m,n)
   parameter (ncmax=20)   !max number of components in mixture
   character hrf*3, herr*255
   character*255 hf(ncmax),hfmix
   DIMENSION Pre(ncmax),Tem(ncmax),Entha(ncmax),Entro(ncmax)
   common /prnterr/ iprnterr
   iprnterr=-3
   i=1
   hf(1)='CO2.FLD'
   hfmix='HMX.BNC'
   hrf='DEF'
   call SETUP (i,hf,hfmix,hrf,ierr,herr)
   if (ierr.ne.0) write (*,*) herr
   call INFO (1,wm,ttp,tnbp,tc,pc,dc,zc,acf,dip,rgas)
   open(5,file='input.dat')
   open(6,file='result.dat')
   open(7,file='DATA.dat')
    do J=1,172
    read(5,*)
    enddo
```

```
      read(5,*)P_high,P_low,T_engine_inlet,AITA_pump,

&AITA_regen,AITA_engine,AITA_refrig,QM1,QM2,T2IN,P2IN,T_environmen
t
**********************************************
      close(5)
      Tem_envi=T_environment+273.15
      P_WATER=P2IN
     T_WATER=T2IN
     QM_WATER=QM2
     Pre(3)=P_low
     Tem(3)=F40D02(REAL(P_low))
     Entha(3)=F23D02(REAL(P_low))
     Entro(3)=F33D02(REAL(P_low))
     Tem(2)=F40D02(REAL(P_low))
     Entha(2)=F24D02(REAL(P_low))
     Entro(2)=F34D02(REAL(P_low))
     Tem(4)= F65D02(REAL(P_high),REAL(Entro(3)))
     Entha(4)=F71D02(REAL(P_high),REAL(Entro(3)))
     Entha(6)=F25D02(REAL(P_high),REAL(T_engine_inlet))
     Entro(6)=F35D02(REAL(P_high),REAL(T_engine_inlet))
     Eee=F25D02(REAL(70),REAL(300-273)) ! whether superheat is needed
    Ttt=F64D02(REAL(10),REAL(Eee))
    Tem(1)=F65D02(REAL(P_low),REAL(Entro(6)))
    Entha(1)=F71D02(REAL(P_low),REAL(Entro(6)))
    H1act=Entha(6)-AITA_engine*(Entha(6)-Entha(1))
    H4act=Entha(3)-(AITA_pump)**(-1)*(Entha(3)-Entha(4))
    Tem(14)=F64D02(REAL(P_high),REAL(H4act))
    Tem(11)=F64D02(REAL(P_low),REAL(H1act))
```

```
      Tem(7)=Tem(14)+(1-AITA_regen)*(Tem(11)-Tem(14))!revised aita_regen
      Entha(7)=F25D02(REAL(P_low),REAL(Tem(7)))
      Entro(7)=F35D02(REAL(P_low),REAL(Tem(7)))
      Tsat8=F40D02(REAL(P_high))
      Entha(8)=Entha(1)+Entha(4)-Entha(7)
      Tem(8)=F64D02(REAL(P_high),REAL(Entha(8)))
      IF(ABS(Tem(8)-Tsat8).GE.1E-3) THEN
          Tem(8)=F64D02(REAL(P_high),REAL(Entha(8)))
          Entro(8)=F35D02(REAL(P_high),REAL(Tem(8)))
          WRITE(*,*)"Point 8:subcool liquid!"
      ENDIF
      IF(ABS(Tem(8)-Tsat8).LT.1E-3) THEN
          Tem(8)=Tsat8
          h81=F23D02(REAL(P_high))
          s81=F33D02(REAL(P_high))
          h82=F24D02(REAL(P_high))
          s82=F34D02(REAL(P_high))
          x8=(Entha(8)-h81)/(h82-h81)
          Entro(8)=s81+x8*(s82-s81)
          WRITE(*,*)"Point 8:Saturated state:x=",x8
      ENDIF
      H1act=Entha(6)-AITA_regen*(Entha(6)-Entha(1))
      H4act=Entha(3)-(AITA_pump)**(-1)*(Entha(3)-Entha(4))
      q2=Entha(7)-Entha(3)!should be aita_engine
      q1=Entha(6)-Entha(3)+(AITA_pump)**(-1)*(Entha(3)-Entha(4))
      Work_p=AITA_engine*(Entha(6)-Entha(1))-
     &(AITA_pump)**(-1)*(Entha(4)-Entha(3))
      q_total_1=q1*QM1
      q_total_2=q2*QM1
      Work_p_total=Work_p*QM1
```

```
      Eff_heat=Work_p/q1        !note:in_re, so not q2/q1
      Tem2=Tem(2)+273.15              ! calculation previous based on C,not K
      COP_refre_re=1/(Tem_envi/Tem2-1)
      COP_refre_act=COP_refre_re*AITA_refrig
      Power_in=q_total_2/COP_refre_act       !only by refrigerator
      Temperature=F64D02(REAL(P_low),REAL(Entha(6)))
      write(*,*)"If expansion instead, T=",Temperature
      T1IN=Tem(8)
      T_CO2_IN=T1IN
      P_CO2_IN=P_high
      QM_CO2=QM1
      CP_WATER=4200
      CP_CO2=F77D02(REAL(P_CO2_IN),REAL(T_CO2_IN))
      WRITE(*,*)"77777",CP_CO2,P_CO2_IN,T_CO2_IN
      WRITE(*,*)"!!",QM_CO2,T1IN,P_low
      N=0
      IF(ABS(QM_WATER*CP_WATER).GE.ABS(CP_CO2*QM_CO2))THEN
            QC_MIN=CP_CO2*QM_CO2
            QC_MAX=QM_WATER*CP_WATER
      ENDIF
      IF(ABS(QM_WATER*CP_WATER).LT.ABS(CP_CO2*QM_CO2))THEN
            QC_MIN=QM_WATER*CP_WATER
            QC_MAX=CP_CO2*QM_CO2
      ENDIF
      AK_INITIAL=1500
  111   N=N+1
      AK_INITIAL=ALFA*AK_INITIAL+(1-ALFA)*AK_RE
      ANTU_RE= AK_INITIAL*AOUT/QC_MIN
      EBXL_RE=1-EXP(-ANTU_RE)
```

```
    Q_RE=EBXL_RE* QC_MIN*ABS(T1IN-T2IN)
    T1OUT=T1IN+ Q_RE/(CP_CO2*QM_CO2)
    T2OUT=T2IN- Q_RE/(QM_WATER*CP_WATER)
    IF(ABS(T1IN-T2IN).GE.ABS(T1OUT-T2OUT)) THEN
          DEATAT_MAX=ABS(T1IN-T2IN)
          DEATAT_MIN=ABS(T1OUT-T2OUT)
    ENDIF
    IF(ABS(T1IN-T2IN).LT.ABS(T1OUT-T2OUT)) THEN
          DEATAT_MAX=ABS(T1OUT-T2OUT)
          DEATAT_MIN=ABS(T1IN-T2IN)
    ENDIF
    WRITE(*,*)"111111",N,T1OUT,T2OUT
    DEATAT_MEAN=(DEATAT_MAX-DEATAT_MIN)/(LOG(DEATAT_MAX/
   &(DEATAT_MIN+1E-30)))
    AK_RE=Q_RE/(AOUT*DEATAT_MEAN)
    EE=ABS(AK_RE-AK_INITIAL)/AK_RE
    IF(EE.GT.1E-3)   GOTO 111
    Tem(5)=T1OUT
    Pre(5)=P_high
    Entha(5)=F25D02(REAL(P_high),REAL(Tem(5)))
    Entro(5)=F35D02(REAL(P_high),REAL(Tem(5)))
    Esupheat=QM_CO2*(Entha(6)-Entha(5))
    Eff_EES=Work_p_total/(Power_in+Esupheat)
    WRITE(*,*)"99999",(1-Tem_envi/(T_engine_inlet+273.16))
    WRITE(*,*)"**********The calculation is in convergence!!*********"
    WRITE(*,*)"**********The relative error=",EE
    WRITE(*,*)"**********The result of HEX A:"
    WRITE(*,*)"Tem(5)=",Tem(5),          "Th2o_out=",T2OUT
    WRITE(*,*)"EBXL=",   EBXL_RE,        "ANTU=",ANTU_RE
```

```
   WRITE(*,*)"K=",   AK_RE
   WRITE(*,*)'**************QMCO2,AK_RE**********************'
   OPEN(6,FILE='QMCO2_AK.DAT',STATUS='REPLACE')
   DO J=1,20
   WRITE(6,*)QM_CO2,T1OUT,EBXL_RE,ANTU_RE,AK_RE
   END DO
   CLOSE(6)
   WRITE(*,*)"CP_CO2*QM_CO2=",CP_CO2*QM_CO2
   WRITE(*,*)"**************Input for EES****************"
   WRITE(*,*)" P_high=",P_high,"bar"," P_low=", P_low,"bar"
   WRITE(*,*)"T_engine_inlet =",T_engine_inlet,"K"
   WRITE(*,*)" AITA_pump=",AITA_pump," AITA_regen=",AITA_regen
   WRITE(*,*) "AITA_engine =",AITA_engine
   WRITE(*,*)"*************Result for EES****************"
   WRITE(*,*)" Eff_heat=",Eff_heat," Work_p_total=", Work_p_total,"W"
   WRITE(*,*)"COP_refre_act =",COP_refre_act, " Eff_EES=",Eff_EES
   WRITE(*,*)"The max power of cold storage:",          !******** EES
  &" Ecold=",Power_in
   WRITE(*,*)"T_environment=",T_environment,"   0C"
   WRITE(*,*)"Power consumption by pump=",QM1*(Entha(4)-Entha(3)),"W"
   WRITE(*,*)"T=",tem(1),tem(2),tem(3),tem(4),
 &tem(5),T_engine_inlet,tem(7),tem(8)
   WRITE(*,*)"Needed power for HEX A=",
 &QM_CO2*(Entha(5)-Entha(8)),"W"
   write(*,*)"//////////////////////////////////////////////////////"
   WRITE(*,*)" Eff_heat=",Eff_heat," Work_p_total=", Work_p_total,"W"
   WRITE(*,*)"COP_refre_act =",COP_refre_act, " Eff_EES=",Eff_EES
   WRITE(*,*)"heat storage=",
  &Esupheat,"W"
```

```
   WRITE(*,*)"cold storage=",
 &Power_in,"W"
   WRITE(*,*)"Maximum electricity storage=",
&Power_in+Esupheat,"W"
  write(*,*)"////////////////////////////////////////////////////"
  WRITE(*,*)"electricity power for HEX 1=",
 &(Entha(5)-Entha(8))*QM_CO2,"W"
   WRITE(*,*)"q2_total=",q2*QM1,"W"
   WRITE(*,*)"***Copyright by Yanping***"
   END
```

A2: Energy storage control strategy in DES

```
!*****************************************************************
!  ------------------------MAIN PROGRAM----------------------------
!*****************************************************************
   PROGRAM MAIN
   implicit double precision(a-h,o-z)
   implicit integer(i-k,m,n)
   DIMENSION Storage_DES(100),Power_storageout(100)
   DIMENSION Power_generate(100)
 **************************** Part (1) ******************************
   Aita_char=0.9
   Aita_dischar=0.5
   Power_wind=12
   write(*,*)"Please input round trip time T:"
   read(*,*)T
   write(*,*)"Please input logic value:Grid control "
   read(*,*)Grid_control
   IF(Grid_control.EQ.1)    THEN
         write(*,*)"Grid demand gap is under control "
         Power_limit=10
        Do k=1,T
        IF(K.LE.T/2.AND.K.GE.0) THEN
            Power_load=4
            Power_storageout(K)=Power_limit+Power_load-Power_wind
        ENDIF
        IF(K.LE.T.AND.K.GE.T/2) THEN
            Power_load=4
            Power_storageout(K)=Power_limit+Power_load-Power_wind
        ENDIF
```

```
        ENDDO
        storagemin=T/2*(Power_storageout(T)/Aita_dischar-
    &Aita_char*Power_storageout(T/2))
        WRITE(*,*)"888",storagemin
        DO K=1,T
        IF(K.LE.T/2.AND.K.GE.0) THEN
            Storage_DES(K)=Aita_char*Power_storageout(K)*K+storagemin
        ENDIF
        IF(K.LE.T.AND.K.GE.T/2) THEN
        Storage_DES(K)=-1/Aita_dischar*(
&Power_storageout(K)*(K-T/2))+Storage_DES(T/2)
        ENDIF
        ENDDO
  ENDIF
  IF(Grid_control.EQ.0)       THEN
        write(*,*)"DES storage is under control"
        SLOPE1=3
        SLOPE2=6
        storagemin=1
        Do k=1,T
        IF(K.LE.T/2.AND.K.GE.0) THEN
            Storage_DES(K)=SLOPE1*K+storagemin
            Power_load=4
            Power_storageout(K)=SLOPE1/Aita_char
            Power_generate(k)=Power_wind+Power_storageout(K)-
Power_load
        ENDIF
        Timestop=(Storage_DES(T/2)-storagemin)/SLOPE2+T/2
         IF(K.LE.Timestop.AND.K.GE.T/2) THEN
            Storage_DES(K)=Storage_DES(T/2)-SLOPE2*(K-T/2)
```

```
            Power_load=6
            Power_storageout(K)=SLOPE2*Aita_dischar
            Power_generate(k)=Power_wind+ Power_storageout(K)-
Power_load
        ENDIF
        IF(K.LE.T.AND.K.GE.Timestop) THEN
            Storage_DES(K)=storagemin
            Power_storageout(K)=0
            Power_generate(k)=Power_wind+ Power_storageout(K)-
Power_load
        ENDIF
        ENDDO
ENDIF
WRITE(*,*)'**************Storage_DES,t**********************'
OPEN(11,FILE='Storage_DES.DAT',STATUS='REPLACE')
DO K=1,T
WRITE(11,*)K,Power_storageout(K),Storage_DES(K)
END DO
CLOSE(11)
WRITE(*,*)'**************Grid generation,t**********************'
OPEN(12,FILE='Power_generate.DAT',STATUS='REPLACE')
DO K=1,T
WRITE(12,*)K,Power_generate(K),Storage_DES(K)
END DO
CLOSE(12)
write(*,*)"The minimum storage should be:", storagemin,"KW"
END
```

A3: Probabilistic model of electrical energy storage (DES system based)

```
!*****************************************************************
!  ------------------------MAIN PROGRAM----------------------------
!*****************************************************************
      PROGRAM MAIN
      implicit double precision(a-h,o-z)
      implicit integer(i-k,m,n)
      DIMENSION Funcv(500),Fvproba(500),Powerv(500)
*********Step1: model for wind energy generation*************
      Expecv=8.5         !expectation value of wind velocity given
      Shapek=2.0                 ! shape parameter given
      xx=1+1/Shapek
      Taox=0
      DO yy=1,1000
      tt=yy/10.0
     Taox=Taox+2.71828**(-tt)*tt**(xx-1)*(tt/yy)
      ENDDO
      cc=Expecv/Taox
      Velocityout=25
      velocityin=3
      Powermax=1.0
      slope=0.1  ! alfa  should be number    (suppose)
      velocityref=Powermax/slope+velocityin
******************Explanation: real velocity vv=zz/10*****************
      Evaluatev=0
      Evaluatep=0
      this=0       !integration of f(v)*dv
      Do zz=1,Velocityout*10
```

```
      vv=zz/10
      Funcv(zz)=Shapek/cc*(vv/cc)**(Shapek-1)*exp(-(vv/cc)**Shapek)
      Fvproba(zz)=1-exp(-(vv/cc)**Shapek)
      IF(vv.LT.velocityin.AND.vv.GT.velocityref) Powerv(zz)=0
      IF(vv.GT.velocityin.AND.vv.LT.velocityref) Powerv(zz)=slope*vv-
      &slope*velocityin
      IF(vv.GT.velocityref.AND.vv.LT.velocityout) Powerv(zz)=Powermax
      ENDDO
**************************calculation for Ev(v),E(Pw)**********************
       DO ZZ=1,Velocityout*10
       vv=zz/10
       Evaluatev=Evaluatev+vv*Funcv(zz)*(vv/zz)
       Evaluatep=Evaluatep+Powerv(zz)*Funcv(zz)*(vv/zz)
       this=this+Funcv(zz)*(vv/zz)
       ENDDO
************************************************************************
       WRITE(*,*)Evaluatev,Evaluatep,Expecv
       WRITE(*,*)'**************fv(v),v**********************'
       OPEN(10,FILE='fv.DAT',STATUS='REPLACE')
       DO zz=1,Velocityout*10
       WRITE(10,*)zz/10,Funcv(zz)
       END DO
       CLOSE(10)
       WRITE(*,*)'**************Fvproba(v),v**********************'
       OPEN(4,FILE='Fvproba.DAT',STATUS='REPLACE')
       DO zz=1,Velocityout*10
       WRITE(4,*)zz/10,Fvproba(zz)
       END DO
       CLOSE(4)
```

```
      WRITE(*,*)'**************Powerv(v),v**********************'
      OPEN(5,FILE='Powerv.DAT',STATUS='REPLACE')
      DO zz=1,Velocityout*10-1
      WRITE(5,*)zz/10,Powerv(zz)
      END DO
      CLOSE(5)
      WRITE(*,*)'**************Fpproba,v**********************'
      OPEN(6,FILE='Fpproba.DAT',STATUS='REPLACE')
      DO zz=1,Velocityout*10-1
      WRITE(6,*)Powerv(zz),Fvproba(zz)+1-Fvproba(velocityout*10)
      END DO
      CLOSE(6)
**************************Step2:model of DES **************************
*************** the evaluated energy storage is the same  **************
      BEITA=0.4
      Edischar=100
123 Aita_dischar=0.5
      Aita_char=0.9
      Powerfp=(Aita_dischar*Edischar+Evaluatep)/this
      tem=Powerfp/slope+velocityin
      theEvaluatep=0
      that=0
      DO ZZ=tem*10,Velocityout*10
      vv=zz/10
      theEvaluatep=theEvaluatep+Powerv(zz)*Funcv(zz)*(vv/zz)
      that=that+Funcv(zz)*(vv/zz)
      ENDDO
      Echar=Aita_char*(theEvaluatep-Powerfp*that)
      WRITE(*,*)'GOOD',Echar,Edischar
```

```
IF(ABS((Echar-Edischar)/(Echar+1E-30)).GT.1E-3) THEN
Edischar=Edischar+(Echar-Edischar)*BEITA
GOTO 123
ENDIF
WRITE(*,*)'E(Sdch)=E(Sch)=',Edischar
WRITE(*,*)'Pfp=',Powerfp
END
```

APPENDIX B Publications

PUBLICATIONS

[1] **Y.P. Du**, Z. G. Qu, C.Y. Zhao, W. Q. Tao. Numerical study of conjugated heat transfer in metal foam filled double-pipe, Int J of Heat and Mass Transfer, 2010, 53 (21): 4899-4907 (SCI: 644NF, EI: 20103313154965).

[2] **Y.P. Du** and Y.L. Ding. Thermal Analysis of Critical Carbon Dioxide: A Heat Transfer Unit Method, 17th Joint Annual Conference of Chinese Society of Chemical Science and Technology (CSCST) and the Society of Chemical Industry(SCI), Oxford, UK, 9th October,2010.

[3] **Y.P. Du**, Y.L. Li and Y.L. Ding. Cryogenic energy storage based on a critical carbon dioxide cycle, International Conference of Substantial Energy Storage(ICSES), Belfast, UK, 21th~24th February,2011.

[4] **Y. P. Du**, Z. G. Qu, H. J Xu, Z. Y. Li, C. Y. Zhao, W. Q. Tao. Numerical simulation of film condensation on vertical plate embedded in metallic foams, Progress in Computational Fluid Dynamics, 2011, 11(3/4), 198-205.

[5] **Y. P. Du**, C. Y. Zhao, Y. Tian, Z. G. Qu. Analytical considerations of flow boiling heat transfer in metal-foam filled tubes, Heat Mass Transfer, 2012, 48 (1), 165-173.

[6] **Y.P. Du** and Y.L. Ding, et al. Systematical investigation of cryogenic energy storage system with critical carbon dioxide, Sustainable Thermal Energy Management (SusTEM), Newcastle, UK, 25th~26th, October, 2011.

[7] **Y.P. Du** and Y.L. Ding. An analytical investigation of the heat transfer behavior of phase change based thermal energy storage material embedded in metal foams, 11th UK Particle Technology Forum (UKPTF), Loughborough, UK, 4th~5th April,2012.

[8] **Y.P. Du** and Y.L. Ding. Enhancement of cold storage and cold extraction in cryogen based energy storage systems: a review. Applied Energy, to be submitted.

[9] **Y.P. Du** and Y.L. Ding. Analytical investigation of discharging behaviour in PCM capsules considering the combined effect of cold radiation and convection. Energy Conversion and Management, to be submitted.

[10] **Y.P. Du** and Y.L. Ding. Cold to power conversion of a piston based engine in a cold energy storage system: part (I): an experimental study. Energy, to be submitted.

[11] **Y.P. Du** and Y.L. Ding. Investigation of charging and discharging behaviour of a phase change material (PCM) capsule for cold storage applications, The 7th World Congress on Particle Technology (WCPT7 2014), Beijing, China, 19th-22th May, 2014.

Bibliography

1. Qureshi WA, Nair NK, Farid MM: **Impact of energy storage in buildings on electricity demand side management**. *Energy Conversion and Management* 2011, 52(5): 2110-2120.
2. IEEJ-The institute of energy economics, Japan,2005.
3. Oren S: **Capacity Payments and Supply Adequacy in a Competitive Electricity Market**. University of California at Berkeley.
4. Swider DJ: **Compressed air energy storage in an electricity system with significant wind power generation**. IEEE *Transactions on energy conversion* 2007, 22(1):95-102.
5. Lane GA: **Solar heat storage—latent heat materials**. vol. I. Boca Raton, FL: CRC Press, Inc, 1983.
6. Abhat A: **Low temperature latent heat thermal energy storage: heat storage materials**. *Solar Energy* 1981, 30(4):313–332.
7. Sharma A, Tyagi VV, Chen CR, Buddhi D: **Review on thermal energy storage with phase change materials and applications**. *Renewable and Sustainable Energy Reviews* 2009, 13:318-345.
8. Zhang YP, Zhou GB, Lin KP, Zhang QL, Di HF: **Application of latent heat thermal energy storage in buildings: State-of-the-art and outlook**. *Building and Environment* 2007, 42(6): 2197-2209.
9. Soares N, Costa JJ, Gaspar AR, Santos P: **Review of Passive PCM latent heat thermal energy storage systems towards buildings' energy efficiency**. *Energy and Buildings* 2013, 59: 82-103.
10. Hasnain SM: **Review on sustainable thermal energy storage technologies, part 2: cool thermal storage**. *Energy Conversion and Management* 1998, 39(11): 1139-1153.
11. Martin V, He B, Setterwall F: **Direct contact PCM-water cold storage**. *Applied Energy* 2010, 87: 2652-2659.
12. Li G, Hwang YH, Radermacher R, Chun HH: **Review of cold storage materials for subzero applications**. *Energy* 2013, 51:1-17.

13. Li G, Hwang YH, Radermacher R: **Review of cold storage materials for air conditioning application**. *International Journal of Refrigeration* 2012, 35: 2053-2077.
14. Cantor S: **DSC study of melting and solidification of salt hydrates**. *Thermochimica Acta* 1978: 26:39-47.
15. Ryu HW, Woo SW, Shin BC, Kim SD: **Prevention of supercooling and stabilization of inorganic salt hydrates as latent heat storage materials**. *Solar Energy Materials and Solar Cells* 1992, 27:161-172.
16. Telkcs M: **Solar energy storage**. *ASHRAE Journal* 1974, 16(9): 38-44.
17. Vonnegut B: **The nucleation of ice formation by silver iodide**. *Journal of Applied Physics* 1947, 18:593-595.
18. Zalba B, Marin JM, Cabeza LF, Mehling H: **Review on thermal energy storage with phase change: materials, heat transfer analysis and applications**. *Applied Thermal Engineering* 2003, 23(3): 251-283.
19. Xiao M, Feng B, Gong KC: **Preparation and performance of shape stabilized phase change thermal storage materials with high thermal conductivity**. *Energy Conversion and Management* 2002, 43(1): 103-108.
20. Mesalhy O, Lafdi K, Elgafy A, Bowman K: **Numerical study of enhancing the thermal conductivity of phase change material (PCM) storage using high thermal conductivity porous matrix**. *Energy Conversion and Management* 2005, 46(6): 847-867.
21. Knowlen C, Hertzberg A, Mattick AT: **Automotive propulsion using liquid nitrogen**. *AIAA* 94-3349, 1994.
22. Knowlen C, Hertzberg A, Mattick AT: **Cryogenic automotive propulsion**. *AIAA* 94-4224, 1994.
23. Chen H, Cong TN, Yang W, Tan C, Li Y, and Ding Y: **Progress in electrical energy storage system: A critical review**. *Progress in Natural Science* 2009, 19: 291-312.
24. Boese HL, Hencey Jr: **Non-Pollution Motors Including Cryogenic Fluid as the Motive Means**. Patent No. 3,681,609, Aug. 1, 1972.
25. Latter AL, Dooley JL, Hammond RP: **Engine System Using Liquid Air and Combustible Fuel**. Patent No. 4,359,118, Nov. 16, 1982.

26. Onyejekwe DC: **Cold storage using eutectic mixture of NaCl/H2O: An application to photovoltaic compressor vapour freezers**. *Solar & Wind Technology* 1989, 6(1): 11–18.
27. Azzouz K, Leducq D, Gobin D: **Performance enhancement of a household refrigerator by addition of latent heat storage**. *International Journal of Refrigeration* 2008, 31(5): 892–901.
28. Azzouz K, Leducq D, Gobin D: **Enhancing the performance of household refrigerators with latent heat storage: An experimental investigation**. *International Journal of Refrigeration* 2009, 32(7): 1634–1644.
29. Bjork E, Palm B: **Refrigerant mass charge distribution in a domestic refrigerator, part I: transient conditions**. *Applied Thermal Engineering* 2006, 26: 829–837.
30. Cheng WL, Mei BJ, Liu YN, Huang YH, Yuan XD: **A novel household refrigerator with shape-stabilized PCM (Phase Change Material) heat storage condensers: An experimental investigation**. *Energy* 2011, 36(10): 5797-5804.
31. Gin B, Farid MM, Bansal PK: **Effect of door opening and defrost cycle on a freezer with phase change panels**. *Energy Conservation and Management* 2010, 51(12):2698-2706.
32. Oró E, Miró L, Farid MM, Cabeza LF: **Improving thermal performance of freezers using phase change materials**. *International Journal of Refrigeration* 2012, 35(4):984-991.
33. Dong JK, Deng SM, Jiang YQ, Xia L, Yao Y: **An experimental study on defrosting heat supplies and energy consumptions during a reverse cycle defrost operation for an air source heat pump**. *Applied Thermal Engineering* 2012, 37: 380-387.
34. Benjamin G, Mohammed F, Pradeep. B: **Performance of Phase Change Panels Inside a Domestic Freezer** [online]. In: Engineering Our Future: Are We up to the Challenge?: 27 - 30 September 2009, Burswood Entertainment Complex. Barton, ACT: Engineers Australia, 2009: [262]-[271].
35. Critoph RE: **An ammonia carbon solar refrigerator for vaccine cooling**. *Renewable Energy* 1994, 5(1-4): 502-508.
36. Telto ZT, Critoph RE: **Adsorption refrigerator using monolithic carbon-ammonia pair**. *International Journal of Refrigeration* 1997, 20(2): 146-155.

37. Cheng WL, Yuan XD: **Numerical analysis of a novel household refrigerator with shape-stabilized PCM(phase change material) heat storage**. *Energy* 2013, 59(15): 265-276.

38. Berdja M, Abbad B, Laidi M, Yahi F: **Numerical simulation of a phase change material (PCM) in a domestic refrigerator powered by photovoltaic energy. Proceedings of CHT-12**. International Symposium on Advances in Computational Heat Transfer. July 1-6, 2012.

39. Gin B, Farid MM: **The use of PCM panels to improve storage condition of frozen food**. *Journal of Food Engineering* 2010, 100(2): 372-376.

40. Marques AC, Davies GF, Evans JA, Maidment GG, Wood ID: **Theoretical modelling and experimental investigation of a thermal energy storage refrigerator**. *Energy* 2013, 55(15): 457-465.

41. Cabeza LF, Mehling H: **Temperature control with phase change materials**. *Thermal Energy Storage for Sustainable Energy Consumption* 2007, 234: 315-321.

42. Liu MC: **Performance analysis of sub type two stage vapour compression refrigeration system with R600a hydrocarbon refrigerant**. National Taipei University of Technology, June 2010.

43. Wang FQ, Maidment G, Missenden J, Tozer R: **The novel use of phase change materials in refrigeration plant. Part 1: Experimental investigation**. *Applied Thermal Engineering* 2007, 27 (17–18): 2893–2901.

44. Wang FQ, Maidment G, Missenden J, Tozer R: **The novel use of phase change materials in refrigeration plant. Part 2: Dynamic simulation model for the combined system**. *Applied Thermal Engineering* 2007, 27 (17–18): 2902–2910.

45. Wang FQ, Maidment G, Missenden J, Tozer R: **The novel use of phase change materials in refrigeration plant. Part 3: PCM for control and energy savings**. *Applied Thermal Engineering* 2007, 27 (17–18): 2911–2918.

46. Cleland AC: **Food Refrigeration Processes—Analysis, Design and Simulation**. Elsevier Science, London, 1990.

47. Tan HB, Li YZ, Tuo HF, Zhou M, Tian BC: **Experimental study on liquid/solid phase change for cold energy storage of Liquefied Natural Gas (LNG) refrigerated vehicle**. *Energy* 2010, 35:1927–1935.
48. Wu XM, Webb RL: **Thermal and hydraulic analysis of a brazed aluminium evaporator**. *Applied Thermal Engineering* 2002, 22:1369-1390.
49. Kim MH, Bullard CW: **Air-side thermal hydraulic performance of multi-louvered fin aluminium heat exchangers**. *International Journal of Refrigeration* 2002, 25:390-400.
50. Chamra LM, Webb RL: **Advanced micro-fin tubes for evaporation**. *International Journal of Heat and Mass Transfer* 1996, 39(9):1827-1838.
51. Schlager LM, Pate MB, Bergles AE: **Evaporation and condensation heat transfer and pressure drop in horizontal, 12.7 mm micro-fin tubes with refrigeration**. *Journal of Heat Transfer* 1990, 112(22): 1041-1047.
52. Ravigururajan TS, Cuta J, McDonald CE, Drost MK : **Effects of heat flux on two-phase flow characteristics of refrigerant flows in a micro-channel heat exchanger**. *American Society of Mechanical Engineers*, Heat Transfer Division, (Publication) HTD 1996, 329(7): 167-178.
53. Cross W, Ramshaw C: **Process intensification: laminar flow heat transfer**. Chemical Engineering Research& Design 1986, 64(4):293–301.
54. Han YH, Liu Y, Li M: **A review of development of micro-channel heat exchanger applied in air-conditioning system**. *Energy Procedia* 2012, 14: 148–153.
55. Radermacher R, Kim K: **Domestic refrigerators: recent developments**. *International Journal of Refrigeration* 1996, 19(1): 61–69.
56. Tulapurkar, C, Subramaniam PR, Thagamani, G, Thiyagarajan R: **Phase change materials for domestic refrigerators to improve food quality and prolong compressor off time**. In: International refrigeration and air conditioning conference at Purdue; 2010.
57. Gerlach DW, Newell TA: **Dual Evaporator Household Refrigerator Performance Testing and Simulation**. University of Illinois at Urbana-Champaign.
58. Miyazaki T, Akisawa A, Saha BB: **The performance analysis of a novel dual evaporator type three-bed adsorption chiller**. *International Journal of Refrigeration* 2010, 33(2): 276–285.

59. Abhat A: **Low temperature latent heat thermal energy storage: heat storage materials**. *Solar Energy* 1983, 30: 313-332.

60. Hägg C: **Ice slurry as secondary fluid in refrigeration systems**. School of Industrial Engineering and Management, Royal Institute of technology (KTH), Licentiate thesis, Stockholm; November 2005.

61. Kumano H, Asaoka T, Saito A, Okawa S: **Study on latent heat of fusion of ice in aqueous solutions**. *International Journal of Refrigeration* 2007, 30:267-273.

62. Torregrosa-Jaime B, López-Navarro A, Corberán JM, Esteban-Matías JC, Klinkner L, Payá J: **Experimental analysis of a paraffin-based cold storage tank**. *International Journal of Refrigeration* 2013, 36(6): 1632-1640.

63. Butala V, Stritih U: **Experimental investigation on PCM cold storage**. *Energy and Buildings* 2009, 41:354-359.

64. Ukrainczyk N, Kurajica S, Šipušić J: **Thermophysical comparison of five commercial paraffin waxes as latent heat storage materials**. *Chemical and Biochemical Engineering* 2010, 24(2): 129-137.

65. Kauranen P, Peippo K, Lund PD: **An organic PCM storage system with adjustable melting temperature**. *Solar Energy* 1991, 46(5): 275-278.

66. Guo NN: **Thermal properties research of the multivariate organic phase change materials for cooling system** (Master thesis). College of power engineering, Chongqing University, PR China; 2008.

67. Michaud F, Mondieig D, Soubzmaigne V, Negrier P, Haget Y, Tauler E: **A system with a less than 2 degree melting window in the range within _31 _C and _45 _C: chlorobenzene-bromobenzene**. *Materials Research Bulletin* 1996, 31(8): 943-950.

68. Gece G: **The use of quantum chemical methods in corrosion inhibitor studies**. *Corrosion Science* 2008, 50(11), 2981-2992.

69. Bouayed M, Rabaa H, Srhiri A, Saillard JY, Bachir AB, Beuze A: **Experimental and theoretical study of organic corrosion inhibitors on iron in acidic medium**. *Corrosion Science* 1998, 41(3): 501–517.

70. Lebrini M, Lagrenée M, Vezin H, Traisnel M, Bentiss F: **Experimental and theoretical study for corrosion inhibition of mild steel in normal**

hydrochloric acid solution by some new macrocyclic polyether compounds. *Corrosion Science* 2007, 49:2254-2269.

71. Quraishi MA, Sardar R: **Corrosion inhibition of mild steel in acid solutions by some aromatic oxadiazoles**. *Materials Chemistry and Physics* 2002,78: 425–431.

72. Stupnišek-Lisac E, Podbršc ˇ ek S, Soric´ T: **Non-toxic organic zinc corrosion inhibitors in hydrochloric acid**. *Journal of Applied Electrochemistry* 1994, 24: 779–784.

73. Touhami F, Aouniti A, Abed Y, Hammouti B, Kertit S, Ramdani A, Elkacemi K: **Corrosion inhibition of armco iron in 1 M HCl media by new bipyrazolic derivatives**. *Corrosion Science* 2000, 42(6): 929–940.

74. Tang L, Li X, Li L, Mu G, Liu G: **Interfacial behavior of 4-(2-pyridylazo) resorcin between steel and hydrochloric acid**. *Surface and Coatings Technology* 2006, 201 (1-2) 384–388.

75. Baran G, Sari A: **Phase change and heat transfer characteristics of a eutectic mixture of palmitic and stearic acids as PCM in a latent heat storage system**. *Energy Conversion and Management* 2003, 44(20):3227-3246.

76. Lv SL, Zhu N, Feng GH: **Eutectic mixtures of capric acid and lauric acid applied in building wallboards for heat energy storage**. *Energy and Buildings* 2006, 38(6): 708-711.

77. Zhang JJ, Zhang JL, He SM, Wu KZ, Liu XD: **Thermal studies on the solid –liquid phase transition in binary systems of fatty acids**. *Thermochimica Acta* 2001, 369(1-2):157–160.

78. Sari A, Kaygusuz K: **Thermal performance of a eutectic mixture of lauric and stearic acids as PCM encapsulated in the annulus of two concentric pipes**. *Solar Energy* 2002, 72(6):493–504.

79. Cedeno FO, Prieto MM, Espina A, Garcia JR: **Measurements of temperature and melting heat of some pure fatty acids and their binary**

and ternary mixtures by differential scanning calorimetry. *Thermochimica Acta* 2001, 369(1-2):39–50.

80. Tayeb A: **Organic–inorganic mixtures for solar energy storage systems**. *Energy Conversion Management* 1995, 36(10):969–974.

81. Feilchenfeld H, Fuchs F, Kahana F, Sarig S: **The melting point adjustment of calcium chloride hexahydrate by addition potassium chloride or calcium bromide hexahydrate**. *Solar Energy* 1985;34:199–201.

82. Jotshi CK, Hsieh CK, Goswami DY, Klausner JF, Srinivasan N: **Thermal storage in ammonium alum/ammonium nitrate eutectic for solar space heating applications**. Applied Thermal Engineering 1998, 120:20–24.

83. Sifrini I: **Ph´enom`enes de cristallisations dans des solutions salines aqueuses `a l'´etat dispers´e et sous forme de gouttes**. Th`ese de Doctorat, Universit´e de Pau et des Pays de l'Adour, 1983.

84. Sassi O, Siffrini I, Dumas JP, Clausse D: **Theoretical curves in thermal analysis for the melting of binaries showing solid solution**, *Phase Transitions* 1988, 13: 101–111.

85. Jamil A, Kousksou T, Zeraouli Y, Gibout S, Dumas JP: **Simulation of the thermal transfer during an eutectic melting of a binary solution**. *Thermochimica Acta* 2006, 441(1):30-34.

86. Lamberg P, Lehtiniemi R, Henell AM: **Numerical and experimental investigation of melting and freezing processes in phase change material storage**. *International Journal of Thermal Sciences* 2004, 43:277-287.

87. Alexiades V, Solomon AD: **Mathematical Modelling of Melting and Freezing Processes**. Hemisphere, Washington, DC, 1993.

88. Myers GE: **Analytical Methods in Conduction Heat Transfer**. McGraw-Hill, New York, 1971.

89. Sparrow EM, Schmidt RR, Ramsey JW: **Experiments on the role of natural convection in the melting of solids**. *Journal of Heat Transfer* 1978, 100: 11–16.

90. Bathelt AG, Viskanta R, Leidenfrost W: **An experimental investigation of natural convection in the melted region around a heated horizontal cylinder**. *Journal of Fluid Mechanisms* 1979, 90: 227–239.

91. Gobin D: **Role de la convection thermique dans les processus de fusion-solidification**. Ecole d_ete, GUT-CET, Mod_elisation num_erique en thermique, Institut d_etudes scientifiques de Carg_ese, 1992.

92. Dincer I, Rosen MA: **Thermal energy storage, Systems and Applications**. John Wiley & Sons, Chichester (England), 2002.

93. Hirata T, Makino Y, Kaneko Y: **Analysis of natural convection melting inside isothermally heated horizontal rectangular capsule**. *Wärme- und Stoffübertag* 1993, 28:1–9.

94. Ho CD, Tu JW: **Evaluation of a recirculation scheme for ice storage melting with air as the working fluid**. *Heat Transfer Engineering* 2008, 29:295–305.

95. Voller V, Cross M: **Accurate solutions of moving boundary problems using the enthalpy method**. *International Journal of Heat Mass Transfer* 1981, 24: 545–556.

96. Costa M, Buddhi D, Oliva A: **Numerical simulation of latent heat thermal energy storage system with enhanced heat conduction**. *Energy Conversion* 1998, 39 (3/4):319–330.

97. Bonacina C, Comini G, Fasano A, Primicerio M: **Numerical solution of phase-change problems**. *International Journal of Heat Mass Transfer* 1973, 16: 1825–1832.

98. Erek A, Ilken Z, Acar MA: **Experimental and numerical investigation of thermal energy storage with a finned tube**. *International Journal of Energy Resources* 2005, 29:283–301.

99. Cabeza LF, Mehling H, Hiebler S, Ziegler F: **Heat transfer enhancement in water when used as PCM in thermal energy storage**. *Applied Thermal Engineering* 2002, 22:1141–1151.

100. Kazmierczak MJ, Nirmalanandhan V: **Heat transfer augmentation for external ice-on-tube TES system using porous cooper mesh to increase volumetric ice production**. *International Journal of Refrigeration* 2006, 29(6):1020–1033.

101. Tong X, Khan JA, Amin MR: **Enhancement of heat transfer by inserting a metal matrix into phase change material**. *Numerical Heat Transfer*, Part A 1996, 30:125–141.

102. Fan L, Khodadadi JM: **Thermal conductivity enhancement of phase change materials for thermal energy storage: a review**. *Renewable and Sustainable Energy Reviews* 2011, 15(1):24–46.

103. Hoover MJ, Grodzka PG, O'Neill MJ: **Space thermal control development**. Lockheed Huntsville Research and Engineering Center Final Report, LMSCHREC D225500; 1971, 81 pp.

104. Knowles TR, Webb GW: **M/PCM composite thermal storage materials**. In: AIAA 22nd Thermophysics Conference; 1987.p. 6 (Paper AIAA-87-1489).

105. Henze HR, Humphrey JAC: **Enhanced heat conduction in phase-change thermal energy storage devices**. *International Journal of Heat and Mass Transfer* 1981,24:459–474.

106. Bentilla EW, Sterrett KF, Karre LE: **Research and development study on thermal control by use of fusible materials**. Northrop Space Laboratories Interim Report (NSL-65-16-1). NASA Marshall Space Flight Center; 1966, 179 pp.

107. De Jong AG, Hoogendoorn CJ: **Improvement of heat transport in paraffins for latent heat storage systems, in thermal storage of solar energy**. In: Proceedings of an International TNO—Symposium. Amsterdam, The Netherlands: Martinus Nijhoff Publishers; 1981. p. 123–33.

108. Velraj R, Seeniraj RV, Hafner B, Faber C, Schwarzer K: **Heat transfer enhancement in a latent heat storage system**. *Solar Energy* 1999;65:171–180.

109. Fukai J, Oishi A, Kodama Y, Kanou M, Miyatake O: **Improvement of discharge characteristics of latent heat thermal storage unit by using carbon fibers**. In: Proceedings of the 5th ASME/JSME Joint Thermal Engineering Conference; 1999.p. 7 (CD ROM, paper AJTE99-6338).

110. Cabeza LF, Mehling H, Hiebler S, Ziegler F: **Heat transfer enhancement in water when used as pcm in thermal energy storage**. *Applied Thermal Engineering* 2002;22:1141–1151.

111. Hirasawa Y, Saito A, Takegoshi E, Imura S: **Study on phase change of heterogeneous composite materials: effects of parameters on solidification process**. *ASME/JSME Thermal Eng Proc* 1991, 1:225–230.

112. Hirasawa Y, Takegoshi E, Saito A, Okui K, Tokisawa M: **An experimental study on melting process of ice containing cooper solids**. In: Proceedings of the 4th symposium on thermal engineering and science for cold regions; 1993. p. 319–325.

113. Shiina Y, Inagaki T: **Study on the efficiency of effective thermal conductivities on melting characteristics of latent heat storage capsules**. *International Journal of Heat and Mass Transfer* 2005, 48:373–383.

114. Hirasawa Y, Takegoshi E, Takeshita E, Saito A: **Phase change characteristics of test materials with heterogeneous composite materials: experimental discussion on meeting process**. *Trans JAR* 1990; 7:77–84.

115. Calvet N: **Stockages thermiques performants et durables pour procedes solaires: des basses aux hautes temperatures**. Pdh Thesis, Université de Perpignan, France; 2010.

116. Yu W, Choi SUS: **The role of interfacial layers in the enhanced thermal conductivity of nanofluids: A renovated Maxwell model**. *Journal of Nanoparticle Research* 2003, 5: 167–171.

117. Maxwell JC, 1873. **Electricity and Magnetism**. Clarendon Press, Oxford, UK.

118. Zhang Y, Faghri A: **Heat transfer enhancement in latent heat thermal energy storage system by using the internally finned tube**. *International Journal of Heat and Mass Transfer* 1996, 15:3165–3173.

119. Hendra R, Hamdani, Mahlia TMI, Masjuki HH: **Thermal and melting heat transfer characteristics in a latent heat storage system using mikro**. *Applied Thermal Engineering* 2005, 25:1503–1515.

120. Agyenim F, Eames P, Smyth M: **Heat transfer enhancement in medium temperature thermal energy storage system using a multitube heat transfer array**. *Renewable Energy* 2010, 35(1):198–207.

121. Trp A, Lenic K, Frankovic B: **Analysis of the influence of operating conditions and geometric parameters on heat transfer in water-paraffin**

shell-and-tube latent thermal energy storage unit. *Applied Thermal Engineering* 2006, 26:1830–1839.

122. Patankar SV: **Numerical heat transfer and fluid flow**. New York: Hemisphere; 1980.
123. Laybourn DR: **Thermal energy storage with encapsulated ice**. *ASHRAE Trans* 1988, 94 (1): 1971-1988.
124. Chen SL, Yue JS: **Thermal performance of cool storage in packed capsules for air conditioning**. *Heat Recovery Systems and CHP* 1991, 11(6): 551–561.
125. Chen SL, Chen CL, Tin CC et al: **An experimental investigation of cold storage in an encapsulated thermal storage tank**. *Experimental Thermal and Fluid Science* 2000, 23(3–4) :133–144.
126. Arnold D: **Laboratory performance of an encapsulated- ice store**. *ASHRAE Trans* 1991, 97: 1170-1178.
127. Adref KT, Eames IW: **Experiments on charging and discharging of spherical thermal (ice) storage elements**. *International Journal of Energy Research* 2002, 26(11): 949–964.
128. Ismail KAR, Henrique JR: **Numerical and experimental study of spherical capsules packed bed latent heat storage system**. *Applied Thermal Engineering* 2002, 22:1705–1716.
129. Ismail KAR, Henrique JR, Silva TM: **A parametric study on ice formation inside a spherical capsule**. *International Journal of Thermal Sciences* 2003, 42:881–887.
130. Hawlader MNA, Uddin MS, Zhu HJ: **Encapsulated phase change materials for thermal energy storage: Experiments and simulation**. *International Journal of Energy Research* 2002, 26(2): 159–171.
131. Cheralathan M, Velraj R, Renganarayanan S: **Performance analysis on industrial refrigeration system integrated with encapsulated PCM-based cool thermal energy storage system**. *International Journal of Energy Research* 2007, 31(14): 1398–1413.
132. Schossig P, Henning HM, Gschwander S, Haussmann T: **Micro-encapsulated phase-change materials integrated into construction materials**. *Solar Energy Materials and Solar Cells* 2005; 89(2–3): 297–306.

133. Farid M, Smith M, Sabbah R, Al-Hallaj S: **Miniaturized refrigeration system with advanced PCM micro encapsulation technology**. Proceedings of the Fifth International Conference on Nanochannels, Microchannels and Minichannels ICNMM2007 June 18-20, 2007, Puebla, Mexico.

134. Hu XX, Zhang YP: **Novel insight and numerical analysis of convective heat transfer enhancement with microencapsulated phase change material slurries: laminar flow in a circular tube with constant heat flux**. *International Journal of Heat and Mass Transfer* 2002, 45(15): 3163-3172.

135. Charunyakorn P, Sengupta S, Roy SK: **Forced convection heat transfer in microencapsulated phase change material slurries: flow in circular ducts**. *International Journal of Heat and Mass Transfer* 1991, 34 (3): 819–833.

136. Goel M, Roy SK, Sengupta S: **Laminar forced convection heat transfer in microencapsulated phase change material suspensions**. *International Journal of Heat and Mass Transfer* 1994, 37 (4): 593–604.

137. Zhang YW, Faghri A: **Analysis of forced convection heat transfer in microcapsulated phase change material suspensions**. *Journal of Thermophysics, Heat Transfer* 1995, 9 (4): 727–732.

138. Yasushi Y, Hiromi T, Alexander TP, Naoyuki K: **Characteristics of microencapsulated PCM slurry as a heat-transfer fluid**. *AIChE J* 1999, 45(4): 696–707.

139. Alisetti EL, Roy SK: **Forced convection heat transfer to phase change material slurries in circular ducts**. *Journal of Thermophysics, Heat Transfer* 2000, 14 (1): 115–118.

140. Mohamed MM: **Solidification of phase change material on vertical cylindrical surface in holdup air bubbles**. *International Journal of Refrigeration* 2005, 28:403–411.

141. Gschwander S, Schossig P, Henning H-M: **Micro-encapsulated paraffin in phase-change slurries**. *Sol Energy Mater Sol Cells* 2005, 89:307–315.

142. Asashina T, Tajiri K, Kosaka M. **Thermal properties of organic and inorganic thermal storage materials in direct contact with heat carriers**. *High Temp–High Press* 1992, 24:415–420.

143. Saito A, Utaka Y, Okuda K, Katayama K: **Basic research on latent heat thermal energy storage by direct contact melting and solidification. 2. Heat transfer characteristics in direct contact solidification of n-eicosane as PCM**. *Nippon Reito Kyokai Ronbunshu* 1986, 3(1):51–59 [in Japanese].

144. Saito A, Utaka Y, Shinoda K, Katayama K: **Basic Research on the latent heat thermal energy storage utilizing the contact melting phenomena**. *Bulletin of JSME* 1986, 29(255): 2946-2952.

145. Kiatsiriroat T, Tiansuwan J, Suparos T, Thalang KN: **Performance analysis of a direct-contact thermal energy storage-solidification**. *Renew Energy* 2000, 20: 195–206.

146. Alhazmy MM, Najjar YSH: **Augmentation of gas turbine performance using air coolers**. *Applied Thermal Engineering* 2004, 24(2-3): 415-429.

147. Anon: **Maximize hot day output with compressor inlet water injection**. *Diesel and Gas Turbine Worldwide* (May–June) (2001) 24–25.

148. Anon: **Swirl flash: one year on**. *Modern Power Systems* (April) (2002) 26–27.

149. Anon: **Fogging improvements for inlet cooling systems**. *Diesel and Gas Turbine Worldwide* (June) (2002) 36–37.

150. Johnson RS: **The theory and operation of evaporative coolers for industrial gas turbine installations**. Paper presented in the Gas Turbine and Aeroengine Congress and Exposition, June 5–9, 1988, Amsterdam, The Netherlands, Paper no. 88-GT-41.

151. Kim TS, Ro ST: **Power augmentation of combined cycle power plants using cold energy of liquefied natural gas**. *Energy* 2000, 25(9): 841-856.

152. Ondryas IS, Wilson DA, Kawamoto M, Haub GL: **Options in gas turbine power augmentation using inlet air chilling, engineering for gas turbine and power**. *Transactions of the ASME* 1991,113: 203–211.

153. Mercer M: **One-stop shop for inlet cooling systems**. *Diesel and Gas Turbine Worldwide* (June) (2002) 10–13.

154. Hernández AC, Medina A, Roco JMM: **Power and efficiency in a regenerative gas turbine**. *Journal of Physics D: Applied Physics* 1995, 28: 2020–2023.

155. Vecchiarelli J, Kawall JG, Wallace JS: **Analysis of a concept for increasing the efficiency of a Brayton cycle via isothermal heat addition**. *International Journal of Energy Research* 1997, 21(2): 113-127.

156. Göktun S, Yavuz H: **Thermal efficiency of a regenerative Brayton cycle with isothermal heat addition**. *Energy Conversion and Management* 1999, 40(12): 1259-1266.

157. Woods WA, Bevan PJ, Bevan DI: **Output and efficiency of the closed cycle gas turbine**. *Proc. Instn Mech. Engrs, Part A* 1991, 205(A1): 59-66.

158. Frost TH, Agnew B, Anderson A: **Optimizations for Brayton-Joule gas turbine cycles**. *Journal of Power and Energy* 1992, 206(4): 283-288.

159. Hung TC, Shai TY, Wang SK: **A review of organic Rankine cycles (ORCs) for the recovery of low-grade waste heat**. *Energy* 1997, 22:661–667.

160. Larjola J: **Electricity from industrial waste heat using high-speed organic Rankine cycle (ORC)**. *Int J Prod Econ* 1995, 41:227–235.

161. Nelson CR: **50% Brake thermal efficiency achieved at 2010 emissions**. In: 12th Annual diesel engine emissions reduction (DEER) conference. 2006.

162. Nelson CR: **In-vehicle exhaust energy recovery for thermal efficiency improvement**. In: 12th Annual diesel engine emissions reduction (DEER) conference. 2006.

163. Lee KM, Kuo SF, Chien ML, Shih YS: **Parameter analysis on organic Rankine cycle energy recovery system**. *Energy Conversion Management* 1988, 28: 129–136.

164. Huang TC: **Waste heat recovery of organic Rankine cycle using dry fluids**. *Energy Conversion and Management* 2001, 42(5): 539-553.

165. Liu BT, Chien KH, Wang CC: **Effect of working fluids on organic Rankine cycle for waste heat recovery**. *Energy* 2004, 29(8): 1207-1217.

166. Hung TC, Shai TY, Wang SK: **A review of organic Rankine cycles (ORCs) for the recovery of low-grade waste heat**. *Energy*, 1997, 22 (7): 661–667.

167. Chen Y, Lundqvist P, Johansson A, Platell P: **A comparative study of the carbon dioxide transcritical power cycle compared with an organic rankine cycle with R123 as working fluid in waste heat recovery**. *Applied thermal engineering* 2006, 26: 2142-2147.

168. Kaushik SC, Singh M, Dubey A: **Thermodynamic modelling of single/dual organic fluid Rankine cycle cooling systems: a comparative study**. *International Journal of Ambient Energy* 1994, 15 (1): 37–50.

169. Manning L, Schneider RN: **Nitrogen Vapor Engine**. Patent No. 3,786,631, Jan. 22, 1974.

170. West CW, Lee LE, Norris AO: **Vehicle Utilizing Cryogen fuel**. Patent No. 4,106,581, Aug.15, 1978.

171. http://www.theaircar.com/

172. http://freeenergy.co.za

173. Oxley AJ: **Methods and Means for Storing Energy**. Patent No. 4,227,374, Oct. 14, 1980.

174. Latter AL, Dooley JL, Hammond RP: **Engine System Using Liquid Air and Combustible Fuel**. Patent No. 4,359,118, Nov. 16, 1982.

175. Williams J, Knowlen C, Mattick AT, Hertzberg A: **Frost-Free Cryogenic Heat Exchangers for Automotive Propulsion**. *AIAA* 97-3168.

176. Knowlen C, Williams J, Mattick AT, Deparis H, Hertzberg A: **Quasi-isothermal expansion engines for liquid nitrogen automotive propulsion**. SAE 972649, 1997.

177. Oró E, Gracia A, Castell A, Farid MM, Cabeza LF: **Review on phase change materials (PCMs) for cold thermal energy storage applications**. *Applied energy* 2012, 99: 513-533.

178. Buongiorno J: **Convective transport in nanofluids**. *Journal of Heat Transfer* 2006, 128: 240–250.

179. Shin D, Banerjee D: **Enhancement of specific heat capacity of high-temperature silica-nanofluids synthesized in alkali chloride salt eutectics for solar thermal-energy storage applications**. *International Journal of Heat and Mass Transfer* 2011, 54(5-6): 1064-1070.

180. Ding MS, Xu K, Jow TR: **Liquid-solid phase diagrams of binary carbonates for lithium batteries**. *Journal of The Electrochemical Society* 2000, 147(5):1688-1694.

181. Nelson IC, Banerjee D, Ponnappan R: **Flow loop experiments using polyalphaolefin**. *Journal of Thermophysics, Heat Transfer* 2009, 23: 752–761.

182. Shin D, Banerjee D: **Enhanced specific heat of silica nanofluid**. *ASME J. Heat Transfer* 2011, 133: 024501–024504, doi:10.1115/1.4002600.

183. Zhou SQ, Ni R: **Measurement of the specific heat capacity of water-based Al2O3 nanofluid**. *Appl. Phys. Lett* . 92, 093123 (2008).

184. Eastman JA, Choi SUS, Li S, Thompson LJ: **Enhanced thermal conductivity through the development of nanofluids**. in: Proceedings of the Symposium on Nanophase and Nanocomposite Materials II, vol. 457, Materials Research Society, 1997, pp. 3–11.

185. Xuan Y, Li Q: **Heat transfer enhancement of nanofluids**. *International Journal of Heat Fluid Flow* 2000, 21: 58–64.

186. Murshed SMS, Leong KC, Yang C: **Enhanced thermal conductivity of TiO2– water based nanofluids**. *International Journal of Thermal Science* 2005, 44: 367–373.

187. Das SK, Putra N, Thiesen P, Roetzel W: **Temperature dependence of thermal conductivity enhancement for nanofluids**. *ASME J. Heat Transfer* 2003, 125: 567–574.

188. Keblinski P, Prasher R, Eapen J: **Thermal conductance of nanofluids: is the controversy over?** *Journal of Nanoparticle Research* 2008, 10: 1089–1097.

189. Yu W, Choi SUS: **The role of interfacial layers in the enhanced thermal conductivity of nanofluids: a renovated Maxwell model**. *Journal of Nanoparticle Research* 2003, 5: 167-171.

190. Lamberg P: **Approximate analytical model for two-phase solidification problem in a finned phase-change material storage**. *Applied Energy* 2004, 77: 131-152.

191. Agyenim F, Hewitt N, Eames P, Smyth M: **A review of materials, heat transfer and phase change problem formulation for latent heat thermal energy storage systems (LHTESS)**. *Renewable and Sustainable Energy Reviews* 2010, 14: 615–628.

192. Zhao, CY, Lu, W, Tian Y: **Heat transfer enhancement for thermal energy storage using metal foams embedded within phase change materials (PCMs)**. *Solar Energy* 2010, 84 (8): 1402-1412.

193. Boomsma K, Poulikakos D: **On the effective thermal conductivity of a threedimensionally structured fluid-saturated metal foam**. *International of Journal of Heat Mass Transfer* 2001, 44: 827 –836.

194. Yang SM, Tao WQ: **Heat Transfer**. Higher Educational Press, 1998.

195. Zhao CY, Tassou SA, Lu TJ: **Analytical considerations of thermal radiation in cellular metal foams with open cells**. *International Journal of Heat and Mass Transfer* 2008, 51(3-4): 929-940.

196. Zhao FY, Ding YL, Chen HS, Li YL, Zhang XJ.: **Cryogenic electricity energy storage** – Report for EPSRC Project: Bio-fuel Micro-Trigeneration with Cryogenic Energy Storage, 2009.

197. Silva GA, Miller Reid C: **Accurate vapor pressure equation for refrigerants**. *Fluid Phase Equilibria* 1995,111(2): 203-212.

198. Silva GA, Hall KR: **A saturated liquid density equation for refrigerants**. *Fluid Phase Equilibria* 1997, 131(1-2): 97-105.

199. Eslami H, Sabzi F: **The ISM Equation of State Applied to Refrigerants**. *International Journal of Thermophysics* 1999, 20(5):1547-1555.

200. Huang FH, Li MH: **An accurate equation of state for carbon dioxide**. University of Oklahoma.